

AERODYNAMIC ANALYSIS OF A PROPELLER IN A TURBULENT BOUNDARY LAYER FLOW

by

Felipe Ferreira Lachowski

A Thesis Submitted to the Faculty of
The College of Engineering and Computer Science
in Partial Fulfillment of the Requirements for the Degree of
Master of Science

Florida Atlantic University

Boca Raton, Florida

May 2013

UMI Number: 1523427

All rights reserved

INFORMATION TO ALL USERS

The quality of this reproduction is dependent upon the quality of the copy submitted.

In the unlikely event that the author did not send a complete manuscript and there are missing pages, these will be noted. Also, if material had to be removed, a note will indicate the deletion.



UMI 1523427

Published by ProQuest LLC (2013). Copyright in the Dissertation held by the Author.

Microform Edition © ProQuest LLC.

All rights reserved. This work is protected against unauthorized copying under Title 17, United States Code



ProQuest LLC.
789 East Eisenhower Parkway
P.O. Box 1346
Ann Arbor, MI 48106 - 1346

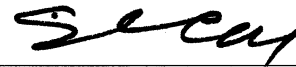
AERODYNAMIC ANALYSIS OF A PROPELLER IN A TURBULENT BOUNDARY LAYER FLOW

by

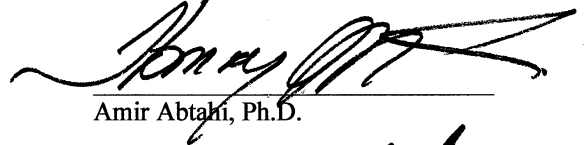
Felipe Ferreira Lachowski

This thesis was prepared under the direction of the candidate's thesis advisor, Dr. Stewart Glegg, Department of Ocean and Mechanical Engineering, and has been approved by the members of his supervisory committee. It was submitted to the faculty of the College of Engineering and Computer Science and was accepted in partial fulfillment of the requirements for the degree of Master of Science.

SUPERVISORY COMMITTEE:



Stewart Glegg, Ph.D.
Thesis Advisor



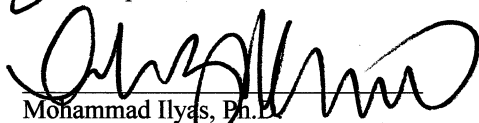
Amir Abtahi, Ph.D.



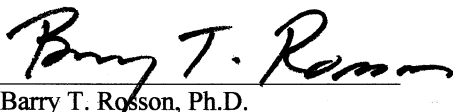
Davood Moslemian, Ph.D.



Javad Hashemi, Ph.D.
Chair, Department of Ocean and Mechanical Engineering



Mohammad Ilyas, Ph.D.
Interim Dean, College of Engineering and Computer Science



Barry T. Rosson, Ph.D.
Dean, Graduate College

April 8, 2013
Date

ACKNOWLEDGEMENTS

The author feels very fortunate to have had so many influential and dedicated human beings along his side throughout the completion of this thesis. First and foremost, he will always be grateful to his mentor Dr. Stewart Glegg for providing the opportunity to work along his side and benefit from his supervision. Dr. Stewart Glegg, a truly involved fluid dynamicist, whose endless knowledge, dedication, career suggestions, and influence will not be forgotten. Also, the author owes a great deal of gratitude to Dr. Davood Moslemian and Dr. Amir Abtahi for their support in this thesis, as well as, throughout the author's undergraduate education.

The author also wishes to acknowledge his fellow team members Skyler Brian and Emi Kawashima for their support, encouragement, and interesting lunch conversations. Also, the author wishes to thank the team of students at Virginia Tech for their assistance in wind tunnel data and their hospitality during a visit to Blacksburg, Virginia. A special thanks to Dr. Nathan Alexander for his indispensable efforts in obtaining all the experimental data and photographs shown in this thesis and constant communication throughout this project.

Furthermore, the author cannot thank enough his amazing parents, beloved girlfriend, family members, and close group of friends for their encouragement and moral support. Besides, getting through these stressful times would not have been possible without them and for that the author thanks you.

Last but most definitely not least, the author is very grateful towards the Office of Naval Research for providing a generous grant (N00014-10-1-0910) which has sponsored this assignment, as well as, Florida Atlantic University's partial funding of the author's education.

On a humorous side note, the author believes that Kaldi, the Ethiopian goatherder, is not acknowledged as much as he should be, for as the legend of "The Dancing Goats" goes, discovering coffee. Therefore, the author thanks Kaldi for over 400 cups of this amazing substance, which has kept the author "dancing" throughout the writing of his thesis.

ABSTRACT

Author: Felipe Ferreira Lachowski
Title: Aerodynamic Analysis of a Propeller in a Turbulent Boundary Layer Flow
Institution: Florida Atlantic University
Thesis Advisor: Dr. Stewart Glegg
Degree: Master of Science
Year: 2013

Simulating the exact chaotic turbulent flow field about any geometry is a dilemma between accuracy and computational resources, which has been continuously studied for just over a hundred years. This thesis is a complete walk-through of the entire process utilized to approximate the flow ingested by a Sevik-type rotor based on solutions to the Reynolds Averaged Navier-Stokes equations (RANS). The Multiple Reference Frame fluid model is utilized by the code of ANSYS-FLUENT and results are validated by experimental wake data. Three open rotor configurations are studied including a uniform inflow and the rotor near a plate with and without a thick boundary layer. Furthermore, observations are made to determine the variation in velocity profiles of the ingested turbulent flow due to varying flow conditions.

DEDICATION

In considering the sacrifices I have made towards the advancement of my understanding of the world of fluid dynamics, I think of my parents. This thesis is dedicated to my mother, Luiza Lachowski, and father, Floriano Lachowski, for their life's dedication, support, and the insurmountable sacrifices they have made to get me where I am today. My parents, whom I consider a blessing, are the reason I have become who I am today.

AERODYNAMIC ANALYSIS OF A PROPELLER IN A TURBULENT BOUNDARY

LAYER FLOW

LIST OF TABLES.....	viii
LIST OF FIGURES.....	ix
CHAPTER 1	
INTRODUCTION	1
1.1 Motivation.....	1
1.2 Thesis Objectives	3
1.2.1 <i>Aerodynamic Analysis of an Axisymmetric Flow on a Propeller.....</i>	3
1.2.2 <i>Aerodynamic Analysis of a Non - Axisymmetric Flow on Propeller.....</i>	3
1.2.3 <i>Aerodynamic Analysis of a Thick Boundary Layer on Propeller.....</i>	3
CHAPTER 2	
LITERATURE REVIEW.....	4
2.1 Introduction.....	4
2.2 Actuator Disk Theory.....	7
2.3 Potential Flow Theory	9
2.3.1 <i>Lifting Line.....</i>	9
2.3.2 <i>Lifting Surface.....</i>	10
2.3.3 <i>Vortex Lattice Method.....</i>	11
2.3.4 <i>Boundary Element Methods.....</i>	12
2.4 Numerical Analysis	14
2.4.1 <i>Reynolds' Averaged Navier - Stokes Equation.....</i>	14
2.4.2 <i>Large Eddy Simulation.....</i>	18
CHAPTER 3	
NUMERICAL MODELS	19
3.1 Introduction.....	19
3.2 Reynolds' Averaged Navier - Stokes Equation	19
3.3 Transport Equation for the Spalart - Allmaras Model.....	20
3.4 Wall Boundary Layer Theory	21

CHAPTER 4		
NUMERICAL METHODS		23
4.1	Overview	23
4.2	Numerical Methods	23
4.2.1	<i>Discretization</i>	23
4.2.2	<i>Domain Interface Treatment</i>	28
4.2.3	<i>Fluid Flow Models</i>	29
4.2.4	<i>Thrust Computation</i>	31
4.2.5	<i>Accuracy and Convergence</i>	31
CHAPTER 5		
COMPUTER AIDED DESIGN, MODELING, AND SOLVER.....		34
5.1	Overview	34
5.2	Geometry Design.....	34
5.2.1	<i>Sevik Propeller</i>	34
5.2.2	<i>Wind Tunnel</i>	36
5.3	Mesh	38
5.3.1	<i>Stationary Domain</i>	38
5.3.2	<i>Rotational Domain</i>	39
5.3.3	<i>Mesh Refinement and Densities</i>	39
5.4	ANSYS – FLUENT Solver.....	42
5.4.1	<i>Problem Setup</i>	42
5.4.2	<i>Solution Setup</i>	49
CHAPTER 6		
EXPERIMENTAL SETUP		53
6.1	Overview	53
6.2	Testing Facility.....	53
6.3	Wind Tunnel Data Collection	53
CHAPTER 7		
CONFIGURATIONS AND DATA SETS.....		56
7.1	Overview	56
7.2	Configurations and Data Sets.....	56
CHAPTER 8		
RESULTS		59
8.1	Overview	59
8.2	CFD Data and Results	59
8.2.1	<i>Configuration 1</i>	60
8.2.2	<i>Configuration 2</i>	62
8.2.3	<i>Configuration 3</i>	62
8.3	CFD Validation	65

8.4	CFD Data Comparison	66
8.4.1	<i>Boundary Layer Profiles</i>	66
8.4.2	<i>Thrust</i>	67
8.5	Configuration 3: Acoustic Data Set.....	67
8.5.1	<i>Wall Y-plus</i>	68
8.5.2	<i>Boundary Layer Measurements</i>	68
CHAPTER 9		
DISCUSSION		70
9.1	RANS Calculations Compared to Experimental Data.....	70
9.2	Model Interpretation	71
9.2.1	<i>Data Validation</i>	75
9.3	Ingested Flow Data Interpretation.....	77
9.3.1	<i>Modifying Configurations</i>	77
9.3.2	<i>Varying Flow Conditions</i>	79
CHAPTER 10		
CONCLUSIONS AND RECOMMENDATIONS		82
10.1	Overview.....	82
10.2	Numerical Methods and CFD	82
10.3	Altering the Ingested Flow for Different Configurations.....	83
10.4	Recommendations	84
10.4.1	<i>Mesh</i>	84
10.4.2	<i>Solver</i>	85
10.4.3	<i>Experimental Data</i>	86
FIGURES		87
NOMENCLATURE		150
APPENDICES.....		153
APPENDIX A.....		154
APPENDIX B.....		161
APPENDIX C.....		164
APPENDIX D.....		165
APPENDIX E.....		168
REFERENCES.....		173

LIST OF TABLES

Table 3.1 – Sections of the Inner Boundary Layer.....	22
Table 5.1 – Propeller Geometry	35
Table 5.2 – Spalart – Allmaras Model Constants.....	43
Table 5.3 – Stationary Zone: Cell Zone Conditions.....	44
Table 5.4 – Rotational Zone: Cell Zone Conditions.....	45
Table 5.5 – Wall Boundary Conditions	46
Table 5.6 – Inlet Boundary Conditions.....	48
Table 5.7 – Residual Criteria	50
Table 5.8 – Solution Methods Settings.....	51
Table 6.1 – Experimental Cases	55
Table 7.1 – Configuration 1 Cases	57
Table 7.2 – Configuration 2 Cases	57
Table 7.3 – Configuration 3 Cases	58
Table 7.4 – Configuration 3 Acoustic Data Set	58
Table 8.1 – Boundary Layer Measurement Locations.....	60
Table 8.2 – Configuration 3: Grid Independence Study.....	64
Table 8.3 – Error in of CFD Measurement	66
Table 8.4 – Normalized Propeller Dimensions	67
Table 8.5 – Normalized Ingested Mean Flow Velocities	69

LIST OF FIGURES

Figure 2.1 – Hydrodynamic Models of Propeller Action	87
Figure 3.1 – Universal Dimensionless Mean Velocity Profile	88
Figure 4.1 – Overview of Pressure – Based Solution Methods	89
Figure 5.1 – Single Blade Diagram of Blade Twist and Flow Direction	90
Figure 5.2 – Geometry Differences (Filet)	90
Figure 5.3 – Geometry Differences (Hub).....	91
Figure 5.4 – Drawing of Configuration 1	92
Figure 5.5 – Drawing of Configuration 3	93
Figure 5.6 – Geometry of Domains and Subdomain.....	94
Figure 5.7 – Mesh of Domain and Subdomain	95
Figure 5.8 – Mesh Densities.....	96
Figure 5.9 – Configuration 1 Mesh at Interfaces.....	97
Figure 5.10 – Configuration 2 and 3 Mesh at Interfaces	98
Figure 5.11 – Cross Section Display of Domain and Subdomain Mesh	99
Figure 5.12 – Cross Section Display of Boundary Layer Mesh.....	100
Figure 5.13 – Front View of Propeller Blade Locations (CFD).....	101
Figure 5.14 – Automatic User Specified Solution Initialization Procedure	101
Figure 6.1 – Overview of 'Stability Wind Tunnel'	102
Figure 6.2 – Test Section Diagram.....	102
Figure 6.3 – Laser and Sensor Experimental Setup	103
Figure 6.4 – Hotwire Probe Experimental Setup	103
Figure 6.5 – Diagram of Propeller Probe Location	104
Figure 7.1 – Planes for Contour Plots (Far Measurements).....	105

Figure 7.2 – Locations for Boundary Layer Plots.....	106
Figure 7.3 – Configuration 1: Node Radial Coordinates (90% Ring).....	107
Figure 7.4 – Configuration 3: Node Radial Coordinates (90% Ring).....	107
Figure 8.1 – Configuration 1: Axial Velocity Contour Plot at Front Interface.....	108
Figure 8.2 – Configuration 1: Wall Y-plus.....	109
Figure 8.3 – Configuration 1: Turbulent Viscosity Ratio.....	109
Figure 8.4 – Configuration 1: Globally Scaled Residual Plot.....	110
Figure 8.5 – Configuration 2: Axial Velocity Contour Plot at Front Interface.....	111
Figure 8.6 – Configuration 2: Globally Scaled Residual Plot.....	112
Figure 8.7 – Configuration 3: Axial Velocity Contour Plot at Front Interface.....	113
Figure 8.8 – Configuration 3: Turbulent Viscosity Ratio.....	114
Figure 8.9 – Configuration 3: Globally Scaled Residual Plot.....	114
Figure 8.10 – Grid Ind. Study Results for $J = 0.72$ (Wake).....	115
Figure 8.11 – Grid Ind. Study Results for $J = 0.79$ (Wake).....	115
Figure 8.12 – Grid Ind. Study Results for $J = 0.98$ (Wake).....	116
Figure 8.13 – Grid Ind. Study Results for $J = 1.31$ (Wake).....	116
Figure 8.14 – Grid Ind. Study Results for $J = 1.44$ (Wake).....	117
Figure 8.15 – Grid Ind. Study Results for $J = 0.72$ (BL).....	117
Figure 8.16 – Configuration 1: CFD Validation for $J = 0.72$ (Wake).....	118
Figure 8.17 – Configuration 1: CFD Validation for $J = 0.79$ (Wake).....	118
Figure 8.18 – Configuration 1: CFD Validation for $J = 0.98$ (Wake).....	119
Figure 8.19 – Configuration 1: CFD Validation for $J = 1.31$ (Wake).....	119
Figure 8.20 – Configuration 1: CFD Validation for $J = 1.44$ (Wake).....	120
Figure 8.21 – Configuration 3: CFD Validation for $J = 1.44$ (BL).....	120
Figure 8.22 – All Configurations BL Data at Inlet.....	121
Figure 8.23 – All Configurations BL Data at 2 Diameters Upstream.....	121
Figure 8.24 – All Configurations BL Data at 1 Diameter Upstream.....	122
Figure 8.25 – All Configurations BL Data at 3 Chords Upstream.....	122

Figure 8.26 – All Configurations BL Data at 2 Chords Upstream.....	123
Figure 8.27 – All Configurations BL Data at 1 Chord Upstream	123
Figure 8.28 – Coefficient of Thrust vs. Advance Ratio.....	124
Figure 8.29 – Acoustic: Wall Y-plus ($J = 0.48$).....	125
Figure 8.30 – Acoustic: Wall Y-plus ($J = 0.72$).....	125
Figure 8.31 – Acoustic: Wall Y-plus ($J = 0.96$).....	126
Figure 8.32 – Acoustic: Wall Y-plus ($J = 1.20$).....	126
Figure 8.33 – Acoustic: Wall Y-plus ($J = 1.44$).....	127
Figure 8.34 – Acoustic: Axial Velocity Contour Plot at Front Interface ($J = 0.48$).....	128
Figure 8.35 – Acoustic: Axial Velocity Contour Plot at Front Interface ($J = 0.72$).....	129
Figure 8.36 – Acoustic: Axial Velocity Contour Plot at Front Interface ($J = 0.96$).....	130
Figure 8.37 – Acoustic: Axial Velocity Contour Plot at Front Interface ($J = 1.20$).....	131
Figure 8.38 – Acoustic: Axial Velocity Contour Plot at Front Interface ($J = 1.44$).....	132
Figure 8.39 – Acoustic: Axial Velocity Contour at 1 & 2 Dia. Upstream ($J = 0.48$).....	133
Figure 8.40 – Acoustic: Axial Velocity Contour at 1 & 2 Dia. Upstream ($J = 0.72$).....	134
Figure 8.41 – Acoustic: Axial Velocity Contour at 1 & 2 Dia. Upstream ($J = 0.96$).....	135
Figure 8.42 – Acoustic: Axial Velocity Contour at 1 & 2 Dia. Upstream ($J = 1.20$).....	136
Figure 8.43 – Acoustic: Axial Velocity Contour at 1 & 2 Dia. Upstream ($J = 1.44$).....	137
Figure 8.44 – Acoustic: Axial Velocity Contour at All Near Stations.	138
Figure 8.45 – Acoustic: BL Profile at Inlet for All Case Files	139
Figure 8.46 – Acoustic: BL Profile at 2 Diameters Upstream for All Case Files.....	139
Figure 8.47 – Acoustic: BL Profile at 1 Diameter Upstream for All Case Files	140
Figure 8.48 – Acoustic: BL Profile at 3 Chord Lengths Upstream for All Case Files.....	140
Figure 8.49 – Acoustic: BL Profile at 2 Chord Lengths Upstream for All Case Files.....	141
Figure 8.50 – Acoustic: BL Profile at 1 Chord Length Upstream for All Case Files	141
Figure 8.51 – Acoustic: BL Profile at All Far Upstream Stations ($J = 0.48$).....	142
Figure 8.52 – Acoustic: BL Profile at All Far Upstream Stations ($J = 0.72$).....	142
Figure 8.53 – Acoustic: BL Profile at All Far Upstream Stations ($J = 0.96$).....	143

Figure 8.54 – Acoustic: BL Profile at All Far Upstream Stations (J = 1.20).....	143
Figure 8.55 – Acoustic: BL Profile at All Far Upstream Stations (J = 1.44).....	144
Figure 8.56 – Acoustic: BL Profile at All Near Upstream Stations (J = 0.48 – AH).....	145
Figure 8.57 – Acoustic: BL Profile at All Near Upstream Stations (J = 0.48 – BH).....	145
Figure 8.58 – Acoustic: BL Profile at All Near Upstream Stations (J = 0.72 – AH).....	146
Figure 8.59 – Acoustic: BL Profile at All Near Upstream Stations (J = 0.72 – BH).....	146
Figure 8.60 – Acoustic: BL Profile at All Near Upstream Stations (J = 0.96 – AH).....	147
Figure 8.61 – Acoustic: BL Profile at All Near Upstream Stations (J = 0.96 – BH).....	147
Figure 8.62 – Acoustic: BL Profile at All Near Upstream Stations (J = 1.20 – AH).....	148
Figure 8.63 – Acoustic: BL Profile at All Near Upstream Stations (J = 1.20 – BH).....	148
Figure 8.64 – Acoustic: BL Profile at All Near Upstream Stations (J = 1.44 – AH).....	149
Figure 8.65 – Acoustic: BL Profile at All Near Upstream Stations (J = 1.44 – BH).....	149

1 INTRODUCTION

1.1 MOTIVATION

Generation of lift is obtained through the concept of circulation around airfoil type configurations interacting with the surrounding fluid whether it is air, water, or other media. Propellers are devices capable of producing lift orthogonal to the incoming (onset) flow; however, other more complicated properties, such as ingested velocity, must also be attained dependent on flow characteristics. Gathering knowledge of the aerodynamic flow for a given geometry allows for further calculations to be performed such as thrust generation, drag, pressure distributions, noise generation, and other variables of interest. One such variable being actively studied, as mentioned by Majumdar & Peake [1], is noise generation. One of the important sources of low speed propeller noise is caused by the interaction of the propeller blades with the ingested turbulence. The turbulent eddies in the upstream turbulent flow are deformed into long and narrow volumes which travel along the constricting streamtube formed by the propeller. In order to determine the noise generation, it is first required to determine the mean nonuniform flow ingested by the propeller and then apply rapid distortion theory and methods developed by Majumdar & Peake [1]. This thesis will focus solely on determining the mean nonuniform ingested flow and these results will be utilized for aero-acoustic computation beyond this thesis.

This thesis considers methods that can be used for both marine and aircraft propellers; yet, there are considerable differences between each. Marine propellers operating in water medium are usually more skewed than aircraft propellers due to their limitation on diameter and furthermore, given the desired generation of lift per unit area, they are prone to cavitation. As Kerwin mentions in his 1986 survey paper [2], these limitations result in blades that are wider with respect to their diameter when compared to aircraft propellers. In addition, marine propellers are commonly found much closer to the rear of a ship. The location of the propeller is mainly due to concerns for propeller efficiency, possibility of damage, and

engine orientation. Hence, inserting the propeller at the stern of a ship greatly influences its interaction with the turbulent nonuniform flow originating from the ship's hull. As mentioned, these interactions lead to strong vibrations which radiate sound. Such characteristics are not limited to marine propellers and may be associated and studied from aircraft propellers. Again this is done in order to improve efficiency and reduce noise radiation as mentioned by Hileman et al. in 2007 [3] and the Blended Wing Body concept presented by Ko et al. in 2003 [4]. As a result of the engine being mounted or embedded in the aircraft fuselage, thick viscous boundary layers are ingested by the propellers, so the inflow includes receiving turbulent rotational flow. This complex flow leads to vibrations and noise production which is the overall concern of this thesis.

In order to study these side effects, it is necessary to analyze and obtain solutions for the viscous rotational flow in the vicinity of a surface such as the hull of a vessel or fuselage of an aircraft. The study carried forth in this thesis will be performed on a propeller developed by Sevik [5] with modifications indicated by Glegg et al. [6]. These modifications will be detailed in Chapter 5. The propeller will be modeled in air while the actual application will be for marine purposes. The results are modeled for air in order to compare to aerodynamic results from experimental tests at Virginia Tech's stability wind tunnel. The results will be given for an open propeller in three different configurations: open rotor with a uniform inflow and an open rotor near a wall with and without a thick boundary layer. Previous studies involving boundary layer ingestion (BLI) propulsion systems are found as early as 1947 by A. Smith et al. [7] where he determined performance improvements using an axisymmetric configuration and an inviscid approach. Also, recently in 2007 A. Plas et. al [8], studied BLI performance for a ducted propulsor utilizing a viscous approach. However, these studies do not lead to in depth aero-acoustic studies on BLI and propeller effects. This thesis will give results utilizing ANSYS – FLUENT to represent predicted velocity profiles at several locations of interest upstream of the propeller. As for this thesis, conclusions will be made based on the three different possible configurations and operational conditions. Further studies will be performed for specific conditions which focus solely on the configuration considering the propeller's proximity to an impenetrable surface and accounting for the rotational viscous flow. These results will be presented in Chapter 7.

1.2 THESIS OBJECTIVES

1.2.1 AERODYNAMIC ANALYSIS OF AN AXISYMMETRIC FLOW ON A PROPELLER

This research will compute the aerodynamic flow through a Sevik 10-blade propeller. All computations will be carried out in ANSYS- FLUENT and a total of three configurations will be considered. The first case study will involve an open propeller with uniform inflow. There will be no interaction between any wall and the propeller. This will be referred to as configuration 1. Five cases will be studied by varying inflow speed at the inlet and propeller rotational velocity. All five cases together will represent one data set for configuration 1.

1.2.2 AERODYNAMIC ANALYSIS OF A NON - AXISYMMETRIC FLOW ON PROPELLER

The second configuration involves an open rotor of diameter 457.20 mm. as in configuration 1, with the addition of a nearby wall. The tip gap between the wall and propeller is 20.3 mm. The inflow velocity will also be constant for this configuration and a boundary layer will form as the flow progresses through the inlet. This will be referred to a 'natural' boundary layer given it was not generated by any obstruction but merely develops on the wall as a function of displacement downstream of the inlet. Five cases will be studied by varying inflow speed at the inlet and propeller rotational velocity. All five cases together will represent one data set for configuration 2.

1.2.3 AERODYNAMIC ANALYSIS OF A THICK BOUNDARY LAYER ON PROPELLER

The third and main focus of this thesis is the addition of a thick boundary layer height of 102 mm at the inlet. This configuration is referred to as configuration 3. The propeller will be stationed exactly as configuration 2 above a plate at the same normal wall distance. The only difference being the addition of a thick boundary layer generated in a wind tunnel. Five cases will be studied by varying inflow speed at the inlet and propeller rotational velocity. All five cases together will represent *one* data set for configuration 3. In addition, another data set will be generated with this configuration and referred to as acoustic data set. The propeller rotational velocity will be maintained at a constant 2734 RPM and the inlet velocity will vary with increments of 5 m/s from case to case. The acoustic data set results will be utilized in future aero-acoustic computations beyond this thesis.

2 LITERATURE REVIEW

2.1 INTRODUCTION

Present methods developed to design and study the flow of propellers are complicated enough to resort to numerical solutions. Numerical procedures require massive computing resources for the analysis of industrial problems such as the one explored in this thesis. It is important to note however, that this resource has not always been available. Analytical solutions have been explored in depth by pioneers such as Rankine, Froude, Prandtl, and Betz. These theories have been revisited numerous times by scientists and mathematicians such as Goldstein, Ludwig and Ginzl and several others. Aerodynamic analysis for the design and analysis of propellers and the flow around them is still a complex task without a simple solution. Nevertheless, simplistic models and assumptions have been fabricated to obtain solutions for propeller performance and they have been very successful.

The first of these approaches was carried out in 1865 by W.J.M. Rankine and in 1889 by Froude using momentum theory to provide the flow through a disk simulating a ship's propeller [9]. This being one of the most basic methods it keeps the problem simple with acceptable accuracy. In 1919 Betz proposed a method called the Radial Distribution of Circulation using potential flow theory; however, this problem was not solved until 1929 by S. Goldstein [10]. Meanwhile, in 1921, Prandtl concluded that the three dimensional problem could be solved by concentrating the circulation around the blades onto individual lifting lines. The flow at each radial section is then computed as a two dimensional problem within the inflow field. The inflow field is imparted by the velocity induced by the free vortex system shed from the lifting line [11]. This theory becomes the basis for lifting line theory. The review by Kerwin [2] specifies that the combination of Prandtl and Goldstein's theories and experimental data allows one to design an optimum propeller. Furthermore, contributions ranging from 1944-1960s by Ludwig & Ginzl

[12], Lerbs [13], and Cox [14] allows for the determination of radial distribution of circulation and the resulting thrust, power and efficiency. According to Kerwin [2], these theories were confirmed by computer in the 1960s. In addition, Ludwig and Ginzler (1944) advanced lifting line theory to develop surface line theory and expanding to chordwise and spanwise calculations [12]. During this time solutions using computers became increasingly popular and necessary for numerical methods. These were further improved by Lighthill [15] in 1951 and Morgan [16] et al. in 1968. Lighthill published correction factors which were used to match up two dimensional flows to three dimensional flows from Lifting Surface Theory and Morgan et al. published corrections factors which corrected for the skew, the form of the radial distribution of circulation, camber, ideal angle due to loading, and blade outline used for Vortex Lattice and Panel methods. Numerical methods were developed to compute and aid in blade design. As mentioned in Kerwin's review [2], in 1981, Brockett [17] developed PROPLS while at the same time Kerwin [18] developed PBD-10. PROPLS is a computer program which incorporates direct numerical integration by evaluating the resulting singular integrals, while PBD-10 reproduces the same calculation using a similar approach referred to as the vortex lattice method [18]. The main objective of these programs was to aid the blade design procedure given that flow characteristic were known. PBD-10 would initiate at some initial pitch and camber, compute the total fluid velocity at several points designated by the user, and then readjust the surface accordingly until convergence. This is an iterative process which would be tedious to reproduce by hand; thus, numerical methods such as these became very advantageous. In 1982, Greely & Kerwin [18] provided details of vortex wake alignment procedures which determined the 'exact' inviscid solution of a set of zero thickness surfaces which represent vortex wakes and blades [18]. However, there were still several concerns with the reliability of these methods. One concern was dealing with the correct placement of the vortex and control points for these theories (vortex lattice and lifting surface). In 1974, Lan [19] published a paper that demonstrated how to determine the correct spacing for these vortices and control points. His concept provides the correct results for the total lift of a flat plate with a parabolic camber line. He proposed that a cosine spacing of control points should be utilized in order to obtain accurate results, specifically the local pressure near the leading edge.

Another, concern was the effects of the hub on the propeller given that all the previous methods ignored the hub effect on the propeller blades. This was since the hub effects produce minor changes to

locations far from the hub. Additionally, the hub section would either be ignored or its influence calculated by method of images. The results are then analyzed in terms of boundary layer characteristics and cavitation; nevertheless, the approach for incorporating the hub was arbitrary [2].

The concept of determining flow characteristics from a given geometry was initiated as in 1955 by Eckhart & Morgan [20], as well as, in 1957 by van Manen [21]. In 1959, Kerwin [22] developed a solution which iterated to match two dimensional section characteristics at a certain radius to an interpolated value of the induced flow using the Goldstein function. During this time period the solutions had complications with the approximation of the blade wake and the radial and chordwise loading distributions which were improved by Tsakonas et al. from 1973-1983. Tsakonas et al. replaced the traditional 'staircase' approximation of the blade wake with a much more accurate helicoidal blade wake which resulted in a much smoother chordwise and radial loading distribution. In general, this substitution took into account the non-uniform flow produce by the hull wake, as well as, the helicoidal geometry given by the propeller blade and the result wake it produces. Eventually, this addition provided more accurate steady and unsteady solutions based on the acceleration potential of the flow [23]. Even with these improvements, lifting surface methods posed problems regarding local errors near the leading edge and hub. This was in part due to the large blade thickness to resist large stresses and the proximity of blades to one another. In the 1980s, Panel Methods, also known as Boundary Elements Method were developed to incorporate blade thickness, spanwise, and chordwise (camber) distribution. This was based on potential flow theory. In 1984, Morgan [24] published the derivation of several algorithms based on Panel methods. Computer program PSF-2 was used in 1984 by Kim & Kobayashi [25] to obtain results using a vortex lattice procedure. Vortex lattice procedures are a similar approach to panel methods and an interesting comparison between the two methods was demonstrated by Hess & Valarezo in [26]. As Hess & Valarezo pointed out, the advantage of panel methods is that they successfully represented the local pressure minimum. It is important to note that Kim & Kobayashi's results did not incorporate Lighthill's correction factors which led to unsuccessful representation of the local pressure minimums. Once the need to calculate the fluid flow velocities given the geometry of the blade became necessary, the hub effects became more pronounced and began to be incorporated into more methods. Specifically, in 1985, Wang applied the surface panel representation of the hub to obtain a more complete propeller design [27].

More recently, theories that are not based on potential flow assumptions but on the Navier Stokes Equations have been developed. Complex models based on the Navier Stokes Equations include Reynolds' Averaged Navier - Stokes methods (RANS), Large Eddy Simulations (LES), Detached Eddy Simulations (DES), and Direct Numerical Simulations (DNS). The latter two will not be described in this thesis as they currently are only feasible for specific simple flows. RANS will be the main focus of the models as it is commonly used and will be compared to lifting line, lifting surface, panel methods, and vortex lattice methods. The main difference is that RANS may be used to analyze viscous flows while methods based on potential flow theory assume inviscid flow. RANS and other CFD models are extensively used in several propeller flow analyses for example Abdel- Masoud et al.[28], Da- Qing [29], Zachariadis and Hall [30], Gaggero et al. [31], and Kuiper [32].

The majority of these earlier models, although accurate to a certain degree, assume inviscid, irrotational, and incompressible flow. These are the necessary assumptions for the potential flow model. Other models, such as RANS, do not have this limitation. The study conducted in this thesis considers the boundary layer flow which is by definition a rotational flow with a mean shear. Thus, the assumption of an ideal fluid is invalid and RANS will be used. The following section will describe several models that can be used for propeller analysis and their main assumptions, as well as, the contributions by some of the scientists and mathematicians involved in their development.

2.2 ACTUATOR DISK THEORY

One of the earliest models used to describe the flow through a propeller was the theory developed by W. J. M. Rankine (1865). The basic concept was to introduce an infinitely thin actuator disk in the flow to describe the discontinuities across the propeller. As mentioned by J. Horlock [33], this theory is known as the “momentum theory” or “actuator disk theory” and it assumes that the velocity and perturbation terms before and after the propeller are equal. The basic concept being that the flow is unrestricted by walls and bound only by ‘free streamlines’. Horlock [33] explains the theory and its derivation in detail with the assumptions that the flow is uniform across the stream at all stations, incompressible, irrotational, and inviscid. It is essential to note that the theory presented by Rankine [34] did in fact account for the propeller action and consequently the thrust it produces; however, the propeller is replaced by an actuator

disk. As a result, this theory does not account for the present propeller geometry and is not very useful for propeller blade design. Rankine's original momentum theory contains three major assumptions. The first being the propeller functions in an ideal fluid. This indicates that there is no energy losses present due to frictional drag. The second being that because the propeller is replaced by an infinitely thin disk. Physically, this means that the propeller is comprised of an infinite number of blades. The third assumption states that rotation is not present (irrotational flow), thus, thrust is produced without imparting rotation to the slipstream. As a result, there is a pressure jump across the disk. Hence, the flow is simply 'actuated' by a disk. In addition to this theory, W. Froude [35] in 1878, describe the Blade Element Theory.

The Blade Element Theory, contrary to Rankine's, accounts for the geometry of the propeller blade. The Blade Element Theory proposes that the blade is split into several sections, known as airfoils, and are analyzed according to the incident velocity. The incident velocity is dependent on the axial flow speed (inflow velocity), as well as, the blade angular velocity which varies linearly spanwise. This approach allows for the calculation of lift and drag at each section of the airfoil. A simple integration across the blade provides the total lift or drag of the blades. Modern theory is founded upon this method. In 1887, R.E. Froude [36] removed the third assumption made in [9] by allowing the propeller to impart rotational velocity to the flow. This new modified theory became known as the Rankine-Froude momentum theory or the general momentum theory of propellers. Individually, both theories contain inconsistencies such as those found when obtaining results dealing with propeller efficiency. Momentum Theory attempts to find the efficiency by utilizing an inviscid model which indicates that efficiency is dependent on speed of advance and thrust coefficient, while the Blade Element Theory suggests that the efficiency approaches one hundred percent, as viscous forces approach zero. These discrepancies in results have led to the combination of both theories for propeller design and analysis. It is common for engineers to utilize momentum theory to determine induced velocities, and then analyze the results using the blade element theory; however, the final results are still not entirely accepted.

Although there are several assumptions made to simplify the problem, Rankine's momentum theory may be adapted to produce reliable results such as those by J. Conway. In 1995, J. Conway [37] calculated the flow through a propeller as a function of radius. The theory is manipulated to describe an analytical solution for an actuator disk with variable radial distribution of load. In this work, Conway [37]

provides a method to solve for the induced flow in closed form. Conway successfully manages to obtain similar solutions to those obtained by Hough & Ordway (1965). Hough & Ordway [38] found solutions for general radial distributions of load by superposition, but the method was too complex to be reproduced without numerical integration. Conway's method constructed a solution that determined the velocity and potential fields induced by a ring vortex as integrals over the possible values of the separation constant of the eigensolutions of Laplace's equation in cylindrical coordinates. The combination of eigenfunctions provides the solution for a blade with constant spanwise load and more general cases [37]. This method utilizes the assumptions of potential flow theory to determine the mean flow through a propeller, so viscous and rotational effects are neglected.

2.3 POTENTIAL FLOW THEORY

A commonly used theory in determining flow characteristics through a propeller is potential flow theory. The flow is assumed to be inviscid, incompressible, and irrotational. Laplace's equation for velocity potential satisfies the continuity equation and setting the curl of the velocity to zero ensures an irrotational flow. Several other methods and theories have emerged from potential flow theory including lifting line theory, lifting surface theory, vortex lattice methods, and panel methods. As described by J. Fay [39], more complex flows require a combination of the velocity potential and stream functions defined for various simple flows and then superimposed to represent more detailed flows. Nonetheless, the majority of the potential flow models described in the following section deals with simply the velocity potential.

2.3.1 LIFTING LINE

Classical hydrodynamic theories model the flow over a propeller as reactions to distributed sources, vortices, sinks, and dipoles about the surface and/or appropriate locations within the blades. As J. Carlton [34] mentions, the earliest concepts of lift were introduced by Lanchester in 1894 to the Birmingham Natural History and Philosophical Society. After a failed attempt to publish a paper to the Physical Society, Lanchester wrote two books, *Aerodynamics* (1907) and *Aerodnetics* (1908). Independently of this work, in 1906, Kutta and Joukowski propose the Kutta- Joukowski Theorem relating lift to circulation. As mentioned by J. Carlton [34], Kutta and Joukowski were unaware of each other's

contributions; hence the theorem is named to honor both. Shortly thereafter, Prandtl [40], known as the father of modern aerodynamics, extended the works of Lanchester [41], in 1918, into what is known as the Lifting Line Theorem, also known as, the Lanchester- Prandtl Wing Theory [42]. As explained by Abbott et al. [43], in the lifting line theory, a vortex is placed within the airfoil, as shown in Figure 2.1 (a), and used to model the circulation along the wingspan. The vortex strength is reduced along the wingspan and the loss in vortex strength is shed as a vortex sheet from the trailing edge, see Figure 2.1 (b). Soon after this proposed theory, several advancements and corrections were published. In 1919, Betz [44] had established the basic form of the minimum energy loss condition by analyzing Prandtl's vortex system in the slipstream of a lightly loaded propeller containing an infinite number of blades. Using the velocity potential, Betz proposes the radial distribution of circulation. This concept of infinite blades leads to a problem with the shed vortices spacing. The spacing between vortices for infinite blades is minimal and this does not represent a case for finite number of blades. Goldstein [10] proposed correction factors for trailing vortices. In 1952, Lerbs [13] wrote an extension to the lifting line theorem. The propeller hub section was incorporated into this model with the assumption that the hub experienced zero circulation. Lerbs proposed that the blades could be represented by a line of radially varying bound vorticity, and in order to satisfy Stokes Theorem a vortex sheet with radially varying strength is required. In 1955, Eckhart and Morgan [20], proposed a method for propeller design. This model is based on two basic assumptions. One indicates that the action provided by the propeller exists; however, the slipstream does not contract. Second, normality of the induced velocity is applicable. This model is applicable for both lightly and moderately loaded propellers. The concept of lifting line only models spanwise loading and in order to obtain more accurate results, chordwise loading must also be modeled; thus leading to another theory known as the lifting surface theory.

2.3.2 LIFTING SURFACE

Prior to the 1960s, several mathematicians and scientists had already began to lay the foundation for the Lifting Surface Theory including contributions by Ludwig and Ginzler [12], Strscheletsky [45], Guilloton [46], and Sparenberg [47]; however, numerical solutions were a necessity and these earlier models had become too complex and tedious to solve by hand. Kerwin [2] mentions that once

computational capabilities became available, Pien [48] published a paper in 1961 and became generally credited with producing the first lifting surface theory. The Lifting Surface model represents the blade as an infinitely thin surface which becomes the blade camber line. On this camber line distributions of vorticity exists and extends both chordwise and spanwise, see Figure 2.1 (c). Thus, the bound circulation is distributed over the chord of the mean line. This theory allows for the calculation of the radial distribution of the bound circulation. Later models represent the thickness of the blade sections by distributing sources and sinks along the chord line [34]. The incident velocity and the distribution of these sources and sinks allow for the approximation of the pressure field along the blade.

Following a similar methodology as the lifting line theory, correction factors were developed for this new theory. In 1968, Morgan et al. [16] introduced these correction factors to correct for camber, ideal angle due to loading, and ideal angle due to thickness. These factors are dependent on chordwise and spanwise load distributions, number of blades, and blade area and shape. Morgan et al. [16] found that the thickness correction factor was independent of the magnitude of the thickness but dependent on the chordwise and spanwise thickness distributions. Applying these correction factors provided engineers with a better understanding of the flow over blades without the need to apply empirical adjustments for determining blade pitch and camber [16]. This theory expanded into more detailed but similar methods such as vortex lattice method and boundary element methods. In general, the lifting surface theory and its successors consist of distributions of spanwise vortices, chordwise vortices, shed vortices, trailing vortices, sources, and sinks.

2.3.3 VORTEX LATTICE METHOD

In 1978, Kerwin and Lee [49] published a paper which possessed new characteristics to the lifting surface theory which was known as the Vortex Lattice Method. This method was largely developed by Kerwin from Massachusetts Institute of Technology and is considered a subclass of the lifting surface theory. The Vortex Lattice approach uses straight line segments which make up the airfoil surface. These line segments begin at the leading edge and end at the trailing edge of the camber line. A representation of the location of the line segments is shown in Figure 2.1 (d). Along these line segments exists a system of line vortices of constant strength. The velocity may then be computed from control points positioned

within the straight line segments. Kerwin and Lee[49] show that the various components of the vortex system can be defined in terms of time and position by applying Kelvin's Theorem and pressure continuity condition over the vortex wake. This is done by analyzing the vortex strength at any point as a vector lying on the blade or vortex sheet. This vector is then resolved into spanwise and chordwise components on the blades. The components then are shed and the vortex sheet emanates from the blades. This procedure allows one to calculate the distributed spanwise vorticity given the boundary conditions of the setup. The spacing of the control points also had to be determined while keeping program stability in mind. In 1974, Lan [19] showed that the exact results for the total lift of a flat plate or parabolic camber line could be determined using cosine spacing. Then in 1982, Kerwin and Greeley [18], proposed the radial spacing (from hub to tip) of the elements for steady flow analysis. Kerwin and Greeley also proposed that the chordwise distribution of singularities should be a cosine function. Lastly, the chordwise distribution of vortices and control points should follow the cosine function analyzed by Lan [19] known as cosine spacing. Another expansion from lifting surface theory is Boundary Element Methods (BEM), which is essentially the same as Panel methods.

2.3.4 BOUNDARY ELEMENT METHODS

Boundary Element Methods have been developed to overcome two complications of lifting surface analysis. The first being local errors near the leading edge of the blades. The second obstacle being the analysis at the hub where the section is relatively thick and blade spacing is minimal. In order to overcome the first problem, Lighthill [15] derived local correction factors. These correction factors were based on lifting surface theory to match the three dimensional flow around the leading edge to the two dimensional flow around the parabolic half-body as defined by J. Carlton in [34]. Some of the earliest works based on this method are from 1967 by Hess and Smith [50]. Based on this earlier work, Hess and Valarezo [26] presented the analysis of flow through a propeller based on panel methods.

The concept of panel methods, another name for boundary element methods, requires the surface of the blade to be covered in panels which contain sources or vortices depending on problem setup as stated by J. Carlton[34]. In the case of zero lift, the surface only contains sources. When lift is present the sources are replaced by vortices which produce circulation, thus generating lift. The panels (surface) form

either a source sheet (zero lift condition) or a vortex sheet (lift generated condition). The strength of the vortex or source varies over the body as to match the normal velocity component to the body with the free stream velocity component. This being true allows the surface to become a streamline of the flow field. The resultant flow field is required to be tangent to the panel surfaces (flow normality condition). The point in the middle of the panel is known as the control point, while the points in between panels are referred to as boundary points. The boundary points are coincident between panels in order to form a continuous surface. Along the panel, the source is assumed to be constant but allowed to vary from panel to panel. In the case of vortex panel, the circulation density varies from boundary point to boundary point. However, directly at the boundary point the circulation is continuous. This satisfies Kutta Condition for a small number of panels. If a large numbers of panels are used, the trailing edge becomes a problematic point. Thus, the number of panels is dependent on the section thickness to chord ratio in order to maintain numerical stability [34]. Hoshino [51] produced a surface panel method which utilizes small hyperboloidal quadrilaterals encompassing the hub and blades, as well as, the wake (trailing vortex). These quadrilaterals have distributions of constant sources and doublets over the hub and blades, while the trailing vortex only contains constant doublet distribution. In order to determine the strength of the source and doublet distributions, the boundary value problems at each control point is solved. By default, this satisfies the Kutta Condition.

In general, the advancements of lifting line theory allowed for the modeling of spanwise loading, and then lifting surface theory added the capability to model spanwise and chordwise loading. Finally, and most recently, vortex lattice methods and panel methods introduced approaches for modeling blade thickness, spanwise loading, and chordwise (camber) loadings. These methods led to the generation and simulation of three dimensional propellers due to the simultaneous advancements in computing power. Nevertheless, with the advances in computing power, other methods of defining flow characteristics through a propeller became available. Such methods include the use of Navier-Stokes equations that can model all of the above characteristics in addition to viscosity, compressibility, and vorticity.

2.4 NUMERICAL ANALYSIS

Modern computational capabilities have grown exponentially over the last ten to fifteen years and so has the field of computational fluid dynamics (CFD). CFD has allowed engineers to analyze and design marine propellers using simulations and models along with other types of problems. The modeling includes RANS, LES, DES, and DNS simulations. RANS solvers compute the viscous effects by solving the continuity equation and momentum equations using appropriate user defined turbulence model and the Reynolds time or space average approach. Together these form a closed set of equations capable of solving flow problems that potential theory cannot. As mentioned above, DES and DNS will not be discussed in this thesis as they are currently only developed for specific simple flows and require tremendous amounts of computational resources. This leads to one of the most important restrictions of computer modeling, the amount of computer effort required to obtain a solution.

2.4.1 REYNOLDS' AVERAGED NAVIER - STOKES EQUATION

One of the most favored methods of analyzing fluid flows is the RANS method because it utilizes less computer resources and thus requires less computing time than LES or DNS solvers. However, RANS simulations can be quite time consuming depending on the grid topology. Grid topology is an active area of research along with cavitating flow modeling, and turbulence modeling as there are several unsolved problems in these areas. As for turbulence modeling, the first two – equation model was proposed by Kolmogorov [52] in 1942, and now several models exist with some being very specific. Among the most common turbulence models are Spalart - Allmaras, $\kappa - \epsilon$, $\kappa - \omega$, and Reynolds stress models. In RANS simulations dealing with marine propellers one major difference between potential flow analysis and RANS is that in RANS, the fluid is modeled while in potential flow models the propeller surface is modeled. Other simulations may require different domains to be modeled; however, the ones mentioned in this thesis will deal with modeling the fluid domain. Modeling the fluid domain requires knowledge of achieving smooth grid distribution throughout the domain while minimizing the number of elements.

Achieving a smooth grid distribution is usually a difficult task due to the fact that there is no one specific route to take for any given scenario. Every problem will require a different mesh, with special attention to curves. If the problem requires boundary layer resolution, special attention is required when

meshing in proximity to the surface. Marine propellers contain many corners, fillets, and curves. Localized grid refinement is a must at all of these points in order to obtain optimum flow structures and characteristics including pressure gradients, tip vortices, fluid velocities, wake representation, and among other things. To fully define these curved surfaces, usually large numbers of cells are required, thus increasing computational time and resources. The usual procedure taken to resolve boundary layers is to use structured grid close to the surface; however, if the entire domain is resolved using structured grids of the same size it will likely produce too many cells. On the other hand, unstructured grids allow for faster meshing and less resources but are less accurate at resolving mean flows in boundary layers. Therefore, wherever boundary layer flow is of specific interest, hybrid methods are commonly used. Hybrid methods use a structured mesh close to the surface and gradually become unstructured for the remainder of the domain. This, in general, reduces the amount of computational resources. The Chimera technique, also known as overlapping grid approach, is an alternative meshing technique. Muscari and Di Mascio [53] in 2005 have successfully used this method to simulate flow through complex geometries. It uses simple structured grids referred to as subgrids. These subgrids are used up to a limited specified fluid region and may overlap each other. The subgrids are then embedded into a parent grid which encompasses the entire fluid domain. The Chimera technique is proven to be useful in modeling tip vortices and propeller flows as accomplished in works by Hsiao and Chahine [54] in 2001 and Kim and Paterson [55] in 2003. Thus, adding to the difficulty of analysis it is clear that there are numerous ways to mesh a problem depending on its geometry.

2.4.1.1 SPALART – ALLMARAS MODEL

Spalart – Allmaras Turbulence Model is a simple one equation model. This model was introduced by Spalart and Allmaras [56] in 1992. A single transport equation is solved for the turbulent viscosity that develops and, using this variable, a local turbulence model is created. The model is then used in the grids analyzed by Navier-Stokes solvers in two and three dimensions. This model is commonly used for rapid conversion in steady state. Flow resolution of wakes, flat plate boundary layers, and pressure gradients are satisfactory to a certain degree; however, this is dependent on user calibration and setup.

2.4.1.2 STANDARD $\kappa - \varepsilon$ TURBULENCE MODEL

The earliest $\kappa - \varepsilon$ model contributions were written by Jones and Launder [57] in 1972; however, in 1982, K. Chien [58] proposed the $\kappa - \varepsilon$ model which is widely used today. The $\kappa - \varepsilon$ model solves two transport equations which include κ (turbulent kinetic energy) and ε (turbulent dissipation). The turbulent dissipation is the rate at which velocity fluctuations dissipate. F.R Menter [59] made comparisons for turbulence models and concluded that this model should be utilized only for fully turbulent flows. There are a few drawbacks to this model since it only determines the eddy viscosity based on a single turbulence length scale. Thus, the turbulent diffusion is calculated only at this length scale. It is known that turbulent diffusion occurs at a range of turbulent length scales and by choosing to model only one, errors is undoubtedly introduced. The Reynolds stresses, turbulent viscosity, and mean velocity gradients are related through the gradient diffusion hypothesis discussed in [60]. This model performs poorly for complex flows with large pressure gradients, steep streamline curvatures, and wherever separation is present. Other related problems include lack of sensitivity to adverse pressure gradients and numerical stiffness due to damping function stability issues. Nevertheless, this model is reliable for flows that do not include separation but are fully turbulent. It is widely utilized despite its known limitations. It is a robust model which is suitable for initial computation and is usually used for preliminary designs and parametric studies [60]. It is common for an engineer to change to a different model for more accurate final analysis. It is important to note that pressure gradients are not only sensitive to the turbulence model but to the mesh development as well.

S. Gaggero et al. [31] recently performed a comparison between RANS and PANEL methods for unsteady propeller flow using a $\kappa - \varepsilon$ turbulence model. The meshing technique for each method differs for each method. As mentioned earlier, the fluid region is meshed for RANS simulation while the surface, including the wake region, is meshed in Panel Methods. Panel methods require the mesh to be rotated at the angular velocity of the propeller. The translational motion was also prescribed in the model. Gaggero et al. concluded that RANS calculates with greater resolution at the blade leading edge whereas the leading edge pressure peak is not completely computed by the panel method. Only at refined levels of meshing, did panel method capture the pressure at the leading edge well enough for comparison to RANS. A downside to RANS being the computing time is much larger for RANS. Although Panel Methods are

efficient enough for design use, a RANS solver is better optimized for design validation. Panel Methods are accurate and more useful for applications of cavitating and unsteady problems. As a result, the comparison of the inviscid potential flow model to the RANS using $\kappa - \varepsilon$ model proves to be quite similar with both benefits and costs.

2.4.1.3 STANDARD $\kappa - \omega$ TURBULENCE MODEL

Also discussed by F.R Menter [60] is the $\kappa - \omega$ turbulence model. As mentioned by D. Wilcox [61], without any prior knowledge to Kolmogorov's work, Saffman formulated a superior turbulence model in 1970 known as the $\kappa - \omega$ model. This model has been revised several times and in 1988 D. Wilcox [62] proposed the standard form of this model. It was later revisited by D. Wilcox [63] in 2008. This is the best model for wall-bounded boundary layer, free shear, and low Reynolds number flows [60]. The Reynolds stresses, turbulent viscosity, and mean velocity gradients are related through the gradient diffusion hypothesis similar to $\kappa - \varepsilon$ model. This model also solves two transport equations. The first equation solves for the turbulent kinetic energy, κ . The other solves for the specific turbulent dissipation rate, also known as turbulent frequency, ω . This model is commonly used in turbomachinery and external aerodynamic flows due to its suitable response to adverse pressure gradients on or near a boundary and flow separation. F. R. Menter [60] also mentions that for numerical stability, this model does not solve for damping functions, as seen in the $\kappa - \varepsilon$ model, and it utilizes Dirichlet boundary conditions to simplify solutions and improve stability. However, this model tends to over predict separation and requires much greater mesh refinement near walls. It is important to note that such refinement may increase computing resources and time to a point where this model becomes unattractive.

Rhee and Joshi [64] analyzed a five bladed C.P.P propeller in open water using a hybrid unstructured mesh and the $\kappa - \omega$ model. The mesh consisted of prismatic cells in the boundary layer and tetrahedral cells at the remaining domain. This allows for the higher resolution required for the boundary layer while minimizing computing time for the remainder of the domain. Using this method, Rhee and Joshi found their K_T and K_Q values differed by eight percent and eleven percent from the experimental data. They also retained good agreement between circumferential averaged axial and tangential velocities but radial velocities were less accurate. However, the velocity fluctuations and wake regions were under predicted when compared to experimental data.

2.4.2 LARGE EDDY SIMULATION

The Large Eddy Simulation (LES) is another turbulence model used in CFD and provides time varying solution. It was initially proposed by J. Smagorinsky [65] in 1963 to simulate large scale eddies observed in atmospheric air currents. LES is widely used in engineering applications including combustion, acoustics, propeller analysis, and other large scale operations. S. Pope [66] provides in detail the derivation for LES turbulent model. An extremely brief concept of LES is a low pass filter is applied to Navier-Stokes equations to eliminate the small scale solutions. Therefore, all that remains is a certain range of length scales of solutions which are larger than those filtered. In essence, the large scale eddies are simulated and vortices smaller than the filter scale is resolved. S. Pope [66] also mentions, in the case where all scales of interest are to be resolved with sufficient spatial and temporal resolution a Direct Numerical Analysis (DNS) is performed; however, this requires tremendous allocations of memory and other computer resources. Returning to LES, by simulating the large scales of the flow field solution, one is able to retain much more reliable results than other RANS based methods. This is because LES simulation captures a part of turbulence dynamics unlike transient RANS.

In 2009, F. Salvatore et al. [67] compared five RANS based models, one LES model, and one Boundary Element Methods (BEM) model for a cavitating propeller in a nonuniform wakefield. The LES and RANS solvers were analyzed from the propeller's frame of reference. Results indicated that pressure fluctuations from a potential flow BEM model provided the most reliable results. As for LES, depending on the grid resolution, time and space scales were found to be solved better using LES than the RANS approaches. The most important aspect of LES was its ability to demonstrate two phase flow structures in the flow which is due to its capability to model large and small eddies. Nevertheless, a much larger amount of computer resources are required for LES simulations.

3 NUMERICAL MODELS

3.1 INTRODUCTION

The application of Reynolds' transport theorem, Newton's laws, and mass conservation equations are the basis for the equations describing fluid flow. The Navier-Stokes equations relate the acceleration of a fluid particle and all forces acting on the fluid per unit mass [39]. However, solutions to this equation are only available for basic flows such as Couette and plane Poiseuille flows which are laminar with predictable mean flow paths. In the case of turbulent flow the fluid flow paths are not predictable. One approach to solving this type of problem is to use the Reynolds' Averaged Navier – Stokes Equations (RANS) which are based on a time average of the unsteady flow parameters.

3.2 REYNOLDS' AVERAGED NAVIER - STOKES EQUATION

The chaotic flow paths of turbulent flow become predictable if averaged over long periods of time; hence the name *averaged* Navier–Stokes equation. The instantaneous velocity components, take u for example, may be broken down into the sum of its time-averaged and time fluctuating quantity, denoted as \bar{u} and u' respectively. As shown in, [39], this decomposition of components can be analyzed over sufficiently large time intervals to average out the fluctuations in the instantaneous velocity. This same procedure is applied to scalars such as pressure. Hence, one is capable of describing only the flow by simplifying Navier–Stokes equations into its time-averaged form while avoiding the time dependent component of the time-averaged flow. The *Reynolds' Averaged Navier Stokes Equations*, in tensor notation, are shown by equation 3.1.

$$\frac{\partial}{\partial t}(\rho\bar{u}_i) + \frac{\partial}{\partial x_j}(\rho\bar{u}_i\bar{u}_j) = -\frac{\partial\bar{P}}{\partial x_i} + \frac{\partial}{\partial x_j}(2\mu S_{ij} - \rho\overline{u'_i u'_j}) \quad 3.1$$

The second term within the rightmost parenthesis in equation 3.1 is known as the *Reynolds stress tensor* defined in 3.2.

$$\tau_{ij} = -\overline{u'_i u'_j} \quad 3.2$$

This is an additional unknown; thus, additional equations are necessary for closure. This process is called turbulence modeling. The complexity of these equations is due to nonlinear terms such as the convective acceleration term, $(\vec{V} \cdot \nabla)\vec{V}$. Traditional methods of solving linear PDEs exactly are not suitable for nonlinear PDEs and only a few methods are known for solving nonlinear PDEs exactly. The nonlinear Navier–Stokes equations may be solved numerically. However, this simulation requires immense computational time and resources and is called direct numerical simulation [68]. Hence, to compromise, the time averaged flow is computed and the Reynolds stress is approximated.

The unknown stress tensor τ_{ij} is approximated by the use of the *Boussinesq Approach* given in equation 3.3. This approximation requires a turbulence model and subsequently, these turbulence models are solved using transport equations to obtain the unknown quantities.

$$\tau_{ij} = -\overline{u'_i u'_j} = 2 \frac{\mu_t}{\rho} (S_{ij}) - \frac{2}{3} \kappa \delta_{ij} = \frac{\mu_t}{\rho} \left(\frac{\partial \overline{u}_i}{\partial x_j} + \frac{\partial \overline{u}_j}{\partial x_i} \right) - \frac{2}{3} \left(\kappa + \frac{\mu_t}{\rho} \frac{\partial u_\kappa}{\partial x_\kappa} \right) \delta_{ij} \quad 3.3$$

In this equation the turbulent or eddy viscosity μ_t is not a fluid property but a *flow* property which changes depending on flow conditions, state of turbulence, and spatial variations [69]. As mentioned by Nguyen [70], the kinetic eddy viscosity term, μ_t in equation 3.3, is assumed to be an isotropic scalar quantity which is not always true; thus this approach is an approximation of the Reynolds stress tensor. No single turbulence model describes all types of flows. Hence, for this thesis, the Spalart-Allmaras (S.A) turbulence model was utilized and will be briefly described.

3.3 TRANSPORT EQUATION FOR THE SPALART - ALLMARAS MODEL

Spalart and Allmaras jointly published a one equation turbulence model in 1992 by modeling the kinematic eddy viscosity as the transport variable [56]. This turbulence model was designed specifically for applications in aerospace which consist largely of wall bounded flows. In general, this model is known to produce acceptable results for boundary layers subjected to adverse pressure gradients [68]. The

simplicity of this model, compared to others, and the acceptable results for wall bounded flow has made this the model of choice for this thesis.

The S.A. model does not calculate the turbulence kinetic energy κ and therefore the Boussinesq hypothesis is simply reduced to the mean strain rate tensor S_{ij} and kinematic turbulent viscosity $\frac{\mu_t}{\rho}$. The single modeled transport variable for turbulent flow becomes the modified kinematic turbulent viscosity $\tilde{\nu}$ which is a modified form of the turbulent kinematic viscosity. The eddy or turbulent viscosity is a turbulent flow property and the flow near the wall is not turbulent. Hence, near the wall, $\tilde{\nu}$ is set to zero because this is a molecular viscosity dominated region. Using a tensor form of Reynolds transport equation $\tilde{\nu}$ is modeled by equation 3.4 [68].

$$\frac{\partial}{\partial t}(\rho\tilde{\nu}) + \frac{\partial}{\partial x_i}(\rho\tilde{\nu}u_i) = G_{\tilde{\nu}} + \frac{1}{\sigma_{\tilde{\nu}}} \left[\frac{\partial}{\partial x_j} \left\{ (\mu + \rho\tilde{\nu}) \frac{\partial \tilde{\nu}}{\partial x_j} \right\} + C_{b2} \rho \left(\frac{\partial \tilde{\nu}}{\partial x_j} \right)^2 \right] - Y_{\tilde{\nu}} + S_{\tilde{\nu}} \quad 3.4$$

In total there are three functions and eight coefficients provided by S.A. model to close the RANS function. These equations and coefficients are found in detail in [68] and [70].

3.4 WALL BOUNDARY LAYER THEORY

The resolution at the near-wall region is based on refinements done to the mesh and whether it is in accordance to the specifications set by the turbulence model selected. The S.A. model, the modified turbulent kinematic viscosity term, $\tilde{\nu}$ is set to zero at the walls. The degree of mesh refinement at the walls dictates how well the viscosity-dominated sublayer is resolved. The theory for inner turbulent boundary layer consists of the viscous sublayer, buffer layer, and log-law region (refer to Figure 3.1) and together become a piecewise set of equations. The piecewise equations are dependent on the locations within the inner boundary layer denoted by the dimensionless wall distance y^+ . Utilizing the y^+ values as referenced from [68], these three regions can be separated as in Table 3.1 and formulations dictated by equation 3.5. These equations are based on a characteristic flow parameter u_* derived from an analogy to laminar flow [39]. The inner layer region has a special property where the shear stress is nearly the same as τ_w ; hence, its name Constant Shear Stress Layer.

Table 3.1 – Sections of the Inner Boundary Layer

SECTION	y^+ RANGE	TYPE	EQUATION
Viscous Sublayer	$y^+ \approx 1$	Linear	Equation 3.6
Buffer Layer	$1 < y^+ < 30$	Combination	N/A
Log – Law Region	$y^+ \geq 30$	Logarithmic	Equation 3.7

$$u_* \equiv \sqrt{\frac{\tau_w}{\rho}}, \quad y^+ \equiv \frac{\rho u_* y}{\mu}, \quad u^+ \equiv \frac{u}{u_*} \quad 3.5$$

The velocity u is found piecewise for each section as shown in Table 3.1 but usually plotted as u^+ . Equation 3.7a is the *law-of-the-wall* and represents the log-law region.

$$u^+ = \frac{u}{u_*} = y^+, \quad \therefore u = \frac{\rho}{\mu} y \quad 3.6$$

$$u^+ = \frac{u}{u_*} = \frac{1}{\kappa_0} \ln \left(\frac{y}{y_0} \right), \quad \kappa_0 = 0.4187 \quad 3.7a$$

$$u^+ = \frac{u}{u_*} = \frac{1}{\kappa_0} \ln E \left(\frac{\rho u_* y}{\mu} \right), \quad \kappa_0 = 0.4187, \quad E = 9.793 \quad 3.7b$$

These methods were first published by von Kármán [71] in 1930 and also found in [39] and [68]. Equation 3.7b is the form used by ANSYS – FLUENT [68] for a smooth surface where E may change due to the roughness height y_0 . The roughness height is defined as the height at which u equals zero as given by the law-of-the-wall; however, the law-of-the-wall is not applied at the wall [39]. The Buffer Layer is the region where both the linear and logarithmic equations attempt to merge. No well-defined equation fits in this region for all flow types; hence, it is approximated as a combination of the linear and logarithmic sections. As shown by Newman in Figure 3.1, an experiment conducted in 1971 by Monin and Yaglom, show the dimensionless mean velocity profile of turbulent flow next to a smooth wall. The three subdivisions are clearly shown by red lines. The leftmost region is the viscous sublayer, the middle region is the buffer region, and the rightmost region is the log-law region. Together, these three sections comprise the inner layer of the boundary layer. CFD closely models this piecewise equation; however, it is grid sensitive. This will be described further in the sections that follow along with the fundamentals of which CFD solver algorithms abide by.

4 NUMERICAL METHODS

4.1 OVERVIEW

In the previous chapter, various theories were discussed; however, for CFD modeling and simulation, a numerical representation of the theory is required in order to simulate the results. ANSYS – FLUENT provides solutions based on several different types of algorithms. The topics to be discussed in the sections that follow include the numerical methods used along with the computation procedure, surface treatments, and CFD flow models. These topics will be briefly discussed as they are detailed in ANSYS – FLUENT theory guide [68].

4.2 NUMERICAL METHODS

Choosing the correct governing equations is required to initiate the computational procedures. Once the solver is chosen, the manner in which governing equations, transport equations, and other scalars are solved dictates accuracy, program efficiency, convergence, and other factors which may affect computer resources.

4.2.1 DISCRETIZATION

Given the intention of implementing numerical analysis techniques, it is first necessary to divide the model into counterparts. Converting a model into discrete parts is a process known as discretization. This applies to the governing equations, as well as general transport equations. Once all these terms have been discretized the CFD process may ensue. Each of these levels of discretization and methods are briefly explained in the sections that follow.

4.2.1.1 DISCRETIZATION OF GENERAL TRANSPORT EQUATION

ANSYS – FLUENT applies conservation laws to individual control volumes, known as cells. These cells comprise the computational grid or mesh. As explained in [68], the control volume technique converts a general scalar transport equation to an algebraic expression which is solved numerically. This is done by applying an integration of the transport equation over the cell volume resulting in a discrete equation for that cell. This process is done in a cell by cell basis encompassing the entire computational domain. Equation 4.1a is a variant of Reynolds transport theorem, equation and referred to as the *general scalar transport equation* [68]. Equation 4.1a is applied per cell volume and the discretized form is shown as equation 4.1b.

$$\iiint_{\mathcal{V}} \frac{\partial}{\partial t} (\rho\varphi) d\mathcal{V} + \iint_S \rho\varphi \vec{V} \cdot d\vec{S} = \iint_S \Gamma_\varphi \nabla\varphi \cdot d\vec{S} + \iiint_{\mathcal{V}} S_\varphi d\mathcal{V} \quad 4.1a$$

$$\frac{\partial}{\partial t} (\rho\varphi) d\mathcal{V} + \sum_f^{N_f} \rho_f \varphi_f \vec{V}_f \cdot \vec{S}_f = \sum_f^{N_f} \Gamma_\varphi \nabla\varphi_f \cdot \vec{S}_f + S_\varphi d\mathcal{V} \quad 4.1b$$

$$a_p \varphi = \sum_{nb} a_{nb} \varphi_{nb} + b \quad 4.1c$$

The subscript f is used to denote a value pertaining to a certain cell face. As by default, in equation 4.1b, neighboring cell face and center values are required for computation of φ . However, these values are not necessarily known and may be required as user inputs such as inlet boundary conditions. Also, equation 4.1b is inherently nonlinear and equation 4.1c is the linearized form of equation 4.1b. The newly introduced variables are denoted in the Nomenclature section. This discretization provides the value of the transport quantity φ stored in the cell center.

4.2.1.2 SPATIAL DISCRETIZATION SCHEMES

In order to determine the values at the cell faces it is necessary to apply a method of spatial discretization. Spatial discretization is a Taylor series expansion of the transport quantity solution about the cell center and used to interpolate any point of interest within the cell, notably the cell face. It should also be noted that the temporal term in equation 4.1b is ignored for steady state solutions as performed in this thesis; hence for temporal discretization techniques refer to [68]. The number of terms of the Taylor series expansion is dependent on user selection of spatial discretization.

A general idea of how to choose the correct order of the Taylor series expansion is to visualize the flow while considering the mesh. If the flow is aligned with the mesh so that the flow vector is mainly normal to the mesh face, zeroth order Taylor series expansion may be acceptable. This is seen in structured meshes analyzing laminar flow on a rectangular duct using quadrilateral or hexahedral mesh [68]. Meanwhile, if the flow is not aligned with the mesh, such as in triangular and tetrahedral based meshes, then first order and above are recommended otherwise numerical diffusion (discretization error) is introduced. A simplistic analogy is to approximate a nonlinear function utilizing a zeroth order Taylor series approximation. The discretization error is analogous to the error of approximation introduced by not accounting for the slope of the nonlinear function. Each scheme may be used independently; however, the proper application and combination will produce more accurate solutions.

Since, quantities are estimated per cell, the directional application of the Taylor series function must be defined. The term “upwind” refers to the upstream direction relative to the cell face value being approximated. This is determined by the velocity vector component normal to the cell face. Another alternative is the central differencing method which approximates quantities based on the average of adjacent cell centroid values and the average of their reconstructed gradients, $\nabla\phi \cdot \vec{r}$. *First Order Upwind*, *Second Order Upwind*, and *Third Order MUSCL* (Monotone Upstream-Centered Schemes for Conservation Laws) spatial discretization schemes are referenced in Appendix A as equations A.2 thru A.4. The ordinal number refers to the number of terms in the Taylor series; hence a zeroth order Taylor series approximation contains only one term. First order upwind assumes that the cell center value is the average of the quantity ϕ throughout the entire cell and this value is applied for any point within the cell. Increased accuracy is attained using greater order Taylor series approximation; however, the highest order currently available is a first order Taylor series approximation. Notice that the Third Order MUSCL scheme is a combination of the second order upwind and the central differencing method and *not* a second order (up to the third term) Taylor series approximation. It simply improvises by averaging the numerical diffusion of adjacent cells. Refer to [68]. The gradient term $\nabla\phi$ used to improve accuracy at the upwind cell face value and its discretizing methods will be discussed next.

4.2.1.3 GRADIENT DISCRETIZATION

The node to node and cell to cell interactions within the computational grid are not always acceptable. This is especially true for unstructured mesh. It is possible that undesirable grid characteristics exist such as grid nodes deviating from one another, poor cell aspect ratio, and other irregularities. This may cause overshoots and undershoots in CFD computation. Choosing the correct discretization method for the diffusion terms aid in correcting and improving accuracy. There are three types of Gradient Evaluation including Green-Gauss Cell-Based, Green-Gauss Node Based, and Least Squares Cell-Based. This thesis utilized the Least Squares Cell-Based Gradient Evaluation which assumes that the change in adjacent cell values of cell c_0 and cell c_i along vector δr_i varies linearly. The system of linear equations that arises is then solved in a least squares sense. This is performed using the Gram-Schmidt process [68]. As mentioned, this gradient is limited in order to prevent overshoots and undershoots due to poor mesh characteristics and regions of rapid changes in flow properties. This is performed using a standard limiter which is of non-differentiable type and its purpose is to limit and trim the solution on cell faces.

4.2.1.4 GOVERNING EQUATIONS DISCRETIZATION

STEADY STATE MOMENTUM EQUATION

In Chapter 3, it was mentioned that the Reynolds transport equation is a fundamental equation for all CFD computation. An application of the transport equation (equation 4.1a) in terms of linear momentum $\varphi = \vec{V}$, produces the vector equation for steady state *Linear Momentum* shown by equation 4.2a.

$$\iint_S \rho \vec{V} (\vec{V} \cdot \vec{n}) d\vec{S} = - \iint_S P \vec{I} d\vec{S} + \iint_S \vec{\tau} d\vec{S} + \iiint_V \vec{F}_{ex} dV \quad 4.2a$$

$$a_p u = \sum_{nb} a_{nb} u_{nb} + \sum P_f A \cdot \hat{i} + S_u \quad 4.2b$$

After discretization and linearization the u component of equation 4.2a is shown in equation 4.2b. The rightmost summation-term in equation 4.2b represents the pressure field and face mass fluxes. If this term is known, then equation 4.2b becomes 4.1c and simple rearrangement of variables produces the velocity field component u . Apply this concept to all components of the momentum equation and the velocity field \vec{V} is obtained. As presented by ANSYS – FLUENT theory guide [68], if the pressure field and face

mass fluxes are not known they are computed as part of the solution. ANSYS – FLUENT stores the values of velocity and pressure at the cell center, and any other spatial location, such as cell face, requires an interpolation.

The large pressure jumps in the flow encountered in this thesis are mainly because of the unstructured mesh orientation and swirling flow conditions called for a second order pressure interpolation scheme. The second-order pressure interpolation scheme applies the same central differencing concept referred in Appendix A by equation A.1, to the convective terms, in order to determine the cell face pressure. A brief overview of additional pressure interpolation schemes are found in Appendix A.

STEADY STATE CONTINUITY EQUATION

The continuity equation is another governing equation which is discretized and later coupled with the momentum equations to perform iterative computation. Equation 4.3a shows the steady state vector form of the continuity equation. Once discretized it becomes equation 4.3b where J_f is the mass flux ρV_n through face f [68].

$$\oiint_S \rho \vec{V} \cdot d\vec{S} = 0 \quad 4.3a$$

$$\sum_f^{N_f} J_f A_f = 0 \quad 4.3b$$

Continuity enforces that the normal velocity at the cell face needs to be related to the velocity value stored at the cell center. Linear interpolation of values from adjacent cell centers leads to unphysical results referred to as ‘checkerboarding’. Its occurrence is due to the equations not being coupled and solutions of the same variable being shared by the same grid. In order to prevent this, J_f is recalculated based on works of Rhie and Chow [72]. As simplified in ANSYS – FLUENT theory guide [68], the face flux J_f , is computed by momentum-weighted averaging of the velocity and using weighted factors based on a_p . This procedure determines an adjusted face flux value which produces an additional condition for pressure known as the Pressure–Velocity Coupling used by the solver to produce solutions. The density for incompressible flow is calculated based on arithmetic average of cell centered values. The density interpolation schemes for compressible flow will not be mentioned in this thesis as it was not required.

4.2.1.5 SOLVER ALGORITHMS

ANSYS – FLUENT provides two types, pressure- based and density-based solver. These solvers are processed based on the selected pressure-velocity coupling scheme known as either coupled or segregated. In this thesis, a pressure-based solver was implemented utilizing a coupled approach. A diagram chart of the process taken by each approach is shown in Figure 4.1. Nevertheless, brief understanding of different approaches is beneficial and presented in Appendix A.

4.2.2 DOMAIN INTERFACE TREATMENT

ANSYS – FLUENT allows computation to be done in different reference frames in order to simplify problem setup depending on flow types and surface interactions. Flows with relative motion involving moving parts require multiple reference frames. More specifically, analysis of fluid flow through multiple stage turbines and compressors may require several moving reference frames. The addition of reference frames increases the complexity of the problem; however, it is a necessary addition since flows with moving parts cannot be modeled using single reference frames. It is important to understand the interaction of these reference frames and their interfaces between each other as quantities must be transformed from frame to frame. The next section will describe how these frames interact mathematically. Complete details and formulation may be found in ANSYS – FLUENT theory guide [68].

4.2.2.1 VELOCITY FORMULATION

Flow quantities may be stored in the absolute or relative frame depending on user selection which facilitates computation. Steady state solutions may be attained relative to a moving reference frame where it would be otherwise unsteady with respect to the absolute frame of reference. Therefore, by computing relative to an unsteady frame allows for steady state computation for the moving reference frame.

In flows with multiple reference frames, it is required to specify which frame of reference to compute in. When the entire domain is reduced to subdomains, each subdomain contains its own velocity formulation (as well as other vectors and scalars). If the user specifies to formulate the velocity field *relative* to the moving reference frame then ANSYS – FLUENT stores these quantities in the frame of reference of each domain. Otherwise, if the user specifies to compute in the *absolute* frame of reference, then every subdomain is computed relative to itself but the quantities are transformed and stored into the

absolute reference frame for all domains. This transformation respects the conservation laws using relative and absolute velocities and the kinematics equations for rigid body motion. It is important to note that transforming from a noninertial frame to an inertial frame requires additional terms for the gradients of velocity which are required to solve the conservation laws, refer to [68]. Additionally, special attention is given to the boundaries or interfaces between these frames of reference.

The interaction of the cells at the interface of subdomains is important since one side contains one reference frame and the other contains another. In order to simplify this situation, ANSYS – FLUENT applies a *local* reference frame to the interface and transforms the velocities adjacent to the interface to the absolute frame of reference. The gradient term, as well as the vector quantities (velocity in this case), are also transferred across the interface. The transfer of quantities; however, is dependent on the fluid flow model selected.

4.2.3 FLUID FLOW MODELS

There are different ways to analyze how the flow is transferred from one frame to another, after all these solutions are being obtained numerically. This causes the flow model chosen to be dependent on flow conditions. Three models are currently offered by ANSYS – FLUENT including Multiple Reference Frame (MRF), Mixing Plane, and Sliding Mesh models. In this thesis, only the MRF and sliding mesh model will be discussed.

4.2.3.1 MRF MODEL

The multiple reference frame model allows for the specifications of cell zones which are also known as subdomains. These cell zones require translational and rotational velocity inputs which are problem specific. The question lies in how ANSYS – FLUENT applies these flow conditions given the mesh locations. The fluid particle position is analogous to the mesh cell centers. In the MRF model, the cells in the mesh do not move and the values of velocities are quantities given per cell at a fixed time. Since the mesh is stationary, computation is inherently in steady state; thus, the solution is an instantaneous flow field computed at the fixed position of all moving parts. This is known as the ‘Frozen Rotor Approach’. However, in cases where rotating parts are present, if strong unsteady interactions between the

subdomains are present, they will not be computed in the MRF model. This will be further discussed in Chapter 8.

Furthermore, at the interface, the cells adjacent to each other require values given by their neighboring cells as described earlier. ANSYS – FLUENT enforces the continuity of the absolute velocity at these interfaces and thus determines the values upstream, downstream, and at the interface. This is the main difference between the MRF and mixing plane model: in the mixing plane model the values at the interface may be averaged over the surface. Therefore the mixing plane model is an attractive model for nonconformal meshes. Although the MRF model computes only steady flows, the MRF model can be utilized to approximate transient flows by computing the time averaged flow field *instantaneously*. In doing so, the MRF model requires the velocity profiles at the interfaces to be relatively uniform and uncomplicated. Additionally, MRF model also serves as initial conditions for the sliding mesh model.

4.2.3.2 SLIDING MESH MODEL

Inherently, the MRF model is limited due to its steady state nature; however, the sliding mesh computes utilizing a moving mesh. The cell zones are allowed to translate and rotate as a rigid body motion. Doing so changes the position of the nodes with time; thus analogous to the position of fluid particles with respect to time. Hence, this model allows simulation of the transient affects due to strong interactions between domains (moving and stationary). The sliding mesh model also allows the deformation of the mesh which is referred to as a dynamic mesh; however, in this thesis deformation is not required. The main value of this method is to determine the circumferential periodicity of the flow which indicates the temporal range of numerical computation. In other words, since the sliding mesh provides justification for the translational and rotational velocities of the nodes, this model is inherently *unsteady*. Hence, the computation requires time steps which in turn require an indicated stoppage time to determine when to cease computation. Therefore, circumferential periodicity must be determined. Once one full period is determined the solutions for all times may be approximated. However, in cases where circumferential periodicity is complicated and occurs over large periods of time, such as a multistage compressor, this model may not be convenient. Any transient computation requires significant increase in time and computation for a converged solution and depending on problem, increased storage space. Without giving the mathematical numerical schemes for temporal discretization for this model the process

of computing using this method will be briefly mentioned. The sliding mesh essentially computes the flow field at an initial time t_i , similar to the MRF, and then once a converged instantaneous solution is obtained at t_i , the mesh is adjusted according to user specifications. Next, at some Δt , the computation is continued to obtain the instantaneous velocity field at $t_i + \Delta t$ until a converged solution is obtained. This process is repeated until the user indicated final time is reached. Clearly the amount of computation is significantly increased. As mentioned, the MRF model can be used as an initial condition for the sliding mesh model, to reduce the number of iterations for t_i .

4.2.4 THRUST COMPUTATION

An important quantity to be obtained from CFD computation is the thrust. The thrust is computed numerically as the dot product of the pressure and viscous forces along the cell face of the surface of interest. The direction of the force vector is user defined. Thus, the addition of the pressure force component and viscous force component along the specified direction provides the total force component in that direction. This is the numerical representation of the momentum integral over a control surface. Further mathematical details are found in ANSYS – FLUENT theory guide [68].

4.2.5 ACCURACY AND CONVERGENCE

Solution accuracy is dependent on the numerical procedures discussed earlier in this thesis. However, a very important condition to consider is that a higher order numerical procedure is not always the best approach. A mesh which contains undesired features based on its cell geometry may increase discretization error which would require a higher order scheme to be applied. The next few concepts will mention influence convergence and accuracy.

4.2.5.1 INITIALIZATION

A successful convergence is completely problem dependent and different for every problem. As with any iteration, if the initial ‘guess’ is close to the actual solution iterations are greatly reduced. Two common methods of initialization are standard initialization and hybrid initialization. The standard initialization method is useful for inputting a guess at a certain location, say the inlet of a tunnel. Another form of initialization is hybrid initialization. This is used to initialize complex geometries; however, it

computes flow by solving Laplace's equation or potential flow theory. Thus, a hybrid initialization for a viscous flow simply prolongs convergence since initial residuals are usually greater.

4.2.5.2 CONVERGENCE CRITERIA

The discretized equations are computed in an iterative manner, as discussed above, and only cease once the maximum residual, set by the user, is met. The level of precision of which a computer can compute a residual is another limiting factor. Infinite precision is not yet possible; however, single and double precision computation is. Single-precision allows up to six orders of magnitude while a double-precision computer may reach up to twelve orders of magnitude. Hence, a single-precision computer will never converge to a residual value of say 10^{-8} . A basic thought worth contemplating. In most cases, such orders of accuracy are not necessary. Majority of problems can be solved using residual values at or below 10^{-3} . This is the default value set by ANSYS – FLUENT for all residuals except energy and P-1 equations where the default value is 10^{-6} . The residuals may be changed at by the user. There are three forms of residuals for the pressure-based solver. They are unscaled, globally scaled (default), and locally scaled residuals.

The globally scaled residual for the general transport variable ϕ is a manipulation of the unscaled residual over the flow rate of ϕ through the domain; hence on a global level. Since the formulation of this residual is based on the discretized equation 4.1c, the residual for the continuity is formulated differently. In general the residual for continuity utilizes the sum of all mass created within the individual cells. This is intuitive as mass is conserved within the control volume; hence, the creation of mass is simply the error. Full details are found in [73]. The default setting in ANSYS – FLUENT is to converge based on globally scaled residuals as this method provides an overview of all cells within the domain.

Another influence on convergence is relaxation factors. Relaxation factors are applied to variables and functions such as for momentum and pressure in order to control the change of ϕ per iteration. When applied to variables it is referred to as under-relaxation of variables or explicit relaxation. Reference [68] details the theoretical procedure for implicit relaxation for transient problems which require time step or time advancement algorithms. Explicit relaxation in general reduces the iteration value change $\Delta\phi$ from the previous computation to the next by a fraction of its $\Delta\phi$ value as shown by equation 4.4. This is

necessary because of the nonlinearity of the equations being solved. Therefore, by computing the change in φ and multiplying by an under-relaxation factor β allows for smoother convergence.

$$\varphi_{new} = \varphi_{old} + \beta \Delta\varphi \quad 4.4$$

The under-relaxation factor is a number less than unity. Thus, a value for β closer to unity would produce an aggressive convergence and a value closer to zero would produce a conservative convergence [73]. This being mentioned, a large β will normally produce faster convergence; however, residual behavior might become oscillatory or even diverge. If this occurs reducing relaxation factors may improve convergence. Additional convergence and accuracy recommendations provided by ANSYS – FLUENT are shown in Appendix A.

5 COMPUTER AIDED DESIGN, MODELING, AND SOLVER

5.1 OVERVIEW

Simulation is not possible without a well-built computer based model and mesh. The computer aided design (CAD) model is where the process begins and proceeds to the meshing of the CAD model. In this chapter, the steps taken to create the geometry and mesh the fluid domains will be discussed. These are the three main steps (Geometry, Mesh, and Solver) which were taken to complete this thesis. In addition, the setup of the ANSYS – FLUENT solver will be mentioned including the entire setup process ranging from boundary conditions through solution post-processing.

5.2 GEOMETRY DESIGN

A ten bladed Sevik propeller is the basis of the problem to be considered. The specifications of the propeller geometry were provided, but an actual digital copy of the model was not available. Therefore, it was required to rebuild this propeller based on the properties given by M. Morton [74].

5.2.1 SEVIK PROPELLER

The Sevik propeller has blades with constant chord along its span (without skew) and squared tips. The blade pitch angle varies nonlinearly. Airfoil geometry is constant along the span with the max airfoil thickness at mid chord for both the root and tip profiles. These properties are summarized in Table 5.1. The diagram of the blade profile and angle of twist is shown in Figure 5.1, with the angle of twist ranging from 55.6 degrees at the root to 21.2 degrees at the tip. FLUENT-ANSYS requires the input of the fluid around the propeller to be modeled; therefore, a rectangular prism encasement was also created. This geometry will be referred in Wind Tunnel section of this chapter.

Table 5.1 – Propeller Geometry

PROPELLER PROPERTIES	
Chord Length	57.2 mm
Blade Span	165.1 mm
Blade Pitch Angle (Root)	55.6 °
Blade Pitch Angle (Tip)	21.2 °
Diameter of Blade Plane	457.2 mm
Hub Diameter	127 mm
AIRFOIL DESIGN	
Max Airfoil Thickness (Root)	0.097 t/c
Max Airfoil Thickness (Tip)	0.84 c

It is important to mention that even though the geometry is simple some variables had to be assumed in order to complete the design process, including the variation of pitch across the entire blade span. Table 5.1 shows the blade pitch only at the root and tip. However, it is mentioned in [6] that this variation is nonlinear. Since the exact variation was not available a linear interpolation was made to obtain the pitch at every spanwise cross section. After a private discussion with Dr. Glegg, it was mentioned that the blade pitch varies as $\tan^{-1}\left(\frac{\Omega r}{v_{in}}\right)$ as in [74]. Another assumption made was the fillet at the blade and hub connection. In order to maintain an airfoil shape throughout the entire spanwise section a fillet or merging of the blade surface to the hub surface was avoided. This creates a geometry which contains a sharp corner where the blade meets the hub (root section). This geometry assumption is shown in Figure 5.2, which compares the actual propeller to the CAD model. This sharp corner in the CAD model is justified since the main objective of this thesis is to obtain inflow data upstream of the propeller and the influence of such features are insignificant. However, this point is important to mention due to problematic regions in the meshing process and shown by the solver which will be discussed in both Mesh and ANSYS – FLUENT Solver sections of this chapter. Fillets could have been created to match the actual propeller; however, without the exact fillet radii measurements it is best to reduce the geometry to no fillets as an improper fillet measurement would cause a reduction of the blade cross-section at the root. Lastly, the hub

anterior and posterior sections were simplified as shown by Figure 5.3. This was necessary in order to simplify meshing, as well as, problem setup in ANSYS – FLUENT. Several modifications were done to the actual propeller in order to reduce noise as seen in Figure 5.3 (a) and (b). The inclusion of foam sections reduce the step heights of the structure holding the propeller in place in order to improve noise measurements made as part of this project. As mentioned, this thesis only focuses on the aerodynamics of the propeller. Therefore, to simplify these structural elements they were removed and the hub anterior and posterior sections were shortened enough to include the entire length of the propeller and hub sections within six chord lengths which is the length of the rotating subdomain. Next, the preparation of the CAD model for the wind tunnel section will be discussed.

5.2.2 WIND TUNNEL

The wind tunnel section represents the inclusion of the entire fluid around the propeller which is necessary in order to model the fluid flow in ANSYS – FLUENT. This represents the fluid while the propeller mentioned above is, in a digital sense, subtracted from the fluid leaving behind a cavity which is modeled as the surface of the propeller. The dimensions of this fluid section, referred to as the wind tunnel section, were created by simply choosing to ignore wall effects on the flow, except in the floor region. Configurations 2 and 3, shown in Figure 5.4, use the same exact geometry while Configuration 1, shown in Figure 5.5, is slightly modified. Arrows are used to denote the coordinate system directions. The inflow direction is in the positive x-axis and in the configuration 2 and 3. The positive y-axis direction is in the spanwise direction towards the propeller and normal to the near wall. The z-axis follows the right hand rule. All three configurations use the same coordinate system directions.

The creation of this region places the origin exactly at the inlet as shown by Figure 5.4 and Figure 5.5, in a manner which the tip of the front hub cone is exactly at coordinates (1500, 0, 0). The dimensions were determined based on measurements in terms of diameters of the propeller. Domain lengths were determined in terms of propeller diameters. The distance upstream of the propeller spanwise centerline is slightly greater than three and a half diameters in length. The distance downstream of the propeller spanwise centerline is slightly greater than seven diameters in length. The lateral distances are slightly larger than three diameters and in the case of configuration 1, this lateral distance extends in both y and z

directions removing the wall. This is the only difference between configuration 1 and configuration 2 and 3. In configuration 2 and 3 the near wall was placed as in the experimental setup. The clearance between the blade tips and the wall is 20.3 mm which leads to a distance from the blade center to the wall of 248.90 mm. Other dimensions were based on preliminary CFD computations of different model setups and lengths. After several trials, these dimensions presented zero wall effects. To clarify, the goal was to create a wind tunnel which allows measurements to be performed without the influence of wall properties on the flow, such as the no slip condition, viscosity effects, wall roughness, etc. Thus, by increasing the distance of the walls from the blades far enough allows the flow measurements to be unaffected by the surrounding walls. As mentioned, the interest in configuration 1 regards no wall influence and configuration 2 and 3 regards *only* the near wall influence. Figure 5.6 shows trimetric views of all domains. Notice in Figure 5.6 (a), the walls are spaced equally, while in Figure 5.6 (b) the near wall affects the flow while all other walls are spaced so as to give no interference. Furthermore, the dimensions of the rotational domain were chosen after several trials to determine the distance from propeller blade tips and distances in front and behind the blades.

The rotational domain was created to model the rotating propeller. This is shown in Figure 5.6 (c) and is the same dimensions for all three configurations. This domain encases the entire propeller measured three chord lengths in front and back of the propeller spanwise centerline. The radial extension is limited to 102% of the propeller's diameter. This dimension was chosen as to provide interaction between the exterior (translating fluid) domain and the interior (rotating fluid) domain giving rotational properties to the tips of the propeller as well as an additional 2% of the diameter. If this region was any larger radially, possible unphysical flow could be simulated. The domain length was chosen as three chord lengths in either direction in order to fully encase the hub sections and most importantly, obtain a relatively uniform flow at the interface of the rotational domain. This is a requirement for utilizing the MRF model as mentioned previously. The shape of the exterior wall encases the propellers as a rectangular prism; however, this has no effect on the flow measurements given the distance of the walls to the propeller. As for the rotational domain, the walls which create this domain are interpreted as interior interfaces in ANSYS – FLUENT and are not to be confused as a physical wall but simply an interface between two

domains. Based on these properties, a CAD model was created using SolidWorks program and then exported as an IGES file into the meshing software which will be discussed in the sections to come.

5.3 MESH

The next crucial phase is the meshing of the geometry. The mesh is dependent on problem specification meaning that depending on what is to be observed or measured determines how the geometry is to be meshed. An example being that if the vortex generated by the blade tips are to be simulated, then a well-defined structured (preferably) mesh is to be located at the blade tips, as well as, the flow leading to it. In this case, refining the mesh at a remote location has little to no influence on the features being observed. Hence, it is important to analyze how the meshing process is to be performed. The mesh was produced using ANSYS – ICEM software and then imported into ANSYS – FLUENT as a mesh file. Next, details of the mesh generation will be provided. At any point in this section, it is recommended to refer to Appendix B for views and annotations of different mesh and mesh regions.

5.3.1 STATIONARY DOMAIN

The stationary domain is the wind tunnel section excluding the rotational domain. Visually, this is equivalent to Figure 5.6 (a) or (b) subtracting Figure 5.6 (c). This domain is referred to as the stationary domain because in ANSYS – FLUENT it has zero translational and rotational velocities. Other specifications will be provided in ANSYS – FLUENT Solver section of this chapter. Mesh densities are also included to refine regions of interest which will be discussed in the section that follows. Figure 5.7 (a) and (b) show the mesh for the stationary domain excluding the rotational domain and propeller. The yellow region in Figure 5.7 (b) is a portion of the wall which was strategically separated from the surrounding walls in order to obtain full control of mesh sizes and inflation rate for that region only, thus reducing the need to refine the entire wall region. Doing so reduces total element size and at the same time refines the regions of interest. The inlet is shown in blue and the outlet is in red. Notice how the center of Figure 5.7 (a) and (b) are refined due to the mesh densities placed at the inlet. This will be discussed in the Mesh Refinement and Densities section of this chapter. The stationary domain contains approximately 47% of all elements within the grid while the remainder is located within the rotational domain. This

shows the level of refinement required to obtain a converged mesh which will be discussed in the Chapter 8. It is a fact that the extension of the walls could be reduced in order to reduce total element size and still obtain reasonable results. Nevertheless, given the extensive resources of the computers used for computation at Florida Atlantic University, the additional elements did not pose any computational problems. Next, general information regarding the rotational domain will be given.

5.3.2 ROTATIONAL DOMAIN

As mentioned, over half of all elements are located within this subdomain due to the need for refinement in order to accurately represent the flow within this region. This region contains complex flow features such as swirl which increases diffusion and numerical error. Therefore, in an attempt to minimize these errors, reduced elements sizes were used in this region, as well as, the ratio of tetrahedral cell increase within a certain region (inflation). A single mesh density was strategically located in this region to enforce inflation in regions of measurement. Figure 5.7 (c) shows the mesh for the rotational domain including the interface in front of the propeller in blue and the interface behind the propeller in red. This color coding follows the same direction as the inlet (blue) and outlet (red) in the stationary domain. The grey region is the radial exterior regions of the domain. The propeller is seen within the domain. The fluid fills this domain from the propeller surface to the interfaces. The propeller surface does not allow penetration of fluid meaning that the interior of the propeller is not meshed and only the surface is. This defines the entire domain mesh and refinement details will be given in the following section.

5.3.3 MESH REFINEMENT AND DENSITIES

In order to accurately capture the flow characteristics and quantities a well-developed mesh is necessary. Flows where the boundary layer is of interest require a locally structured mesh comprised of rectangular prism or hexahedral elements; however, for complex geometries obtaining such mesh characteristics becomes more difficult. If prism layers are formed at surfaces it is required to ensure that the overall mesh quality has not been degenerated due to geometry complexities. This was the case for the geometry in this thesis. Prism layers were attempted; however, the overall mesh quality was reduced drastically. Therefore, an unstructured mesh was created in surface regions and tetrahedral elements were

used to replace the elements in the boundary layer. Several meshes were generated and computed using different inflation ratios and element sizes until a final mesh was used for comparison to experimental data.

The domains and subdomains were refined slightly different depending flow characteristics. Mesh surface is dominated by quadrilateral-type elements and follows edges and curves dictated by geometry. This allows the majority of the elements at the surfaces to be quadrilaterals. Additionally, the volume mesh type is mainly tetrahedral which is better suited for fluid flow computation. Mesh element sizes are denoted by units of 3D space which may be scaled depending on user preference. In this setup, the mesh was not scaled and therefore the units used in generating the geometry (mm) were maintained. The maximum element size was set to 200 mm and the minimum to 1 mm. Surface curvature and proximity based refinement was utilized in order to capture the blade edges correctly. This however, creates tiny elements are the blade root where the hub meets the blade. Since no filets were created, ANSYS – ICEM attempts to recreate the surface by placing minimum sized elements which later introduce problems related to wall y^+ values in the solver. This will be discussed in Chapter 8. If the mesh sizes in this region were larger, ANSYS – ICEM would not be able to correctly mesh these sharp corners and thus would create additional surfaces to patch the sharp corners. The mesh method used is robust (Octree). Complete details of these methods and types are found in ANSYS – ICEM help manual [75]. Further refinements were necessary to fully define the boundary layer and wake regions utilizing the mesh density feature.

The regions of focus include the flow leading to the propeller, as well as, the region in the wake. Configurations 2 and 3 need an additional refinement for the boundary layer region in the near wall. Therefore, a mesh density (cells per unit volume) has been set for all configurations shown in Figure 5.8. Mesh density is set by a maximum element size and/or inflation ratio; thus, limiting the maximum cell size within a created volume. The number of cells per unit volume is then computed by ANSYS – ICEM to user specification. In Figure 5.8 (a), the darker region is the wake refinement density set to a maximum size of 50 while the orange region is the boundary layer refinement density set to a maximum size of 20 with inflation ratio of 1.3. Inflation ratios are set to zero in these densities unless otherwise stated. This inflation dictates the ratio increase in tetrahedral size in the outer portions of the density. This allows the solver to fully capture the boundary layer profiles. The wake refinement includes a rectangular prism initiating at the inlet and extending past the propeller to a length of 2650 mm. with edge lengths of 600mm

and center located at the origin. Therefore it encompasses the propeller blades entirely and extends through the downstream wake region. The boundary layer refinement region exists only in configuration 2 and 3 and is another rectangular prism set flush with floor and extending in the y-direction 102 mm (boundary layer height). It also initiates at the inlet and extends 2224 mm in the x-direction. This allows for refinement in the boundary layer past the regions of measurement. This refinement is applied for configuration 2 and 3 with the same density box dimensions.

Another density refinement applied for all configurations is a triangular prism shaped density zone. This is shown in Figure 5.8 (b). It extends within the rotational domain and refines the region of measurement for comparison to experimental data. The dimensions include a base initiating at x value of 1837 mm outwards to an x value of 1990 mm. There is an inflation ratio of 1.1 for the exterior of this density. The triangular shape allows for further refinement within the regions of experimental measurement. Another feature is limitations set to surfaces which limit the growth of tetrahedral elements. Limitations were placed along the entire propeller surface, wall boundary layer section shown in yellow in Figure 5.7 (a), along the rotational domain interfaces, and within the fluid region of the rotational domain. Together these densities and refinements produced a final mesh of 3, 819, 656 total elements for configuration 1 and 5, 128, 872 total elements for configuration 2 and 3.

The main refinement difference shown in Figure 5.9 and Figure 5.10 is at the wall region. Notice that all configurations include refined regions at the interfaces, as well as, the blades regions. The unstructured mesh in Figure 5.11 (a) clearly shows the inflation applied to the surfaces and at the boundary layer regions. A main difference is presented by Figure 5.9 and Figure 5.10 showing the refinement at the bottom of the propeller in configuration 1 is the same as in the top. This is because configuration 1 is an axisymmetric flow without wall influences; thus, refinement is not needed at the bottom region of the propeller. A general circumferential refinement is applied to configuration 1 instead using densities and inflations as mentioned previously. Refinements of the stationary and rotational domains are shown in full detail in Figure 5.11 (a) and (b) respectively. Notice how well defined the rotational domain is compared to the stationary domain. This was necessary in order to obtain grid independence in this region. This study will be further discussed in the Chapter 8. Figure 5.12 (a) and (b) show a cross section in the XY plane of the mesh definition at the propeller surface and boundary between the blade tips and near wall.

Measurements are to be taken in these regions. These are regions were locally structured prism layer mesh would be most beneficial.

Once all mesh refinements are included, the mesh quality, skew, and aspect ratios were checked to ensure they all met requirements set by [73]. If the mesh quality is below recommended level elements are smoothed by ANSYS – ICEM and rechecked for accepted quality. In some cases, if the mesh contains inferior quality several surface smoothing operations, such as the Laplace Smoothing, can reduce the refinement levels set by the mesh densities and surface limitations. However, it is suggested that if more than a few smoothing operations are needed to improve mesh quality, it is better to change configuration settings and remesh. The final mesh used for computation met all recommendations by ANSYS – FLUENT user’s manual [73]. Once this phase is completed, the mesh was ready to be imported into ANSYS – FLUENT solver.

5.4 ANSYS – FLUENT SOLVER

All computation was performed by ANSYS – FLUENT and alternating solver inputs including boundary conditions, cell zone conditions, turbulence models, velocity formulation, solver type, solutions methods, discretization schemes, relaxation factors, and initialization methods. In addition, different types of mesh were also used until the optimum method was established which met all recommendations given by [73] and [75] and provided the best convergence and results. These trial and errors accumulated to over a hundred combined iterations of the geometry, mesh, and solver phases. The conditions which were chosen for the final presentations will be discussed below.

5.4.1 PROBLEM SETUP

Under the problem setup of ANSYS – FLUENT, details are provided by the user which indicate frame computation procedures, reference frames, turbulence models and turbulent conditions, and setting up fluid zones and boundary conditions. All configurations retained the same problem setup except for the boundary conditions and cell zone conditions depending on flow characteristics. These were changed per configuration and flow conditions.

A pressure based solver and an absolute velocity formulation was chosen to perform the computation. The MRF fluid model was chosen for steady state computation of the propeller in different configurations. Given that the experimental testing of the propeller was in air, the same fluid was chosen for CFD analysis. Although, insignificant for fluid dynamics computation involving only fluid flow without heat transfer, the solid material chosen to represent all walls was aluminum.

5.4.1.1 MODELS

The turbulence model utilized was the Spalart – Allmaras model given its ability to resolve boundary layers for external flow and performance under adverse pressure gradients. Also, its' one equation simplicity makes it an attractive alternative. Several other turbulence models were tested including $\kappa - \epsilon$ standard model, $\kappa - \epsilon$ realizable model, $\kappa - \epsilon$ model with and without near-wall treatments, $\kappa - \omega$ standard, $\kappa - \omega$ SST, and the Reynolds Stress model. One of the main reasons for choosing the Spalart – Allmaras model was due to the type of mesh generated. Spalart – Allmaras is less demanding than the other turbulence models and allows for unstructured mesh to be used and corrects for poor mesh regions along the walls where meshing is most complicated for complex geometries. Using the mesh generated, all other models (RSM, $\kappa - \epsilon$, and $\kappa - \omega$) produced similar results to the S.A. model. The constants used for this turbulence model are listed in Table 5.2. The S.A. production option chosen was vorticity – based; however, to increase resolution of vortices a strain/vorticity – based production is recommended. Both options were attempted and showed little to no difference in results. This is in part due to the MRF limitations and inability to resolve vortices shed from the blade tips as this is an unsteady fluid instability.

Table 5.2 – Spalart – Allmaras Model Constants

MODEL CONSTANTS	
C_{b1}	0.1355
C_{b2}	0.622
C_{v1}	7.1
C_{w2}	0.3
C_{w3}	2
Prandtl Number	0.667

5.4.1.2 CELL ZONE CONDITIONS

Cell zone conditions were equal for all configurations, except configuration 3 acoustic data. However, all configurations and flow conditions shared the same frame motion characteristics. They all included two zones, the stationary and rotational zone. The stationary zone and rotational zone each include its own reference frame. Table 5.3 and Table 5.4 show the details of the setup of these reference frames depending on flow conditions.

Table 5.3 – Stationary Zone: Cell Zone Conditions

ALL CONFIGURATIONS AND DATA SETS	
Rotation – Axis Origin	(0, 0, 0)
Rotation – Axis Direction	(1, 0, 0)
Translational Velocity	0 m/s
Rotational Velocity	0 RPM
Relative Specification	Absolute
UDF: Zone Motion Function	None

The stationary zone does not require translational velocity since that inflow velocity is applied as a boundary condition. The rotational cell zone conditions only change for the acoustic data since the results obtained for these cases will be used for aero-acoustic measurements for another study. Otherwise the data obtained from ranging rotational velocity along with varying inlet velocity, discussed in the next section, will be used for convergence studies and comparison to available experimental results. As mentioned, experimental results are only available for the range of propeller rotational velocities in Table 5.4. Another interesting aspect of this section is the shape chosen for the cell zones. It is important to note that the rotational domain is cylindrical in shape which allows imparted rotational properties (set by the solver) to be circumferentially equal. A cubed shape would not be suitable for problems involving rotation due to the sharp corners. ANSYS – FLUENT would apply rotational flow within the volume which would flow obliquely to the lateral surfaces, in respect to axial velocity. This would have unphysical properties and lead to error. Therefore, for rotational reference frame, it is recommended that flow is either normal or tangent to the interfaces. In addition, the rectangular prism shape of the inlet and exterior wall does not

have rotational properties at the walls and provide no influence on the flow given its distance from the propeller.

Table 5.4 – Rotational Zone: Cell Zone Conditions

ALL CONFIGURATIONS EXPERIMENTAL DATA SET	CONFIGURATION 3 ACOUSTIC DATA SET
Rotation – Axis Origin	
(0, 0, 0)	
Rotation – Axis Direction	
(1, 0, 0)	
Translational Velocity	
0 m/s	
Rotational Velocity	
1500 RPM	2734 RPM
2000 RPM	
2502 RPM	
2734 RPM	
Relative Specification	
Absolute	
UDF: Zone Motion Function	
None	

5.4.1.3 BOUNDARY CONDITIONS

Boundary conditions are set in reference to the adjacent cell zone. Therefore, to set a boundary condition one must first determine the type. Each surface and fluid regions require a setup of boundary conditions and much care must be taken to arrange them correctly. All operating conditions are set referenced to the origin with atmospheric pressure being the operating pressure. This may be changed depending if the results are to be output as gage or absolute. The first of the boundary conditions mentioned will be walls. These include the exterior wall of the tunnel, nearby wall (when applicable), and surfaces of the propeller. Table 5.5 shows the setup for all of the wall conditions. Note that the nearby wall retains the same conditions as the other walls of the wind tunnel. The only reason the wall was separated (shown in yellow, Figure 5.7 (b)), was to obtain full control in ANSYS – ICEM of that region.

Nevertheless, it is still considered part of the external wall of the tunnel and retains the same boundary conditions. Configuration 1 did not have this wall and only had external wall setup as shown by Table 5.5. The boundary layer is accounted for in the turbulence model and cells of the mesh not in the boundary conditions. In order to interpret the setup correctly, refer to the adjacent cell zone to each surface. The wall motion is set in respect to the adjacent cell zone; therefore, a propeller which is rotating at a constant rotational velocity with the fluid around it (set by the cell zone conditions) is relatively stationary. ANSYS – FLUENT interprets a stationary wall setting as stationary with respect to the absolute frame of reference; hence, it is best to indicate moving wall (private conversation with ANSYS support engineers). This gives the user full control of the surface motion relative to the cell zone.

Table 5.5 – Wall Boundary Conditions

PROPELLER SURFACE	WIND TUNNEL SURFACE
Adjacent Cell Zone	
Rotational Cell Zone	Stationary Cell Zone
Wall Motion	
Moving Rotational Wall	Moving Rotational Wall
Motion	
Relative to Adjacent Cell Zone	Absolute
Speed	
0 RPM	0 RPM
Rotation – Axis Origin	
(0, 0, 0)	
Rotation – Axis Direction	
(1, 0, 0)	
Shear Condition	
No – Slip Condition	
Wall Roughness	
Height of 0 mm (smooth wall) and roughness constant of 0.5 (default)	

Table 5.5 is interpreted for the propeller walls as the following: a moving wall, with rotational speed of zero RPM relative to the adjacent cell zone in the rotation axis of equal to that of the fluid (adjacent cell

zone). Since the propeller is stationary with respect to the fluid around it and the fluid in the rotational zone is rotating with respect to the absolute frame of reference at the RPM indicated by the flow conditions, then the propeller is interpreted as rotating with respect to the absolute frame of reference. This is how rotation is applied to a surface. Similarly, the interpretation of the tunnel walls is as follows: a moving wall with respect to the absolute frame of reference given rotational velocity of zero RPM and translational velocity of zero m/s in the direction of rotation set by the user. This is a bit confusing at first; however, it is the appropriate setting for a stationary wall since there is another moving reference frame within the entire domain. Once the absolute frame is selected and zero velocities are applied, the conservation laws are reverted to $\omega = 0$ forms. The default roughness height and constant were used to resemble a smooth wall. Once again, note that the inlet velocities are not applied as translational velocities in the wall boundary condition as that would imply that the wall is physically moving. Table 5.5 values did not change for any configuration or data set. Rotational and inflow velocities were only changed in the cell zones conditions (rotational zone) and inlet boundary conditions respectively.

Likewise, the inlet boundary conditions are given by Table 5.6. This boundary condition changed for each of the acoustic data results since the angular velocity of the propeller wall (boundary conditions) were kept constant and had varying advance ratios. The inputs for turbulence are based on experimental setup and wind tunnel specifications set by [76]. User defined functions (UDF) were utilized in order to apply an inlet boundary layer (1/7 Power Law) with a height of 102mm and a varying case by case nominal velocity. Configuration 1 and 2 applied constant inlet velocities which varied cases by case from 15 m/s to 30 m/s depending on case's advance ratio. Note that for configuration 1, the propeller is stationed in the middle of the domain with zero wall influence except for the no-slip condition on the propeller surface. Configuration 2 does have a near wall; however, no special functions were applied for the boundary layer definition. Hence, the inlet velocity is constant throughout, except for the boundary layer created by the no-slip condition. Configuration 3 has a thick boundary layer of 102 mm in height applied by the UDF mentioned. This is the same boundary layer applied for the acoustic data set, the only difference being the varying boundary conditions set by the rotational velocity in the cell zones and the inlet velocities. The UDF code generated for the 15 m/s case is shown in Appendix C. This is a self-modified version of a generic code provided by an ANSYS tutorial [77]. The only difference between UDF scripts is the

variable U , refer to the UDF code in Appendix C, which varies from 10 to 30 depending on case studied. These UDFs were individually loaded into ANSYS – FLUENT and set as the x-velocity component (Define -> User-Defined -> Functions -> Interpreted). The Y and Z velocities were set to zero. In the case where the x-velocity is constant no UDF was selected, and a simple input of the designated inlet velocity was made.

Table 5.6 – Inlet Boundary Conditions

CONFIGURATION		
1 and 2	3	3
EXPERIMENTAL DATA		ACOUSTIC DATA
Velocity Specification Method		
Components		
Coordinate System		
Cartesian		
Reference Frame		
Absolute		
X - Velocity		
Constant 15 m/s	UDF 15 m/s	UDF 10m/s
		UDF 15 m/s
		UDF 20 m/s
Constant 30 m/s	UDF 30 m/s	UDF 25 m/s
		UDF 30 m/s
TURBULENCE		
Turbulent Intensity		
1 %		
Hydraulic Diameter		
1795.23 mm		

Lastly, all other boundary conditions were the same for all configurations and data sets. All internal bodies, interpreted as fluid zones by ANSYS – FLUENT, were of type interior, all interfaces

between cell zones were set as type interior, and lastly, the outlet was set as an outflow surface with a flow rate weighting of one. This ensures that the mass conservation is applied to this boundary and relates to the mass flow through the inlet since there is no mass flow through the wind tunnel walls. These conditions being set, the next step in the solver phase is to set up the solution methods, controls, and discretization schemes.

5.4.2 SOLUTION SETUP

In this section of the solver, the user specifies crucial discretization techniques which rely heavily on the understanding of each discretization. Due to the importance of selecting the correct technique based on type of problem and problem specific characteristics, Chapter 4 details the most important discretization schemes for the type of flow studied in this thesis.

5.4.2.1 PRE-COMPUTATION RECOMMENDATIONS

Before the iteration process begins it is important to follow the recommendations provided earlier by ANSYS – FLUENT. In doing so allows the solution to converge more rapidly and possibly be more accurate. The procedure used to obtain results in this thesis was the same for all configurations and data sets. The procedure included running the first set of iterations using first order coupled discretization schemes, then switching to higher order for the remainder of iterations. Following the higher order discretization, a series of reduction to under-relaxation factors were completed. This will be detailed next. Different cases were run using a step up approach where solutions for lower RPM cases were used for higher RPM cases as recommended by ANSYS – FLUENT [73] and mentioned in previous sections.

5.4.2.2 INITIALIZATION

Due to the numerous pre-computation procedures, especially when running several modifications of mesh and solver, for several cases, and for several configurations, it becomes a nuisance to manually change the settings for each run. The turbulent flow through the propeller in this thesis is incompressible and viscous and results in complex motion; therefore a hybrid initialization was avoided due to it being a potential flow based model. Hybrid initialization shows no improvement in solution; however, it presented an increase in iterations and thus computation time. Therefore, all configurations and data sets were performed using standard initialization. Initialization was made through the inlet and the first thirty

iterations were performed using first order discretization for all types. After these thirty iterations, the order of discretization was increased to second order for two hundred additional iterations. This was followed by five total reductions of under-relaxation factors. These reductions were spaced apart by fifty to forty iterations each as detailed in Figure 5.14. The number of iterations determined for each command was determined thorough user experience of the solver. After several attempts an understanding of when a solution should converge becomes clear. This is, of course, different for every problem. If convergence occurs in between any of the procedures set by the command lines, ANSYS – FLUENT will automatically end the computation. As shown by Figure 5.14 the under-relaxation factor initiate at their default values and decrease to 0.05 for modified turbulence viscosity, 0.05 for turbulence viscosity, and 0.2 for body forces. Explicit relaxation factors and Courant number were left unchanged. The residual were scaled globally as is the default. The criteria used are shown in Table 5.7. The range given for continuity of residuals indicates that the solutions required a maximum of 0.01 to a minimum of 0.001 in residual values in order to assume convergence.

Table 5.7 – Residual Criteria

RESIDUAL	ABSOLUTE CRITERIA
Continuity	0.001 - 0.01
X – Velocity	0.001
Y – Velocity	0.001
Z – Velocity	0.001
Modified Turbulence Viscosity	0.001

This range is required because the range of advance ratios creates a range of convergence limitations and therefore had to be interpreted individually. All cases and configurations met the convergence criteria and will be discussed further in Chapter 9. Once all of the solution controls are modified and ready, computation may begin. The next section details which solution methods were used for the bulk of the iterations.

5.4.2.3 COMPUTATION SOLUTION METHODS

The solution methods used for the final 90% of all iterations are shown in Table 5.8. Several other methods were attempted prior to choosing these final settings. They include using the standard, PRESTO!, second order, and body force weighted pressure interpolation schemes. A general overview of the outcomes of each pressure interpolation scheme is as follows. The standard pressure scheme was utilized simply for the initial problem startup in the initialization procedure for the first thirty iterations. However, convergence was made using PRESTO!, second order, and body force weighted scheme. PRESTO! interpolation scheme did not provide sufficient accuracy for this flow type; hence, body force weighted and second order were tested.

Table 5.8 – Solution Methods Settings

SOLUTION METHODS	
Pressure – Velocity Coupling	
Scheme	Coupled
Spatial Discretization	
Gradient	Least Squares Cell Based
Pressure	Second Order
Momentum	Second Order Upwind
Modified Turbulent Viscosity	Second Order Upwind

Second order and body force weighted schemes perform better for axisymmetric swirl calculations compared to PRESTO!. Body force weighted showed little to no difference in results compared to the second order scheme; thus, the second order was utilized for all final computations. Additionally, momentum and modified turbulent viscosity discretization were also changed from first order up to third order MUSCL. First order was used for initialization; however, third order MUSCL was used to determine if greater accuracy is possible. Comparison of second order and third order MUSCL results show little to no difference in results. Therefore, the extra computational effort needed for third order MUSCL scheme was avoided by using second order scheme for both momentum and modified turbulent viscosity. After all additional calculation checks and mesh checks were performed in ANSYS – FLUENT, calculation began.

Once a converged solution was obtained per case, the solution was then ready for post processing and data extraction process.

5.4.2.4 SOLUTION POST PROCESSING

Most post processing was completed in ANSYS – FLUENT utilizing surfaces and lines created in the regions of interest which were then used for data extraction. These regions of interest include the wake region, upstream boundary layers, and inlet. This will be detailed in the Chapter 7. CFD Post processing was also utilized to visually interpret data and simulation. Lastly, data was organized and prepared for presentation using MATLAB.

6 EXPERIMENTAL SETUP

6.1 OVERVIEW

In this chapter, details regarding Virginia Polytechnic Institute and State University's (Virginia Tech) testing facility and experimental procedures will be presented along with a brief description of wind tunnel dimensions and instruments used. The intent is to provide the reader with insight of experimental data acquired and methods used to obtain it. In general, this will be a short section as the bulk of this thesis relies on the CFD replication and results for future aero-acoustic measurements.

6.2 TESTING FACILITY

The testing facility is located in the college of engineering at Virginia Tech located in Blacksburg, Virginia. Its large wind tunnel is referred to as the 'Stability Tunnel' and is powered by a 0.45 MW variable speed DC motor. The fan is 4.3 meters in diameter and capable of reaching up to 600 RPM. If no blockage is present maximum wind speeds may reach 80 m/s. The wind tunnel is a closed loop system shown by Figure 6.1 with a test section of 1.74 meters in height and 1.85 meters in width shown in Figure 6.2. These measurements were the basis for determining the hydraulic diameter for the turbulence input conditions in ANSYS – FLUENT. As shown in Figure 6.2, the setup is for aero-acoustic measurements where the test walls are made of Kevlar which would include the near wall. This is one assumption where a smooth surface was utilized in CFD results instead of Kevlar roughness.

6.3 WIND TUNNEL DATA COLLECTION

As mentioned, majority of experimental measurements will be for aero-acoustic data hence the setup shown in Figure 6.2. Therefore, aerodynamic measurements are limited. Experimental results were obtained by Dr. Nathan Alexander under the direction of Dr. William Davenport of Virginia Tech. The

thick boundary layer was produced by trips set upstream of the propeller which produced boundary layer heights of 102 mm at approximately 0.79 meters (31 inches) upstream of the propeller. This data was measured using a hotwire probe. In addition, Dr. Alexander determined blade position using a photodiode and laser system built at Virginia Tech. The sensor was placed upstream of the blades and the laser was structurally stationed at the hub of the propeller setup shown in Figure 6.3.

Velocity measurements were determined using the same hotwire probe used to measure the boundary layer height. More specifically, a quadwire four sensor probe containing wires of five microns in diameter and 1.2 mm in length and manufactured by Auspex Corporation. The hotwire location was set behind the propeller as shown in Figure 6.4. The hotwire probe is capable of measuring three dimensional components of velocity. The location of the velocity measurement in Figure 6.5 (a) and (b) show a side view and front view, respectively, of the propeller and once again color coding blue to show the side towards the inlet and red to represent the side towards the outlet. The axial distance between the leading edge of the blades and the probe is 36.6 mm (0.64 chord lengths) which is equivalent to 46.94 mm. from the spanwise center plane and the probe plane of measurement. In Figure 6.5 (b) a thin grey dashed line represents the ring of measurement at 90% propeller radius and within the probe plane of measurement. The angular reference is also shown in Figure 6.5 (b), in orange, where 0° is at the vertical bottom of the propeller centerline and 180° is at the vertical top of the propeller centerline. Clockwise movement past the 0° mark relates to a positive angular change and a counter clockwise movement past the 0° mark of the centerline indicates a negative angular change. The probe is represented in Figure 6.5 (a) and (b) by a red rectangle and red dot respectively. Based on this setup, only results for configuration 3 have been obtained.

The procedure for data collection included a time delay measurement of the averaged velocities at the probe location, also known as phase averaging. As the propeller rotated at the specified advance ratio, the laser and sensor would locate the blade positions and synchronize the measurement time with the propeller angular rotation, $\theta = \omega t$. At time equal zero seconds, the blade leading edge was exactly at the -5° mark (probe location). It is important to note that the probe location never changes and all measurements are taken from the probe's location. Several blade passes and several data measurements were taken and each measurement was synchronized to the same exact location of the blades relative to the probe. The measurements taken were averaged to produce a single data point. This is the equivalent to

RANS by time averaging the velocity fluctuations from each blade. Figure 5.13 shows the range of measurement (52.5°) obtained in the rotating frame. However, only 36° are needed because the flow is periodic and time averaged. It is important to understand that data is available for 36° of rotation which translates to a blade's leading edge to the following blade's leading edge. However, this data is obtained at a single point in space (probe location) over a period of time dictated by $\theta = \omega t$. This procedure was carried out for a total of five cases shown in Table 6.1.

Table 6.1 – Experimental Cases

AVAILABLE EXPERIMENTAL CASE DATA		
Advance Ratio	Nominal Inflow Velocity	Rotational Velocity
0.72	15 m/s	2734 RPM
0.79	15 m/s	2502 RPM
0.98	15 m/s	2000 RPM
1.31	15 m/s	1500 RPM
1.44	30 m/s	2734 RPM

7 CONFIGURATIONS AND DATA SETS

7.1 OVERVIEW

This chapter details all configurations, data sets, and cases studied. The differences of each configuration are outlined and the meticulous process of data exporting will be discussed. In addition, boundary layer measurement locations are detailed and explained in order to clearly present the locations for inflow measurements.

7.2 CONFIGURATIONS AND DATA SETS

As mentioned previously, configurations refer to the type of boundaries and inlet conditions. Configuration 1 applies to axisymmetric flow where the inlet velocity is a constant value throughout. Shown in Table 7.1, are all the case combinations for configuration 1. Configuration 2 is similar to configuration 1; however, it has the addition of the near-wall or plate next to the propeller. In configuration 2, the no-slip condition is present given the proximity of the plate to the propeller. However, a crucial difference between configuration 2 and 3 is the wall boundary layer. Configuration 2 has a constant inflow velocity which produces a 'natural' thin boundary layer due to the no-slip wall condition. The cases for configuration 2 are shown in Table 7.2. Configuration 3 studies the effects of the inflow velocity profiles ingested by the rotor with the inclusion of a thick boundary layer of 102 mm. in height as produced during the experiments. This is simulated by applying an UDF for each case depending on the inflow velocity in order to enforce a thick boundary layer at the inlet. The cases for configuration 3 are shown in Table 7.3.

Table 7.1 – Configuration 1 Cases

CONFIGURATION 1 DATA SET (AXISYMETRIC FLOW – NO WALL INFLUENCE)		
Advance Ratio	Constant Inflow Velocity	Rotational Velocity
0.72	15 m/s	2734 RPM
0.79	15 m/s	2502 RPM
0.98	15 m/s	2000 RPM
1.31	15 m/s	1500 RPM
1.44	30 m/s	2734 RPM

Table 7.2 – Configuration 2 Cases

CONFIGURATION 2 DATA SET (NEAR-WALL INCLUSION)		
Advance Ratio	Constant Inflow Velocity	Rotational Velocity
0.72	15 m/s	2734 RPM
0.79	15 m/s	2502 RPM
0.98	15 m/s	2000 RPM
1.31	15 m/s	1500 RPM
1.44	30 m/s	2734 RPM

Notice that all three configurations have the same cases but varying inlet and boundary conditions. The aero-acoustic data sets are based on configuration 3; however, the rotational velocity is unchanged for each case and instead only the inflow velocity is changed as shown in Table 7.4. A separate UDF has to be generated for each case in order to ensure that the nominal velocity is maintained as prescribed while including the thick boundary layer with height of 102 mm for all cases.

Table 7.3 – Configuration 3 Cases

CONFIGURATION 3 DATA SET (NEAR-WALL & THICK BOUNDARY LAYER INCLUSIONS)		
Advance Ratio	<i>Nominal Inflow Velocity</i>	Rotational Velocity
0.72	15 m/s	2734 RPM
0.79	15 m/s	2502 RPM
0.98	15 m/s	2000 RPM
1.31	15 m/s	1500 RPM
1.44	30 m/s	2734 RPM

Table 7.4 – Configuration 3 Acoustic Data Set

CONFIGURATION 3 ACOUSTIC DATA SET (NEAR-WALL & THICK BOUNDARY LAYER INCLUSIONS)		
Advance Ratio	<i>Nominal Inflow Velocity</i>	Rotational Velocity
0.48	10 m/s	2734 RPM
0.72	15 m/s	2734 RPM
0.96	20 m/s	2734 RPM
1.20	25 m/s	2734 RPM
1.44	30 m/s	2734 RPM

8 RESULTS

8.1 OVERVIEW

In this chapter data and results from CFD and experimentation will be presented and compared. Discussion of results and comparison will be kept to a minimum and will be presented in detail in the subsequent chapter. CFD results were obtained for all configurations and data sets. Configurations 1 and 3 will be utilized for CFD validation through wake and boundary layer velocity measurements compared to experimental results. In addition, all three configurations will include comparison of upstream boundary layer measurements to further understand the effects of near wall inclusions and thick boundary layers. Lastly, the results obtained for future acoustic measurements will be presented at locations of interest upstream of the propeller blades.

8.2 CFD DATA AND RESULTS

In order to present CFD generated results, measurements are taken at far and near locations *upstream* of the propeller blades spanwise center plane. These locations are shown by Table 8.1. In addition, a contour plot of the normalized axial velocity (x-direction) will be presented at these locations. To clarify the locations of far measurements, where contour plot will be generated, a diagram showing the planes of far measurement is shown in Figure 7.1. Figure 7.2 (a) and (b) show the locations of the boundary layer measurements at the far regions and near regions respectively.

Grid independence studies must be performed prior to obtaining and interpreting final results. A grid independence study is a series of strategic mesh refinements to produce more refined mesh in regions of interest. Solutions obtained from these grids retain the same inputs; the only change is the actual grid or mesh. The results are then compared and a study is made to determine if the solution has become independent of grid size. Due to the large amount of data gathered, a selective process was used in order to

show and interpret only the most relevant information. Grid independence studies were completed for all configurations; however, only configuration 3 grid independence will be mentioned.

Table 8.1 – Boundary Layer Measurement Locations

BOUNDARY LAYER MEASUREMENT LOCATIONS		
Blade Reference	Location	Distance from Inlet
Far Measurements	Inlet	0 mm
	Two Diameters	748.80 mm
	One Diameter	1206 mm
Near Measurements	Three Chord Lengths	1491 mm
	Two Chord Lengths	1548.8 mm
	One Chord Length	1606 mm

8.2.1 CONFIGURATION 1

This configuration includes zero wall effects on the flow through the propeller and resembles axisymmetric flow. Grid independence studies were performed and a final mesh of 3,819,656 elements was utilized for all results regarding configuration 1. All mesh quality verifications were met. Additionally, all ANSYS – FLUENT recommendations regarding fluid model (MRF), mesh, and turbulence model mentioned earlier will be shown.

8.2.1.1 VERIFY INTERFACE FLOW IS UNIFORM

As previously mentioned, the MRF model requires that the flow at the front interface be relatively uniform. A contour plot of the axial velocity for $J = 0.72$ is shown in Figure 8.1(a) of the front interface. This contour plot expands through the entire front interface, which in relation to the propeller, is 102% of the propeller diameter. $J = 0.72$ was chosen because for all the cases analyzed in Table 7.1, this contained the highest thrust producing flow and therefore had the least uniform contour plot of axial velocity at the front interface. Figure 8.1(a) is on a global scale in order to compare to the fluid within the entire domain. This plot shows the velocity field is relatively uniform and therefore justifies the use of MRF model; however, with certain limitation which will be discussed in the next chapter. The change in the middle is a location where the flow is reaching the stagnation point of the conical front hub tip (refer to Figure 7.1).

Figure 8.1(b) shows the same location with contour plot axes now locally scaled. This clearly shows the local variations of axial velocity and the distinct axisymmetric flow properties.

8.2.1.2 VERIFY WALL Y-PLUS VALUES

One of the verifications recommended for a reasonable mesh is that the wall y^+ values must meet the criteria suggested by ANSYS –FLUENT in order to use Spalart-Allmaras enhanced wall functions. A $y^+ > 30$ is recommended; therefore a plot of $y^+ \leq 30$ was generated at all surfaces within every domain. A contour plot of $J = 0.79$, shown in Figure 8.2, was generate and zoomed into the locations where problematic regions in the mesh exists. These regions are locations where y^+ values are *below* the suggested values. As the advance ratio increases these regions are reduced. This will be shown in detail for configuration 3 and these errors will be discussed in Chapter 9.

8.2.1.3 VERIFY FULLY TURBULENT FLOW

Another ANSYS-FLUENT recommendation is that to use Spalart-Allmaras turbulence model the entire flow region must be fully turbulent. This is determined using a simple comparison of turbulent viscosity and molecular viscosity known as the turbulent viscosity ratio. A fully turbulent flow is indicated as having a turbulent viscosity ratio of greater than two, $\frac{\mu_t}{\mu} > 2$. Hence, to show only the regions which *do not* meet this criterion ($\frac{\mu_t}{\mu} \leq 2$) a contour plot of the flow within the entire fluid domain and subdomain was used and is shown in Figure 8.3. The rest of the domain is not shown since it meets the ratio requirements. Clearly, the flow is fully turbulent as required by this turbulence model.

8.2.1.4 RESIDUALS

The case of $J = 0.79$ was used to illustrate the convergence procedure. Figure 8.4 shows the globally scaled residual plot and indicates the locations where changes were made for more reliable convergence as mentioned in Chapter 5. Convergence was reached for this case at about 100 or so iterations; however, further attempts to reduce residual values are made by reducing relaxation factors and other discretization schemes.

8.2.2 CONFIGURATION 2

This configuration includes only the near-wall effect on the flow through the propeller and therefore does not represent fully axisymmetric flow. All grid independence studies and mesh quality verifications are performed for this configuration. However, these results, as well as, wall y^+ , and turbulent flow verifications will be shown in Configuration 3 section since both utilized the exactly the same mesh with similar flow conditions. The only difference, as outlined in Table 7.2, is the constant inflow boundary condition.

8.2.2.1 VERIFY INTERFACE FLOW IS UNIFORM

This configuration contains a near-wall where configuration 1 did not. The front interface contour will be shown in the same order as was done for configuration 1 with the globally scaled and then a locally scaled color map. Figure 8.5 (a) shows a relatively uniform front interface flow in global scale. However, to determine flow characteristics a local scale is shown in Figure 8.5 (b). This clearly shows a non-axisymmetric flow indicating non-uniform flow in the local scale. Chapter 9 will discuss these results.

8.2.2.2 RESIDUALS

The case of $J = 0.98$ was used to illustrate the convergence procedure for configuration 2. A different advance ratio was chosen in order to show a variety of residuals; nonetheless, all configurations converged in similar manners. Figure 8.6 shows the globally scaled residual plot for this advance ratio.

8.2.3 CONFIGURATION 3

This configuration includes near-wall affects and enforces a thick boundary layer at the inflow of 102 mm in height. Grid independence studies were performed and a final mesh of 5,128,872 elements was utilized for all results regarding configurations 2 and 3. All mesh quality verifications were met. ANSYS – FLUENT recommendations regarding MRF model (uni form flow) and turbulence model (fully turbulent) will be shown in this section; however, mesh (wall y^+) investigation will be shown in detail in the acoustic data set. In addition, a full mesh convergence study will be demonstrated in this section. Information regarding velocity profiles in the rear interface is shown in Appendix D.

8.2.3.1 VERIFY INTERFACE FLOW IS UNIFORM

A contour plot of the axial velocity for $J = 0.72$ is shown in Figure 8.7 where the globally scaled velocity contour map, Figure 8.7 (a), shows relatively uniform flow and the locally scaled contour map, Figure 8.7 (b), confirms non-axisymmetric flow resulting in non-uniform velocity profiles as seen for configuration 2. Discussion will be provided in Chapter 9.

8.2.3.2 VERIFY FULLY TURBULENT FLOW

Fully turbulent flow is determined by the turbulent viscosity ratio as mentioned earlier. Figure 8.8 shows only the regions which *do not* meet this criterion ($\frac{\mu_t}{\mu} \leq 2$). The rest of the domain is not shown since it does meet the ratio requirements. Once again, the same locations are shown as compared to configuration 1, with the addition of a speck at the near-wall just under the propeller blades. This is due to extreme refinements in this region and effects will be discussed in the next chapter.

8.2.3.3 RESIDUALS

The case of $J = 1.44$ was used to illustrate the convergence procedure. It is clear that this advance ratio converges more rapidly and at lower residual values than others given the lower thrust producing flow characteristics. To reiterate, all configurations converged in a similar manner (similar residual plots) depending on advance ratio.

8.2.3.4 GRID INDEPENDENCE STUDY

A grid independence study has been performed for all configurations; however, only the grid independence study for configuration 3 will be shown in this thesis due to the extensive amount of data. Table 8.2 shows five different grid sizes initiating with the original mesh, referred to as mesh zero, and increasing refinement in strategic locations until a final converged grid is used for final result computation. Results for each case for configuration 3 were run for each mesh generated. The solutions were compared and plotted, for each case and mesh, along the 90% radius circumferential line shown in Figure 7.2 labeled as 'Measurement Ring at 90% Radius'. Perfect node alignment would contain all measurement nodes at a radial coordinate of 205.740 mm. The radial spacing of the nodes along this ring for the final mesh used in configuration 1 and 3 is shown by Figure 7.3 and Figure 7.4, respectively. During comparison, the axial velocity was normalized by the nominal inflow velocity and plotted as the ordinates. The abscissa was

comprised of the angular coordinates along the 90% radius ring. A selective process was made to choose only the most significant changes shown by mesh zero (M0), one (M1), three (M3), and five (M5). These results are shown in Figure 8.10 thru Figure 8.14 and the legend designates mesh identity as M0, M1, M3, and M5. When observing these plots it's important to note the normalized axes and its small changes when judging a converged mesh as a close up of the plots may be misleading.

Table 8.2 – Configuration 3: Grid Independence Study

GRID INDEPENDENCE STUDY		
Mesh ID Number	Total Element Size	Refinement Description
M0	679,254	Original coarse mesh
M1	1,748,134	Add: Wake mesh density, surface refinements
M2	2,547,426	Add: Prism Layers to surfaces
M3	2,557,232	Remove: Prism Layers from surfaces Add: BL mesh density, wake mesh density and surface refinements
M4	4,243,693	Add: Wake measurement plane mesh density
M5	5,128,872	Add: Refine wake measurement plane mesh density, refine propeller surface

In addition, a convergence check using boundary layer measurement was made at 0.79 m. upstream of the propeller. The axial velocity is once again normalized by nominal inflow velocity but this time makes up the ordinates. The abscissa is comprised of the normal distance from the plate (y-direction) normalized by the boundary layer height at the inflow (102 mm). The results are shown in Figure 8.15. A convergence here shows almost identical values at all points ($J = 0.72$ case). This is because the flow in this region is barely interrupted by the rotation of the blades; thus the explaining why the wake measurements were done in more detail. The grid study shows that between the third and fifth mesh, relatively equivalent results were being acquired. Mesh three could have been used for all computation; however, the refinement of mesh five produced smoother results and was therefore a more attractive choice.

8.3 CFD VALIDATION

The results obtained through CFD measurements and simulation must be validated by known data. In this case, experimental data was extremely limited and a fair attempt at validating the wake and boundary layer data to CFD data was made. Given the nature of this type of flow, comparisons using Configuration 1 wake results will be made with experimental measurements. These measurements are all taken at the 90% radius ring; however, experimental data was taken at a single spatial location (probe position) and phase averaged. These comparisons are made on the basis of comparing quasi-axial symmetric flow (experimental data) to axisymmetric flow (configuration 1 CFD data). It is important to note that comparison of configuration 3 wake results will *not* be made due to uncertainties of measurements downstream of the blades. Wake measurements for configuration 3 are similar to configuration 1; however, the predicted flow separation due to higher thrust conditions and near wall interaction produces noisy data which needs to be considered by further analysis. Hence, information *downstream of blades* will not be provided as they contain discretization and turbulence modeling errors which are transferred downstream (upwind scheme). However, a validation is made using configuration 3 boundary layer profiles at 0.79 m (31 inches) upstream of the blades since this region is unaffected by errors downstream.

The MRF model is an attempt to approximate the solution based on the instantaneous flow field. This relies on the ‘frozen rotor approach’ which dictates the flow field according to the blade positions. The blades’ position for all three configurations remains the same, as shown in Figure 5.13. The fundamental principle of understanding the relation between instantaneous CFD data and experimental results lies on the positions of the blades. This will be mentioned in detail in Chapter 9. As for now, only the data obtained will be presented. All cases for configuration 1 (wake data) are shown in Figure 8.16 thru Figure 8.20. Since the distance of axis tick marks may be visually misleading, a normalized summation of the difference between CFD normalized velocity and experimental normalized velocity data in the range of -5° thru 31° (36°) as shown by equation 8.1. This provides a basic mathematical interpretation of the differences between data sets and is summarized in Table 8.3.

$$error = \frac{\sum_{i=1}^N |V_i^{Exp} - V_i^{CFD}|}{V_{in}} \quad 8.1$$

Experimental boundary layer measurements, taken at 0.79 m (31 inches) upstream of the blades, were compared to configuration 3 results and are given by Figure 8.21. The validation data is in agreement with experimental data. This case of $J = 1.44$ is a zero thrust case which maintains the flow unmodified by the propeller. Table 8.3 presents the difference between experimental and CFD data based on equation 8.1.

Table 8.3 – Error in of CFD Measurement

CFD MEASUREMENT PERCENT ERROR		
Advance Ratio	CONFIGURATION 1 (Wake)	CONFIGURATION 3 (Boundary Layer)
0.72	143.60%	N/A
0.79	111.87%	N/A
0.98	40.79%	N/A
1.31	12.40%	N/A
1.44	2.50%	9.05%

8.4 CFD DATA COMPARISON

The results which this thesis mainly focuses in interpreting are shown within this section. Data will include boundary layer measurements at locations specified in Chapter 6. The next section will focus on demonstrating solely the results for the acoustic data set. Configurations 1 thru 3 are compared in order to determine the effects of zero near-wall effects, near-wall effects, and thick boundary layers on the ingested flow through the propeller. The justification for using data upstream of the blades, given the known errors due to flow separation and discretization errors, is that the data downstream of the blades do not affect data upstream due to the upwind scheme.

8.4.1 BOUNDARY LAYER PROFILES

In configuration 1 thru 3, comparison of boundary layer measurements located at the inlet, two diameters, one diameter, three chord lengths, two chord lengths, and one chord length upstream of blades are presented together (all configurations) per individual location. These are plotted along the y-axis, at $z = 0$, and varying x-location, as shown in Figure 7.1 and Figure 7.2. These boundary layer profiles for $J = 0.72$ are presented in Figure 8.22 thru Figure 8.27. The features in the boundary layer profiles for one thru

three chord lengths upstream of the propeller are due to the geometry. At three chord lengths, the profile is in close proximity to the conical hub tip and thus approaches zero velocity. The upstream hub tip is at a normalized value of 2.44, $\left(\frac{248.9mm}{102mm}\right)$. Other useful normalized locations on the propeller are shown in Table 8.4. In plots regarding one and two chord lengths upstream, the lines originate from at the plate and proceed through the hub section, refer to Figure 7.2. There is a discontinuity in these plots. This is because velocities go to zero due to the no-slip condition at the hub surface locations. This advance ratio was chosen because the changes in normalized velocities between the configurations were most noticeable.

Table 8.4 – Normalized Propeller Dimensions

NORMALIZED PROPELLER DIMENSIONS (D/δ)	
Blade Tips (Bottom)	0.20
Blade Root (Bottom)	1.82
Propeller Hub Centerline	2.44
Blade Root (Top)	3.06
Blade Tips (Top)	4.68

8.4.2 THRUST

Thrust was also computed numerically using the pressure force and viscous forces throughout the surfaces of the blades as mentioned in Chapter 4. A thrust curve was generated using data from all cases and all configurations. The acoustic data set and configuration 3 data set are analyzed as one. The coefficient of thrust is plotted against advance ratio for all configurations and is shown in Figure 8.28.

8.5 CONFIGURATION 3: ACOUSTIC DATA SET

Illustrating the flow field through a propeller is a meticulous process with various ways of demonstrating data in various locations. In order to present a full planar view of the boundary layer measurements at locations of interest a contour plot of the axial velocity was generated at the planes indicated in Figure 7.1. A more detailed measurement of the boundary layer is generated at the locations of interest by plotting CFD data along lines presented earlier. All contour plots for velocity profiles at the rear interfaces are shown in Appendix D. Note these rear profiles are not circumferentially averaged and show

the instantaneous flow field. A more appropriate representation would be to apply a circumferential filter to 'smear' the profile velocities accordingly and fully represent an averaged flow field.

8.5.1 WALL Y-PLUS

It is important to show the wall y^+ values for all cases in this data set because boundary layer profiles will be used for aero-acoustic predictions and must therefore be verified carefully. Each case wall y^+ values in this data set are shown in Figure 8.29 thru Figure 8.33. These are contour plots of regions which did not meet $y^+ > 30$ criteria. Nevertheless, everywhere else on in the flow field meets this recommendation and results are still valid as will be discussed in Chapter 9.

8.5.2 BOUNDARY LAYER MEASUREMENTS

Interface flow fields are plotted locally scaled in Figure 8.34 thru Figure 8.38. These contour plots show the local axial flow at the front interface plane, as well as, a contour plot including the interface plane and extending down to the wall to show the boundary layer as it spans across the plate. It is important to note that these are locally scaled values in order to show the changes locally; however, globally scaled contour plots show a relatively uniform flow field at the interface similar to prior cases used to validate MRF model uniform inflow requirement. The axial velocity flow field at one and two diameters upstream of the propeller is shown in Figure 8.39 thru Figure 8.43.

Additionally, velocity contours at all near stations (one, two, and three chords upstream of the blades) for all configuration 3 acoustic data set cases are shown in Figure 8.44. In this plot, vertically, the operational range (cases) is shown for each chord length distance upstream of the propeller. Horizontally, individual cases are shown for each near station. All axis labels and spacing are assumed to align vertically and horizontally. The y-axis represents the setup y distance normalized by propeller radius, and the x-axis represents the setup z distance normalized by the propeller radius. The contours are normalized by the inflow velocity for each case. These profiles originate at the origin and span to 102% of the propeller radius (span of the interface). This is the azimuthal distribution of axial velocities averaged every 36° which will be detailed in Chapter 9.

Moreover, for a detailed analysis of the boundary layer as it progresses into the propeller, plots were generated along lines normal to the wall. These results are presented in Figure 8.45 thru Figure 8.50.

They are shown per location with all cases plotted together. An alternative method of representing the data providing a different view of results is also expressed as individual cases plotted through all locations upstream. They are separated into far (greater than three chord lengths) upstream stations, as shown in Figure 8.51 thru Figure 8.55, and near (less than or equal to three chords lengths) upstream stations, as shown in Figure 8.56 thru Figure 8.65. Figures which include chord lengths upstream from the propeller are shown as separate plots in Figure 8.56 thru Figure 8.65 due to the discontinuity at the hub section. Doing so also allows for amplification of the data in individual hub sections, as well as, determining the average of the normalized flow velocity per location above and below hub. The ingested mean flow velocity at one chord upstream is shown in Table 8.5. Continuous versions of these plots are given in Appendix E. These results will be discussed in the following chapter.

Table 8.5 – Normalized Ingested Mean Flow Velocities

NORMALIZED INGESTED MEAN FLOW VELOCITIES			
Case	Below Hub Section	Above Hub Section	Difference
J = 0.48	1.50	1.34	0.16
J = 0.72	1.24	1.17	0.07
J = 0.96	1.12	1.09	0.03
J = 1.20	1.04	1.05	-0.01
J = 1.44	0.99	1.02	-0.03

9 DISCUSSION

9.1 RANS CALCULATIONS COMPARED TO EXPERIMENTAL DATA

Experimental data, as has been discussed in Chapter 6, has been obtained for the flow over a single fixed spatial point (probe location) with varying time intervals of 0.5° related by $\theta = \omega t$. A simple substitution of the angular step size of 0.5° based on angular rotation of the blades determines the measurement point in the rotating frame. Since there are ten blades only 36° of blade rotation is required to express a fully periodic flow.

The CFD model used in this thesis is a model which utilizes other models and so forth. In general, CFD requires MRF model to represent RANS model. The MRF model is a steady state approximation which gives the time averaged flow field in the rotating frame by imparting a rotational flow to the fluid within the rotating domain. There is a one to one relationship between the RANS calculation in the rotating frame and the phase averaged probe measurements. In CFD model, the geometry was imported with configuration shown in Figure 5.13 and Figure 6.5. The blade within the -5° to 31° degree range will be referred to as blade '1' for illustrative purposes. To synchronize the measurement using MRF model and experimental data it is required to match the experimental time data to the CFD data based on blade position. In doing so, the CFD data represents the flow field at time t_{CFD} which matches t_{EXP} by measuring the angular distance of CFD geometry blade '1' LE from the -5° mark. However, the MRF model performs better when the flow is axisymmetric due to interface flow uniformity; thus the comparison of the axisymmetric case, configuration 1, to experimental data. Notice the angular periodicity of configuration 1 case in Figure 8.20. Also, notice the noisy data produced by the highest thrust case in Figure 8.16. This is because of inaccuracies associated at the downstream flow due to the predicted flow separation by both Spalart-Allmaras turbulence model and MRF model. In order to improve computation at these conditions

more accurate, in respect to boundary layer resolution, turbulence models such as the SST $\kappa - \omega$ turbulence model, as well as, a fluid flow model capable of capturing unsteady flow characteristics are required. It should also be noted that further improvements of mesh should be created along blade sections for more accurate boundary layer resolution. Due to time constraints, only the utilized data region upstream of the blades has been improved. Since inaccuracies produced by flow separation emanates from the blades, the flow downstream will rely on the inaccurate values from the blade regions (upwind scheme). Notice that a zero thrust case, $J = 1.44$ does not contain flow separation and wake results are in agreement with experimental data shown in Table 8.3. This error is further increased with the addition of the wall, as wall y^+ errors are introduced, and this will be mentioned later in this chapter. Nevertheless, this only indicates that the wake data should be improved; however, the upstream data utilized in this thesis remains acceptable as the upwind scheme does not allow the flow separation errors affect upstream flow calculations.

9.2 MODEL INTERPRETATION

The flow field being studied includes a complex rotational flow that was modeled using a rotational domain which interfaces with a stationary domain using a steady state approach. This is justified by assumption that the flow over the front interface of the rotational domain is relatively uniform. Other meshes were considered in which different interface distances in relation to the propeller blades were used; however, anything under three chord lengths upstream of the propeller blades produced a highly irregular flow field over the front interface due to rotation of the flow in close proximity to the propeller blades. If the rotational domain was shortened the flow field at the front interface resembled that of the rear interface, as shown in Appendix D. Additionally, the radial size of the rotational domain was formed in order to maintain as much accuracy as possible with minimal unphysical flow interactions. In other words, care was taken to not size the rotational domain much larger than the rotor. Technically, this is a significant approximation because if this domain is much larger than the rotor, the imparted velocity would cover a region where rotation is otherwise inexistent. To maintain as much accuracy as possible, a rotational domain encompassing only the propeller blades should be used; however, the interface front flow field would be highly nonuniform in a non-axisymmetric flow. The use of the MRF model in general, is

justified because even though it imparts rotational velocities to locations where flow may not be rotating, a time average of the flow in a particular location would still produce similar results to the MRF model. After all, the MRF model is a steady-state approximation.

The $J = 0.72$ cases (Figure 8.1 (a), Figure 8.5 (a), and Figure 8.7 (a)) were chosen to present the flow field since *higher* advance ratios produced a much more uniform flow over the interface surface. Therefore, a case of $J = 0.72$ gives one of the worst case scenarios due to its increased thrust production which increases distortion about the flow field. The case of $J = 0.48$ is actually the highest thrust producing case; however, it was not a shared advance ratio between all three configurations. Hence, the highest thrust producing case for all three configurations ($J = 0.72$) was used. The flow speed at the front interface, shown in Figure 8.1 (a), Figure 8.5 (a), and Figure 8.7 (a), present relatively uniform flow; thus, justifying the use of the MRF model. Nonetheless, this fluid model is *not* the best model to represent the flow and superior alternatives and recommendations will be provided in Chapter 10.

Another model requirement is that for the Spalart-Allmaras model a fully turbulent flow must be present. Computing the Reynolds' number for this flow type places it in the vicinity of $Re = 4 \times 10^5$, which typically indicates turbulent flow. Additionally, this requirement can be evaluated on a per cell basis, as shown in Figure 8.3 and Figure 8.8 by evaluating the turbulent viscosity ratio. The only regions which fail this fully turbulent criterion is located at the propeller blade root section. This is due to the size of the elements within this region as discussed in the meshing process. The neglect of adding fillets to this region causes ANSYS-ICEM to model the sharp corners by using very small elements. In these regions the flow is laminar; thus numerically, the turbulent viscosity ratio is drastically reduced. Therefore, this is an insignificant numerical error which may be neglected. An improved mesh would correct for this error in cases where flow data is to be attained in this region. However, for this study this is not a cause for concern. A value which is a concern is the wall y^+ values.

Majority of the CFD results obtained in this thesis rely on boundary layer resolution which requires prism layers which are structured and grow normal to the surface. Generating prism layers for simple structures such as cubes and flat plates is extremely simple; however, applying prism layers to highly curved surfaces such as the blades of a propeller and hub sections, is a cumbersome task. Several attempts were made to apply this type of mesh to a few elements from the surface and then retain an

unstructured form for the rest of the domain; however, the results did not change by much. Other attempts were made to create prism layers which progressed further into the unstructured domain containing the blades but this caused severe skewness problems and a large decrease in mesh quality. Hence, prism layers were avoided and caused problems with wall y^+ values which were minimized through refinement and coarsening where necessary. Figure 8.2 and Figure 8.29 thru Figure 8.33 show the wall y^+ values for several cases. Configurations 2 and 3 use the same mesh and have similar values. All wall y^+ values that are too small lie in regions of blade leading and trailing edges, tip, root, and nose cone. This is shown in Figure 8.2 where all other figures do not show the wall y^+ values at the blades as it is not significant and detrimental to all solutions, especially upwind data where all boundary layer information was gathered. Hence, for configuration 3 wall y^+ results, only the significant hub data is shown. The low wall y^+ values have an effect on the local fluid and downstream data. This is because the boundary layer is not properly resolved. The relative amount of local fluid affected is, of course, dependent on domain size. During discretization in Chapter 4, the governing equations were shown to apply per cell volume. Hence, mass conservation is applied at all individual volumes. If the local flow contains inaccurate boundary layer data which cause say, an increase in velocity. The surrounding fluid, being applied the conservation of mass principle, will have to account for this velocity and numerically change the values on the surrounding cells. Thus, it's the conservation of mass principle relative to the computational domain size which dictates how much of the local flow is affected. Nevertheless, the downstream data is still affected due to upwind scheme.

The regions in front of the hub section contain only a few very small regions of wall y^+ values under the recommended $y^+ > 30$. This is due to series of local refinement and coarsening using the adapt feature in ANSYS – FLUENT. The wall y^+ values in the near-wall regions are not shown because they are all *over* the recommended value. In addition, in Figure 8.29 thru Figure 8.33, the wall y^+ values are given for all acoustic data cases. In $J = 0.48$, poor wall y^+ values exists below the blade region due to fine refinement necessary to mesh this complex region and high flow velocities. Due to the large domain, the boundary layer measurements are not affected by the regions underneath the blades. These problematic regions decrease with an increase in advance ratio as seen in the figures that follow $J = 0.48$ because of the shear computed at the wall. The shear at the wall increases with higher advance ratio; thus, increasing

characteristic velocity in the boundary layer region expressed by equations 3.5. Reiterating that all configuration 3 cases use the same mesh, the distance from the wall (y) of the first cell at the surface (used to compute y^+ equation 3.5) is the same for all cases in configuration 3 data set including acoustic data set. Consequently, a combination of increased characteristic velocity and low y values (due to refinement in mesh) produces a low wall y^+ value.

As mentioned, a grid independence study is vital to ensure that refining the grid does not modify the solutions. Table 8.2 gives all the refinements and grids tested for configuration 3. The same has been done for configuration 1; however, these results are not shown for as they would be redundant. Convergence tests of the four chosen meshes are shown in Figure 8.10 thru Figure 8.14. The final grid of over five million cells was used because it provided a much smoother set of results compared to previous grids. Figure 8.10 thru Figure 8.12 still show noisy data at the most refined mesh; however, this is because of flow separation which produces unreliable data and introduces numerical diffusion at the wake region for these cases. There is no need to attempt a mesh convergence over erroneous regions except to improve the boundary layer over the blades in order to fully resolve the turbulent flow. Regardless, convergence results for all cases are shown since the lower thrust producing cases show acceptable convergence. In order to judge grid independence, a MATLAB script was generated which splits the range of angular coordinates into ten groups of data. These groups of data are separated by a range of 36° . All values of normalized velocity within each group are then averaged. This is performed for all grids. Each group corresponding to the same group in another grid size is compared and a percent difference is found. The average of the percent differences per grid was used as a criterion in determining grid independence. As a result, grid/mesh 3 already showed signs of convergence; however, mesh 5 was utilized due to its smoother results.

Figure 8.15 shows an excellent convergence over the resolved boundary layer at 0.79 m. (31 in.) upstream of the blades for $J = 0.72$. This region is unaffected by the errors in the flow present downstream of the propeller even at lower advance ratios. Mesh convergence is much more prominent for higher advance ratios and this has to do with the turbulence model, mesh, and MRF model and will be further discussed in Chapter 10.

9.2.1 DATA VALIDATION

Very limited experimental data was available for this study. The axisymmetry of configuration 1 was used relate to the periodic plot of experimentally measured wake data. This configuration was used to validate CFD data because the MRF model is not the most suited model to represent the flow with the wall present. Further mesh improvements must be performed and wake data recomputed for proper judgment. Figure 8.16 thru Figure 8.20 show the wake profiles at 90% propeller radius ring behind the propeller. The case of $J = 0.72$ and 0.79 show numerical noise. The residuals for these runs showed oscillatory convergence; hence the application of reduced under relaxation factors. As mentioned in equation 4.4, the oscillatory behavior was reduced by a series of five relaxation factor reductions. This prolonged the converging process; but, made a very smooth transition as shown in Figure 8.4, Figure 8.6, and Figure 8.9. All configurations and data sets presented similar residuals for each advance ratio. More rapid convergence occurred at higher advance ratios; hence, not all under-relation levels were necessary. A smoother convergence aided by these relaxation factor reductions produced better solutions with less oscillatory behaviors especially notable for higher advance ratios.

The noisy behavior at low advance ratios indicate that there is increased numerical error at these flow characteristics; hence, an average technique of adjacent cells' numerical diffusion was attempted. This attempt is known as third order MUSCL. However, no improvements were found between a second order and third order MUSCL discretization. Since, this produced no benefits; efforts were made to improve the mesh while maintaining acceptable cell quality and properties. Refinements were made to the mesh; however, mathematically, as shown in Chapter 4, further refinement reduces the gradient discretization between cells and wake features become averaged out. In other words, the velocity field simply becomes noisy and no distinct flow features can be observed. A notable mesh feature is also the node positions of the 90% ring which is shown by Figure 7.4. Ideally, these locations should be at an angular coordinate exactly equal to 90% of the propeller diameter or 205.74 mm. Although the difference is insignificant between nodes (where data is measured) this miniscule difference may also be the cause for noise in the measurement. Refinement reduces this distance as may be compared by the less refined configuration 1 mesh and configuration 3 mesh nodal radial coordinates (Figure 7.3 and Figure 7.4) at the cost of greater computational effort. This is as far as this mesh could go in terms of accuracy, refinement,

and discretization errors. Hence, the mesh was reverted to mesh five and a more efficient mesh is recommended in order to reduce discretization error and improve computational efficiency.

Nevertheless, the results generated here still provide useful information. Notice that discretization errors are far less noticeable and significantly reduced at advance ratios greater than 0.79. This indicates that the complications mentioned earlier is not solely an issue relying on a more efficient mesh but the MRF model application as well. Figure 8.16 and Figure 8.17 provide the first insight that these advance ratios, high thrust flow cases, are not accurately represented by the MRF model and/or S.A model because the blade loads are too high, given the increase in angle of attack, leading to flow separation that occurs downstream of the blades. Flow separation involves rotating turbulent flow, the velocity vectors are oblique to the cell faces which introduce numerical diffusion transferred to downstream cells. In addition, unsteady interactions of the interfaces are too significant to be approximated by MRF. Configuration 1, $J = 0.98$ thru $J = 1.44$, it is clearly shown that periodic peaks and wake deficit features are present. At these advance ratios the MRF model is capable of reproducing the same pattern of flow as measured experimentally. Quantitatively, the results vary by less than 15% for $J = 1.31$ and higher while $J = 1.31$ shows too high of an error to be acceptable. At the highest advance ratios, as shown in Table 8.3, the results are acceptable. Overall, wake data for all cases are not reliable given errors which may be corrected by improving mesh regions of separated flow. This was not a concern for this thesis since only inflow data is considered; however, if wake data becomes a necessity then these corrections should be performed.

Configuration 3 boundary layer profiles were validate with experimental results shown in Figure 8.21 and error computed in Table 8.3. Experimentally, it is difficult to capture the boundary layer profiles nearest to the wall especially with the bulky quadwire probe used; hence, the experimental measurements do not fully show the viscous sublayer region. The CFD and experimental data are in agreement at the location of measurement and serves as a successful validation for data upstream of blades. Additional experimental data at a range of advance ratios would be beneficial; however, data is limited.

Although a fair attempt was made to validate CFD data based on experimental data it is shown that wake measurements need improvement; however, ingested data is acceptable. Nevertheless, wake data at higher advance ratios have much higher agreement with experimental data; thus for these cases the current MRF model is a suitable approximation method. Conversely, more accurate CFD models will be

suggested for future computation in order to ensure accuracy for all cases instead of only for those with higher advance ratios.

9.3 INGESTED FLOW DATA INTERPRETATION

9.3.1 MODIFYING CONFIGURATIONS

Figure 8.22 shows the normalized inlet velocity profiles. This is correctly portrayed and it is important to note that for configuration 1 the line crosses the y-axis because there is no plate present. Configuration 2 shows a constant inflow, except at a normal wall distance of zero. The abrupt change in velocity is due to the no-slip condition combined with the constant inflow velocity. A ‘natural’ boundary layer will develop as the particle progresses further downstream. Lastly, configuration 3 shows the thick boundary layer with a normalized height of one and normalized velocity of one. Again, normalization of velocity is based on nominal inflow velocity and the normal distance from wall is normalized by boundary layer height of 102 mm. for all configurations. Configuration 1 does not contain a boundary layer or a wall; however, the origin is shared by all configurations and the same principles of normalization apply.

The progression of velocity profile from the inlet down to the propeller blades is shown Figure 8.22 thru Figure 8.27. The case of $J = 0.72$ is chosen to demonstrate the change in velocity profiles for all cases because this contains a more intense flow field and flow variations are more visible. As velocity profiles progress from inlet to one diameter upstream of the propeller, boundary layer height and mean flow velocities are increased for all configurations. Configuration 1 does not have a boundary layer in this region; hence only a velocity increase is shown. Once the propeller hub is reached, configuration 1 obtains a boundary layer due to the no-slip condition. In this region the changes in velocity profiles are prominent. At three chord lengths, configuration 1 demonstrates a symmetric velocity profile above and below the hub. All configurations present equivalent velocity profiles *above* the propeller from three chords to one chord upstream. This is because the flow in all configurations is almost identical *above* the hub but a very different scenario below. Below the propeller hub section, configuration 1 only has one boundary layer emanating from the surface of the hub. Configurations 2 and 3 each contain two boundary layers, one emanating from the hub surface and another from the plate (near-wall). The velocity profile below the hub is much rounder for configuration 3 compared to configuration 2 at three chord lengths away but become

equally sloped as they reached the blades. It is important to note that hub effects should be neglected, or at least set aside for now since the hub could have been modeled in several different shapes and sizes. The main idea here is the velocity profile propagation into the rotor, especially at the gap between the blades and wall.

Given the similarities of configuration 2 and 3, the next part of the discussion will consider them together and compare both to configuration 1. Thus far, the conclusion which may be deduced from these configurations is that an added plate does introduce instabilities at the blade tips. Configuration 1 does not have the non-uniform profiles seen in configuration 2 and 3 (Figure 8.27). The less uniform profiles achieved by adding a wall near the propeller cause velocity fluctuations at the tip of the blades as the blades cross this non uniform boundary layer. As Plas et al. [8] mentions, the noise generated due to this instability is broadband in nature and referred to as distortion noise. Distortion noise is also experienced in engines which have separate intake flows [8] and this can be related to configuration 2 and 3 given the unobstructed flow above the hub and constricted flow beneath. Notice Figure 8.27 plots the velocity profile along a constant radial direction (in Cartesian coordinates along the y-axis). The variation along this radial direction is nonlinearly smooth above the propeller but much more curvaceous below. The top of the hub profile shows smooth radial transition. Therefore, the flow velocity has large gradient along the radius for configuration 3. The flow from configuration 1 is uniform circumferentially and smooth radially and the flow for configuration 3 is neither. These conditions are currently in active study as mentioned in Chapter 1. Studies regarding boundary layer ingested propulsion systems such as [8], indicate that engine performance is improved and less power requirements are necessary. A. Plas et al. [8] states, “The benefit of boundary layer ingestion comes from re-energizing the aircraft wake.” This concept is based on idealized conditions including an engine which ingests 100% boundary layer flow hence requiring less power input to produce the same amount of thrust.

In cases where near-wall effects are present as in configuration 2 and 3, the addition of a thick boundary layer improves conditions of the velocity profile ingested by the rotor. Figure 8.27 shows that the boundary layer profile for configuration 3 is more uniform than configuration 2 at the bottom of the hub. Hence, if the rotor experiences near-wall effects, adding a thick viscous boundary layer to the flow could lead to reduced structural blade fluctuations and increased performance. Figure 8.28 shows a thrust curve

for all configurations and although almost insignificant, increases in thrust are detected from configuration 1 to 2 to 3, respectively. Although, this is a minor change and conclusions cannot be made directly they do serve as *indicators* of performance and structural stability improvements. Next, further study of different cases will be made for configuration 3's acoustic data set.

9.3.2 VARYING FLOW CONDITIONS

The effects of adding a wall to an axisymmetric flow and then adding a thick boundary layer has been discussed. Now focus is turned to the effects of varying the advance ratio on boundary layer velocity profiles at *each* station. Then another interpretation will be made on the boundary layer velocity profiles as they *progress* within the far measurement region and within the near measurement region. As for the latter observation, only one case is necessary for discussion since results show a general trend; however, data for all cases are presented ranging from Figure 8.51 thru Figure 8.65. The results discussed here apply to all configuration 3 data sets.

Shown in Figure 8.44 thru Figure 8.50 are the normalized velocity boundary layer profiles at each station mentioned. The circumferential distribution (Figure 8.44) will be discussed after the radial distribution (Figure 8.45 thru Figure 8.50). At the inlet all cases show an overlap, as expected, indicating correct inlet boundary conditions. Moving further downstream in relation to the inlet, it is clear the highest thrust producing case ($J = 0.48$) increases boundary layer velocity profiles. At one diameter upstream of the propeller, the relationship of decreasing advance ratio indicates increase in flow field velocities as is in agreement with the definition of advance ratio. At three chords upstream of the propeller, it is noticeable that the stream velocities approaching the hub tip are increased for decreasing advance ratios indicating greater pressure fluctuations in these regions and CFD results, although not shown, confirm this. The velocity profiles just above and below the hub section increase in velocity from case to case. Table 8.4 shows the relationship between the size of the propeller and boundary layer height (102 mm). This information will be used to visualize the spanwise flow across the propeller in relation to the normalized velocity profile data presented. Observing all cases together shows an obvious increase in velocity from case to case; however, it is interesting to note the amount of change in velocity varies nonlinearly. In addition, flow becomes more distorted at the boundary layer beneath the hub at higher advance ratios.

A general trend is observed for all cases; hence, the case of $J = 0.48$ will be used in this discussion. Figure 8.51 shows the change in boundary layer velocity profiles as it progresses downstream with the same trend in velocity increase mentioned earlier. More importantly, Figure 8.55 and Figure 8.57 (also shown together in Appendix E) amplify the change in boundary layer profiles as they progress above and below the hub section and into the propeller. Above the normalized distance of 4.68 (propeller blade tip) the flow converges to the same velocity as this would be represented as the outer region of flow contraction into the propeller as indicated by actuator disk models. Turning to Figure 8.57, notice how the velocity at all three locations barely change at the plate. In addition, the velocity at all three locations seem to merge almost at the same normalized distance value for all cases of approximately 0.25. This is slightly greater than the normalized distance of the propeller blade tip closest to the plate (see Table 8.4). Analyzing the ingested flow as separate portions above and below the profile it is noticed that the bottom ingested portion of the velocity profile, ranging from normalized distances of 0.20 to 1.82, is more uniform than the ingested portion above the hub ranging from 3.06 to 4.68. At this point, refer to Table 8.5. This is the average of the top and bottom portions of the velocity profile at one chord downstream. Notice that the differences between normalized mean flow velocities of the flow above and below the hub are very small. Even the higher thrust case only has approximately 16% difference between the top and bottom mean flow velocity profiles. This equates to 1.4 m/s difference for an inflow of 10 m/s (case of $J = 0.48$). Increased advance ratio shows even further decrease in ingested mean flow velocity. Hence, it is the more uniform flow profile which makes this concept attractive.

Although this portion of the boundary layer is more uniform, the blade crosses less uniform region of boundary layer between the wall and blade tips (normalized distance of 0 to 0.2). This portion, if somehow eliminated would reduce the cyclic stress on the fluctuating blades and reduce broadband noise generated, possibly even below configuration 1. However, it is present and must be interpreted. As the blades cross this non uniform section of the velocity profile, the blade angle of attack will change and drastic changes cause increased noise. Ideally, the blades would be most stable in a completely steady uniform flow; hence, a flow such as the one experienced here shows that the blades experience nonuniform velocity fluctuations. The near wall region between the blade tips and wall experience the greatest fluctuations; however, only the radial distribution has been analyzed and the circumferential distribution is necessary for

any conclusion regarding noise. It is true that at lower advance ratios, Figure 8.50, the velocity variations at the propeller tip is increased, but at lower advance ratio and possibly off design operation these variations are reduced greatly. Therefore, in cases where a propeller is near a wall the nonuniform flow can be minimized by adding a thick boundary layer to the flow, this minimizes the fluctuations present between the blade tips and near wall.

Noise and vibration is caused by the azimuthal variations in flow velocity shown by Figure 8.45. To obtain these results a circumferential filter was applied to these velocity profiles to phase average the flow near the blades to eliminate the 'frozen rotor' effect. ANSYS – FLUENT data points were interpolated by MATLAB to provide equally spaced points. A moving average of one tenth of the equally space points (since the rotor has ten blades) along a fixed radius was applied and the contour plots produced. These plots show that azimuthally, only one spike in the circumferential flow occurs which would alter the blade angle of attack at that span. However, this is change in angle of attack occurs at low frequencies (a blade rotating at 2734 rpm (45.6 Hz)) which would not produce any significant increase in broadband noise. The hotspots shown in these contour plots may be unphysical results due to the imparted velocity throughout the entire rotating domain. Notice that at higher thrust cases these hotspots travel larger angular distances than lower thrust cases (due to inflow velocity changes) which may be originating at the interface and transferred as upwind numerical error at the interface.

10 CONCLUSIONS AND RECOMMENDATIONS

10.1 OVERVIEW

Simulating the turbulent flow field about any geometry is a problem that has been studied for over a hundred years. The numerical methods presented in this thesis attempt to simulate the flow through a propeller and study the ingested turbulent flow. This was approached by employing three different configurations involving an open rotor with no flow obstruction, an open rotor near a plate, and an open rotor near a plate with thick turbulent boundary layer. The simulations utilized RANS to simplify the turbulent flow using closure from the Spalart-Allmaras turbulence model. ANSYS – FLUENT was utilized to compute the flow using these models based on its MRF model. Furthermore, a variety of flow characteristics were presented for each configuration and, in addition, configuration 3 was studied extensively. These results, referred to as the acoustic data set (given its purpose in future computation regarding acoustic predictions) were used to make a quantitative study of the velocity profiles as they progress into the rotor.

10.2 NUMERICAL METHODS AND CFD

The flow through a propeller is by nature three dimensional, complex, rotational, and inherently unsteady. Estimates of the wake deficit behind the rotor was found to be dominated by numerical noise apart from $J = 1.31$ and $J = 1.44$ cases. This is because for $J = 1.31$ and $J = 1.44$ cases the angle of attack is reduced and flow separation becomes less of a concern. The mesh used in this thesis does not refine the blades appropriately to capture these turbulent features correctly; thus, the noisy data observed for low advance ratios. In addition, the MRF model does not capture transient flow features. As for evaluation on the accuracy of the Spalart-Allmaras turbulence model, the boundary layer region at the blades should first

be correctly meshed in order to fully resolve these flow features and the boundary layer profile. Then the cases may be reanalyzed and compared to experimental results. Given the limited availability of experimental data, an attempt was made to validate CFD wake data to experimental wake results; however, results show that the current setup is incapable of correctly predicting the wake flow field.

The contrary can be said for inflow data. This thesis studies the inflow into the propeller and CFD results at 0.79 m (31 inches) upstream of the propeller is in agreement with experimental data. The numerical errors introduced downstream of the propeller do not propagate upstream due to upwind discretization schemes. As for the MRF model, attention has been given to the front interface of the rotational domain. Hence, a flow with less acceleration generates a more uniform flow field over the front interface. As a result, the approximations of the MRF model are more accurate. Therefore, the flow field can be approximated in a steady state manner by using the MRF model. Nevertheless, to fully represent the entire range of possible advance ratios, another fluid model should be used capable of capturing unsteady flow features such as the Sliding Mesh Model.

The Spalart-Allmaras turbulence model produces well defined boundary layer profiles (based on inflow data). This model performs very well for this part of the flow. Evaluation of the turbulence model for this flow type may be made based on the mesh features. This is because the regions which could be improved most are near to surfaces. However, acceptable results were still attained because CFD does not require the viscous sub-layer at the surface to be reproduced. Overall, mesh quality, refinement, and performance was satisfactory for the boundary layer and provided valuable information that will be used for analysis.

10.3 ALTERING THE INGESTED FLOW FOR DIFFERENT CONFIGURATIONS

Changing configurations provides an understanding of how the ingested flow depends on the boundary conditions. The idea of having a rotor in close proximity to a surface to allow the ingesting of a thick boundary layer from a surface such as a ship's hull or fuselage of an aircraft, as in [3] and [4], is an area of active study. Comparing an unobstructed flow to one which is obstructed by a wall on one side shows that non-uniform velocity profiles are introduced due to the added shear on the flow because of the near wall. Also, for the axisymmetric case, the flow velocity distribution along the blades is uniform

circumferentially but radially the flow field changes gradually. When a wall is introduced, the velocity profile distribution on the blades is non-axisymmetric and contains non-uniform profiles at the tip of the propeller. Hence, circumferential gradient of the flow field is no longer constant and the gradient of the flow field radially is nonlinear. This, however, may be minimized by adding the thick boundary layer to the flow; however, no significant noise increase can be deduced given the low frequency and magnitude of circumferential velocity changes. This was analyzed through the operational range of configuration 3.

10.4 RECOMMENDATIONS

10.4.1 MESH

A major improvement of boundary layer results can be made by altering the mesh. The mesh is a major contributor to accuracy and convergence. Regions near the surfaces should be refined to fully resolve the boundary layer. This includes the propeller hub and near wall. If data in the wake is of interest then the surfaces of the blades must also be refined to fully capture boundary layers and turbulent flow features. This is concept is problem specific. As for the axisymmetric case, the wall regions are insignificant and may be ignored given its distance from the propeller; however, the surface of the propeller cannot. The surface should be constructed of prism layers and special care should be given to the initial cell height from the surface. This is because it is used to calculate the wall y^+ values; hence, this may become an iterative process. Special care should be given in choosing the correct inflation rate. The inflation rate applied to the prism layers should be exponential in order to fully resolve the boundary layer. This becomes an iterative process between wall y^+ values, mesh quality, and number of data points that make up the boundary layer profile. If the characteristic velocity is known over the blades, then wall y^+ values can be adjusted in ANSYS – ICEM by setting initial cell heights. The height of the last prism layer should be analyzed in order to not conflict with the rotating flow above. It should be noted that as the final height of the prism layers change so should inflation rates. This type of mesh construction can be applied to any surface where boundary layer profiles are concerned including the propeller blades and edges. However, the sharp blade edges would provide an additional difficulty due to its curvature along the airfoil. Hence, it is suggested that a C-type mesh or better be constructed at every airfoil and extruded spanwise. Additionally, the mesh quality usually deteriorates when prism layers are produced at large heights as it

conflicts with the tetrahedrals above. Ensuring that high quality, low skew, and aspect ratios are maintained is a must. Of course, these recommendations must only be applied relative to what is being measured and the flow leading to it.

Although the wake was only used to validate CFD data and no data regarding the wake was analyzed in this study, the data from this region shows the importance of applying refinements relative to what is being measured. In an attempt to validate CFD data using experimental data in the wake region, several refinements were made to improve the wake regions even though no wake measurements were required. Therefore, if this region (wake) was ignored and only the regions upstream of the propeller were refined, there would be a large decrease in total grid size without sacrificing accuracy in the upstream regions; thus, improving mesh efficiency and decreasing computational resources. Additionally, if wake data is concerned, a better mesh convergence would be obtained if the surface of the propeller (blades, blade edges, tip, etc.) was refined and this could be established with less than the 5 million cells used. This is why it is important to refine the correct regions depending on what is being measured.

Improved accuracy can also be obtained by controlling cell node positions. Since the data is obtained at the nodes, producing a mesh which contains nodes exactly on the measurement plane produces less variance in the data. As mentioned, data is gathered at nodes and not interpolated between cells. Alternatively, a MATLAB script could also be produced to apply interpolation to a small volume around the region being measured.

10.4.2 SOLVER

10.4.2.1 FLOW MODEL

The current utilization of the MRF model has proven to be less reliable at lower advance ratios because the flow at these conditions produces strong interactions between the stationary domain and rotational domain. This is due to the 'Frozen Rotor' approach which ignores blade rotation. Therefore, it is recommended that to account for the unsteady interactions between interfaces an unsteady approach be used such as the sliding mesh model. The results obtained from MRF model are recommended as initial conditions for a sliding mesh model since the increased accuracy increases resource demands. Lastly, the chosen time steps must resolve the circumferentially periodic flow.

10.4.2.2 ACTUATOR DISK THEORY

As the inflow data is concerned, another option of analysis is the Actuator Disk Theory. This theory will not provide valuable information downstream of the propeller; however, provides simple means of calculating the ingested flow. The propeller is replaced by a pressure jump in the flow and upstream flow data can be computed; however, the assumptions of an ideal fluid must be made and wall interactions will not be considered. Hence, this theory may be used to cross check RANS based solutions.

10.4.3 EXPERIMENTAL DATA

Unfortunately, the experimental data gathered was geared for aero-acoustic analysis therefore only limited flow data was obtained. It is recommended that more experimental data be gathered for comparison with the computer simulations especially upstream along the boundary layers. Interesting locations would be at one diameter, two chord lengths and one chord length upstream of the propeller blades.

FIGURES

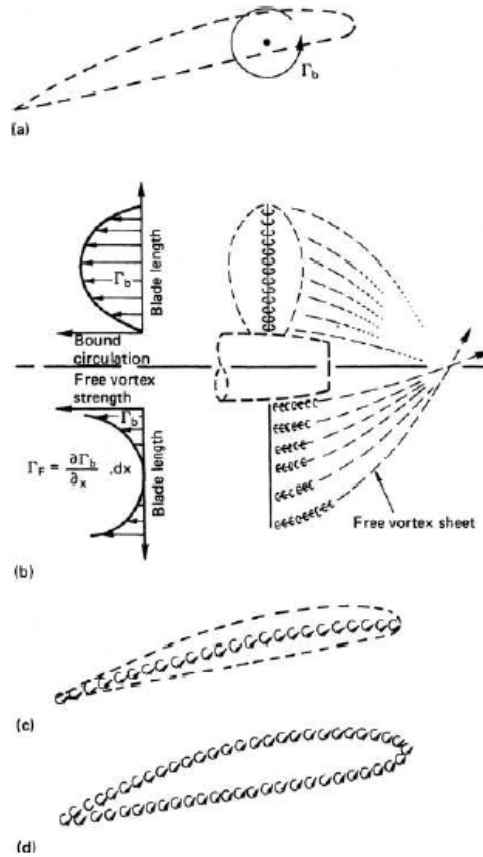


Figure 2.1 – Hydrodynamic Models of Propeller Action

(a) Lifting line
 (b) Lifting line model of propeller action
 (c) Lifting surface
 (d) Surface vorticity.
 Diagram and caption from [34].

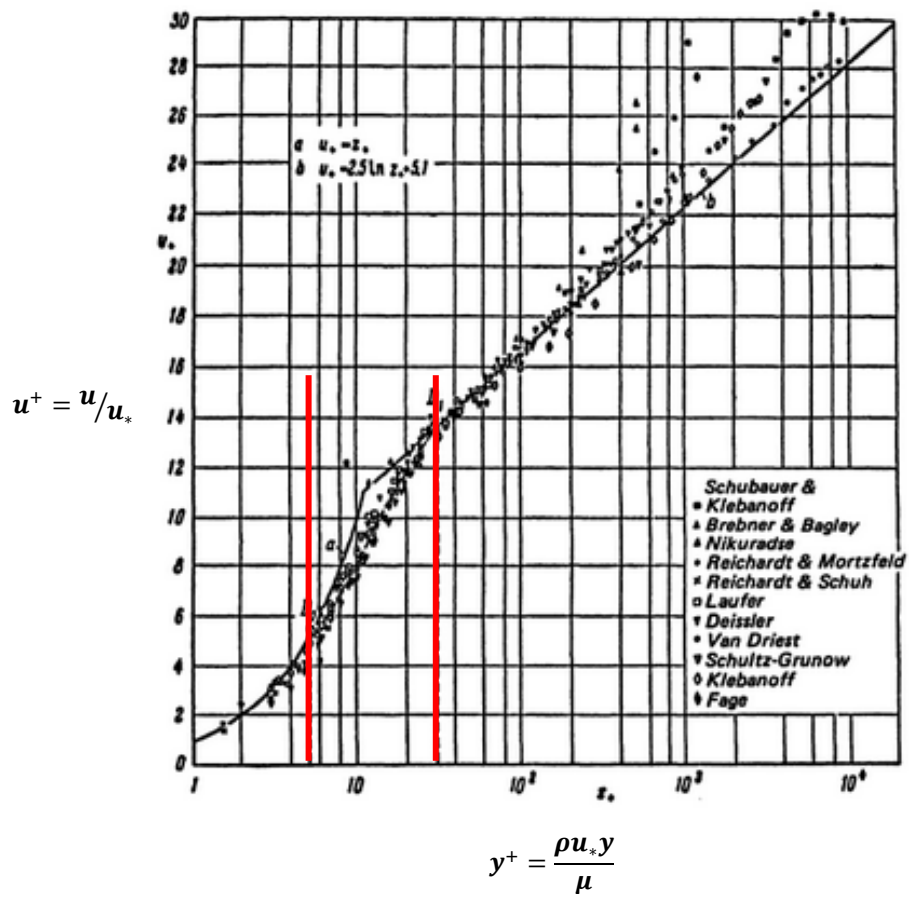


Figure 3.1 – Universal Dimensionless Mean Velocity Profile

Turbulent flow close to a smooth wall, showing turbulent boundary layer regions separated by red lines.

(From Monin and Yaglom) [78]

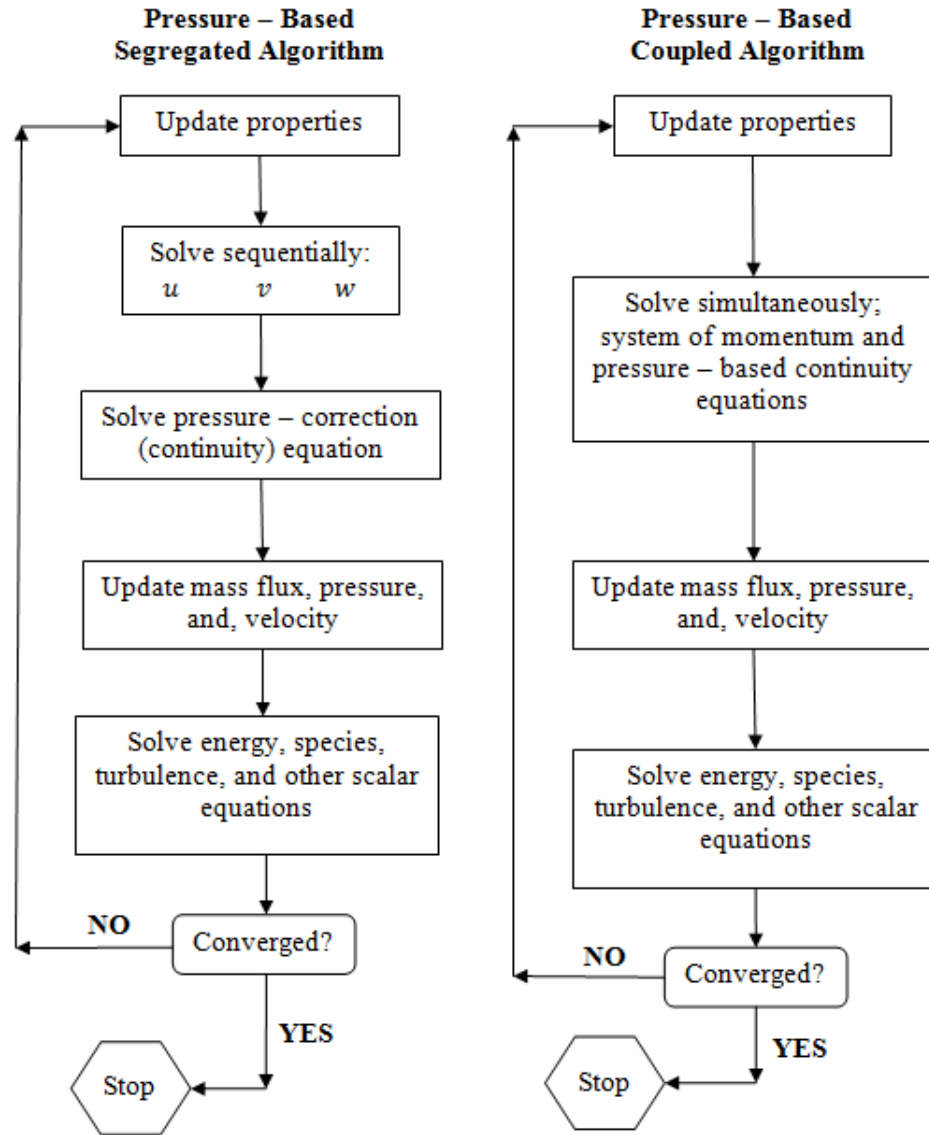


Figure 4.1 – Overview of Pressure – Based Solution Methods

Chart Diagram obtained from ANSYS – FLUENT Theory Guide in Overview of Flow Solvers section [68]

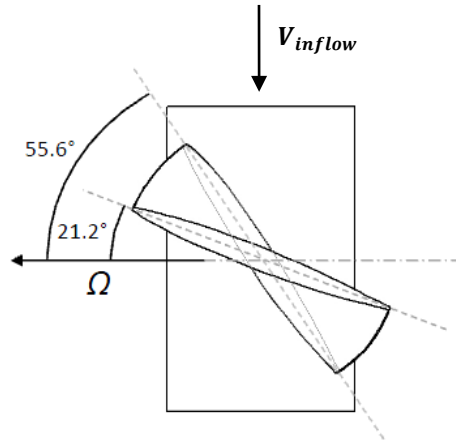


Figure 5.1 – Single Blade Diagram of Blade Twist and Flow Direction

Showing flow direction and blade rotation. Blade twist varies nonlinearly from 55.6° (root) to 21.2° (tip).
Figure obtained from Glegg et al. [6].

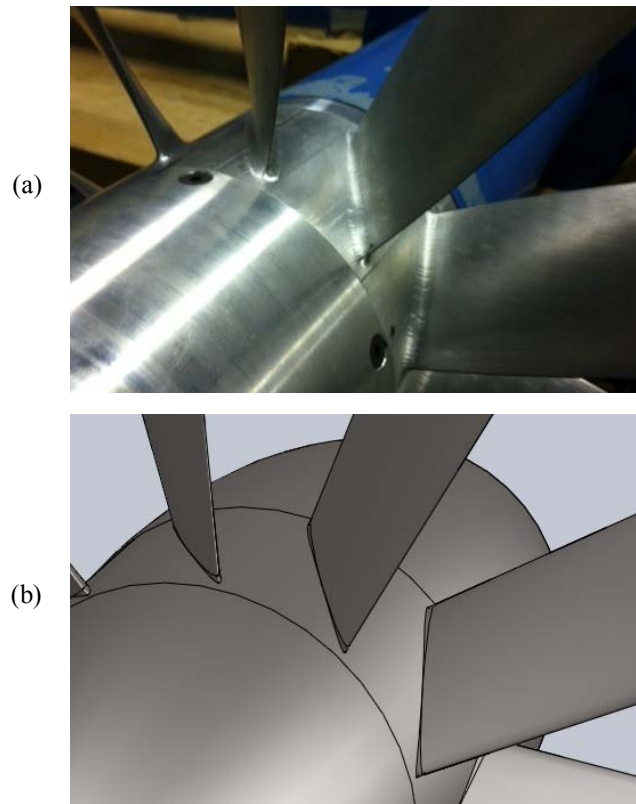


Figure 5.2 – Geometry Differences (Filet)

(a) Actual Propeller - Showing at fillet at root of blades.
(b) CAD model - Showing no fillet at root of blades (sharp merge).

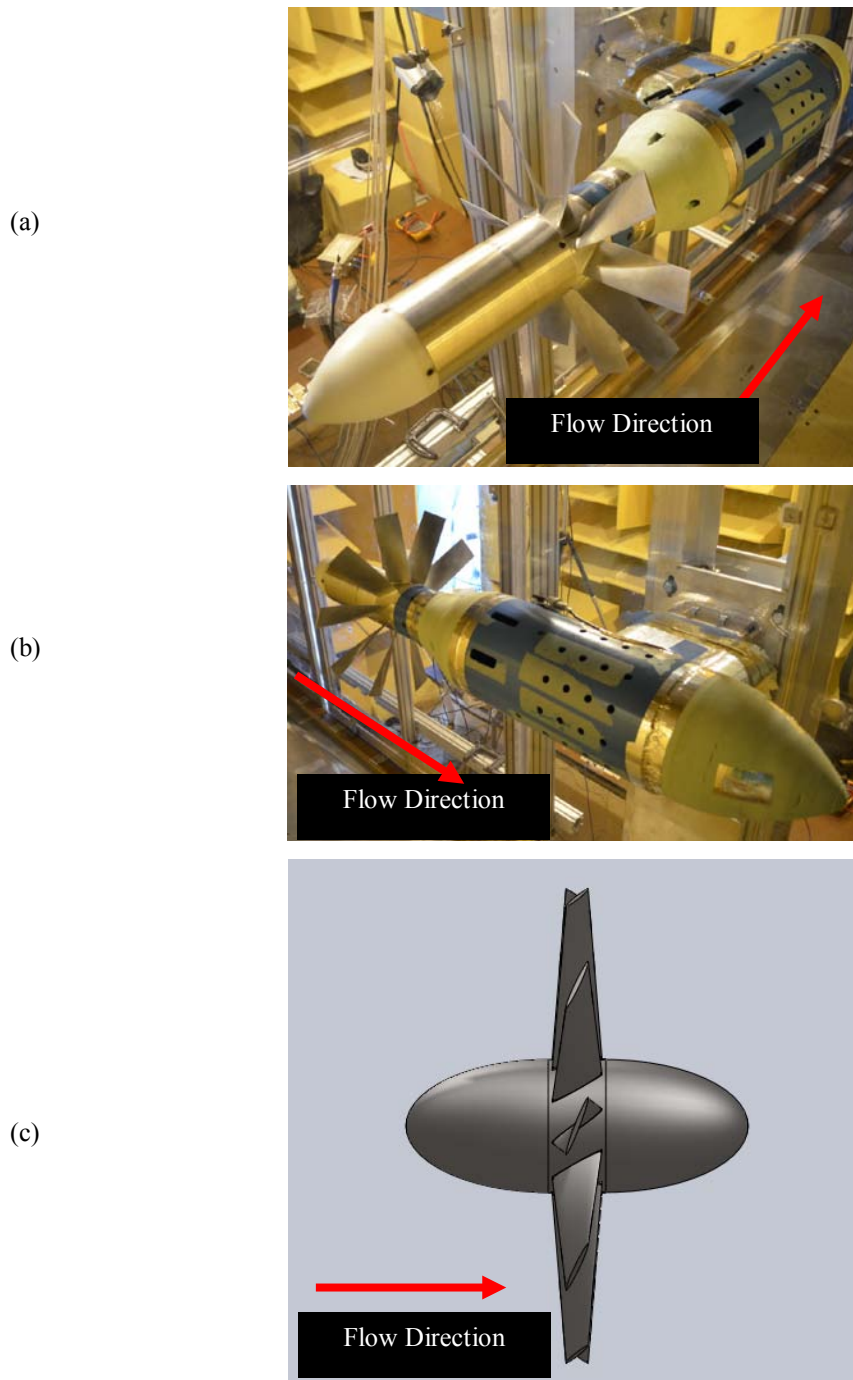
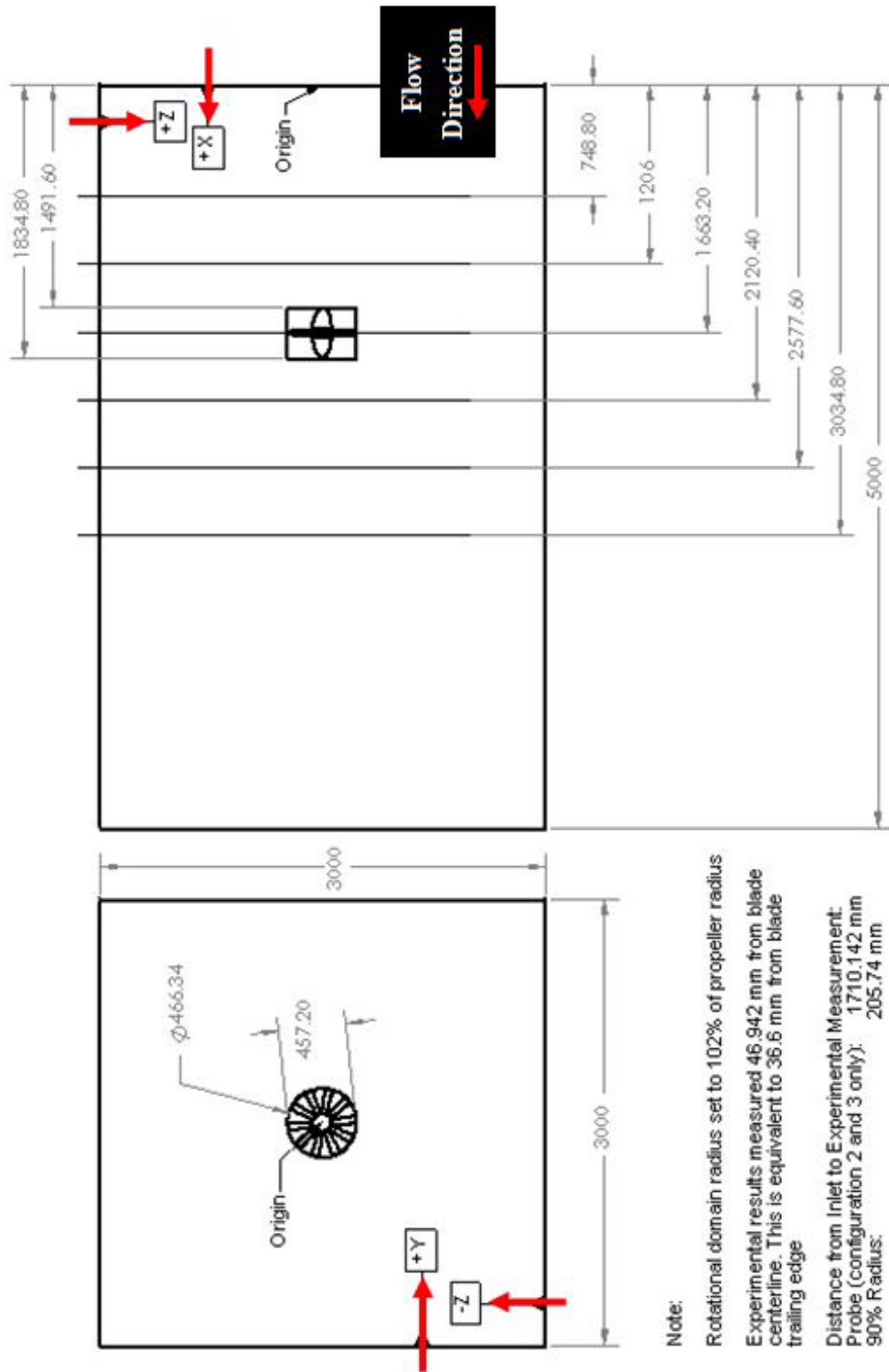


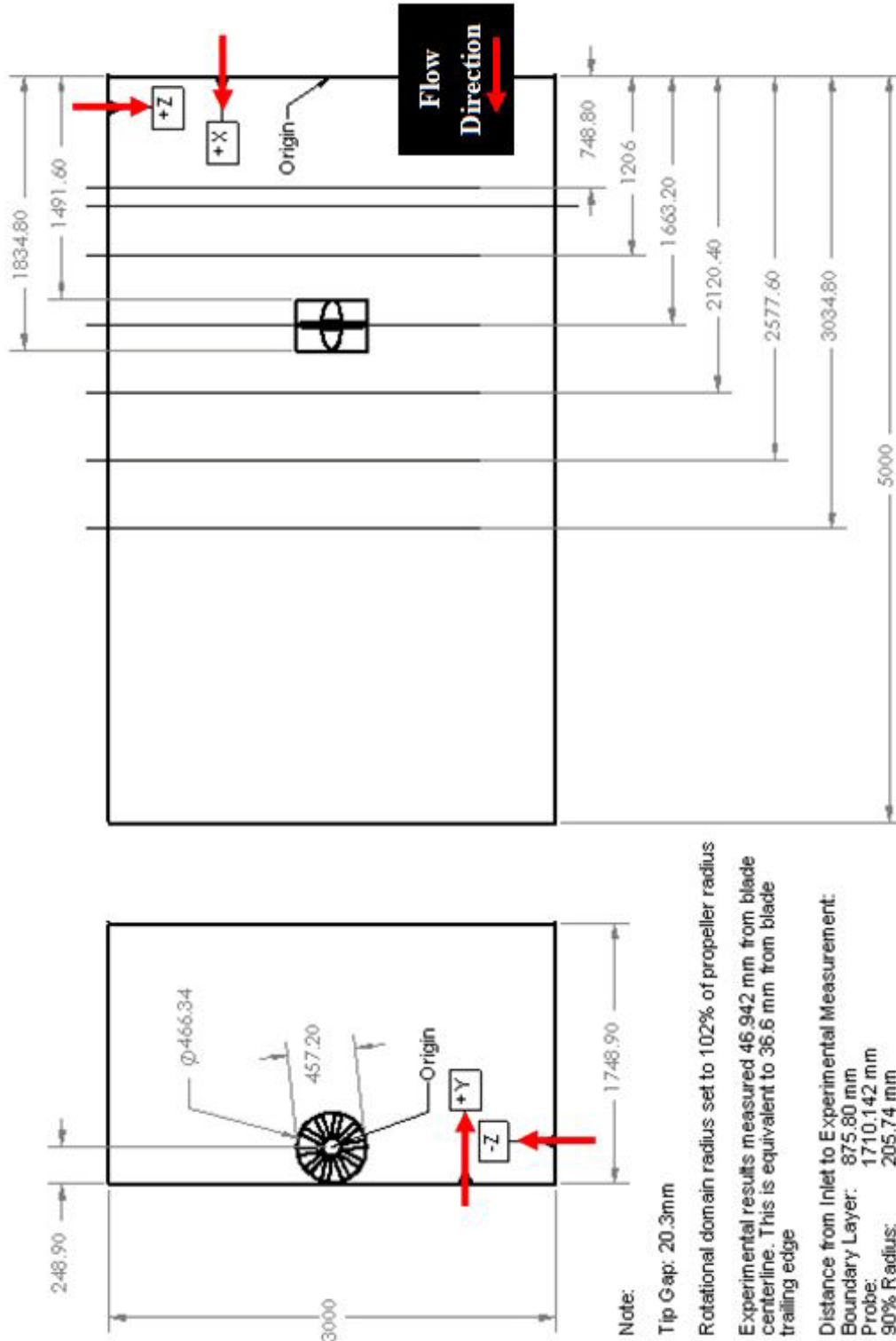
Figure 5.3 – Geometry Differences (Hub)

(a) Actual Propeller - Showing anterior section of hub.
 (b) Actual Propeller - Showing posterior section of hub.
 (c) CAD model - Showing simplified hub sections.
 (a-b) Courtesy of Dr. Nathan Alexander



PROPELLER AND TUNNEL - CONFIGURATION 1

Figure 5.4 – Drawing of Configuration 1



PROPELLER AND TUNNEL - CONFIGURATION 3

Figure 5.5 – Drawing of Configuration 3

Configuration 2 uses the same drawing of Configuration 3

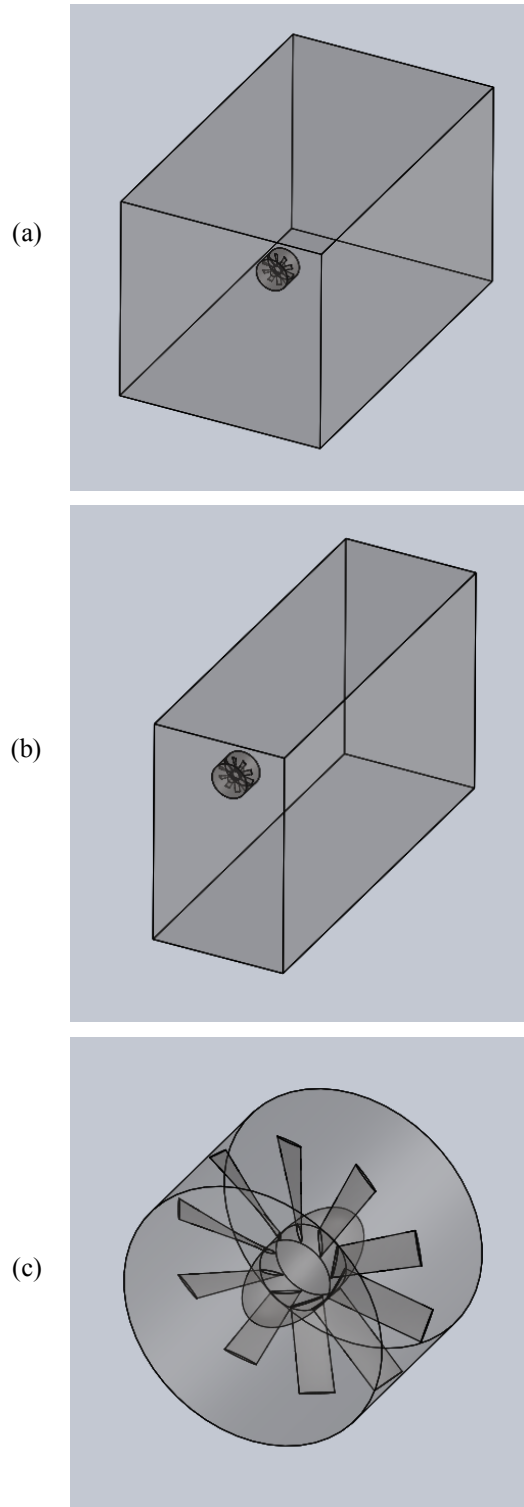


Figure 5.6 – Geometry of Domains and Subdomain

(a) Configuration 1 view of all domains
 (b) Configuration 2 and 3 view of all domains
 (c) Configuration 1, 2, and 3 view of rotational subdomain.

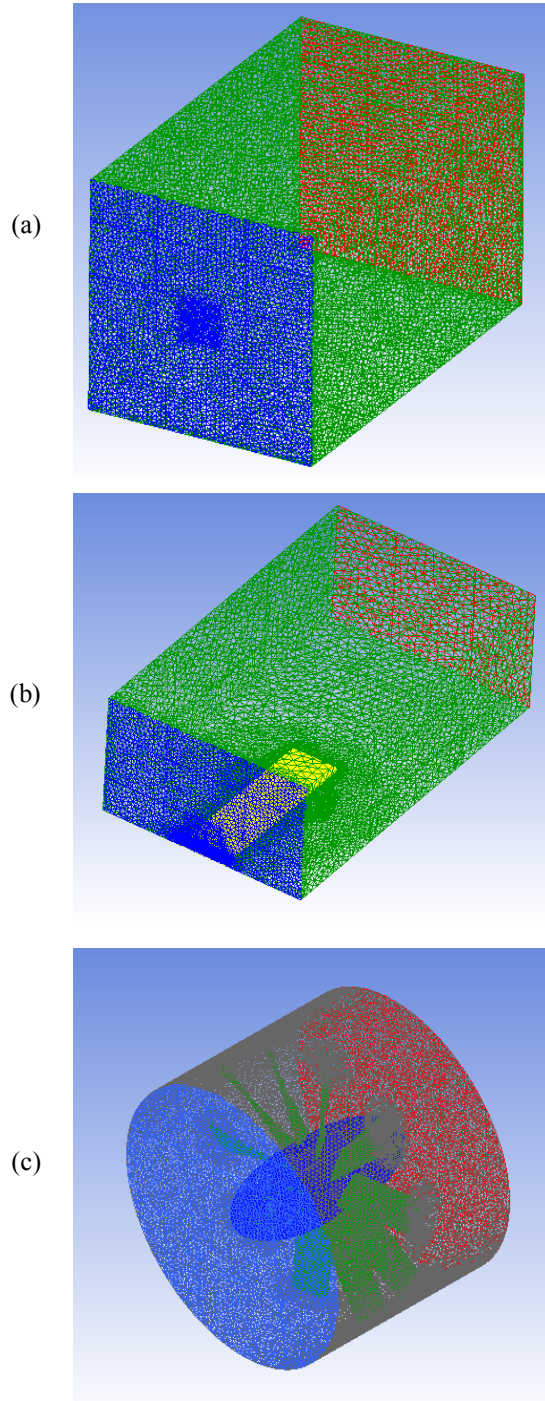
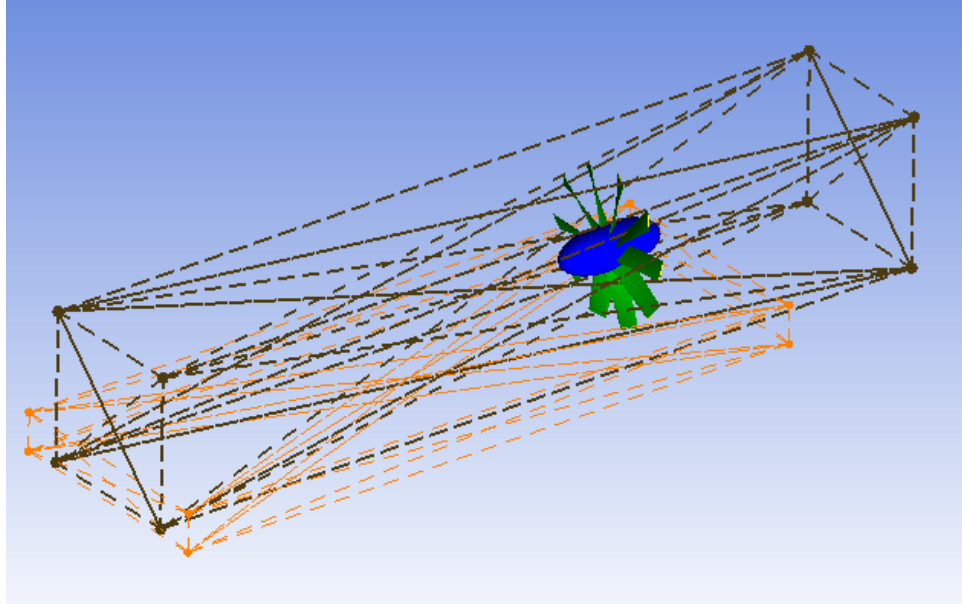


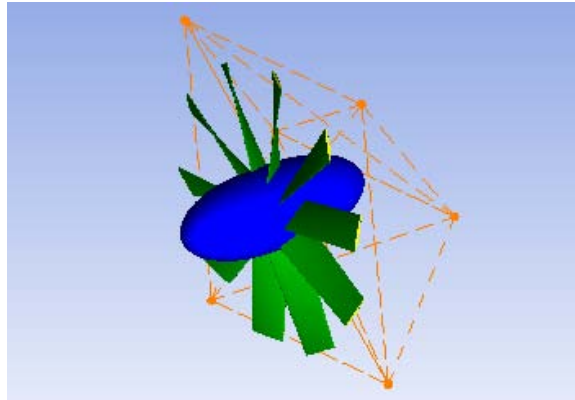
Figure 5.7 – Mesh of Domain and Subdomain

(a) Stationary Domain (Configuration 1) without propeller and rotational domain (b) Stationary Domain (Configuration 2 and 3) without propeller and rotational domain. Blue – Inlet, Red – Outlet, Yellow – Boundary layer wall, Green – Exterior walls. (c) Rotational Domain mesh including propeller. Blue – Interface in front of propeller, Red – Interface in back of propeller, Grey – Interface radial to propeller.

(a)



(b)



(a) Mesh Densities in Stationary and Rotational Domain.

Dark brown – Wake Density

Orange – Boundary Layer Density

(b) Mesh Density in Rotational Domain.

Orange – Experimental measurement region.

Figure 5.8 – Mesh Densities

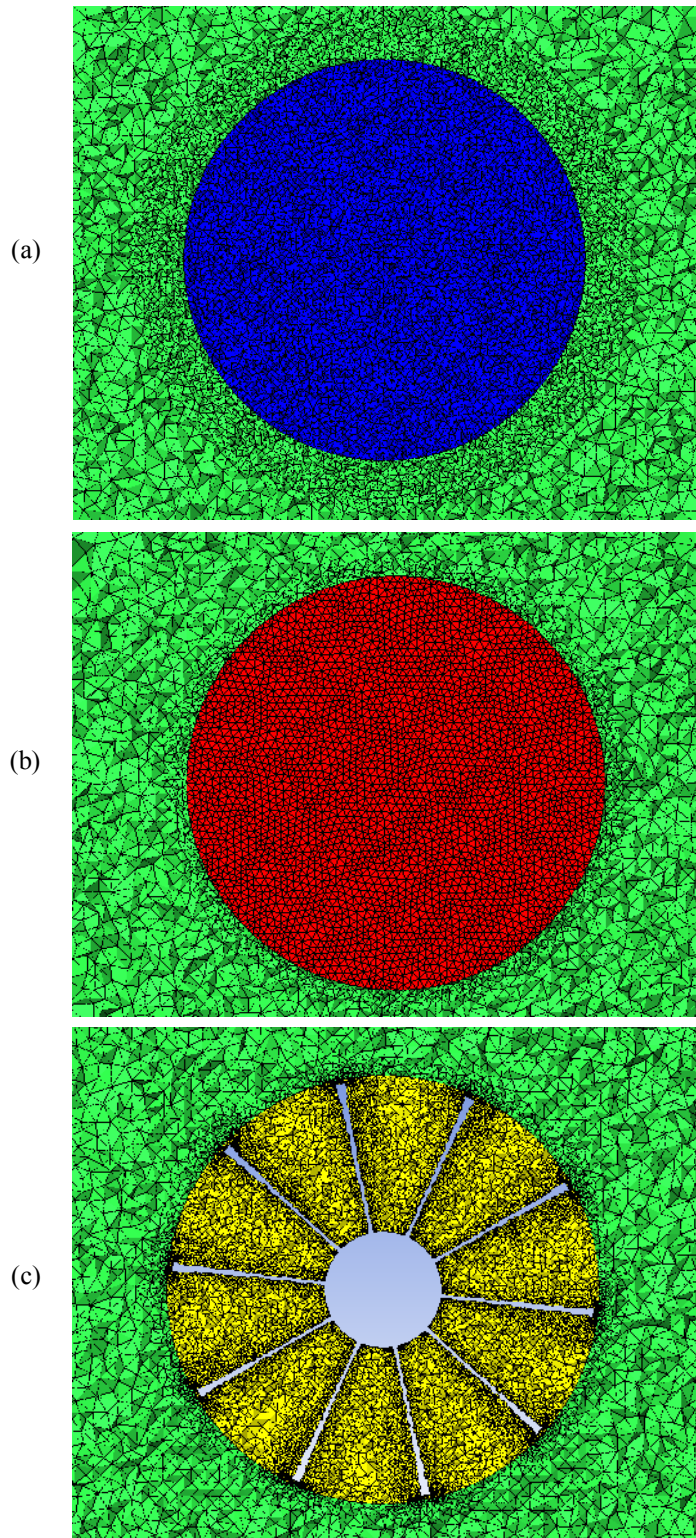


Figure 5.9 – Configuration 1
Mesh at Interfaces

(a) Front interface (blue) and surrounding stationary domain mesh (green). (b) Rear interface (red) and surrounding stationary domain mesh (green). (c) Plane at blade spanwise centerline (yellow) and surrounding stationary domain mesh (green)

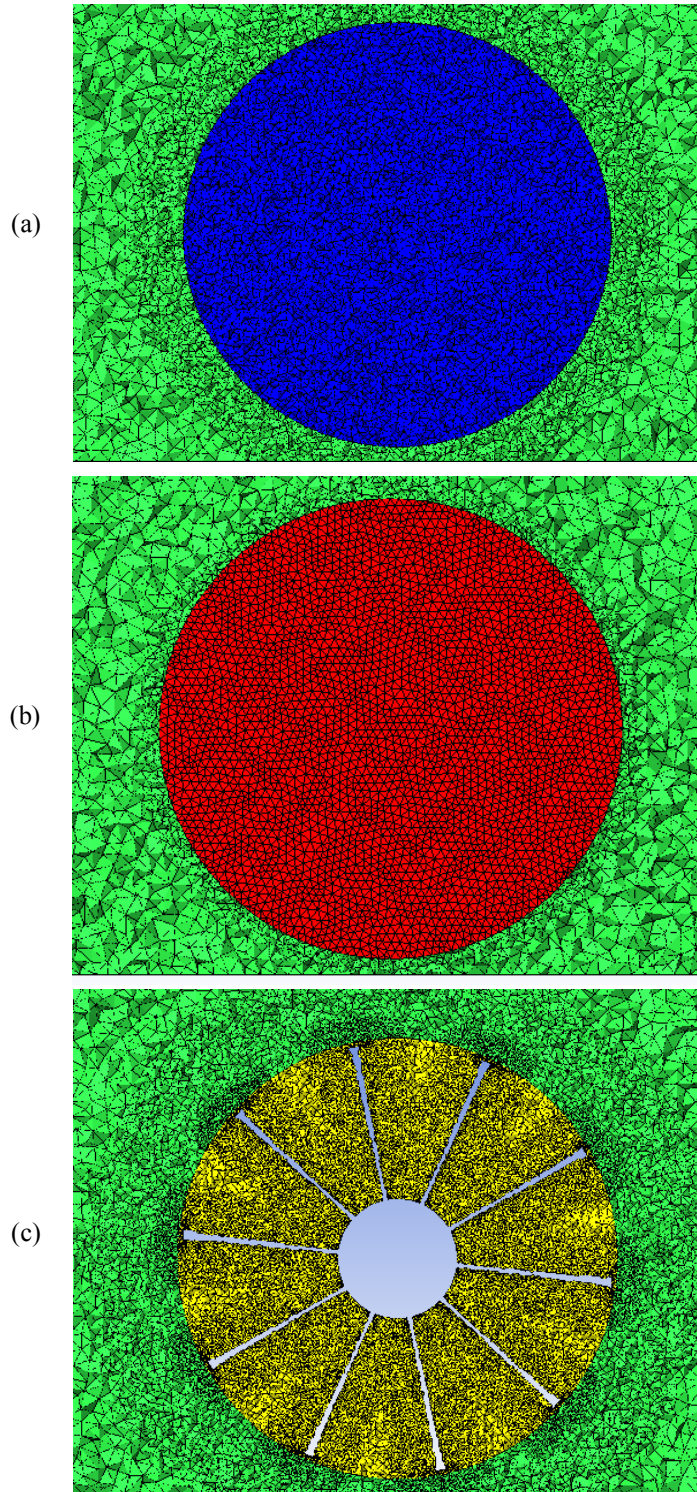


Figure 5.10 – Configuration 2 and 3 Mesh at Interfaces

(a) Front interface (blue) and surrounding stationary domain mesh (green). (b) Rear interface (red) and surrounding stationary domain mesh (green). (c) Plane at blade spanwise centerline (yellow) and surrounding stationary domain mesh (green). (a-c) is extended down to the near-wall.

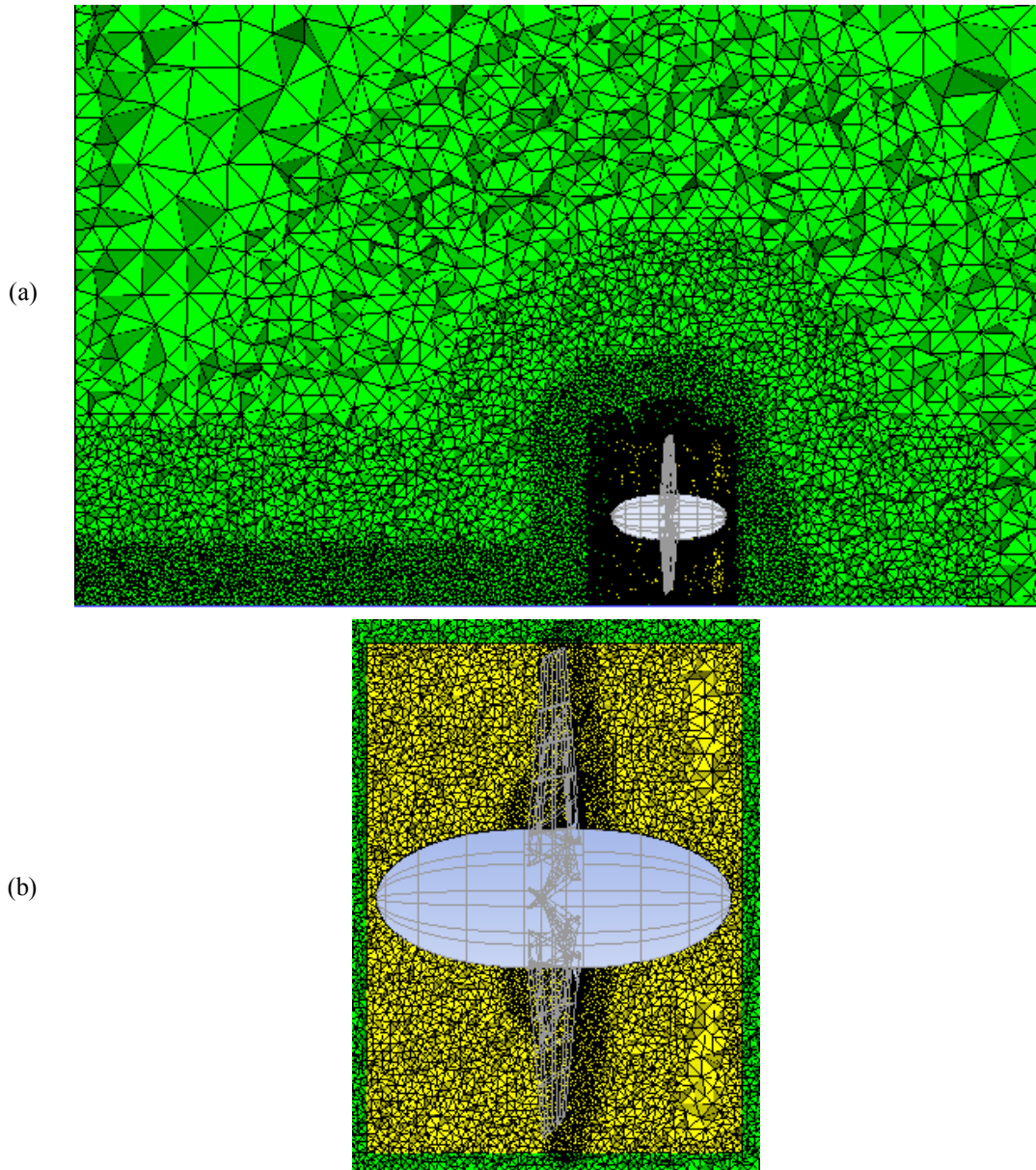


Figure 5.11 – Cross Section Display of Domain and Subdomain Mesh

(a) Stationary Domain (green) and rotational domain (yellow). Propeller is shown in grey. Shows inflation, density, and surface refinements.
 (b) Rotational domain mesh refinement. Inflow direction is from left to right.

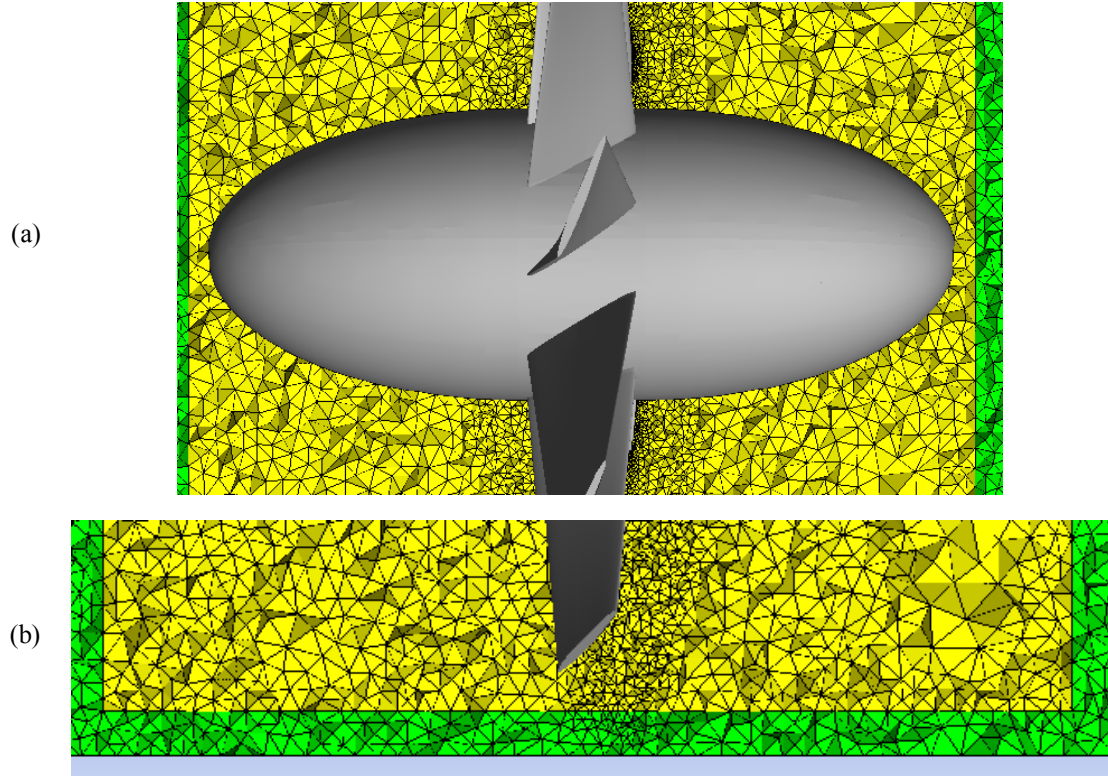


Figure 5.12 – Cross Section Display of Boundary Layer Mesh

- (a) Cross section of boundary layer refinement at surface of propeller.
- (b) Cross section of boundary layer refinement at near wall. Blade tip is shown in grey.

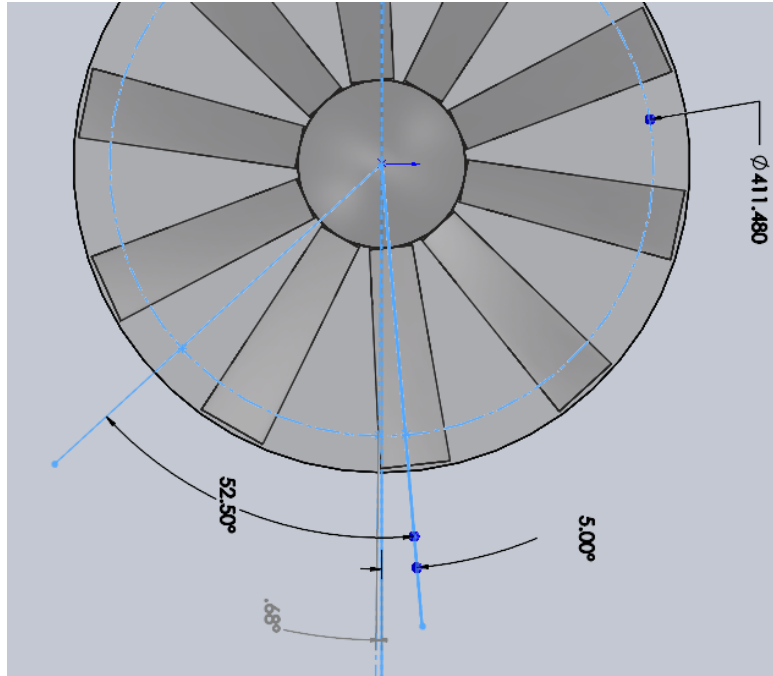


Figure 5.13 – Front View of Propeller Blade Locations (CFD)

CFD propeller position at time of CFD computation showing reference values to experimental Results

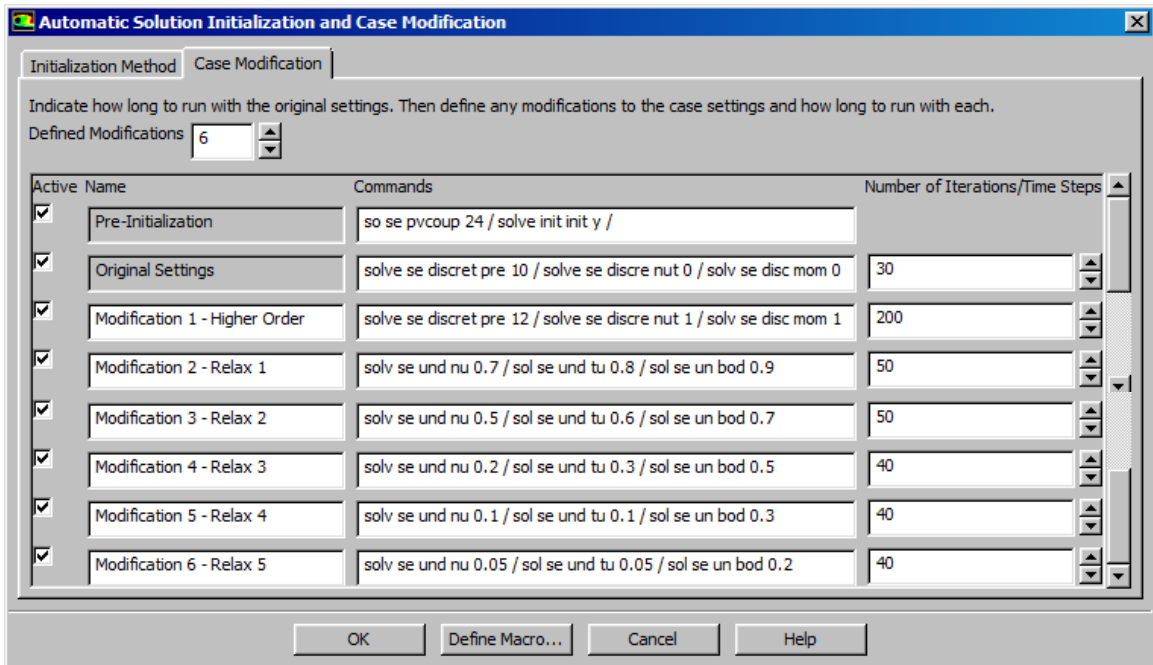


Figure 5.14 – Automatic User Specified Solution Initialization Procedure

Shows list of commands in order of iterations, performed till convergence.

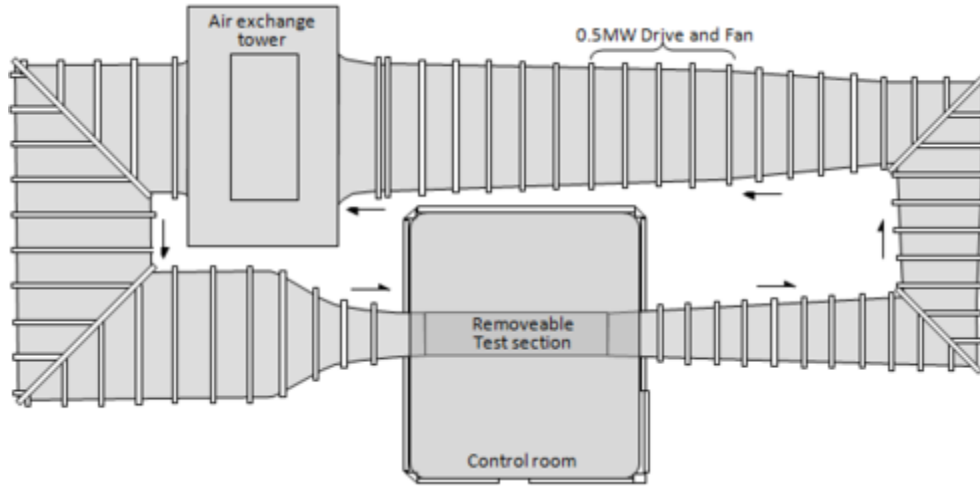


Figure 6.1 – Overview of 'Stability Wind Tunnel'

Figure provided by [79]

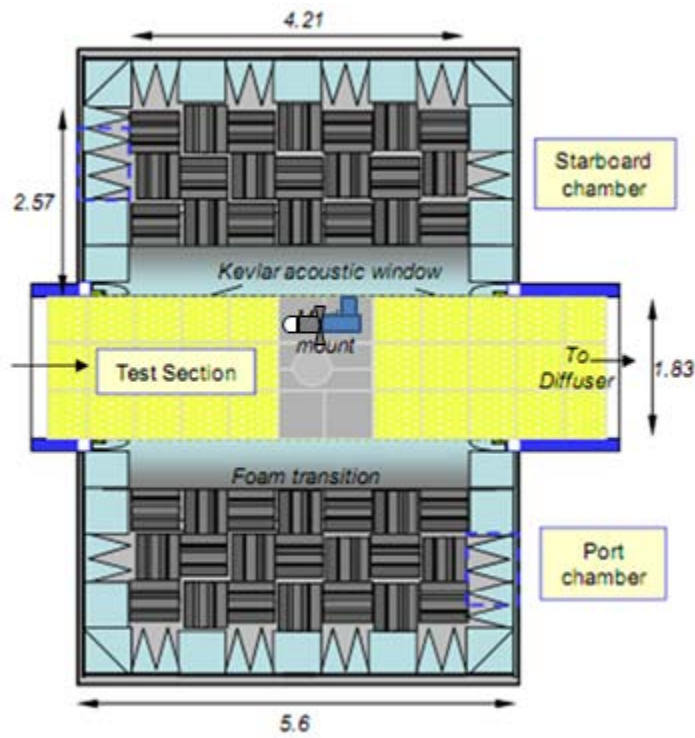


Figure 6.2 – Test Section Diagram

Courtesy of Dr. Nathan Alexander

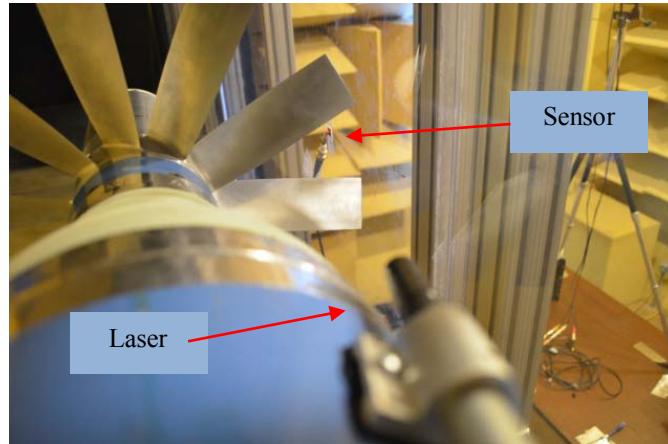


Figure 6.3 – Laser and Sensor Experimental Setup

Laser and sensor are used to determine propeller blade positions.
Courtesy of Dr. Nathan Alexander



Figure 6.4 – Hotwire Probe Experimental Setup

Hot wire probe behind propeller. Red dot is also seen from the laser used for synchronizing blade position and measurements.
Courtesy of Dr. Nathan Alexander

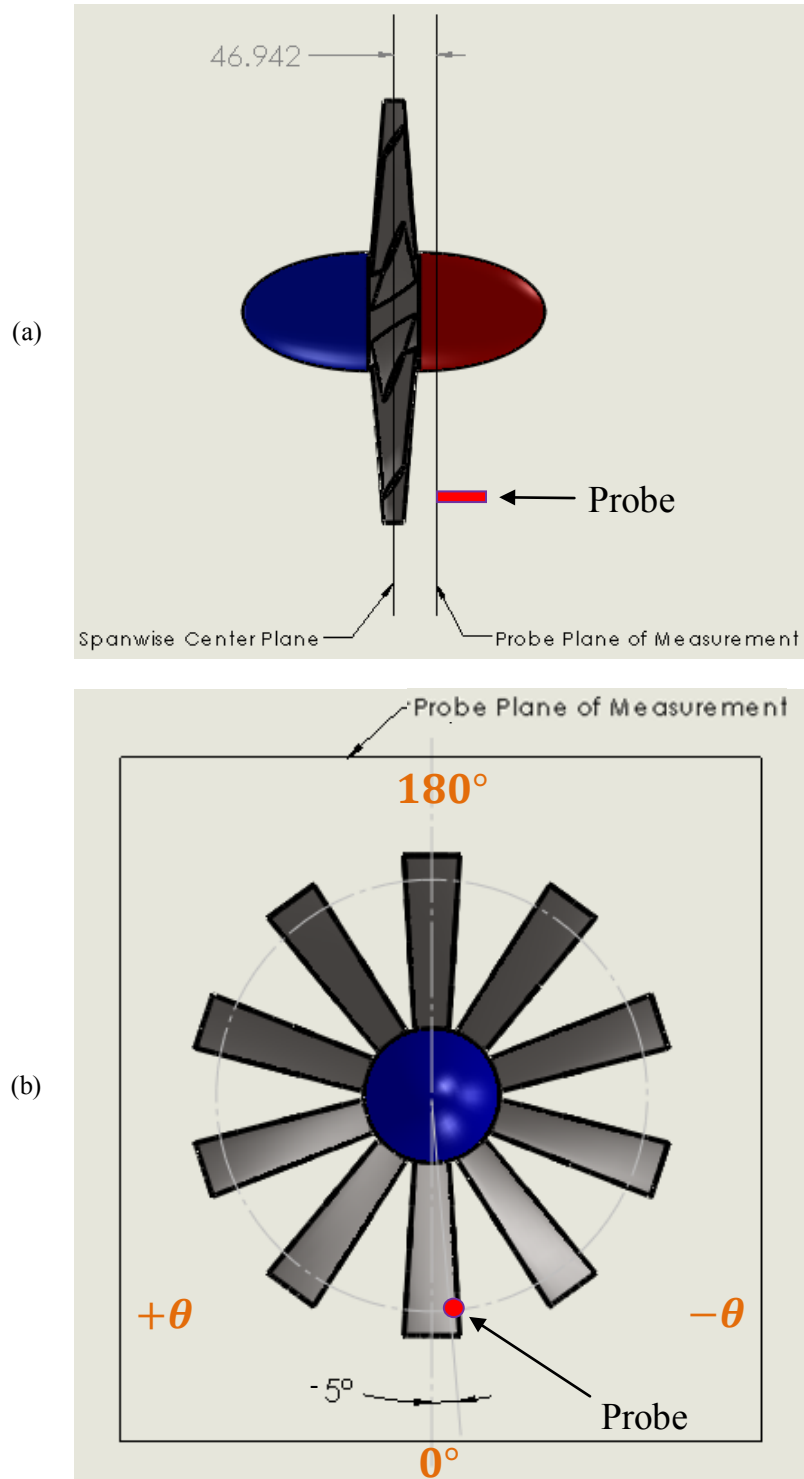


Figure 6.5 – Diagram of Propeller Probe Location

(a) Side view of propeller and respective planes.
 (b) Front view of propeller and probe location.
 Blue – denotes direction towards inlet (upstream of blades).
 Red – denotes direction toward outlet (downstream of blades).

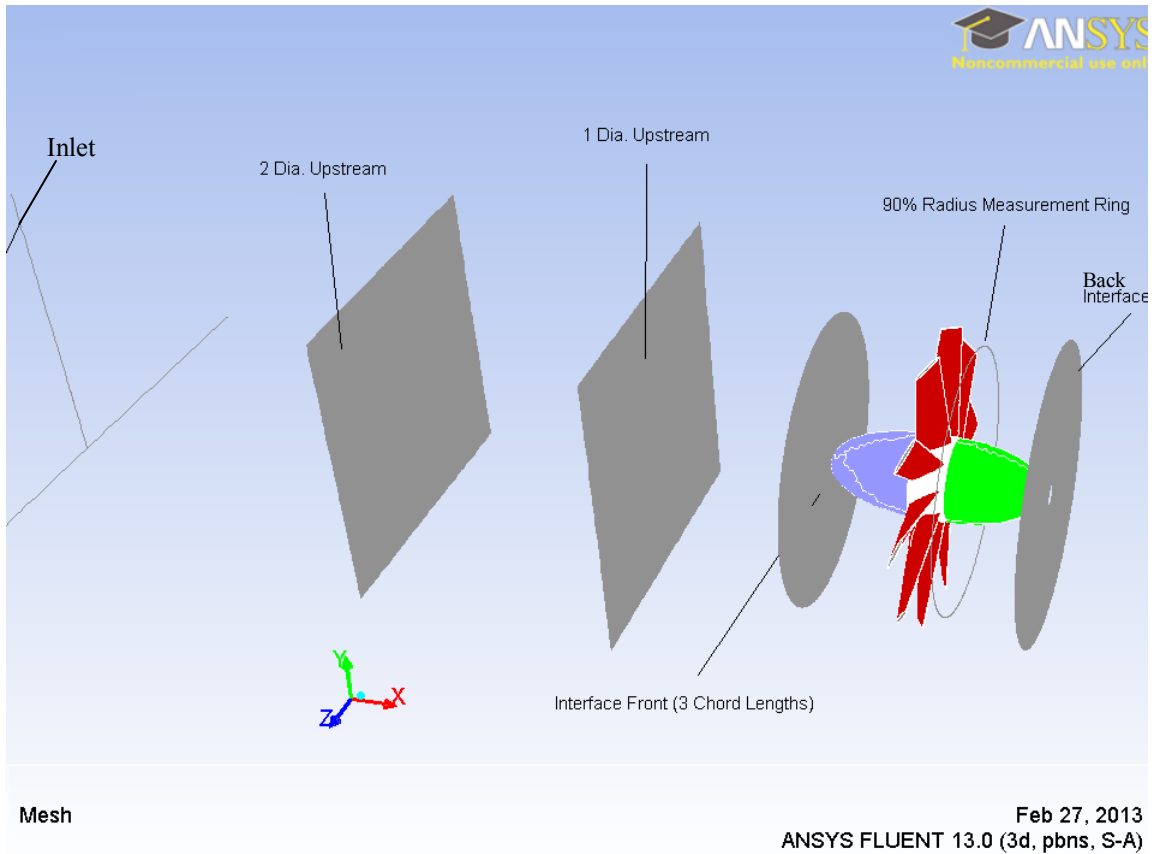


Figure 7.1 – Planes for Contour Plots
(Far Measurements)

Contour plots are generated over these planes.
Also shown, is the 90% radius measurement
ring where wake measurements are made.

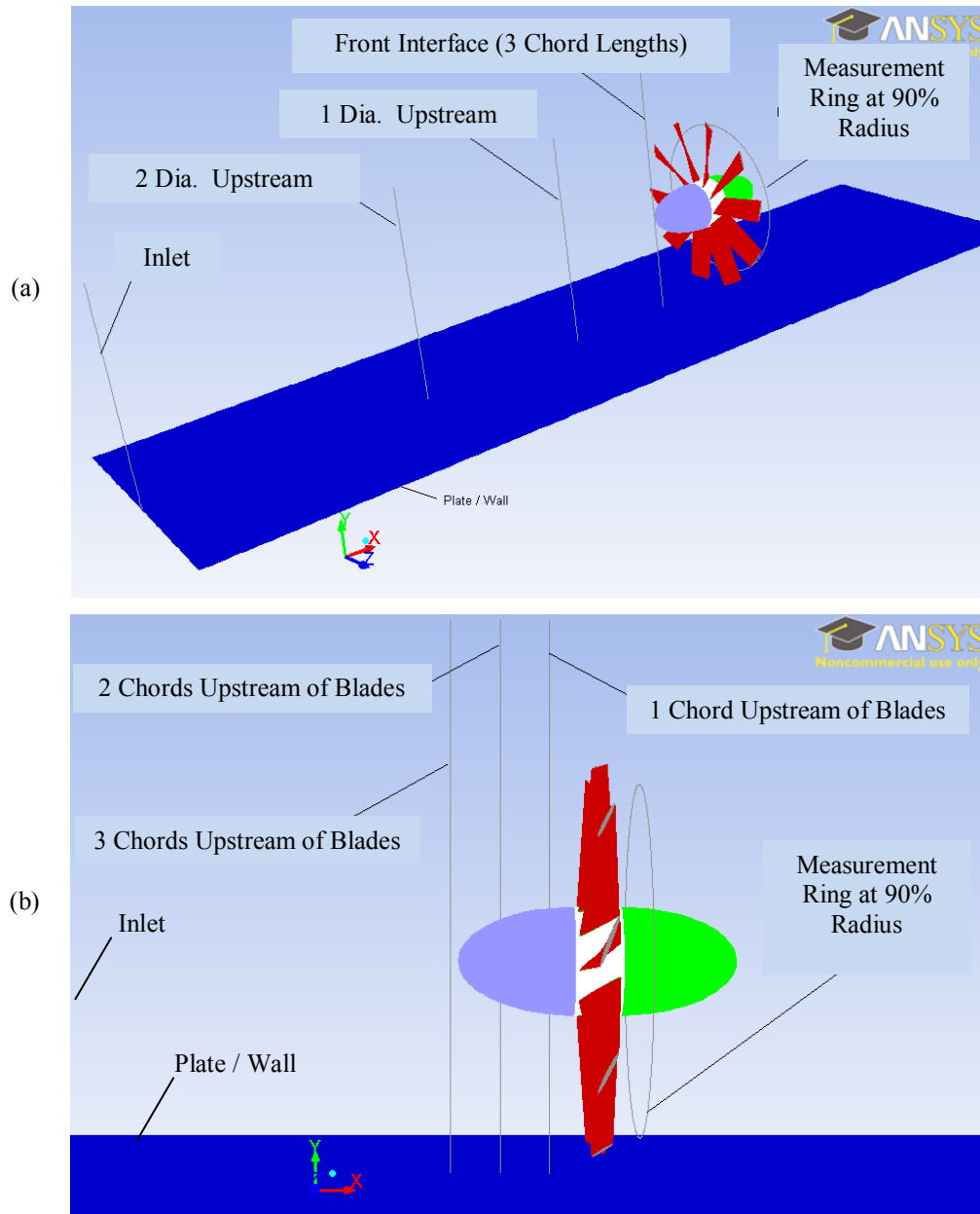


Figure 7.2 – Locations for Boundary Layer Plots

(a) Far Measurements
 (b) Near Measurements
 Boundary layer plots are generated over these lines. Also shown, is the 90% radius measurement ring where wake measurements are made.

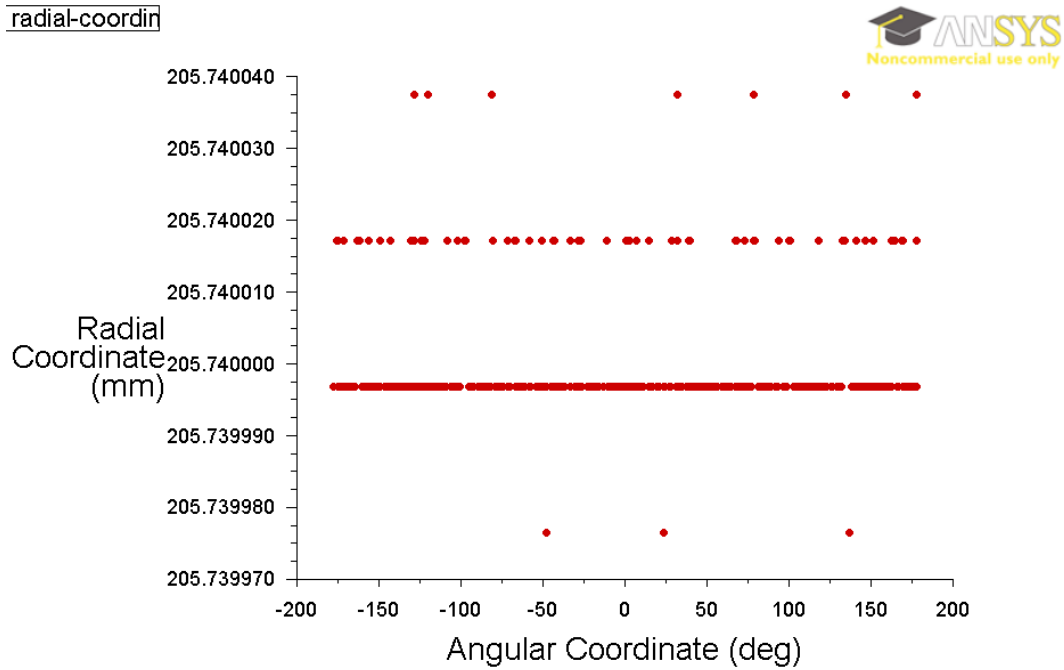


Figure 7.3 – Configuration 1: Node Radial Coordinates (90% Ring)

Configuration 1
Radial coordinates of nodes comprising 90% ring at experimental measurement plane

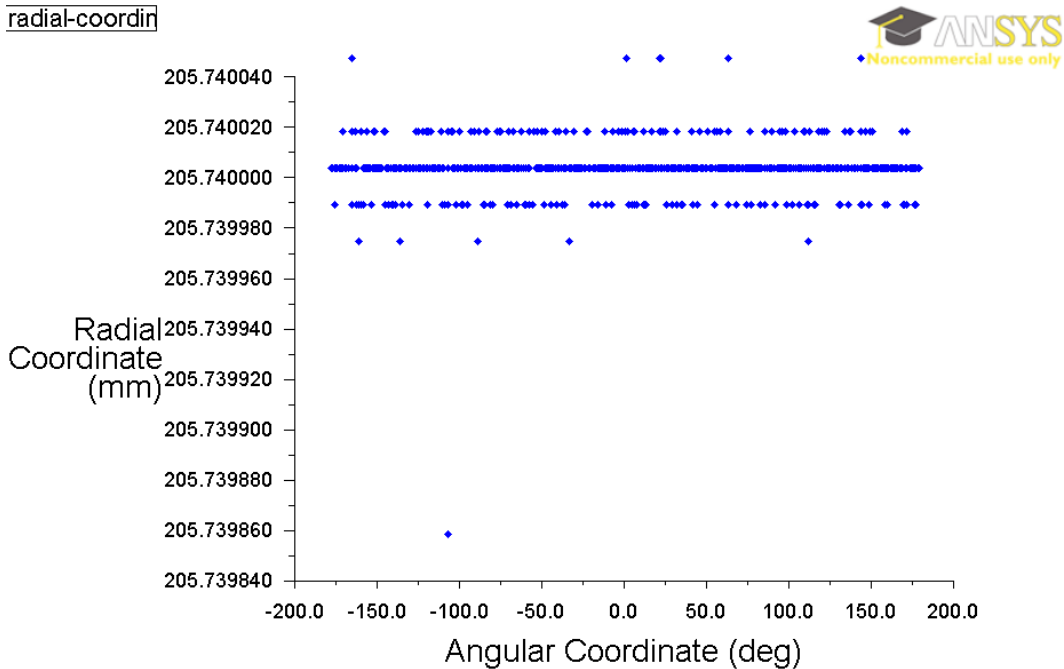


Figure 7.4 – Configuration 3: Node Radial Coordinates (90% Ring)

Configuration 3
Radial coordinates of nodes comprising 90% ring at experimental measurement plane

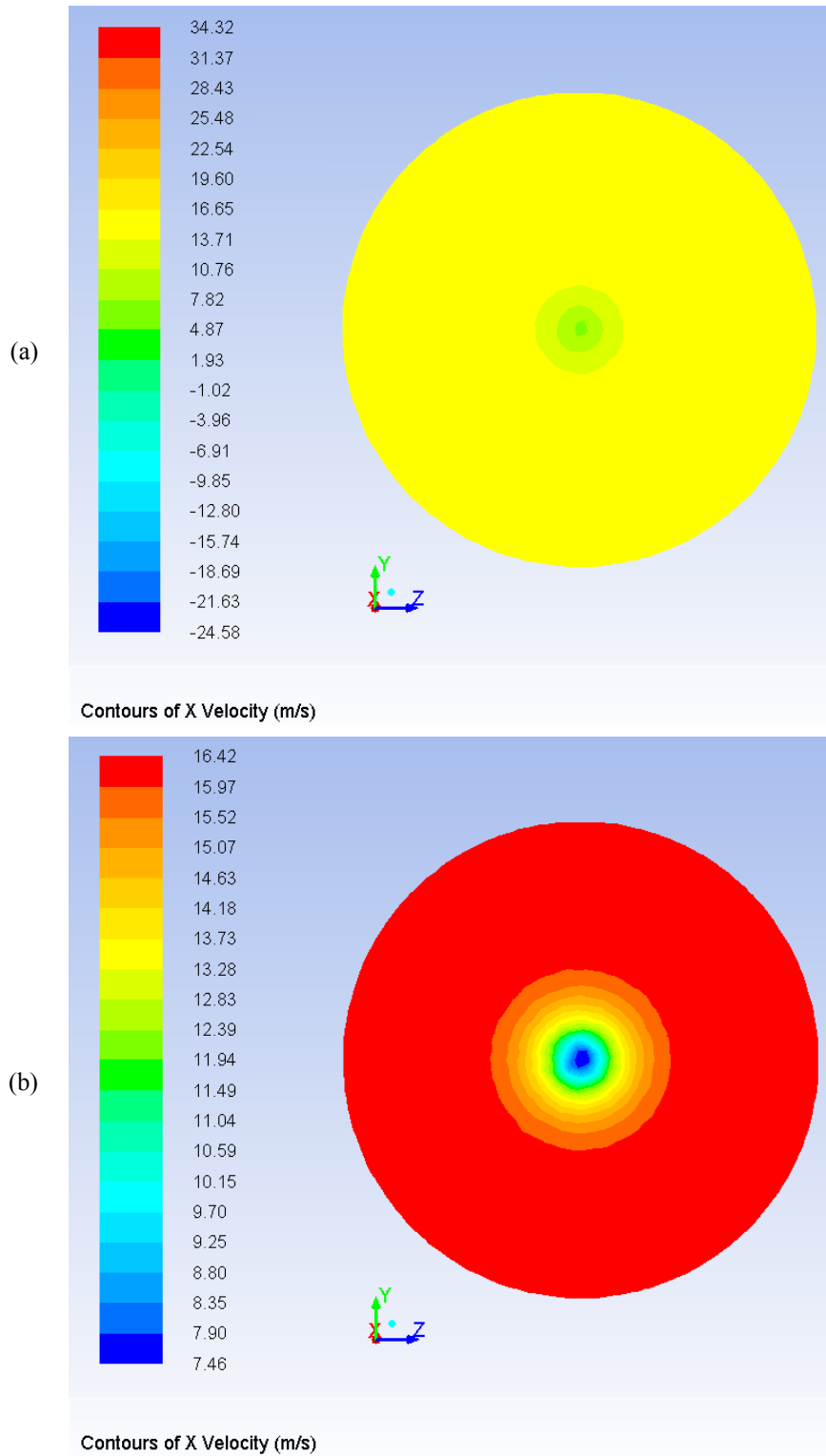


Figure 8.1 – Configuration 1: Axial Velocity Contour Plot at Front Interface

Configuration 1 Case of $J = 0.72$
 (a) Contour color map shown in global scale.
 (b) Contour color map shown in local scale.

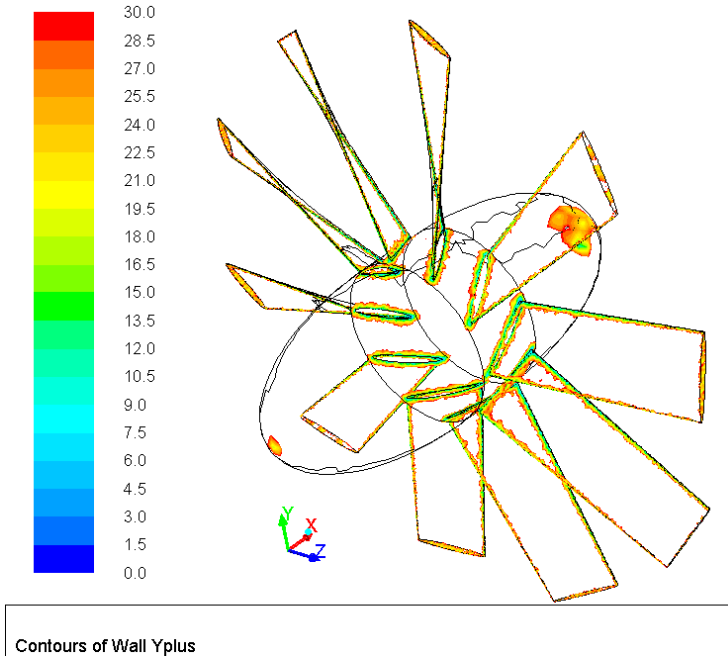


Figure 8.2 – Configuration 1: Wall Y-plus

Configuration 1 Case of $J = 0.79$
Regions with wall y^+ values below recommendation are shown. All other wall locations meet recommended values

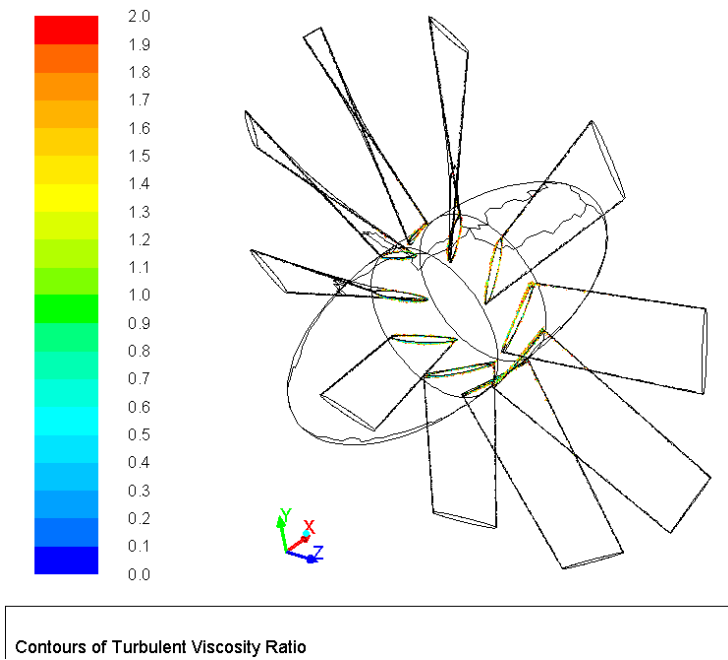


Figure 8.3 – Configuration 1: Turbulent Viscosity Ratio

Configuration 1 Case of $J = 0.79$
Regions with turbulent viscosity ratio below recommendation are shown. All other regions meet recommended values

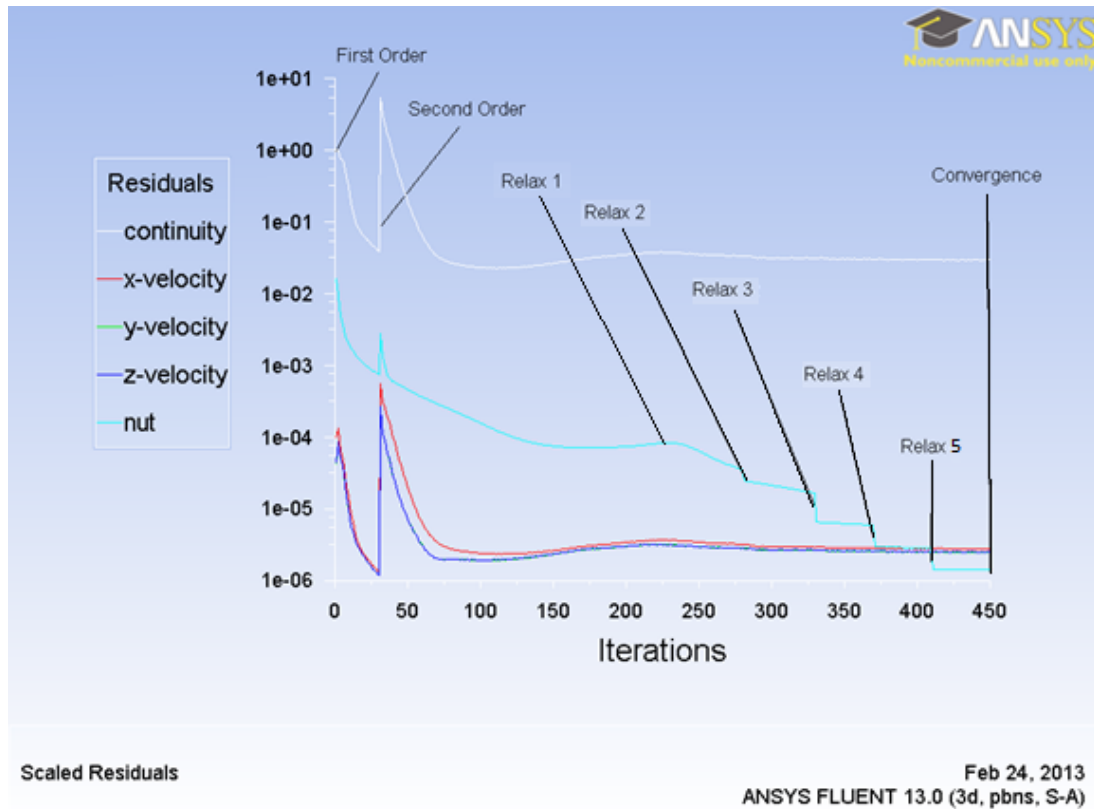


Figure 8.4 – Configuration 1: Globally Scaled Residual Plot

Configuration 1 Case of $J = 0.79$ Showing levels of order increments and under-relaxation factor decreases.

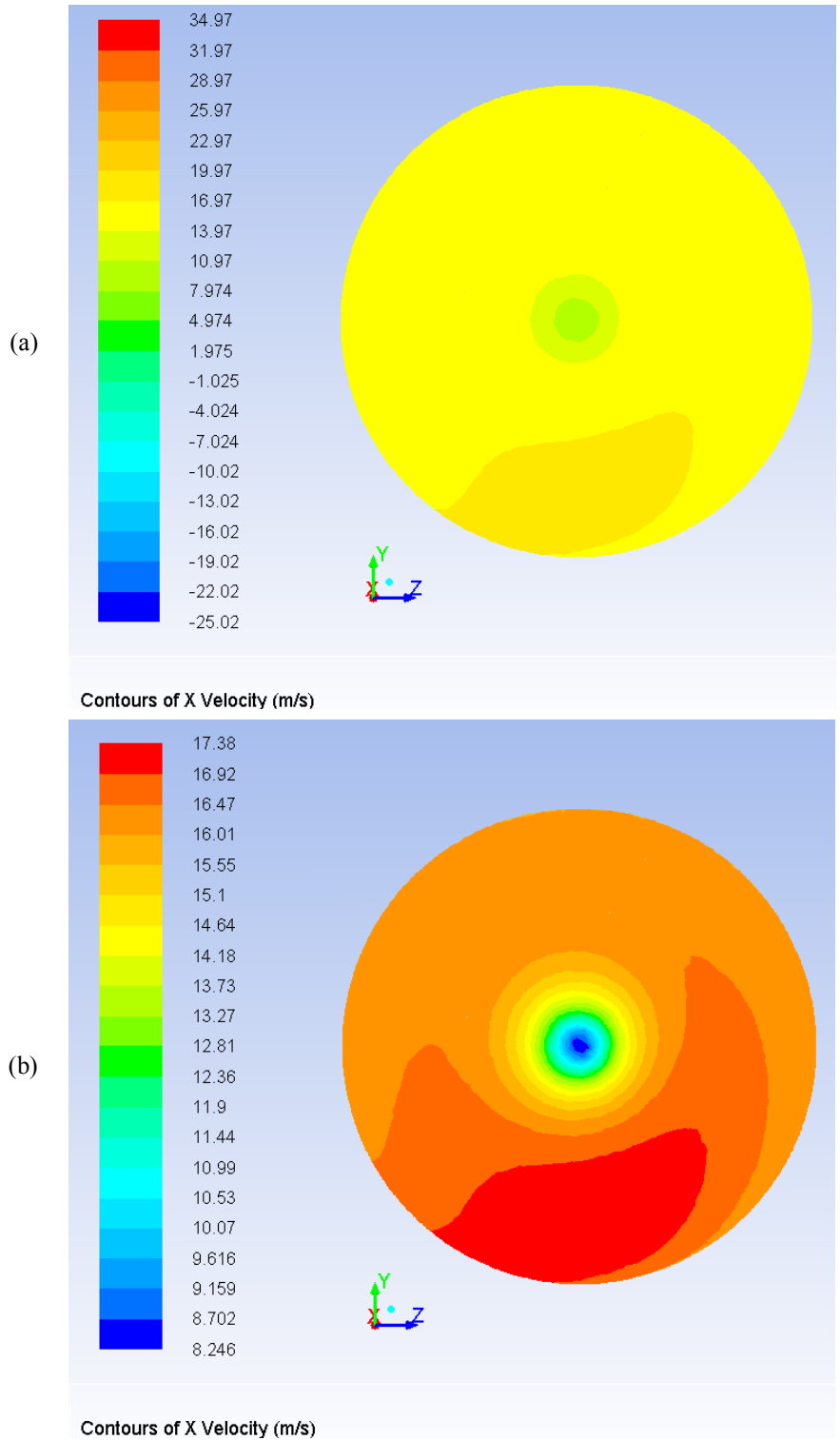
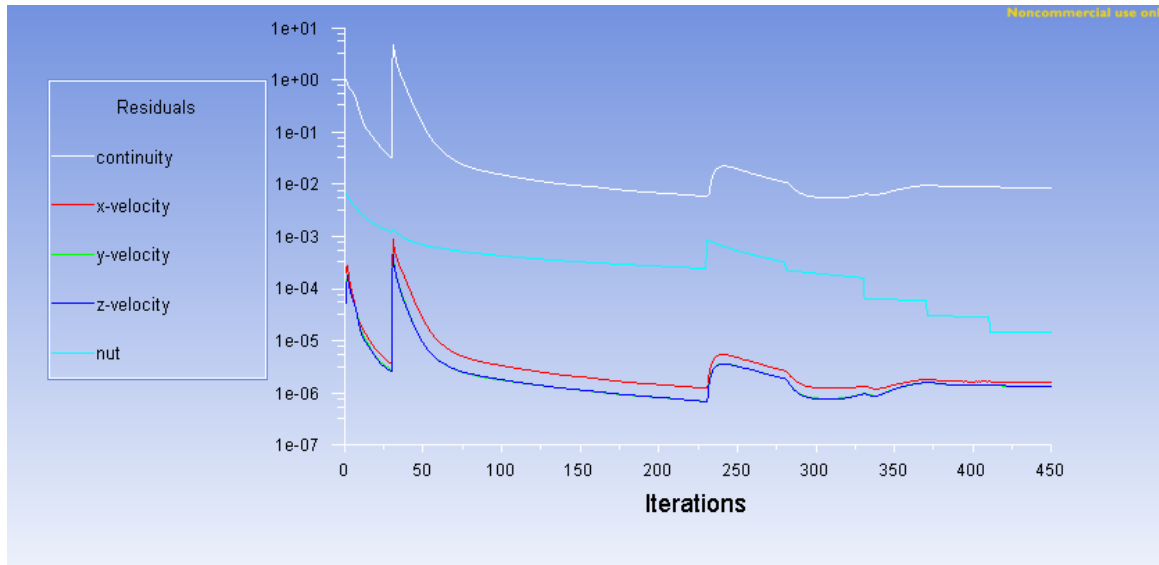


Figure 8.5 – Configuration 2: Axial Velocity Contour Plot at Front Interface

Configuration 2 Case of $J = 0.72$
 (a) Contour color map shown in global scale.
 (b) Contour color map shown in local scale.

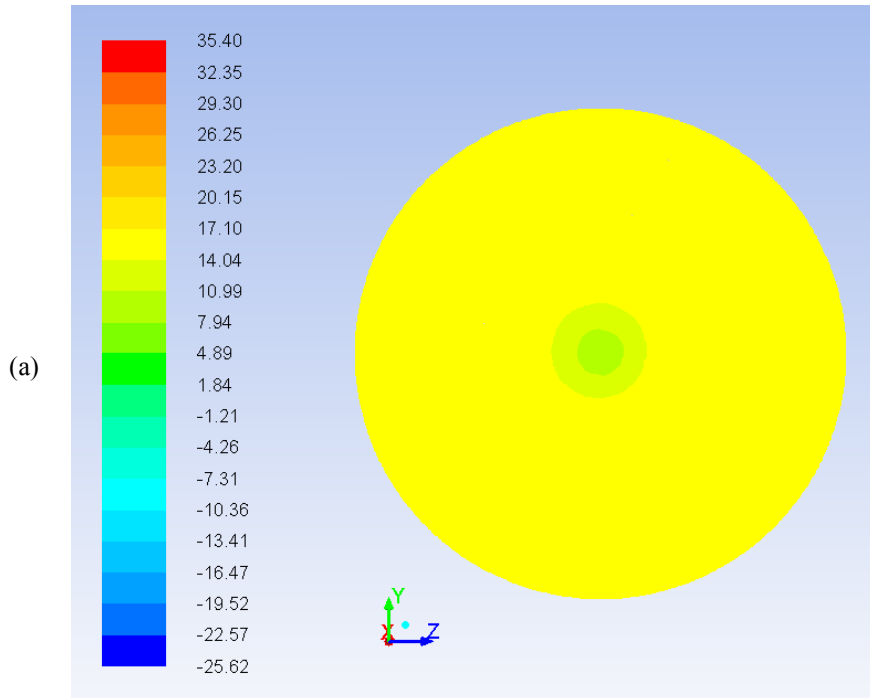


Scaled Residuals

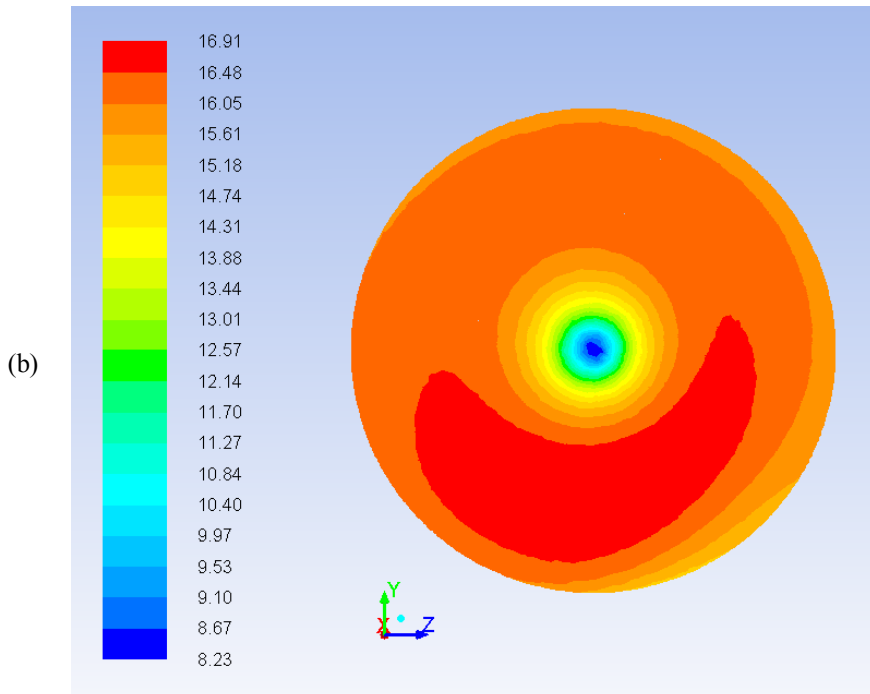
Feb 20, 2013
ANSYS FLUENT 13.0 (3d, pbns, S-A)

Figure 8.6 – Configuration 2: Globally Scaled Residual Plot

Configuration 2 Case of $J = 0.98$
Showing levels of order increments and under-relaxation factor decreases.



Contours of X Velocity (m/s)



Contours of X Velocity (m/s)

Figure 8.7 – Configuration 3: Axial Velocity Contour Plot at Front Interface

Configuration 3 Case of $J = 0.72$
 (a) Contour color map shown in global scale.
 (b) Contour color map shown in local scale.

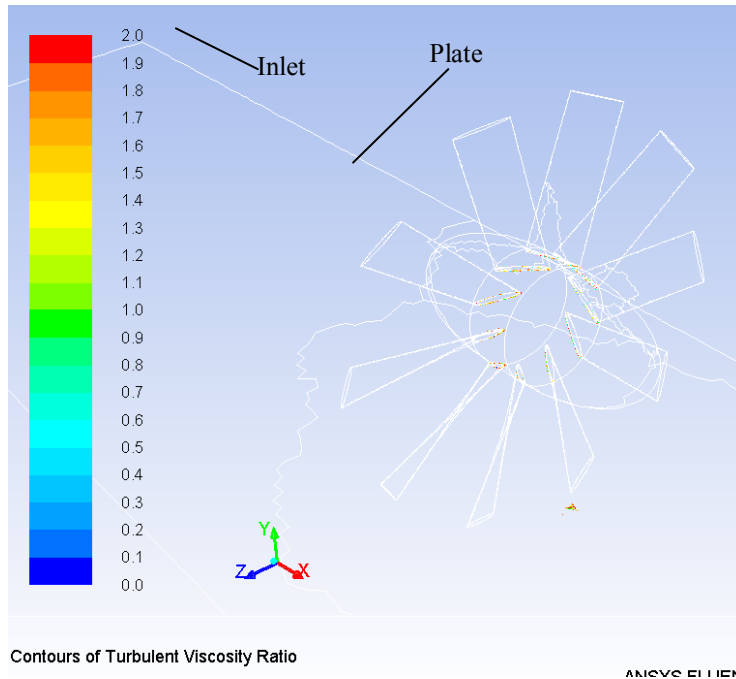


Figure 8.8 – Configuration 3: Turbulent Viscosity Ratio

Configuration 3 Case of $J = 0.79$
 Regions with turbulent viscosity ratio below recommendation are shown. All other regions meet recommended values

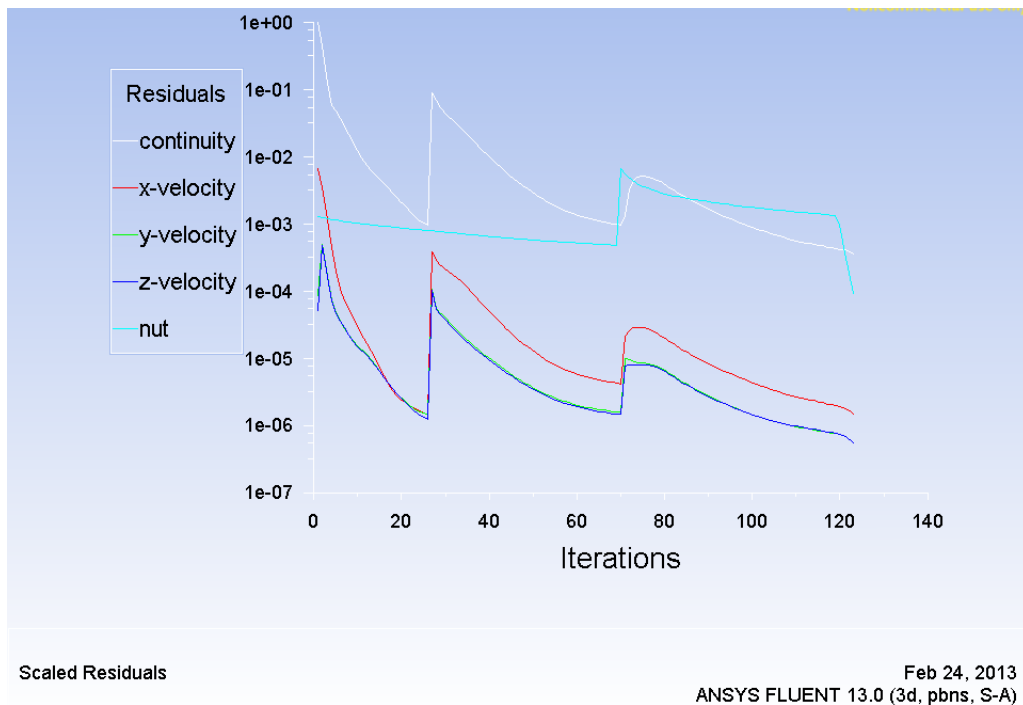


Figure 8.9 – Configuration 3: Globally Scaled Residual Plot

Configuration 3 case of $J = 1.44$
 Showing levels of order increments and under-relaxation factor decreases.

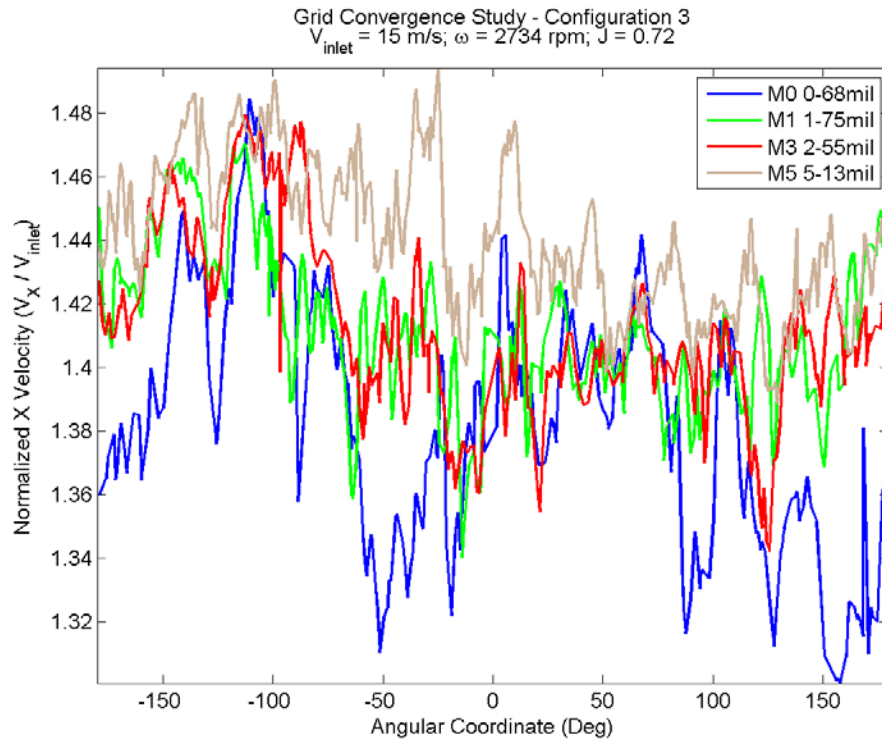


Figure 8.10 – Grid Ind. Study Results for $J = 0.72$ (Wake)

Configuration 3

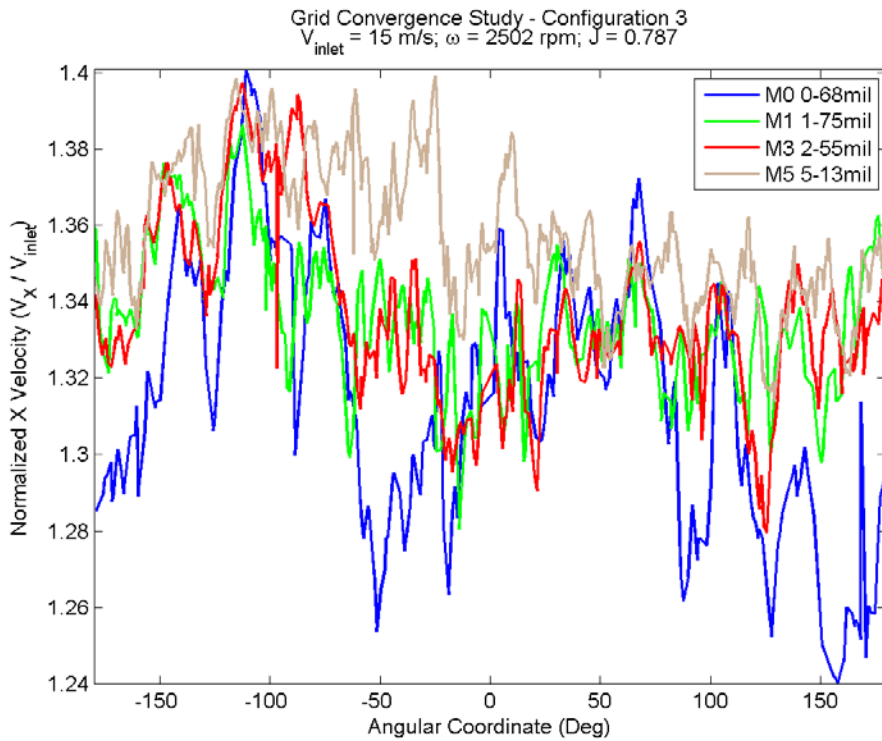


Figure 8.11 – Grid Ind. Study Results for $J = 0.79$ (Wake)

Configuration 3

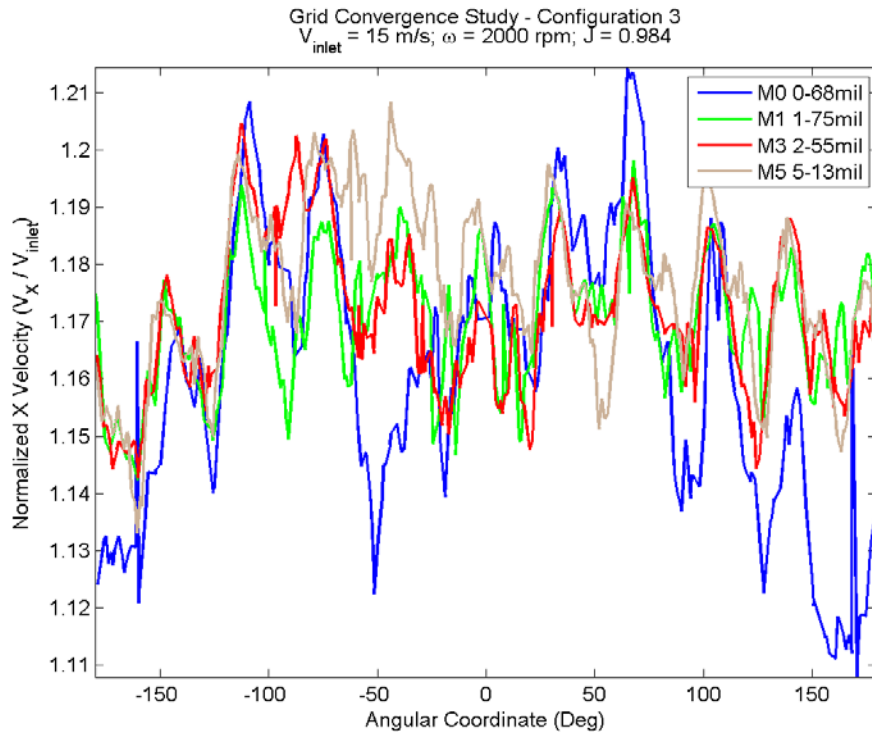


Figure 8.12 – Grid Ind. Study Results for $J = 0.98$ (Wake)

Configuration 3

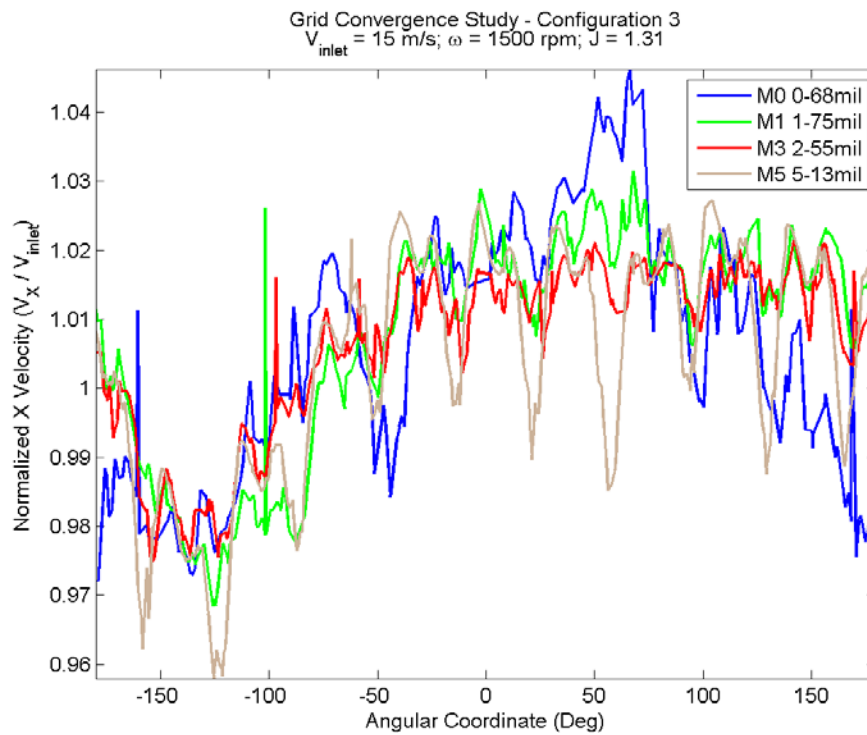


Figure 8.13 – Grid Ind. Study Results for $J = 1.31$ (Wake)

Configuration 3

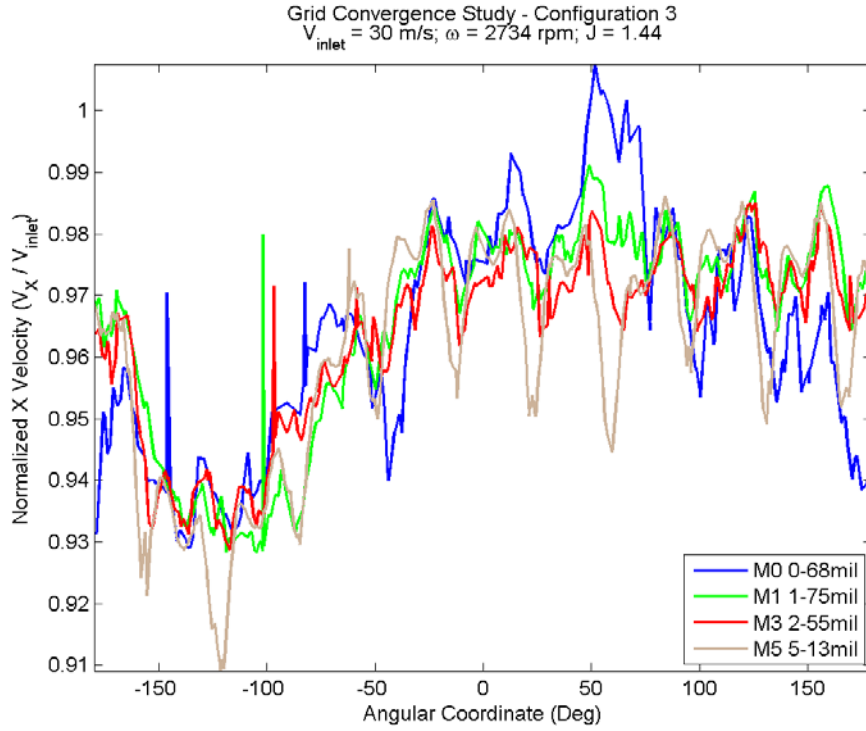


Figure 8.14 – Grid Ind. Study Results for $J = 1.44$ (Wake)

Configuration 3

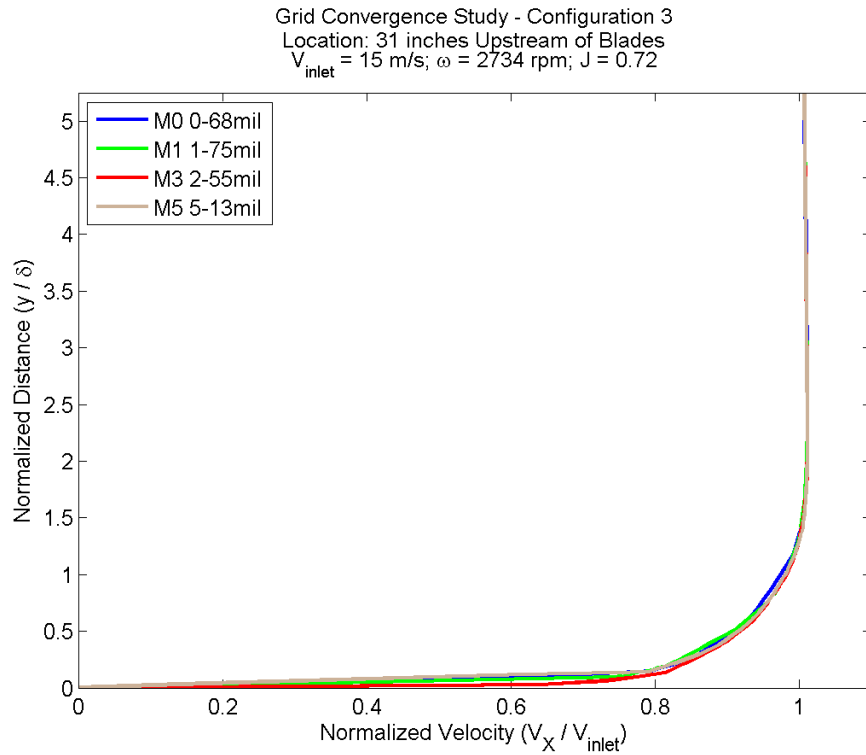


Figure 8.15 – Grid Ind. Study Results for $J = 0.72$ (BL)

Configuration 3

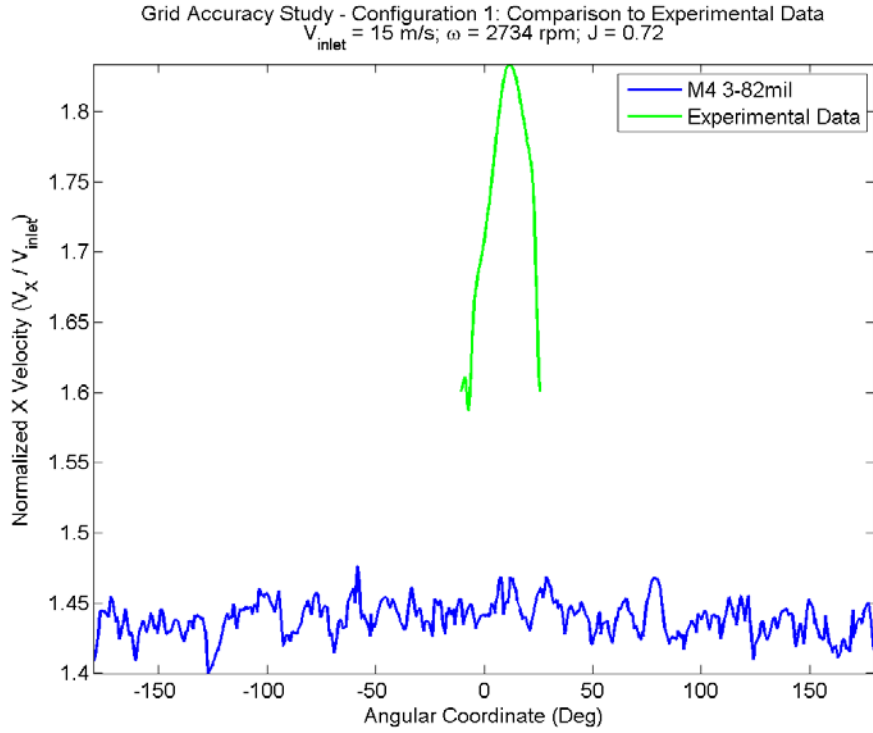


Figure 8.16 – Configuration 1: CFD Validation for $J = 0.72$ (Wake)

Configuration 1

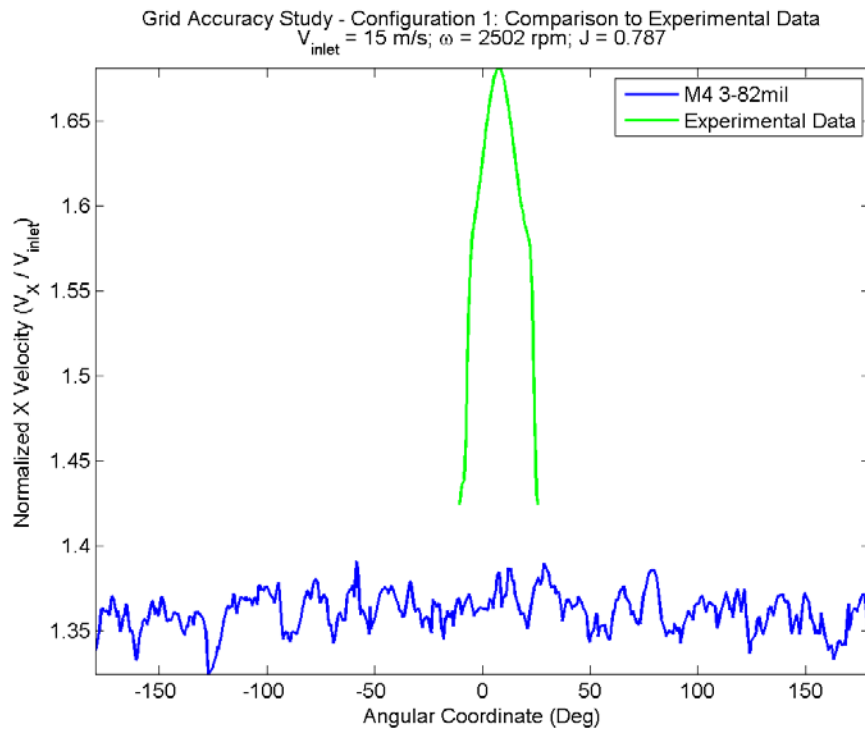


Figure 8.17 – Configuration 1: CFD Validation for $J = 0.79$ (Wake)

Configuration 1

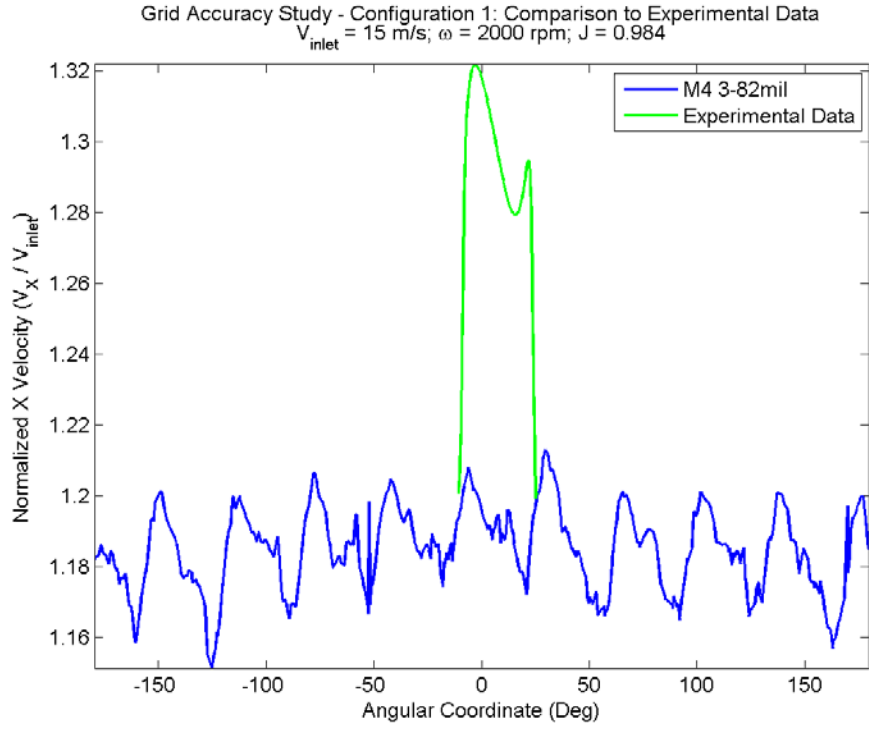


Figure 8.18 – Configuration 1: CFD Validation for $J = 0.98$ (Wake)

Configuration 1

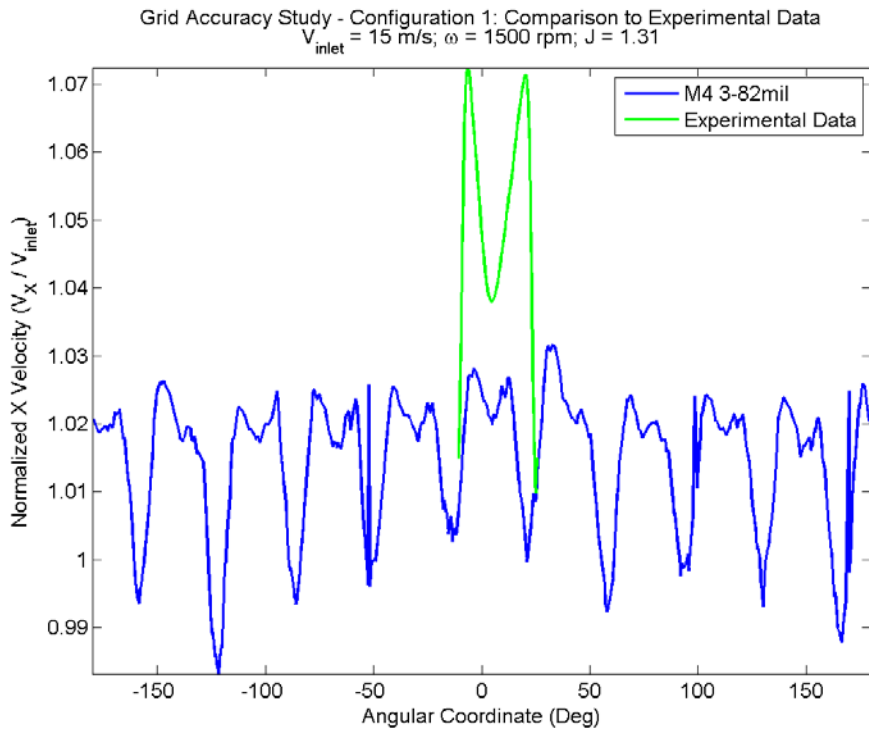


Figure 8.19 – Configuration 1: CFD Validation for $J = 1.31$ (Wake)

Configuration 1

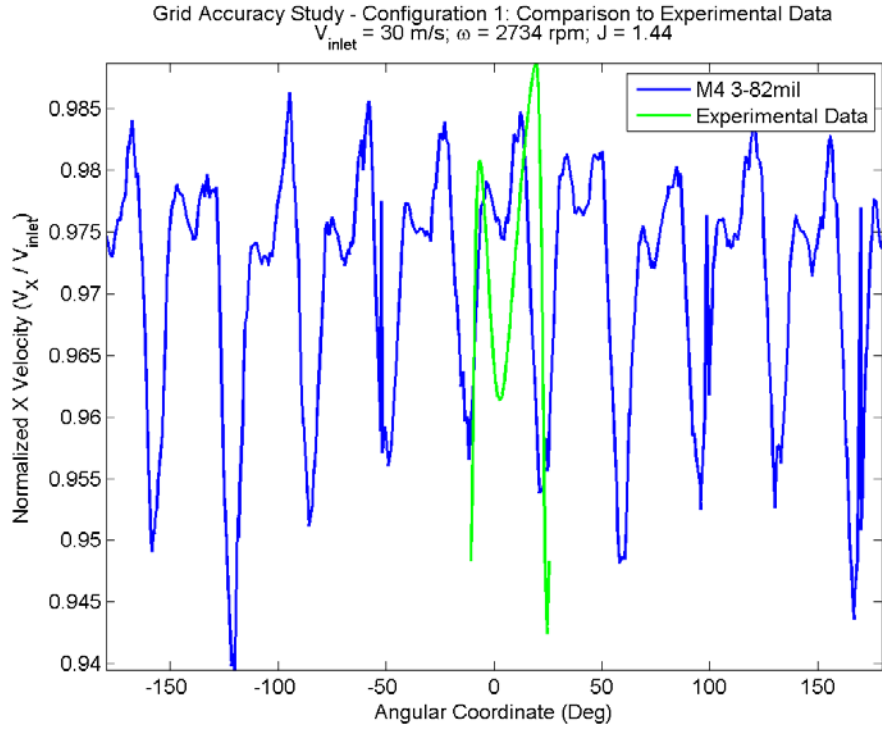


Figure 8.20 – Configuration 1: CFD Validation for $J = 1.44$ (Wake)

Configuration 1

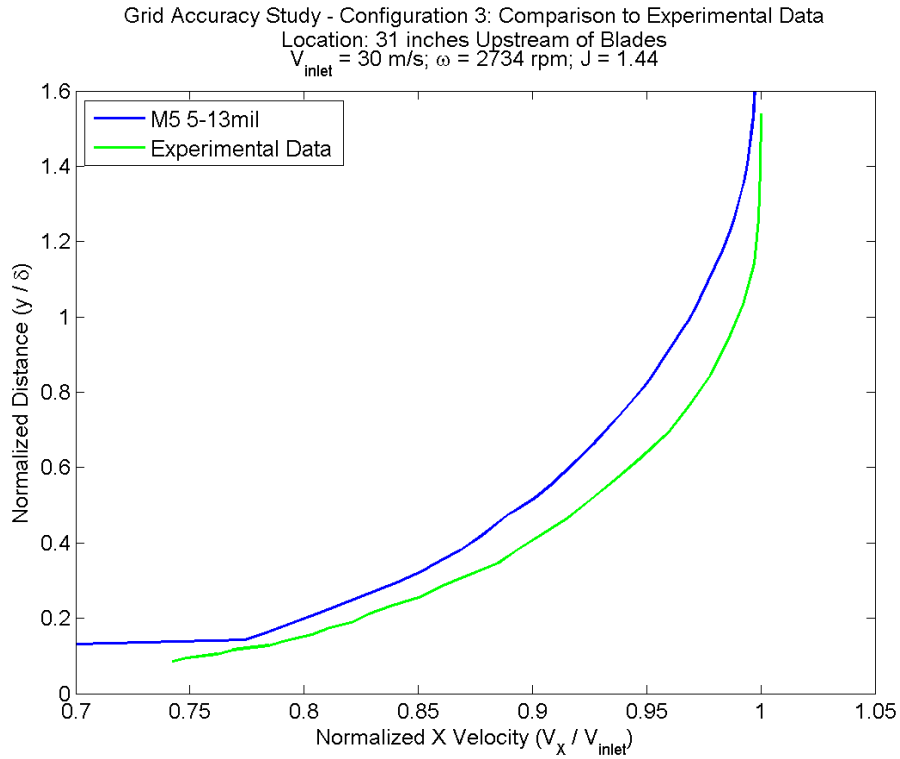


Figure 8.21 – Configuration 3: CFD Validation for $J = 1.44$ (BL)

Configuration 3

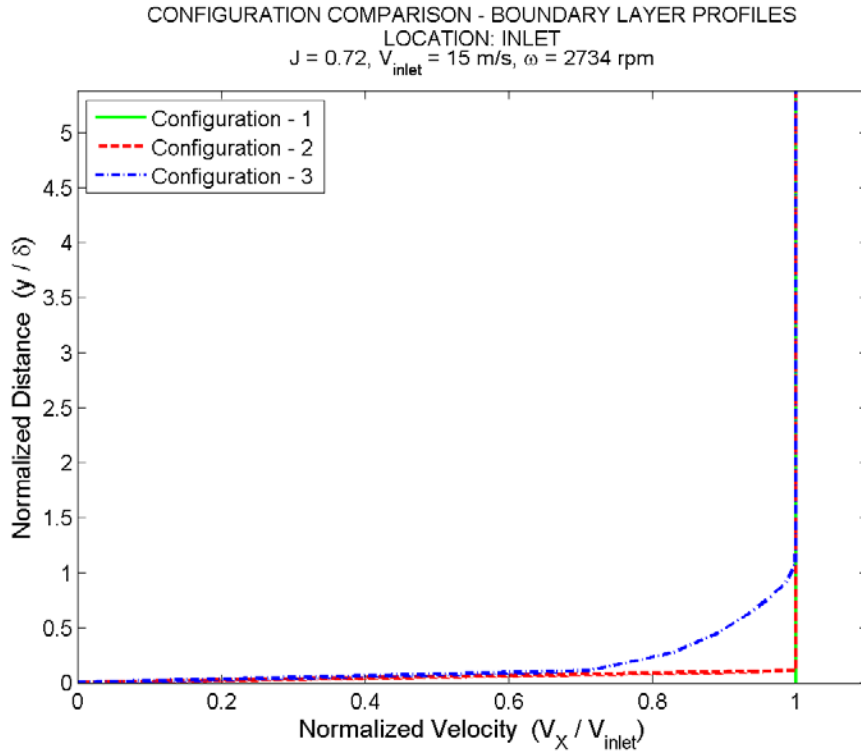


Figure 8.22 – All Configurations BL Data at Inlet

All cases of $J = 0.72$

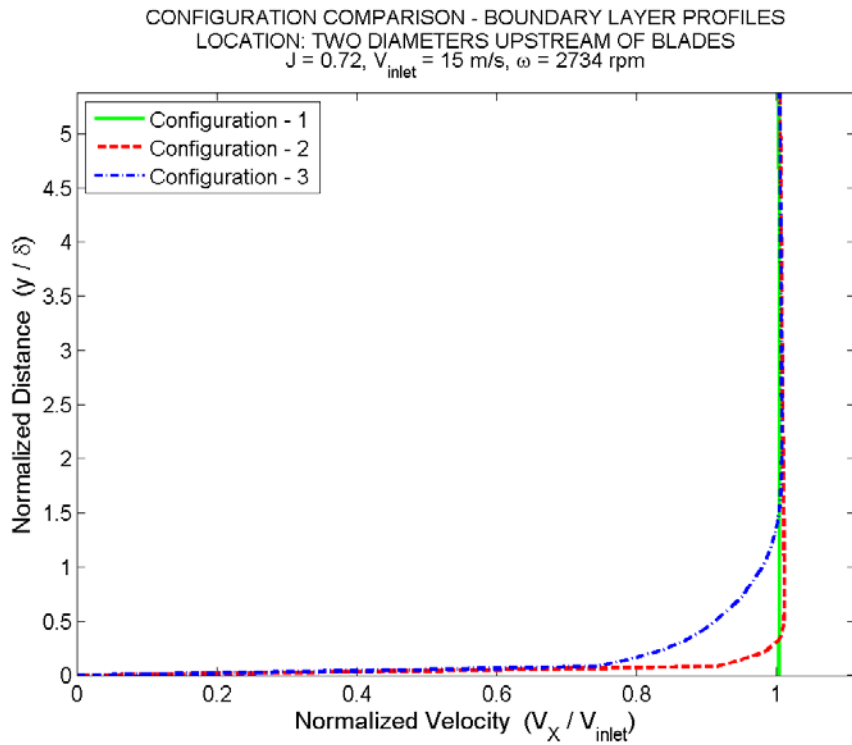


Figure 8.23 – All Configurations BL Data at 2 Diameters Upstream

All cases of $J = 0.72$

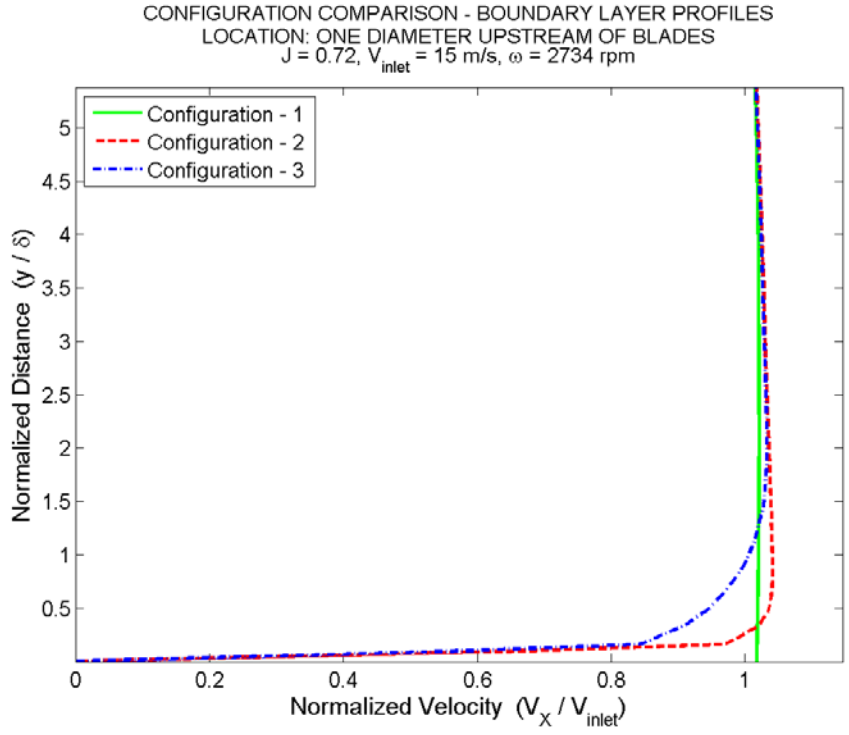


Figure 8.24 – All Configurations BL Data at 1 Diameter Upstream

All cases of $J = 0.72$

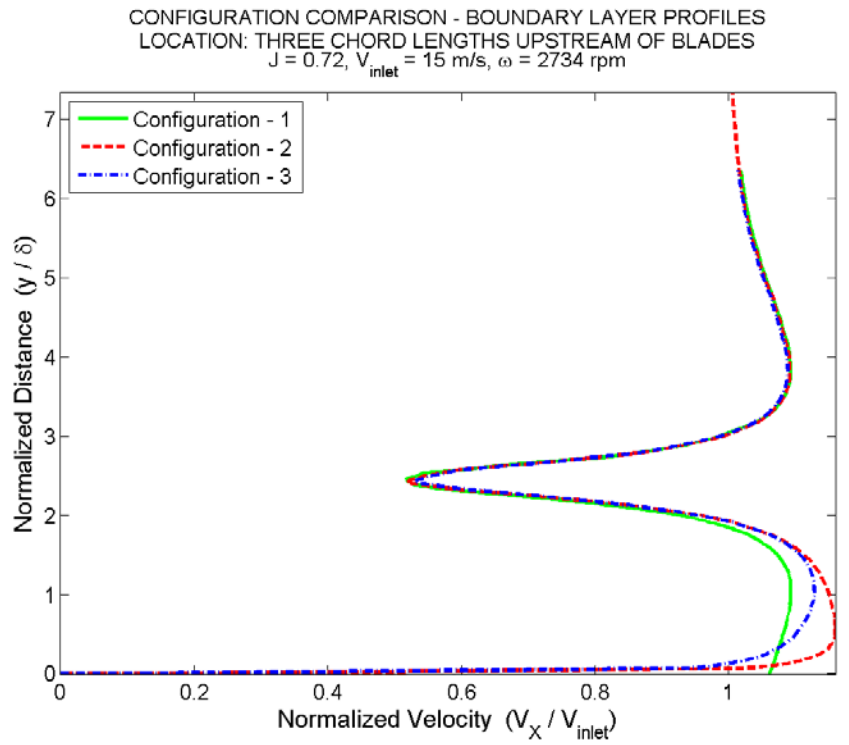


Figure 8.25 – All Configurations BL Data at 3 Chords Upstream

All cases of $J = 0.72$

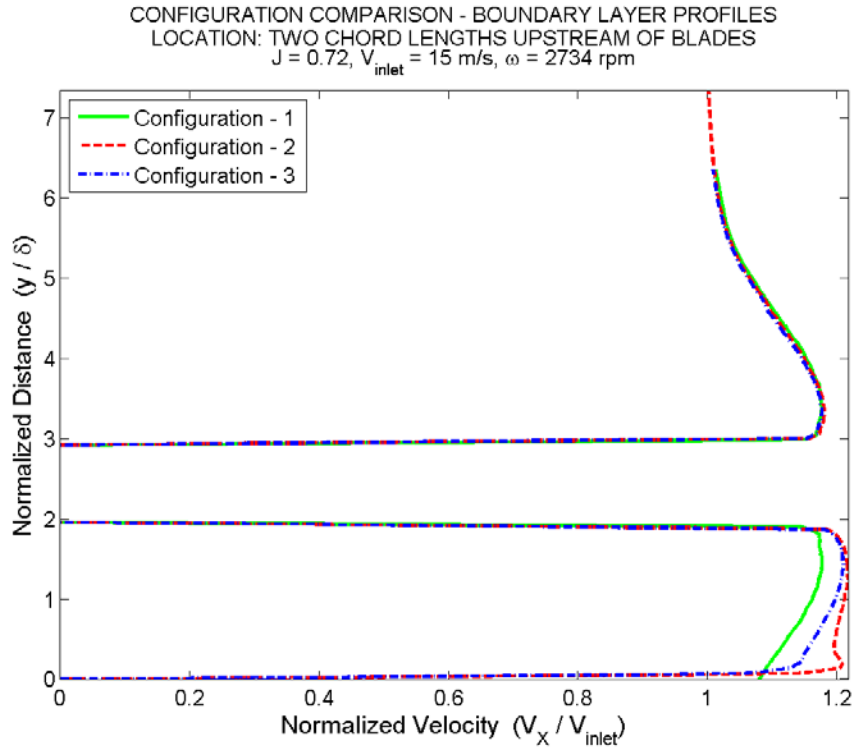


Figure 8.26 – All Configurations BL Data at 2 Chords Upstream

All cases of $J = 0.72$

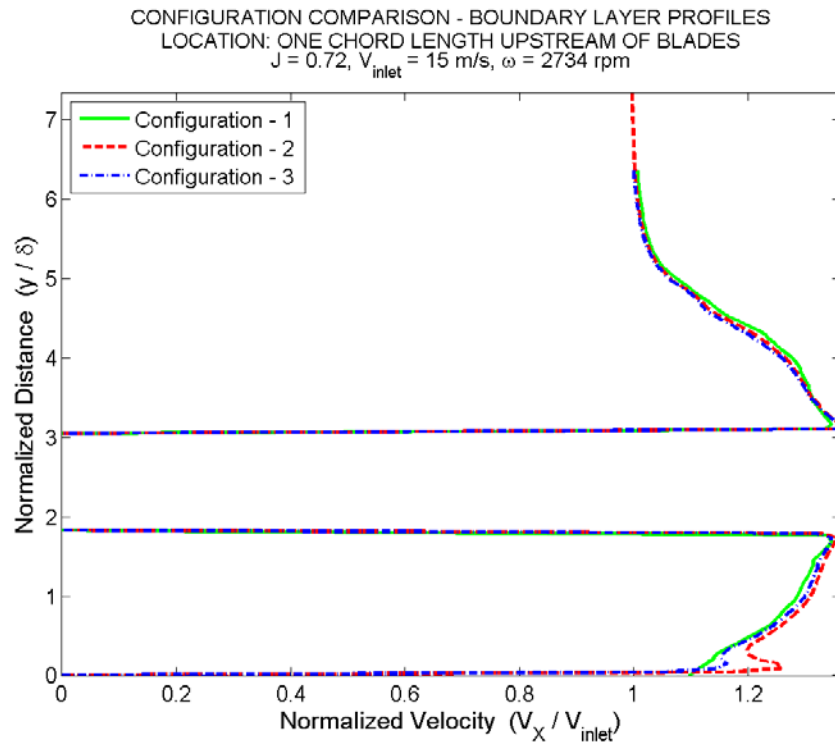


Figure 8.27 – All Configurations BL Data at 1 Chord Upstream

All cases of $J = 0.72$

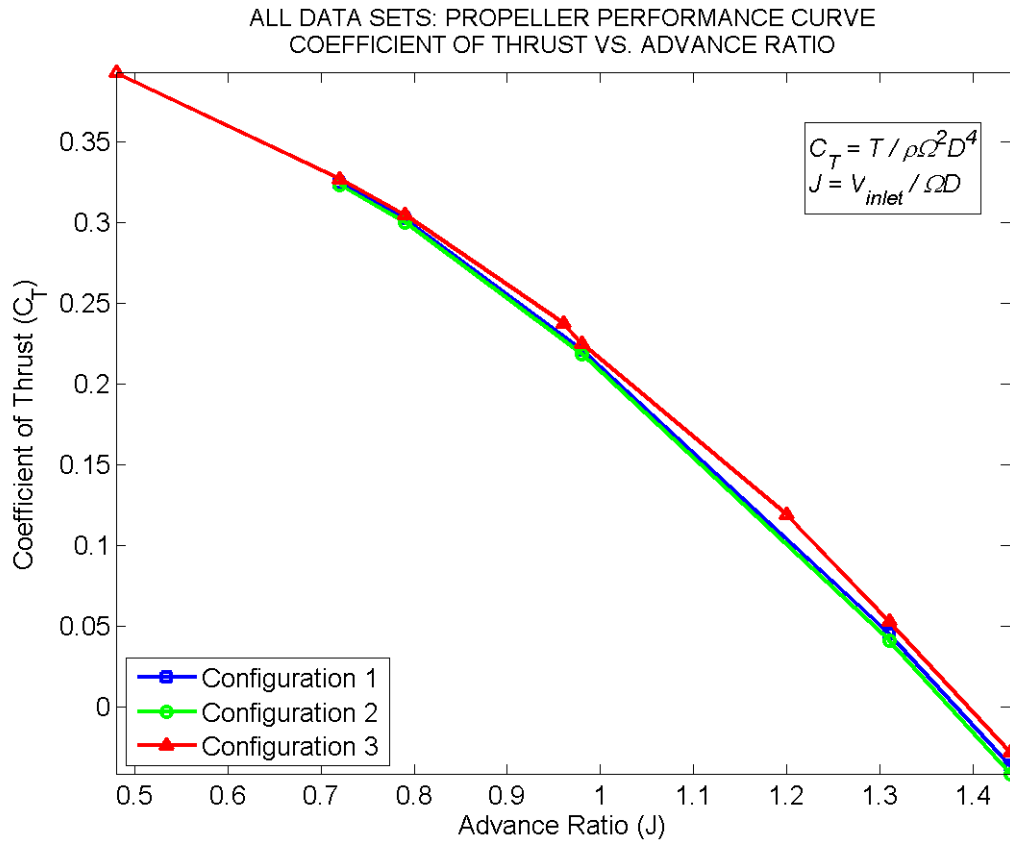


Figure 8.28 – Coefficient of Thrust vs. Advance Ratio

All configurations and all data sets. Acoustic data set is represented with configuration 3.

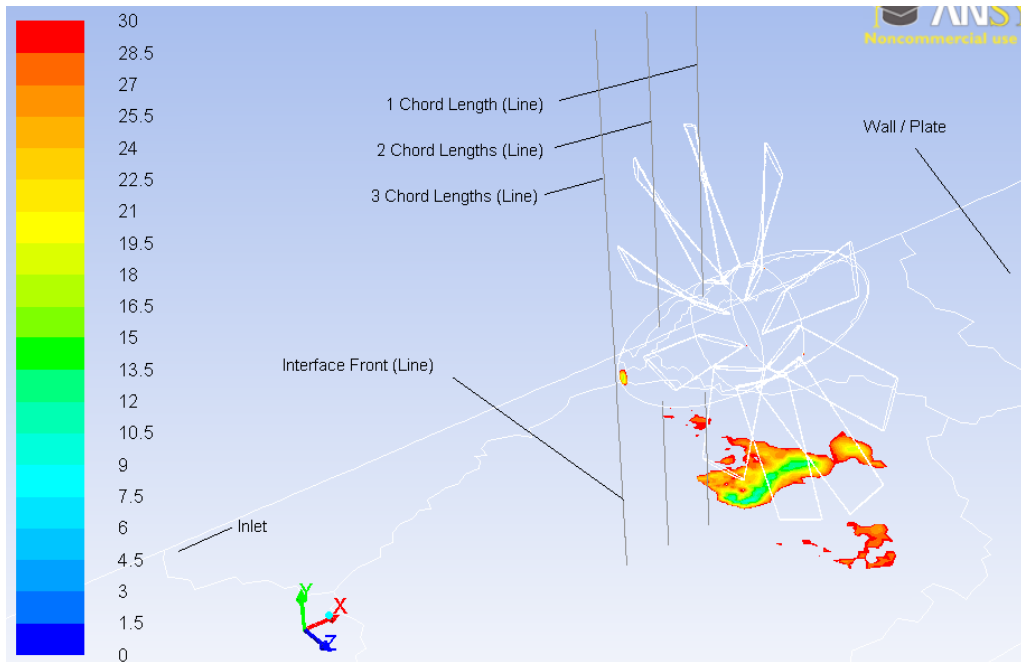


Figure 8.29 – Acoustic: Wall Y-plus ($J = 0.48$)

Configuration 3 Case of $J = 0.48$
 Regions with wall y^+ values below recommendation are shown. All other wall locations meet recommended values

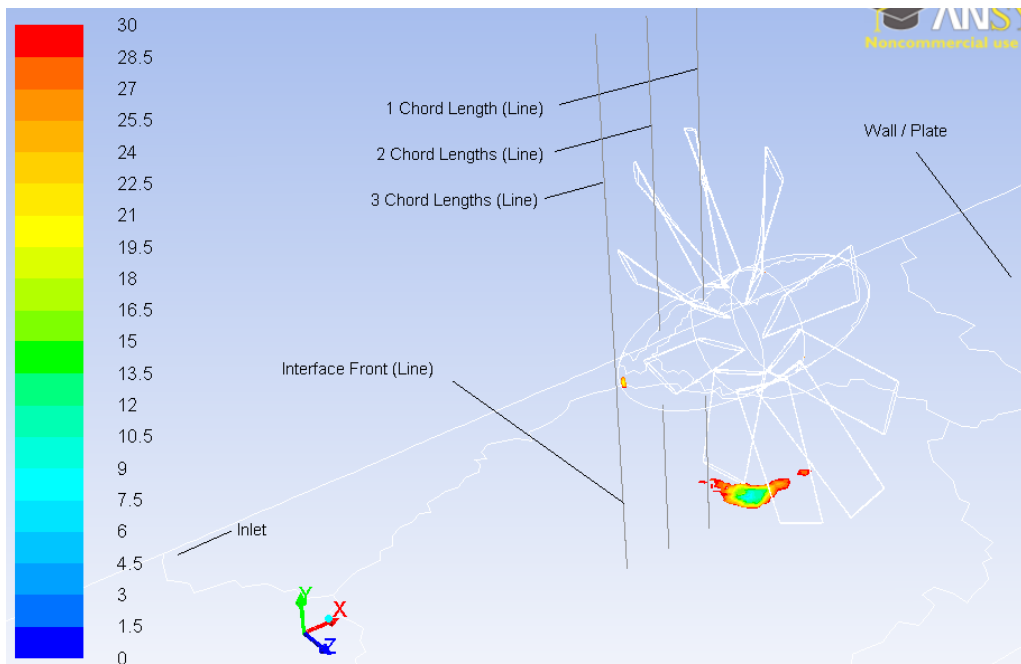


Figure 8.30 – Acoustic: Wall Y-plus ($J = 0.72$)

Configuration 3 Case of $J = 0.72$
 Regions with wall y^+ values below recommendation are shown. All other wall locations meet recommended values

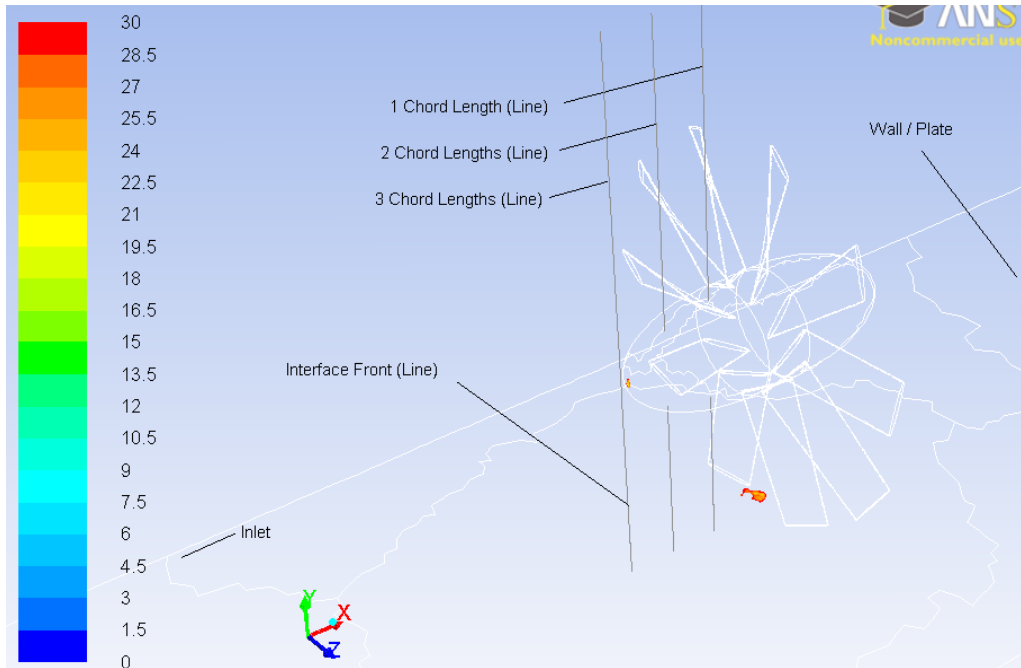


Figure 8.31 – Acoustic: Wall Y-plus ($J = 0.96$)

Configuration 3 Case of $J = 0.96$
 Regions with wall y^+ values below recommendation are shown. All other wall locations meet recommended values

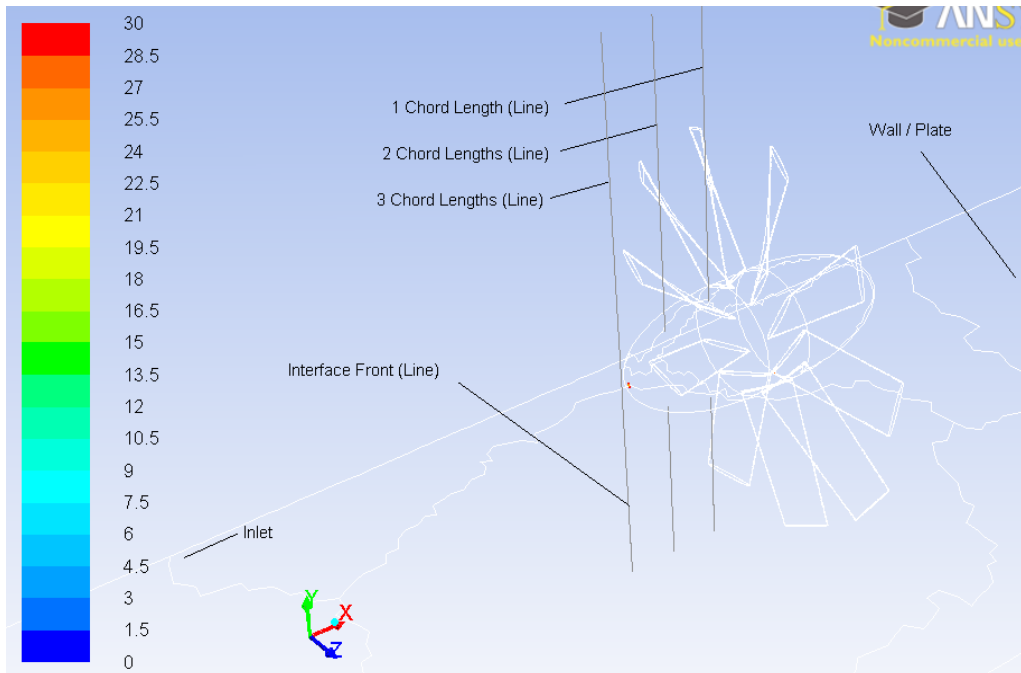


Figure 8.32 – Acoustic: Wall Y-plus ($J = 1.20$)

Configuration 3 Case of $J = 1.20$
 Regions with wall y^+ values below recommendation are shown. All other wall locations meet recommended values

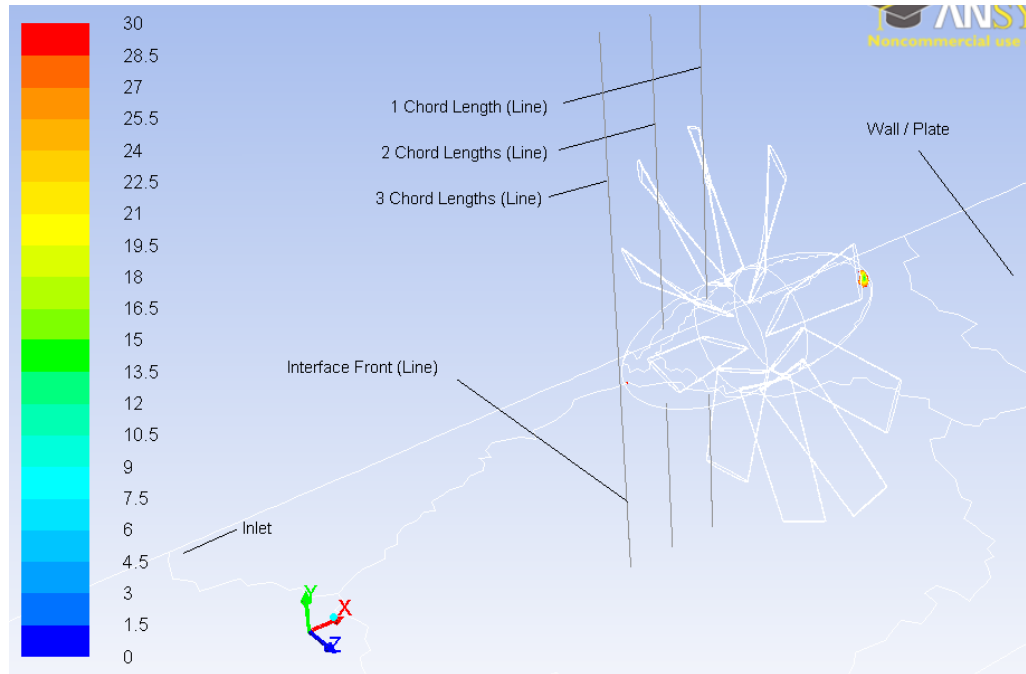


Figure 8.33 – Acoustic: Wall Y-plus ($J = 1.44$)

Configuration 3 Case of $J = 1.44$
 Regions with wall y^+ values below recommendation are shown. All other wall locations meet recommended values

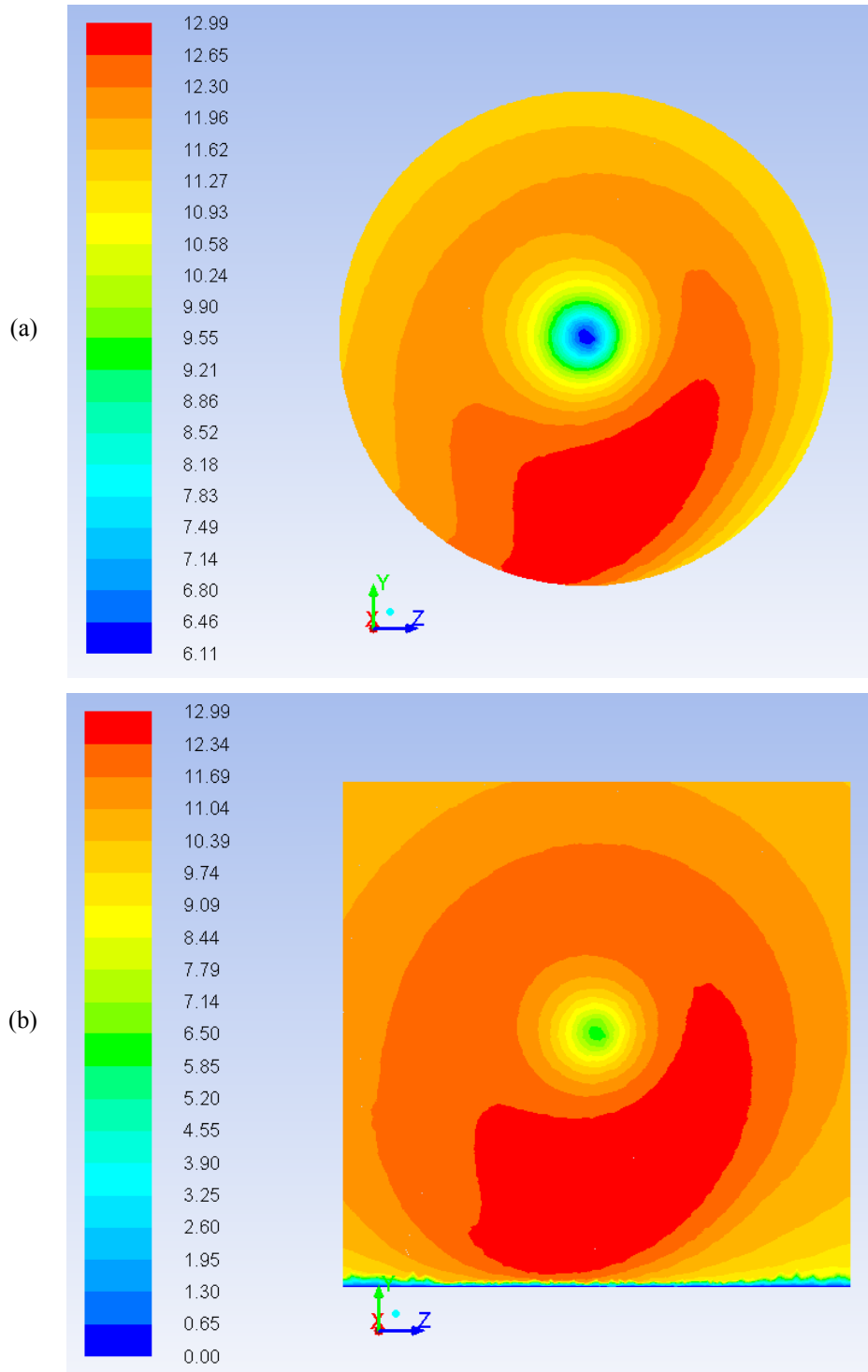


Figure 8.34 – Acoustic: Axial Velocity Contour Plot at Front Interface ($J = 0.48$)

Configuration 3 Case of $J = 0.48$
 (a) Contour plot showing interface.
 (b) Contour showing interface and boundary layer.

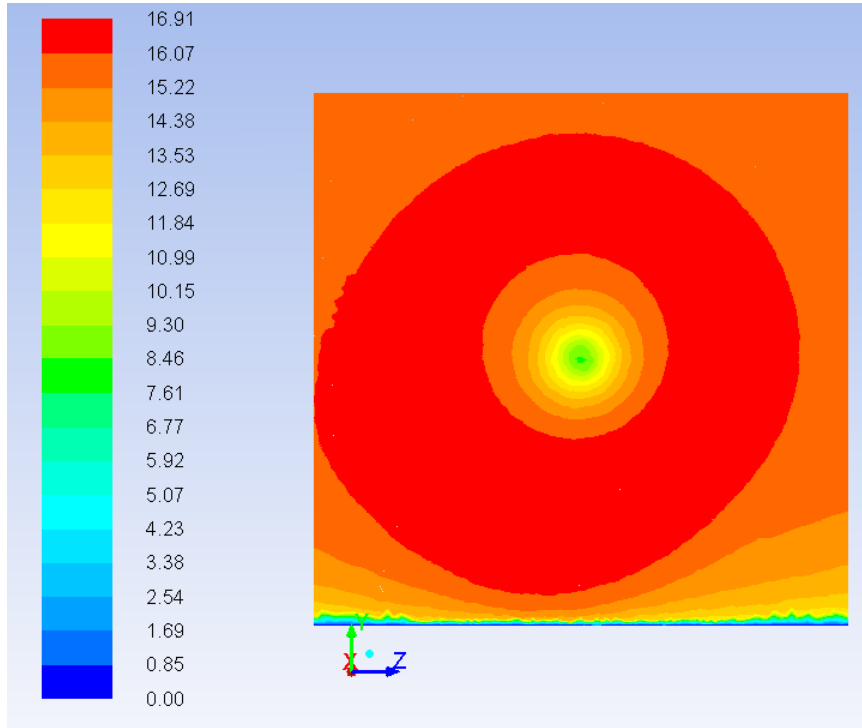


Figure 8.35 – Acoustic: Axial Velocity Contour Plot at Front Interface ($J = 0.72$)

Configuration 3 Case of $J = 0.72$
 Contour showing interface and boundary layer.
 Interface only plot is shown in Figure 8.7 (b)

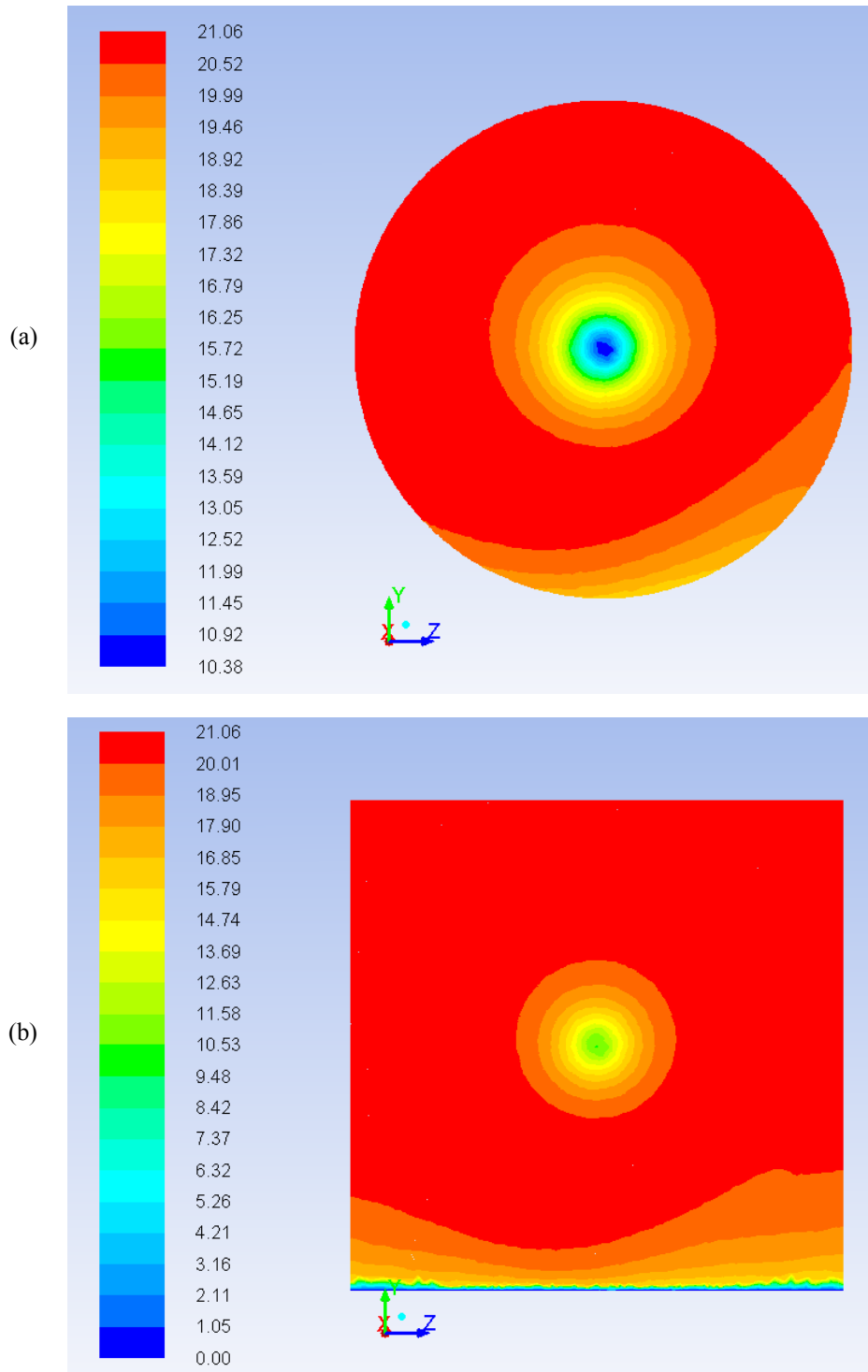


Figure 8.36 – Acoustic: Axial Velocity Contour Plot at Front Interface ($J = 0.96$)

Configuration 3 Case of $J = 0.96$
 (a) Contour plot showing interface.
 (b) Contour showing interface and boundary layer.

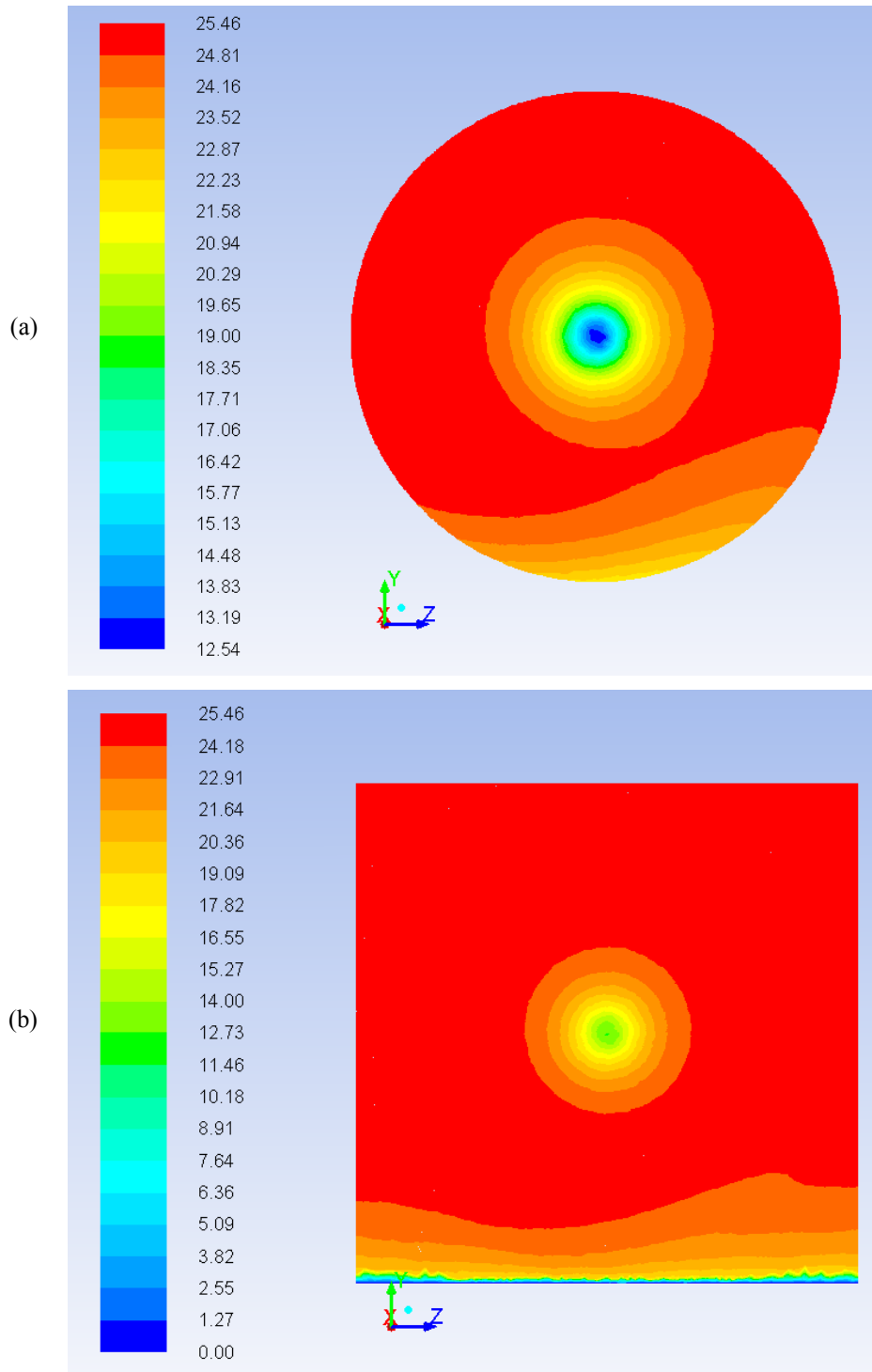


Figure 8.37 – Acoustic: Axial Velocity Contour Plot at Front Interface ($J = 1.20$)

Configuration 3 Case of $J = 1.20$
 (a) Contour plot showing interface.
 (b) Contour showing interface and boundary layer.

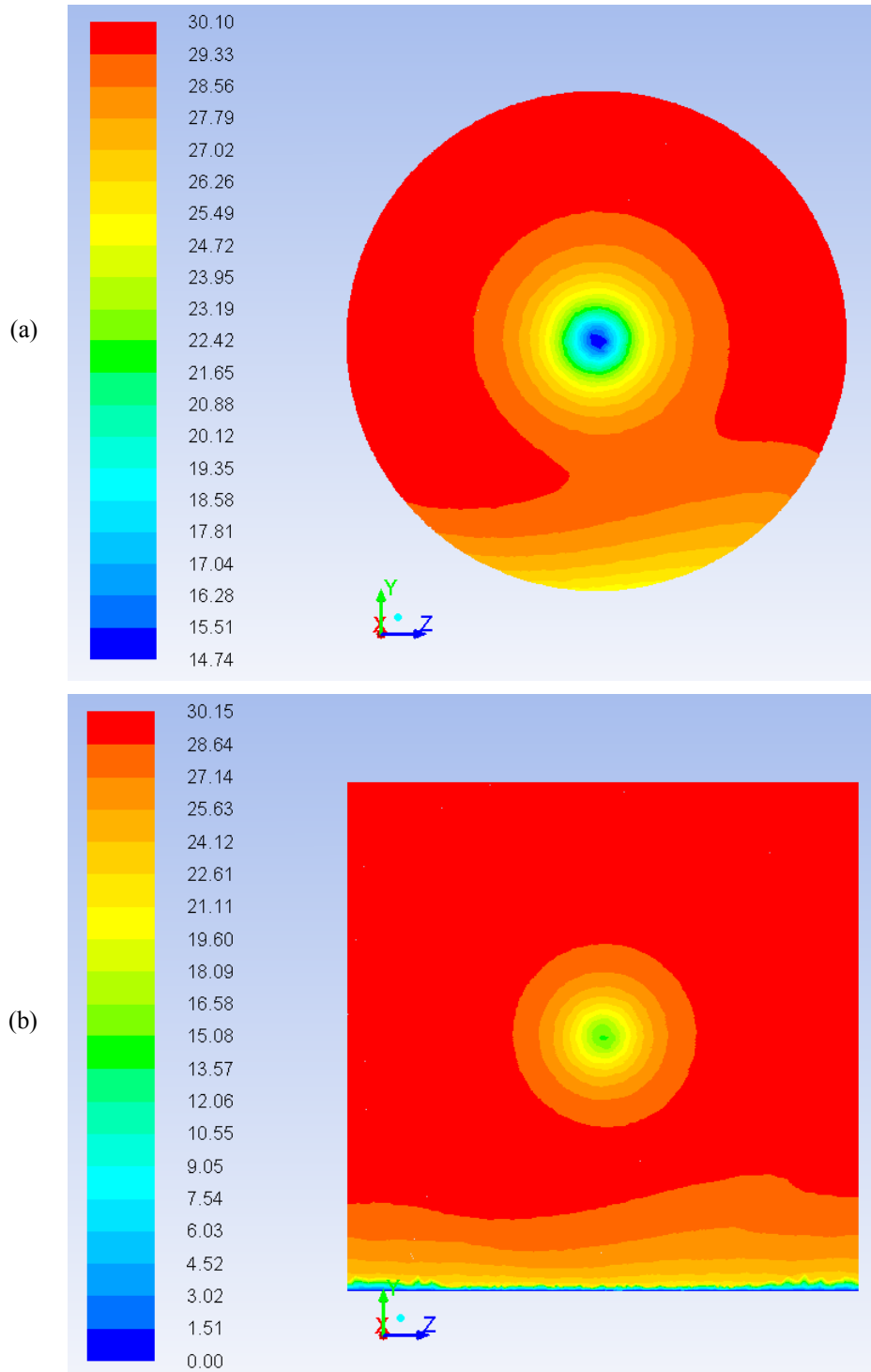


Figure 8.38 – Acoustic: Axial Velocity Contour Plot at Front Interface ($J = 1.44$)

Configuration 3 Case of $J = 1.44$
 (a) Contour plot showing interface.
 (b) Contour showing interface and boundary layer.

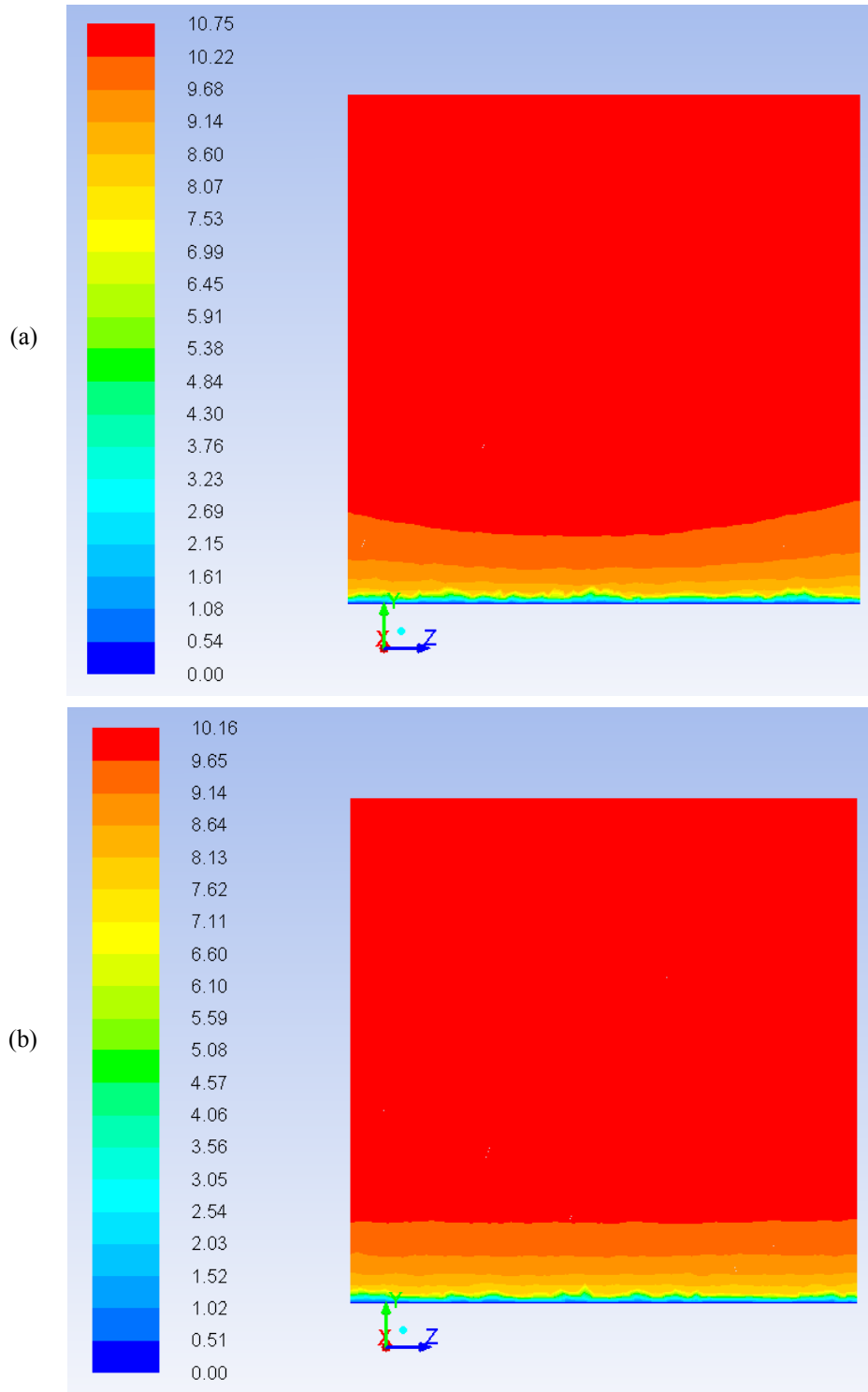


Figure 8.39 – Acoustic: Axial Velocity Contour at 1 & 2 Dia. Upstream ($J = 0.48$)

Configuration 3 Case of $J = 0.48$
 (a) Contour plot at two diameters.
 (b) Contour plot at one diameter.
 (a – b) Referenced upstream of blades.

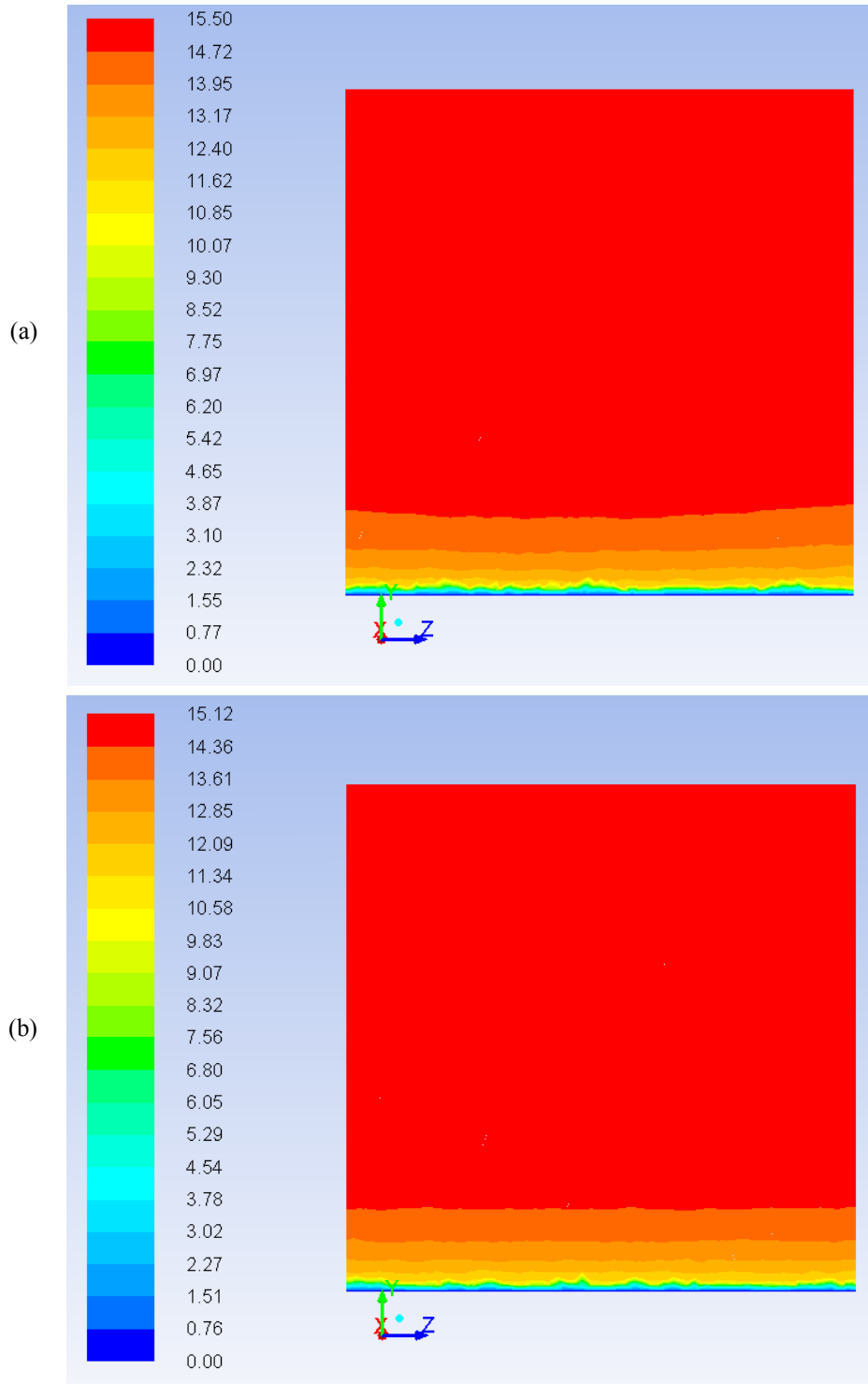


Figure 8.40 – Acoustic: Axial Velocity Contour at 1 & 2 Dia. Upstream ($J = 0.72$)

Configuration 3 Case of $J = 0.72$
 (a) Contour plot at two diameters.
 (b) Contour plot at one diameter.
 (a – b) Referenced upstream of blades.

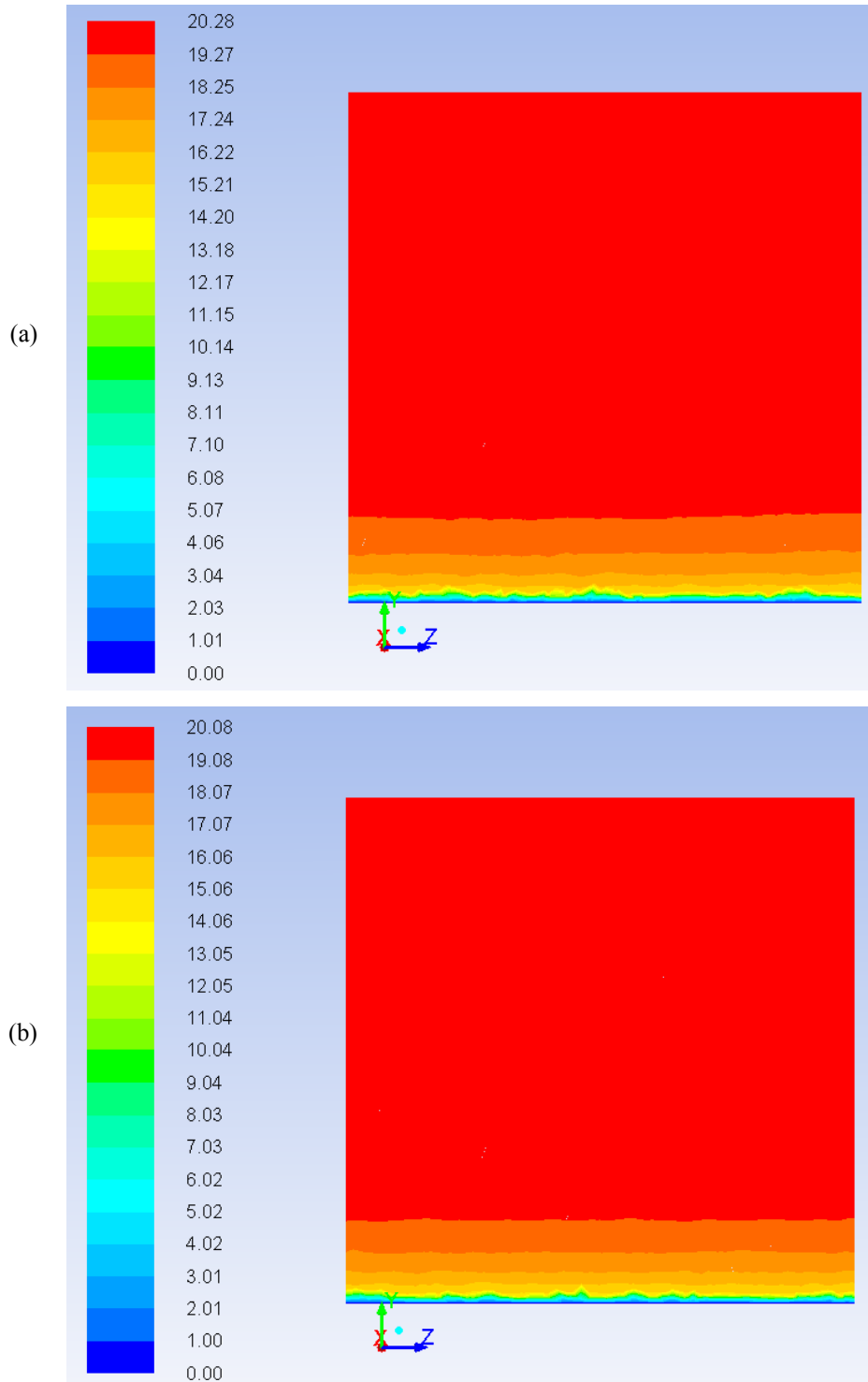


Figure 8.41 – Acoustic: Axial Velocity Contour at 1 & 2 Dia. Upstream ($J = 0.96$)

Configuration 3 Case of $J = 0.96$
 (a) Contour plot at two diameters.
 (b) Contour plot at one diameter.
 (a – b) Referenced upstream of blades.

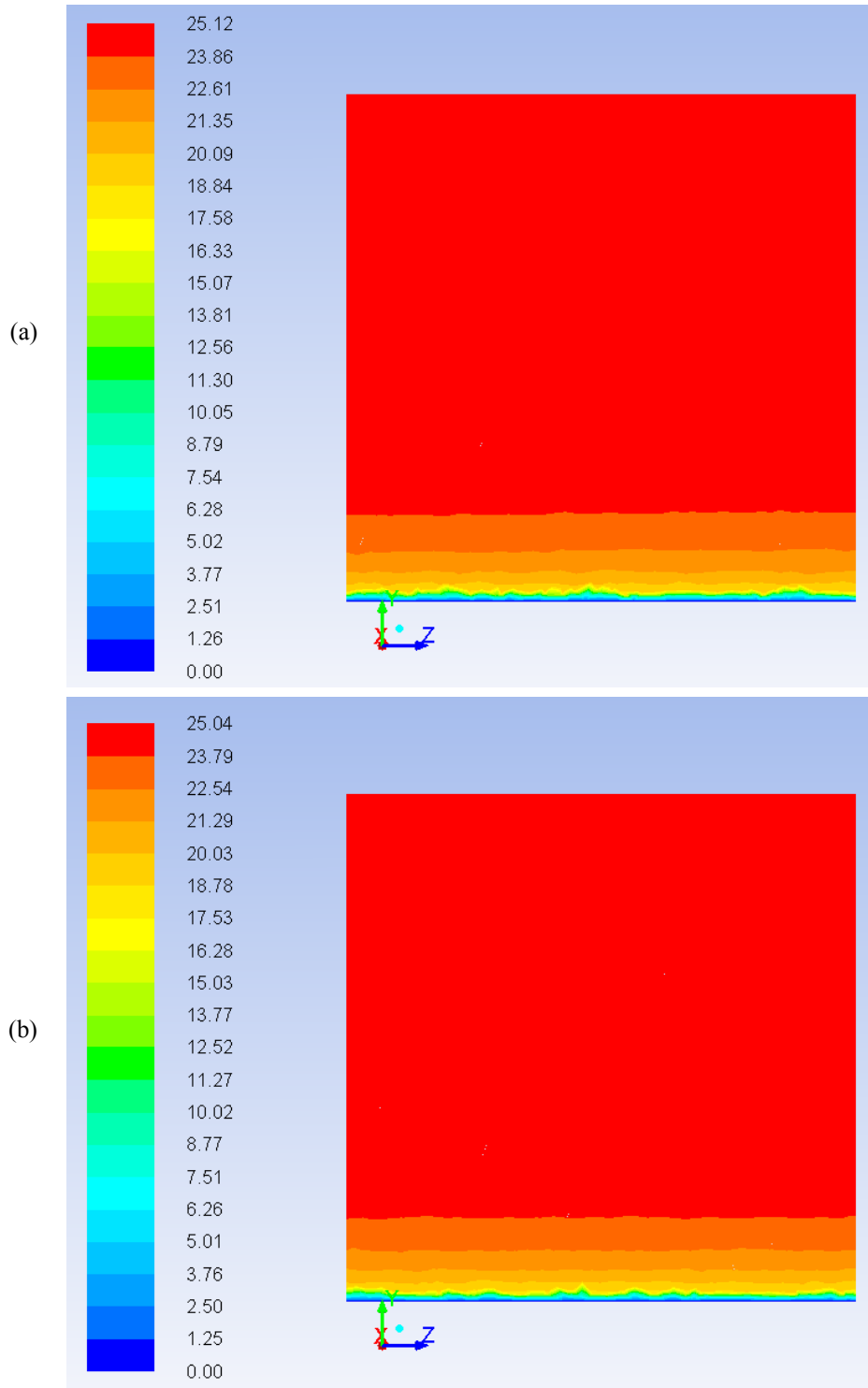


Figure 8.42 – Acoustic: Axial Velocity Contour at 1 & 2 Dia. Upstream ($J = 1.20$)

Configuration 3 Case of $J = 1.20$
 (a) Contour plot at two diameters.
 (b) Contour plot at one diameter.
 (a – b) Referenced upstream of blades.

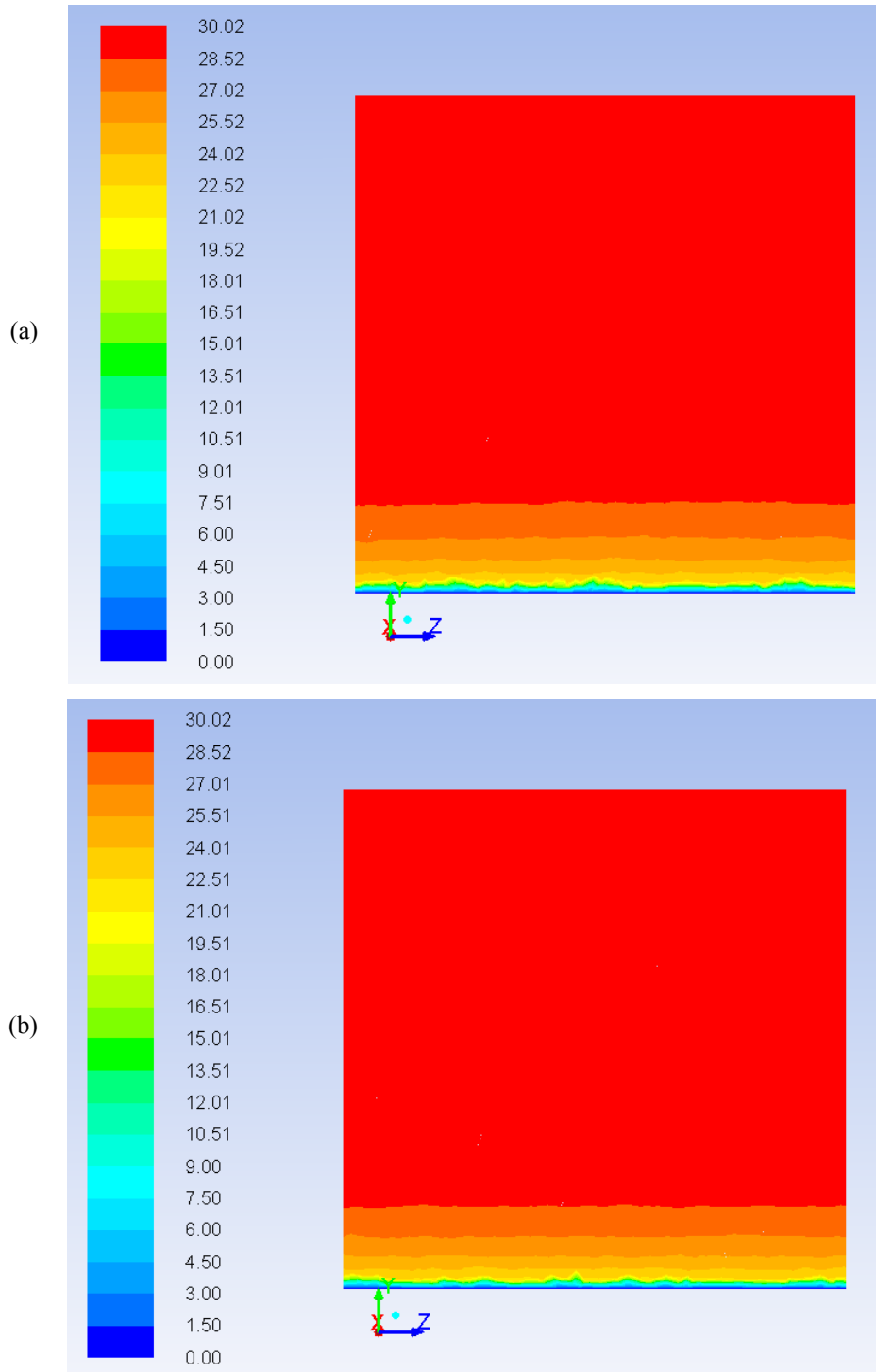


Figure 8.43 – Acoustic: Axial Velocity Contour at 1 & 2 Dia. Upstream ($J = 1.44$)

Configuration 3 Case of $J = 1.44$
 (a) Contour plot at two diameters.
 (b) Contour plot at one diameter.
 (a – b) Referenced upstream of blades.

Configuration 3 - Acoustic Data: Inflow Velocity Contours

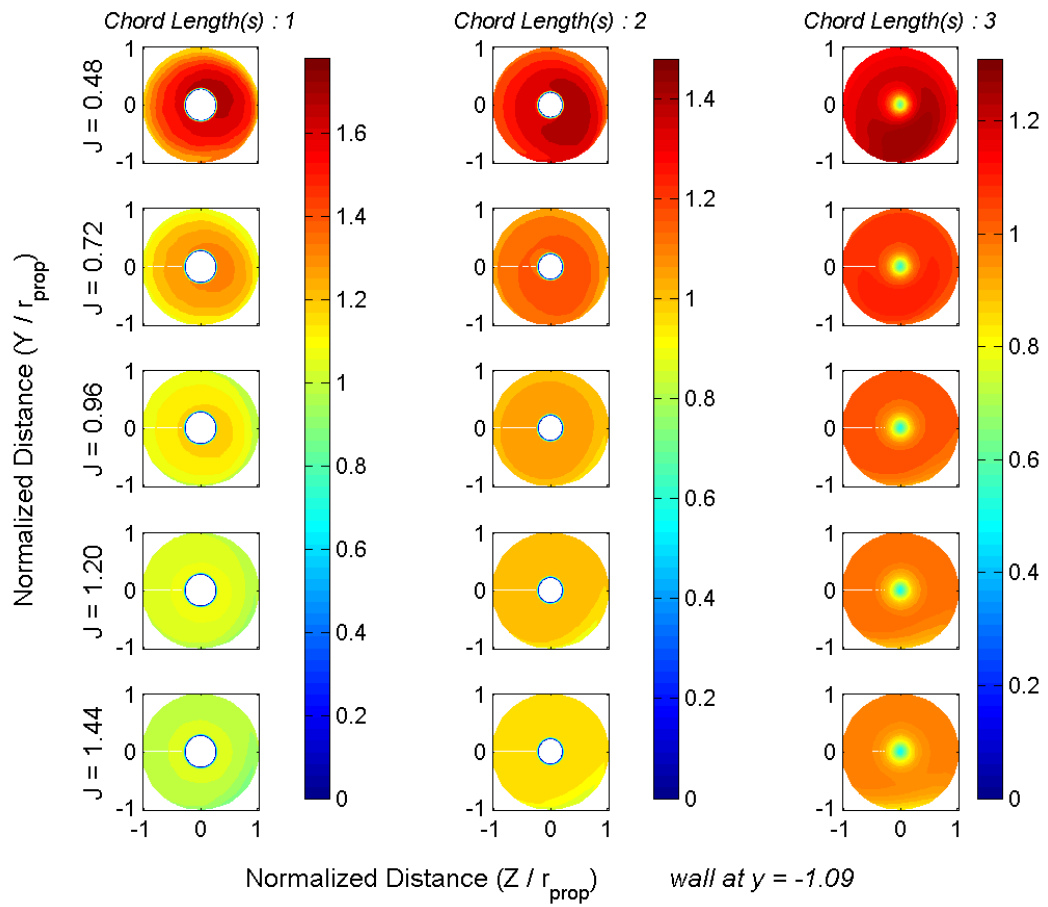


Figure 8.44 – Acoustic: Axial Velocity Contour at All Near Stations.

Configuration 3
 All acoustic data set cases at all near stations are shown with normalized distances (propeller radius) and velocities (inflow velocity).

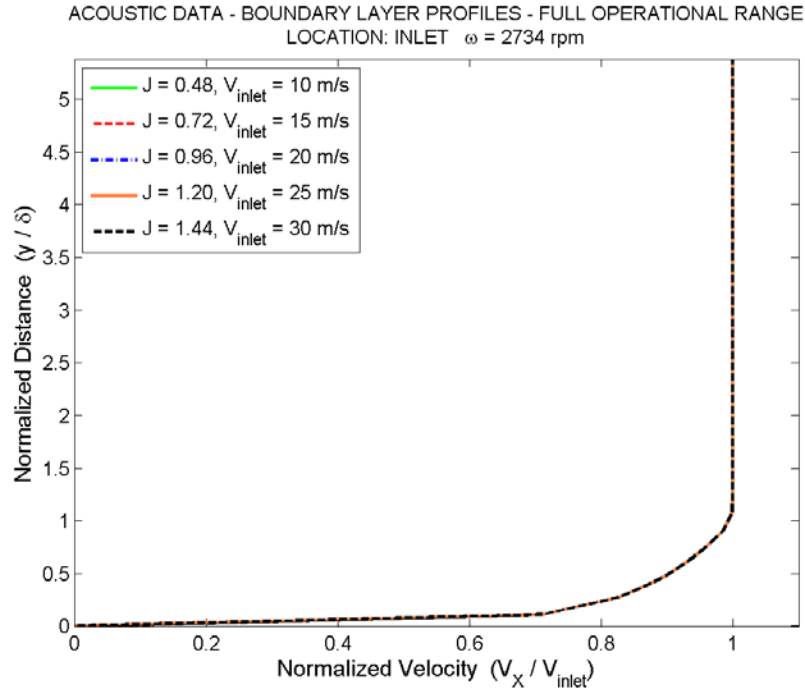


Figure 8.45 – Acoustic: BL Profile at Inlet for All Case Files

All acoustic data set cases are plotted on the same chart demonstrating the change in boundary layer profile with advance ratio.

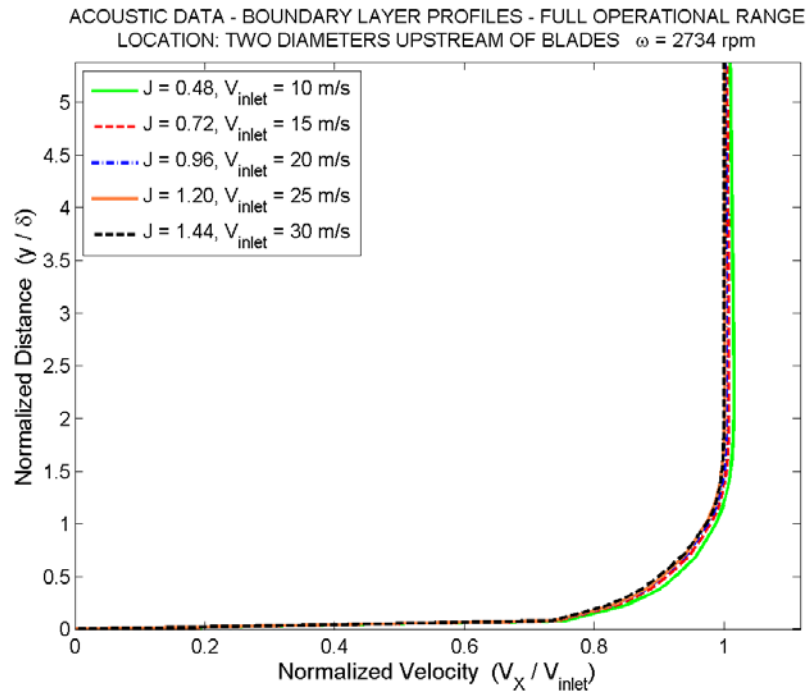


Figure 8.46 – Acoustic: BL Profile at 2 Diameters Upstream for All Case Files

All acoustic data set cases are plotted on the same chart demonstrating the change in boundary layer profile with advance ratio.

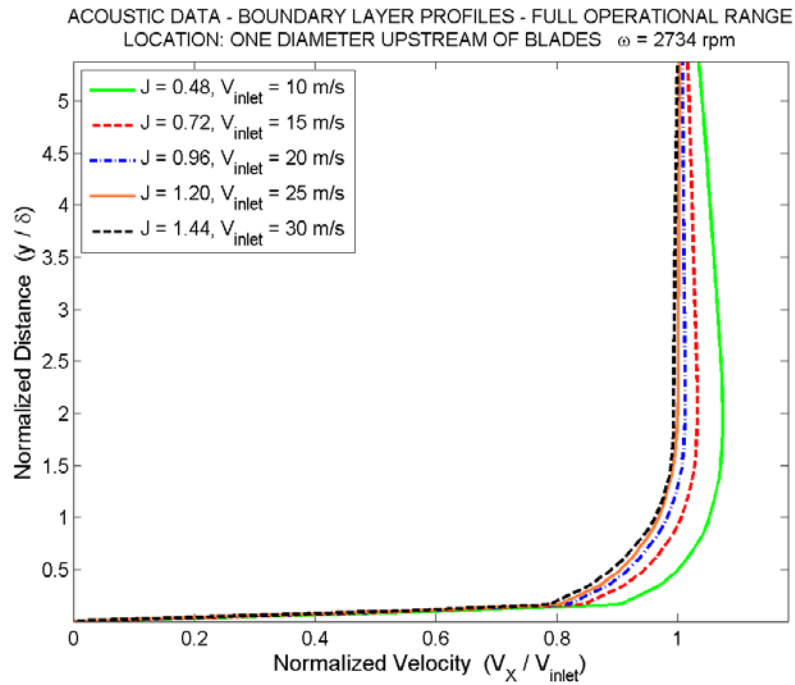


Figure 8.47 – Acoustic: BL Profile at 1 Diameter Upstream for All Case Files

All acoustic data set cases are plotted on the same chart demonstrating the change in boundary layer profile with advance ratio.

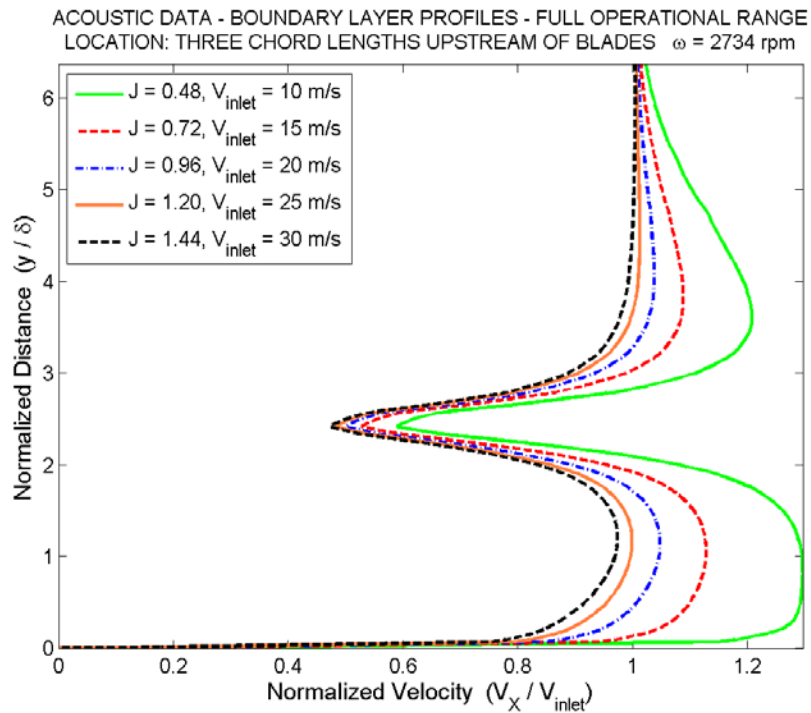


Figure 8.48 – Acoustic: BL Profile at 3 Chord Lengths Upstream for All Case Files

All acoustic data set cases are plotted on the same chart demonstrating the change in boundary layer profile with advance ratio.

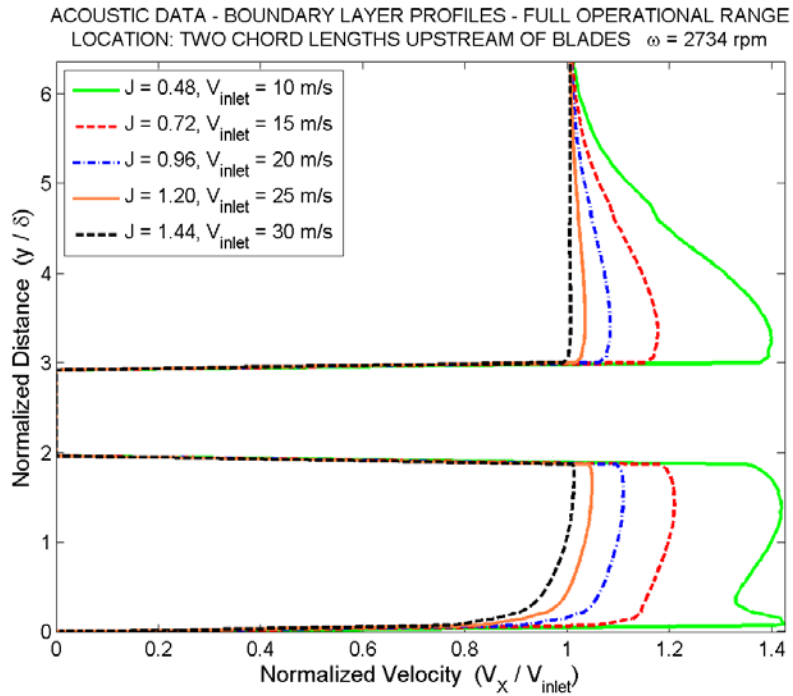


Figure 8.49 – Acoustic: BL Profile at 2 Chord Lengths Upstream for All Case Files

All acoustic data set cases are plotted on the same chart demonstrating the change in boundary layer profile with advance ratio.

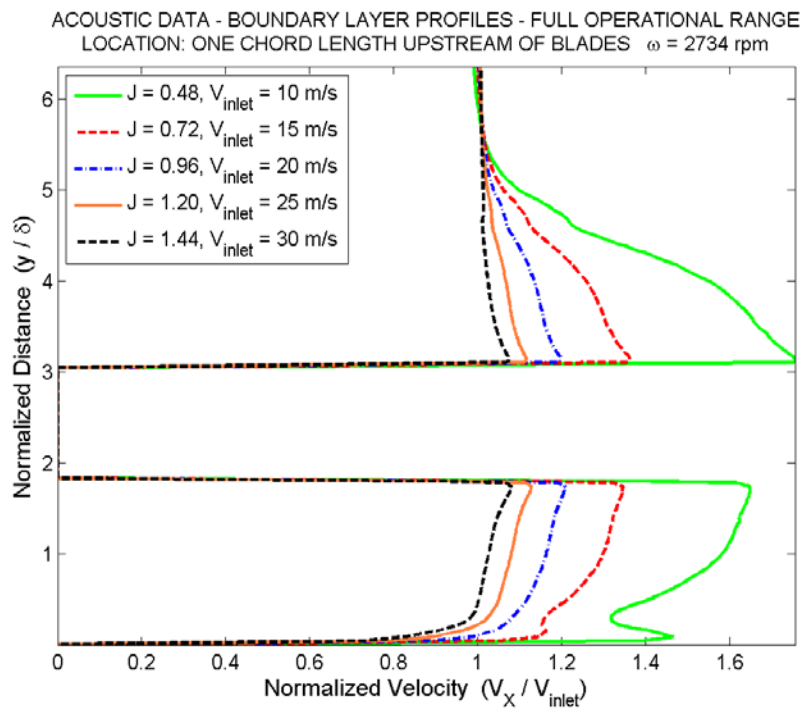


Figure 8.50 – Acoustic: BL Profile at 1 Chord Length Upstream for All Case Files

All acoustic data set cases are plotted on the same chart demonstrating the change in boundary layer profile with advance ratio.

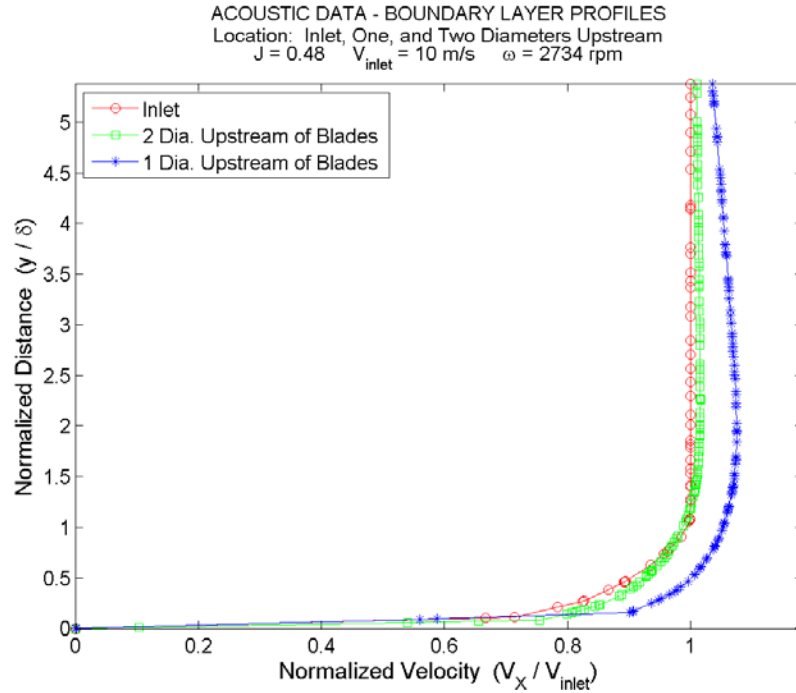


Figure 8.51 – Acoustic: BL Profile at All Far Upstream Stations ($J = 0.48$)

Configuration 3 Case for $J = 0.48$
 Boundary layer profiles at all far upstream stations demonstrating the change in boundary layer profile with location.

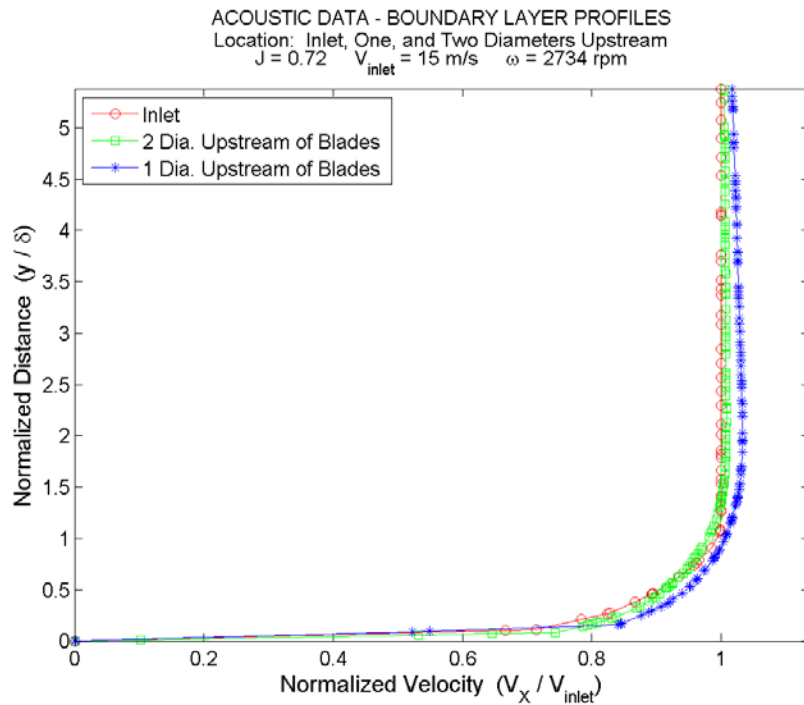


Figure 8.52 – Acoustic: BL Profile at All Far Upstream Stations ($J = 0.72$)

Configuration 3 Case for $J = 0.72$
 Boundary layer profiles at all far upstream stations demonstrating the change in boundary layer profile with location.

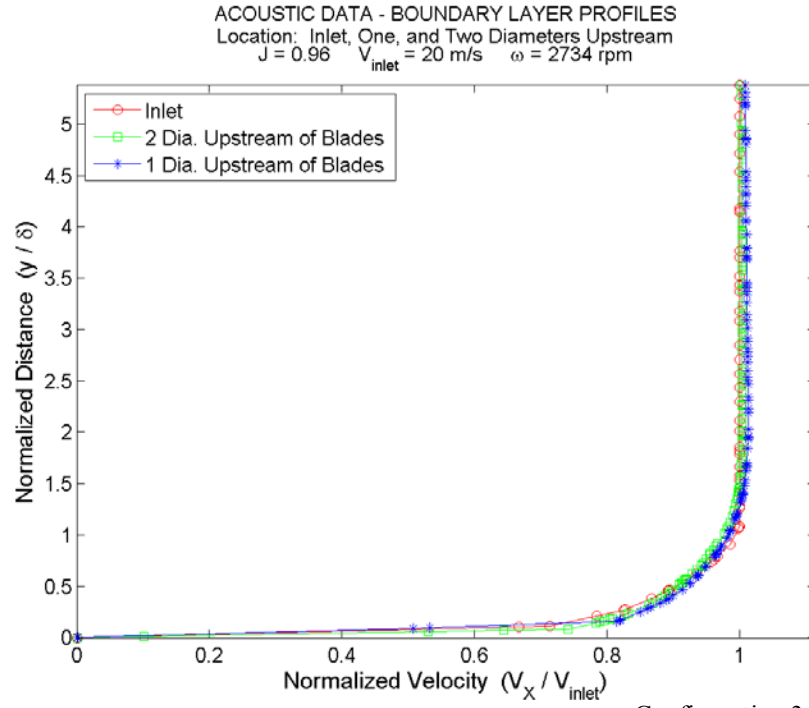


Figure 8.53 – Acoustic: BL Profile at All Far Upstream Stations ($J = 0.96$)

Configuration 3 Case for $J = 0.96$
 Boundary layer profiles at all far upstream stations demonstrating the change in boundary layer profile with location.

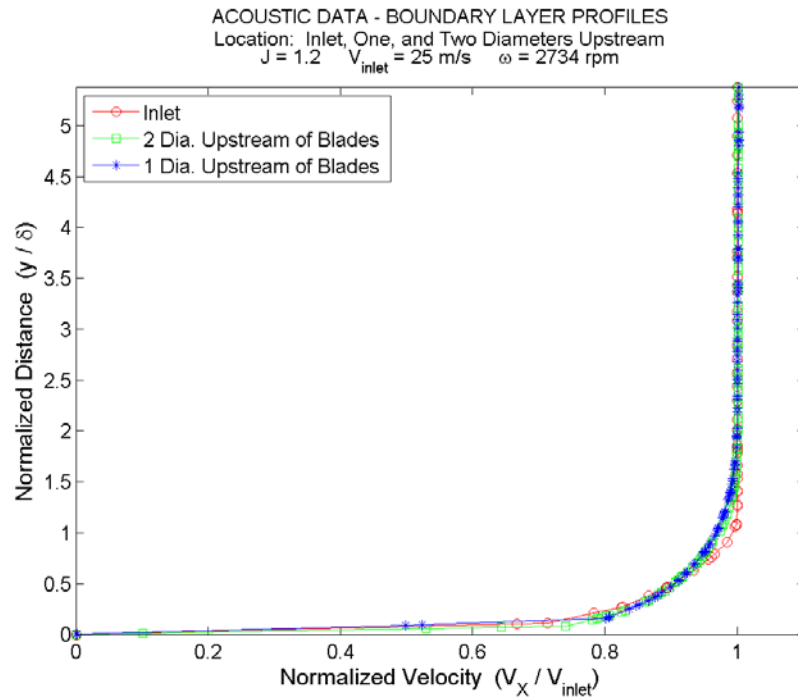


Figure 8.54 – Acoustic: BL Profile at All Far Upstream Stations ($J = 1.20$)

Configuration 3 Case for $J = 1.20$
 Boundary layer profiles at all far upstream stations demonstrating the change in boundary layer profile with location.

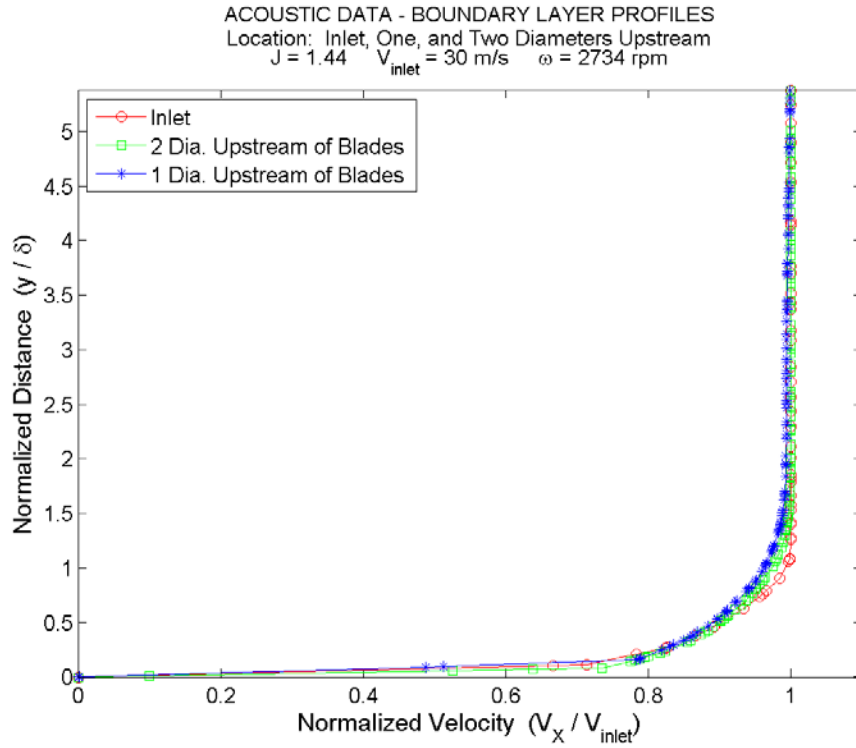


Figure 8.55 – Acoustic: BL Profile at All Far Upstream Stations ($J = 1.44$)

Configuration 3 Case for $J = 1.44$
 Boundary layer profiles at all far upstream stations demonstrating the change in boundary layer profile with location.

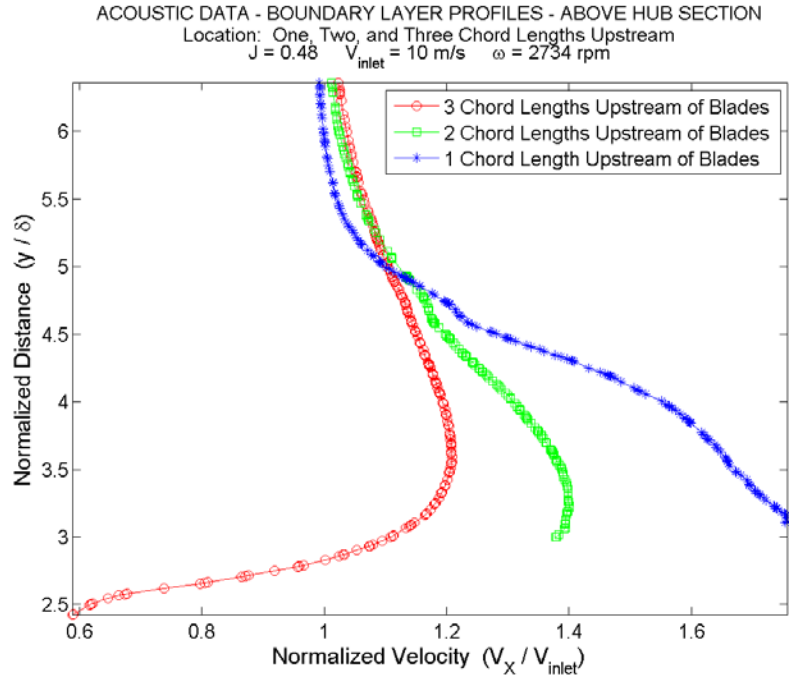


Figure 8.56 – Acoustic: BL Profile at All Near Upstream Stations ($J = 0.48 - AH$)

Configuration 3 Case for $J = 0.48$
 Boundary layer profiles at all near upstream stations above hub demonstrating the change in boundary layer profile with location.

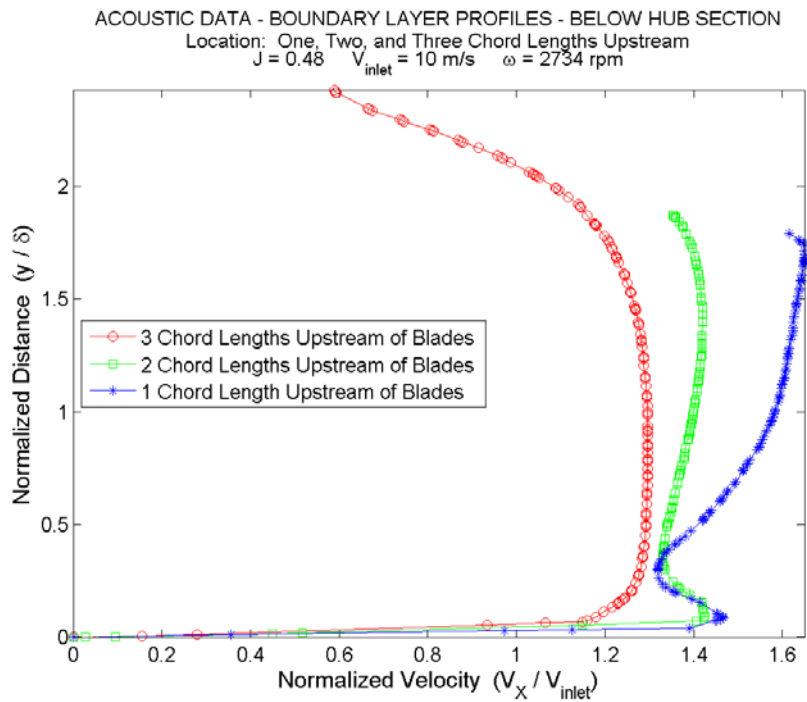


Figure 8.57 – Acoustic: BL Profile at All Near Upstream Stations ($J = 0.48 - BH$)

Configuration 3 Case for $J = 0.48$
 Boundary layer profiles at all near upstream stations below hub demonstrating the change in boundary layer profile with location.

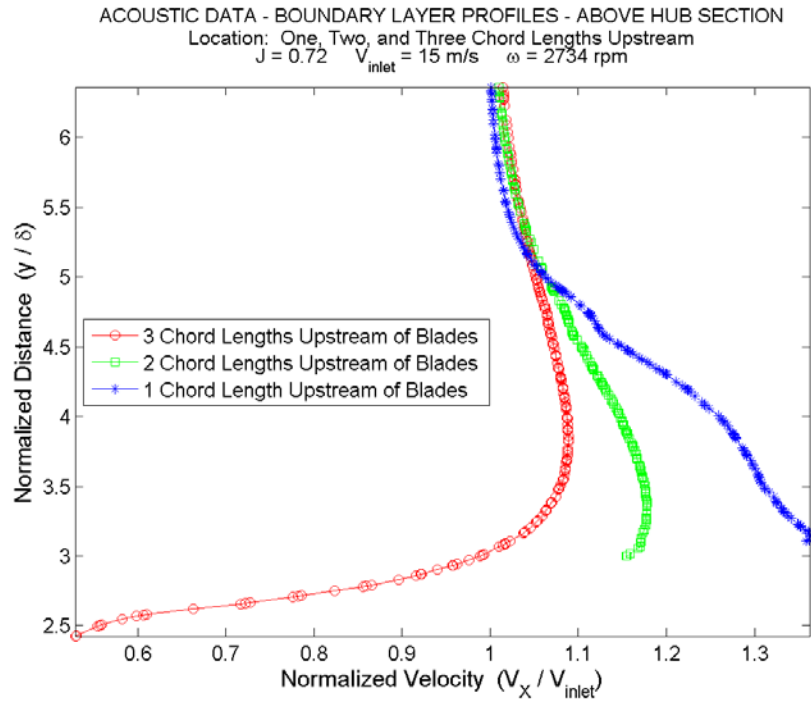


Figure 8.58 – Acoustic: BL Profile at All Near Upstream Stations ($J = 0.72 - AH$)

Configuration 3 Case for $J = 0.72$
 Boundary layer profiles at all near upstream stations above hub demonstrating the change in boundary layer profile with location.

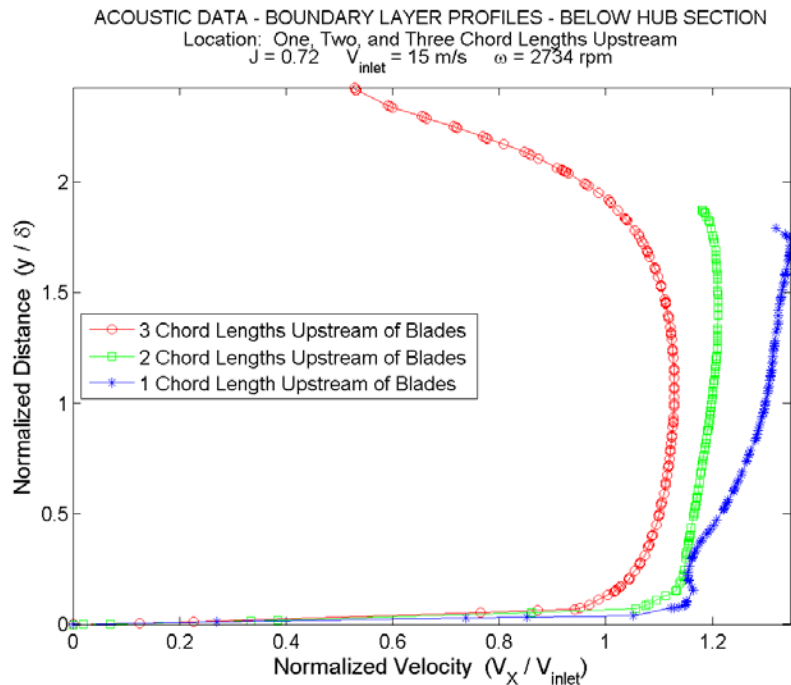


Figure 8.59 – Acoustic: BL Profile at All Near Upstream Stations ($J = 0.72 - BH$)

Configuration 3 Case for $J = 0.72$
 Boundary layer profiles at all near upstream stations below hub demonstrating the change in boundary layer profile with location.

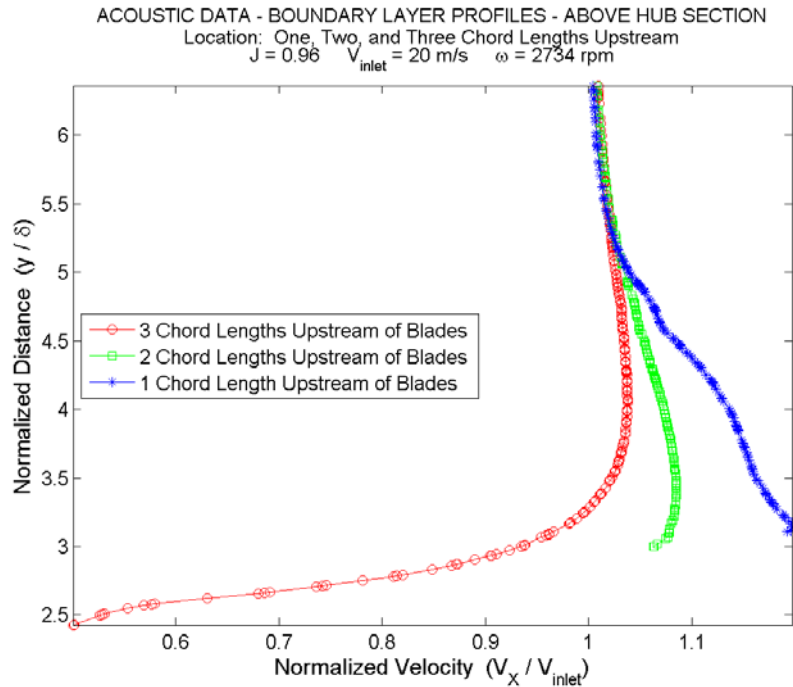


Figure 8.60 – Acoustic: BL Profile at All Near Upstream Stations ($J = 0.96 - AH$)

Configuration 3 Case for $J = 0.96$
 Boundary layer profiles at all near upstream stations above hub demonstrating the change in boundary layer profile with location.

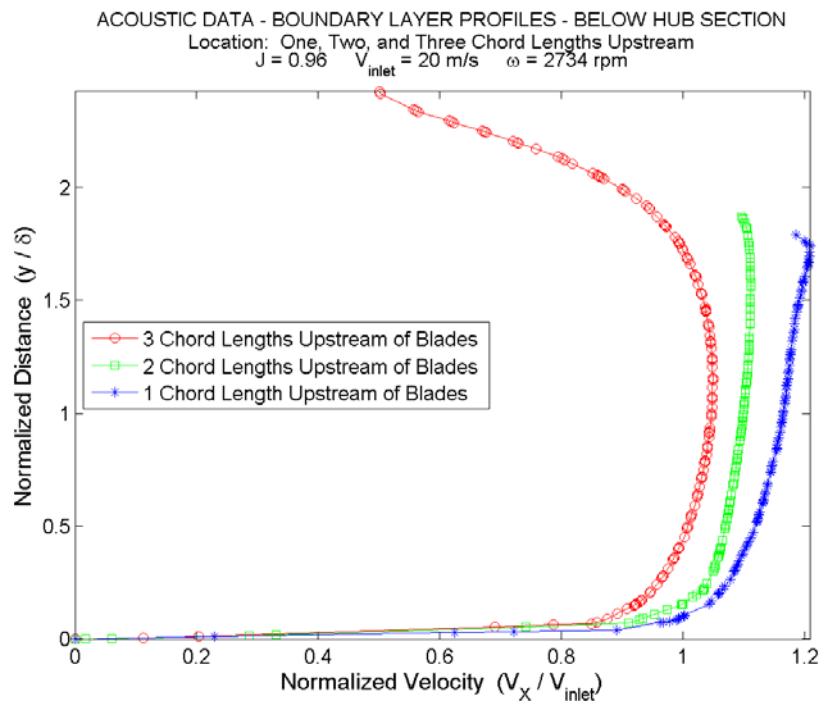


Figure 8.61 – Acoustic: BL Profile at All Near Upstream Stations ($J = 0.96 - BH$)

Configuration 3 Case for $J = 0.96$
 Boundary layer profiles at all near upstream stations below hub demonstrating the change in boundary layer profile with location.

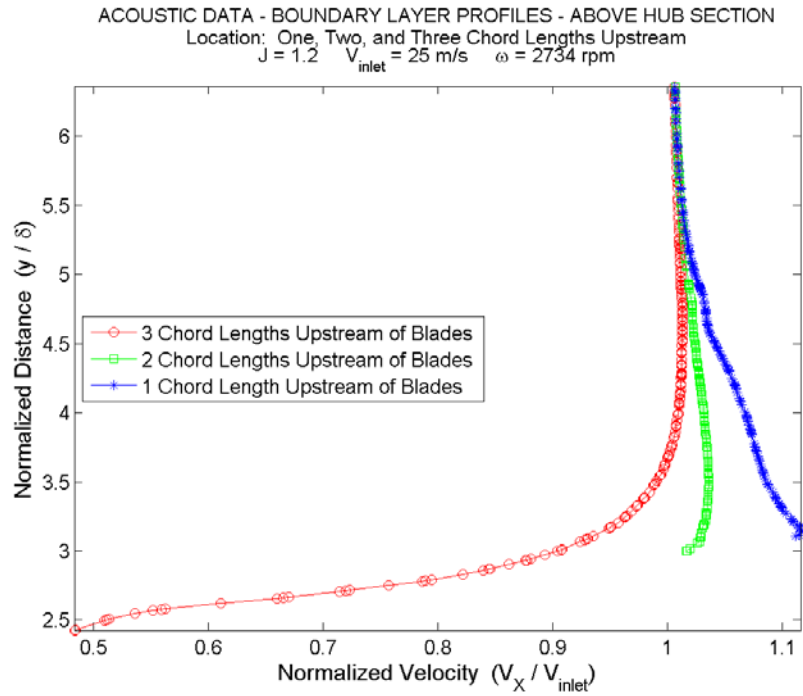


Figure 8.62 – Acoustic: BL Profile at All Near Upstream Stations ($J = 1.20 - AH$)

Configuration 3 Case for $J = 1.20$
 Boundary layer profiles at all near upstream stations above hub demonstrating the change in boundary layer profile with location.

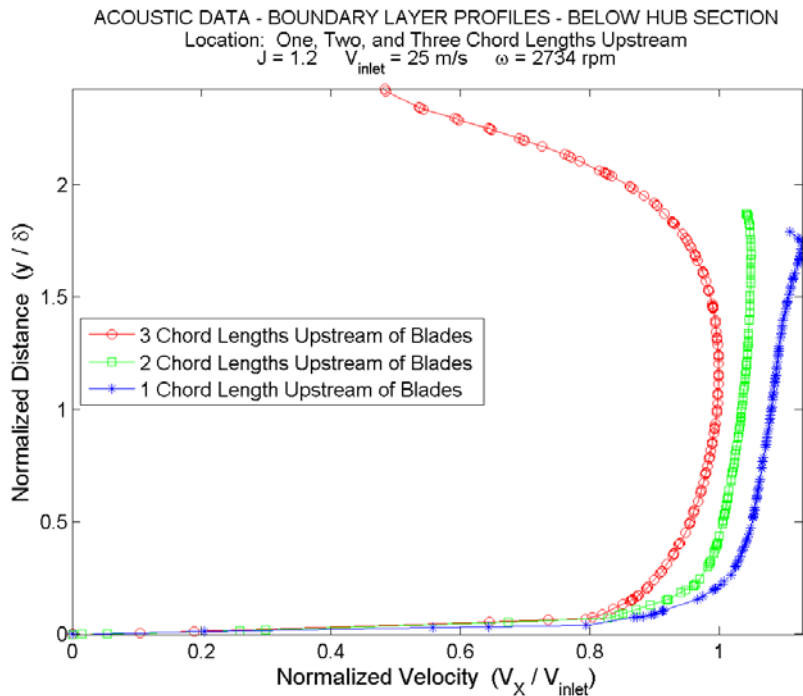


Figure 8.63 – Acoustic: BL Profile at All Near Upstream Stations ($J = 1.20 - BH$)

Configuration 3 Case for $J = 1.20$
 Boundary layer profiles at all near upstream stations below hub demonstrating the change in boundary layer profile with location.

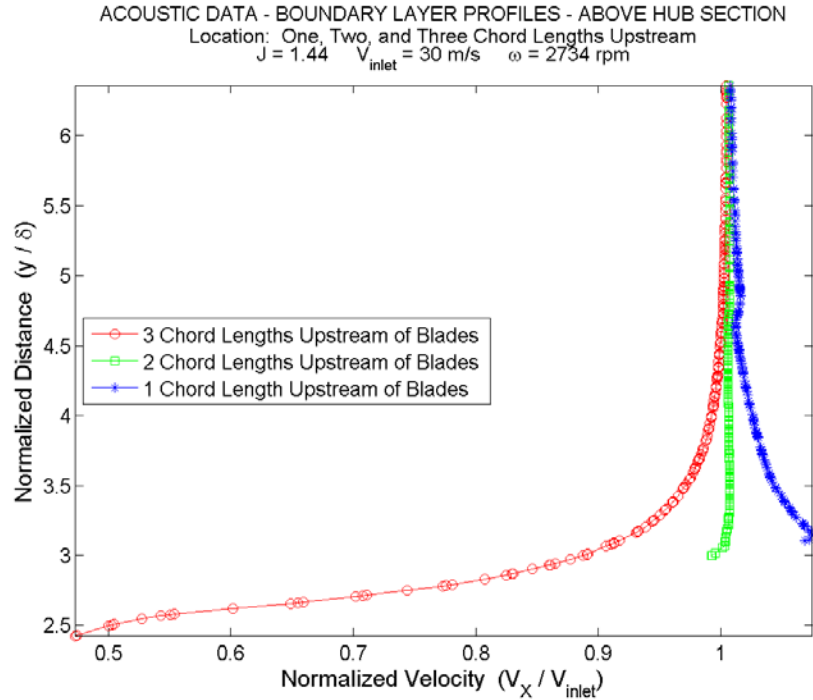


Figure 8.64 – Acoustic: BL Profile at All Near Upstream Stations ($J = 1.44 - AH$)

Configuration 3 Case for $J = 1.44$
 Boundary layer profiles at all near upstream stations above hub demonstrating the change in boundary layer profile with location.

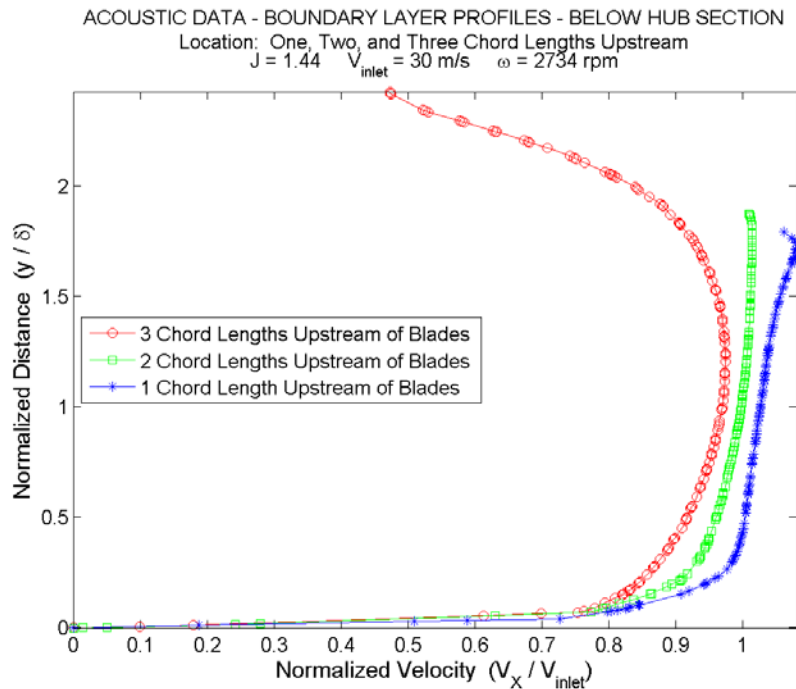


Figure 8.65 – Acoustic: BL Profile at All Near Upstream Stations ($J = 1.44 - BH$)

Configuration 3 Case for $J = 1.44$
 Boundary layer profiles at all near upstream stations below hub demonstrating the change in boundary layer profile with location.

NOMENCLATURE

NUMERICAL MODELS

S	control surface
\mathcal{V}	control volume
u^+	dimensionless velocity
y^+	dimensionless wall distance
μ_t	eddy or turbulent viscosity
\vec{F}_{ex}	external force vector
P'	fluctuating pressure
u', v', w'	fluctuating velocity component
ρ	fluid density
\vec{g}	gravity vector
x, y, z	instantaneous Cartesian position coordinates
u, v, w	instantaneous Cartesian velocity coordinates
u_i, u_j	instantaneous velocity coordinates in tensor notation
κ_0	Kármán constant
ν	kinematic molecular viscosity
S_{ij}	mean strain rate tensor
$\tilde{\nu}$	modified kinematic viscosity
μ	molecular viscosity
\vec{M}	momentum vector
\vec{n}	normal vector pointing away from control surface
P	pressure

q_i	Reynolds flux
τ_{ij}	Reynolds stress tensor
y_0	roughness height
u_*	shear or frictional velocity (characteristic flow parameter)
$\bar{\tau}$	stress tensor
t	time
\bar{P}	time – averaged pressure
$\bar{u}, \bar{v}, \bar{w}$	time – averaged velocity component
Φ	total amount of φ
φ	transport quantity
κ	turbulence kinetic energy
$\sigma_{\bar{v}}, C_{b2}$	turbulence model constants
$S_{\bar{v}}$	turbulence model source term
Y_v	turbulent viscosity destruction
G_v	turbulent viscosity production
\vec{V}	velocity vector
τ_w	wall shear stress

NUMERICAL METHODS

\vec{S}_f	area of cell face f , given by $ \vec{S} = S_x \hat{i} + S_y \hat{j} = \vec{S} \cdot \hat{n} $
φ_{fCD}	cell face value of φ utilizing central differencing scheme
φ_{fFOU}	cell face value of φ utilizing first order upwind scheme
φ_{fSOU}	cell face value of φ utilizing second order upwind scheme
φ_{fMUSCL}	cell face value of φ utilizing third order MUSCL scheme
b	coefficient
J_f	continuity equation face flux

ρ_f	density at face f
γ_φ	diffusion coefficient for φ
\vec{r}	displacement vector from the upstream cell centroid to the centroid of the cell face
R_{CGS}	globally scaled residual for continuity
$R_{\varphi GS}$	globally scaled residual for the general transport variable φ
$\nabla\varphi_f$	gradient of φ_f at face f
I	identity matrix
a_{nb}	linearized coefficient for φ_{nb}
a_p	linearized coefficient for φ
J_f	mass flux through face f equal to ρV_n
nb	neighbor cells
N_f	number of faces enclosing cell
$P_f A \cdot \hat{i}$	pressure field and face mass fluxes
S_u	source of u
S_φ	source of φ per unit volume
\vec{S}	surface area vector
V_n	the normal velocity at the face of cell f
β	under-relaxation factor
φ_f	value of φ convected through face f
\vec{V}_f	velocity vector at face f

APPENDICES

APPENDIX A

SPATIAL DISCRETIZATION SCHEMES

$$\varphi_{f_{CD}} = \frac{1}{2}(\varphi_0 + \varphi_1) + \frac{1}{2}(\nabla\varphi_0 \cdot \vec{r}_0 + \nabla\varphi_1 \cdot \vec{r}_1) \quad A.1$$

$$\varphi_{f_{FOU}} = \varphi \quad A.2$$

$$\varphi_{f_{SOU}} = \varphi + \nabla\varphi \cdot \vec{r} \quad A.3$$

$$\varphi_{f_{MUSCL}} = \xi\varphi_{f_{CD}} + (1 - \xi)\varphi_{f_{SOU}} \quad A.4$$

BRIEF OVERVIEW OF PRESSURE INTERPOLATION SCHEMES

The first pressure interpolation scheme described is the Standard Pressure Interpolation Scheme. This is the default interpolation scheme used by ANSYS – FLUENT. Interpolation for cell face pressure value is given by utilizing momentum equation coefficients. This is detailed in ANSYS – FLUENT theory guide [68] and as long as pressure variation is smooth this method works well. Nonetheless, if large gradients exist between cells, the pressure profile will also contain large gradients at the cell face. Thus, when solving the discrete equation for velocity, one may observe overshoot and/or undershoot of cell velocity. A method of overcoming this problem is to refine the mesh at areas where large gradient occur in order to fully capture the variation of pressure. Also, ANSYS – FLUENT takes the pressure gradient at the wall to equal zero which is acceptable for boundary layer, but not for surfaces with curvature and strong body forces [68]. This results in velocity vectors pointing perpendicular to the walls. Another pressure interpolation scheme is the linear interpolation scheme. This scheme simply takes the average of pressure values at neighboring cell centers and applies it to the cell face. The body-force weighted scheme is another interpolation scheme which provides results as accurate as the second-order scheme by assuming that the normal gradient of the difference between pressure and body forces is constant. Lastly, the PRESTO! (PREssure STaggering Option) scheme applies a continuity balance to the control volumes (in staggered orientation) at the cell face to compute the cell face pressure.

OVERVIEW OF ANSYS – FLUENT SOLVERS

The pressure-based solver is generally used for incompressible low speed flows while the density-based solver is generally used for compressible high speed flows. As mentioned, this is generally the case and the original intent; however, exceptions do exist [73]. There are two relevant segregated approaches which are to be considered based on mesh characteristics. These two segregated approaches are SIMPLE and SIMPLEC. PISO is another segregated approach; however, it is recommended for transient problems. As for the coupled approach, it is more expensive but solves the problem, as the name has it, in a coupled manner.

The SIMPLE and SIMPLEC are very similar segregated approaches. They are algorithms based on the projection method, also known as, the predictor-corrector approach. The main difference lies in the ability for SIMPLEC to correct for mesh skewness which is very useful if mesh contains highly skewed and distorted elements. Known issues with highly skewed and distorted meshes include reversed flow and more commonly, divergence. In brief, the SIMPLE method enforces mass conservation by utilizing relationship between velocity and pressure corrections; thus obtaining the pressure field. The guessed value for the pressure field is entered and adjusted by the face flux values. The cell pressure correction is determined from the discrete continuity equation, equation 4.3b, which is then linearized taking the form of equation A.5 known as the *Pressure – Correction Equation*. The second term in the equation is a source and is known as the net flow rate into the cell [68].

$$a_p P' = \sum_{nb} a_{nb} P'_{nb} + \sum_f^{N_f} J_f A_f \quad A.5$$

ANSYS – FLUENT calculates P' using an algebraic multigrid method (AMG) and once this value is obtained it is multiplied by an under-relaxation factor. The under-relaxation variable is discussed in the Convergence Criteria section within this chapter. Finally, the corrected face flux J_f is recalculated by inputting P as the new guessed values for pressure. This process repeats for every iteration and satisfies the discrete continuity equation. It is important to note that this algorithm solves the pressure correction equation separate from the momentum equation and the individual solution variables are decoupled from the governing equations. They are then solved *individually and sequentially* using the Gauss-Seidel

method. Since only one equation is solved at a time, only one set of values is stored into memory at a time. This approach is much less memory intensive but the convergence process is slower.

The coupled approach solves the momentum and pressure-based continuity equations *simultaneously* by combining equations, 4.2b, 4.3b, and the pressure interpolation scheme. This complex procedure is outlined in [68]. The result is a system of equations efficiently solved simultaneously by the coupled AMG solver providing better performance compared to segregated approaches. Nonetheless, the system of equations contains various variables stored into the memory bank; thus, becoming 150% to 200% more resource intensive than the segregated approach [68].

ANSYS – FLUENT SETUP RECOMMENDATIONS

Obtaining successful convergence is most often reliant on a well-produced mesh. It is important to have a mesh which is fine enough to capture the relevant flow features such as boundary layers, while at the same time maintaining as low cell count as possible as to not bog down computation. It is suggested that the user attempts to visualize the flow features being measured and incorporate it into the mesh. An example being, the smallest turbulence scales captured by CFD are limited to the cell spacing generated by the user. Structured meshes are usually recommended for best accuracy; however, they are often difficult to produce due to complex geometry features. Complete details on cell structure, techniques, and other mesh related information may be found in ICEM's Help Manual [75].

In order to reproduce a complex geometric feature such as an airfoil it is required to create fine cells on and about the region. If the mesh contains irregularities such as high skew, low aspect ratio, low quality, or any combination of these undesirable characteristics, the solution could be returned as inaccurate or even diverge. These characteristics indicate how well a cell was created, a 2D example being a square. If the cell is supposed to be a square but mesh topology forces the square to be distorted in order to conform to a curved line per say, then the geometric properties of the cell are changed. There are several reasons for mesh distortion including node to node integrations, overlapping volumes, etc. In general, these irregularities are calculated differently for every element type and the description that follows is to provide a general concept of these irregularities. The cell skewness is based on angular distortion of the cell, as an example, a square might resemble a rhombus. This is not necessarily an inferior skew but serves as an example. Aspect ratio accounts for how stretched the cell is comparing its largest length to its shortest length. An ideal cell has aspect ratio of unity; hence, low aspect ratios may indicate large gradients to be detected and lead to inaccuracies. Cell quality is derived from other variables such as the aspect ratio, skew, determinant, etc. As mentioned, these features have different formulas per element type [75]. Mesh elements containing these features reduce the numerical stability of the discretization algorithms. In addition, special consideration must be given to certain locations in the domain, in specific the boundary layer regions. ANSYS – FLUENT has recommendations for the mesh in order to improve accuracy and convergence.

Initiating at the boundaries, ANSYS – FLUENT [68] recommends that if using the Spalart – Allmaras turbulence model, for optimum boundary layer resolution y^+ values must be equal to or near 1 or greater than 30 for the entire computational domain surfaces. In other words, avoid having y^+ values in the buffer region mentioned in Chapter 3. Meeting this recommendation, allows for more consistent wall shear stress resolution. A result of the applied wall functions, equations 3.5 thru 3.7. The enhanced wall treatment is implemented by ANSYS – FLUENT whenever the mesh is not sufficiently fine to resolve the viscous sublayer ($y^+ \approx 1$). If the mesh lies in the buffer region, $1 < y^+ < 30$, then conflicts may occur since no enhanced wall treatment is available and grids within this region should therefore be avoided. If the mesh maintains $y^+ > 30$, then enhanced wall functions are by default used to provide most accurate results. Also, unless the entire boundary layer region is resolved to $y^+ \approx 1$, the S.A model becomes less sensitive to very fine meshes with y^+ values less than 30. This is because if a certain region contains y^+ values in the buffer region range, ANSYS – FLUENT applies the logarithmic laws which are extended to the viscous sublayer. As mentioned, the viscous sublayer resembles linear characteristics and the log law application is inappropriate in this region. Hence, as a suggestion, unless structured prism elements are created to meet $y^+ \approx 1$, choose to produce elements, structured prism layers if possible, with $y^+ > 30$. Furthermore, to improve accuracy and convergence, besides mesh improvements, it is important to consider numerical dissipation errors.

Another important convergence criterion is to minimize numerical dissipation as mentioned in spatial discretization section of this report. This allows for more accurate prediction of gradient values during computation. In addition, as recommended by [68], for turbulent flows first order and power law schemes should not be utilized as it overdamps the energy of resolved eddies leading to inaccuracies. Turbulence scales resolved by CFD require second order or higher to obtain its full development; hence, it is also important to consider a higher order spatial and gradient discretization and pressure interpolation. Nevertheless, one must consider how to initialize the problem and modify the inputs as the solution converges either by using the automated system or manually. ANSYS – FLUENT recommends to begin with first order schemes and if needed use laminar solver settings for turbomachinery type problems. After a few iterations change to correct turbulent model, increase the order, pressure, and gradient schemes. In the case of turbomachinery type problems with high revolutions, gradually increase the number of

revolutions per time until the design parameter is reached [73]. Also, to account for better convergence recommendations are given for residuals and relaxation factors.

It is necessary to have an overall convergence based on the entire domain, as in the case of using globally scaled residuals; however, sometimes the default order of residual cannot be reached and the solution will not converge. As in the case of this thesis, another method of determining convergence is to increase the residual for the problematic variable to a certain value and then check the locally scaled residuals as a contour plot. This allows the for convergence judgment based on problematic regions. The pressure – based solver only stores mass imbalance. In order to obtain all residuals the command prompt must be utilized and by entering “solve/set/expert” and once it prompts to save residuals for post-processing, indicate “yes” followed by the ENTER key [73]. ANSYS – FLUENT recommends that iterations be continued for at least an additional fifty iterations prior to observing that residuals have leveled out. The recommendations included in this section are not meant for every problem but serves as a guide to incompressible inviscid flows.

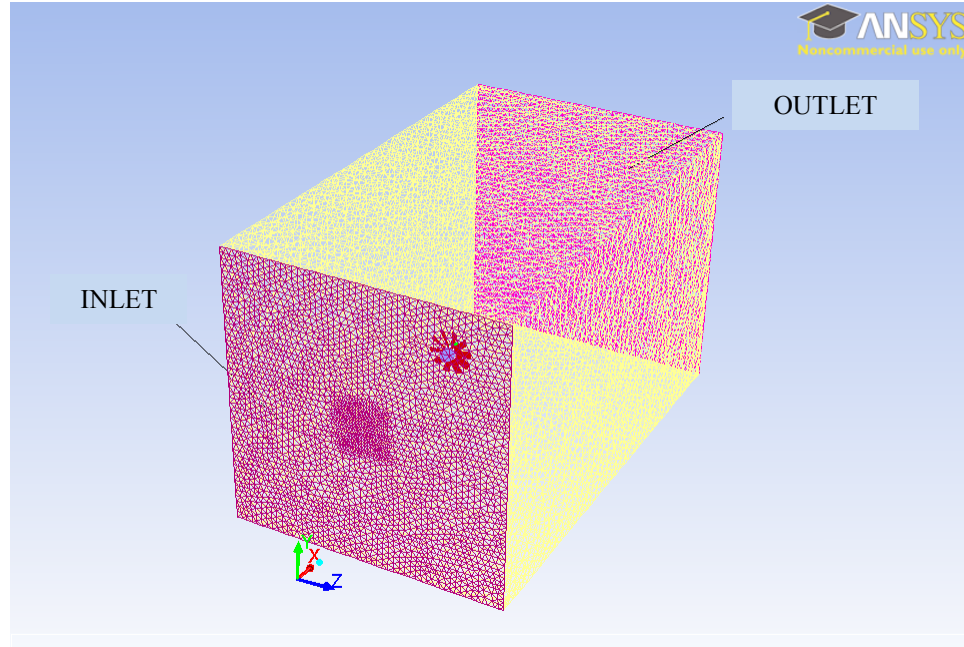
EXPORTING FLUENT DATA

ANSYS – FLUENT solution data was exported into ASCII files and applying a text file extension (.txt). Quantities were exported at node values. Once data was exported into text files it was completely post-processed in MATLAB. Data sets for configuration 1 and 3 include wake measurements taken at spatial location of the entire 360° ring at the probe measurement plane (refer to Figure 6.5). These results are to be used to validate CFD results to experimental results. show and interpret only the most relevant information. Grid independence studies were completed for all configurations; however, only configuration 3 grid independence will be mentioned.

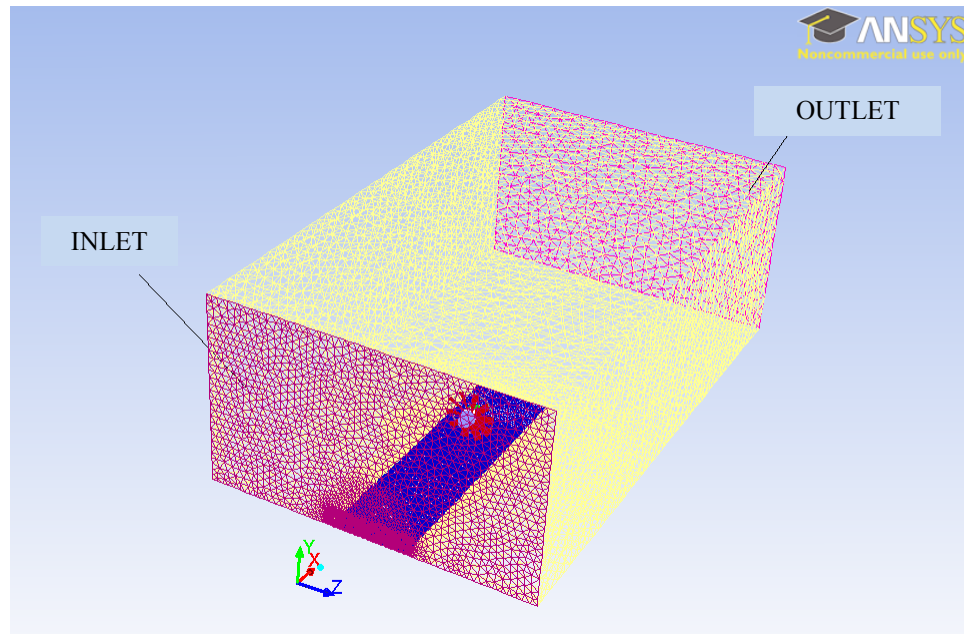
Table 8.1 shows the locations where measurements are taken for interpreting the effects of axisymmetric flow, near-wall inclusion, and thick boundary layer inclusion on the rotor ingested turbulent flow. This produced large amounts of data which had to be processed and analyzed. MATLAB scripts were created capable of importing ANSYS – FLUENT data files from any configuration and data set. Once imported, other MATLAB scripts were created to compare the large amounts of data and generate plots and details automatically.

APPENDIX B

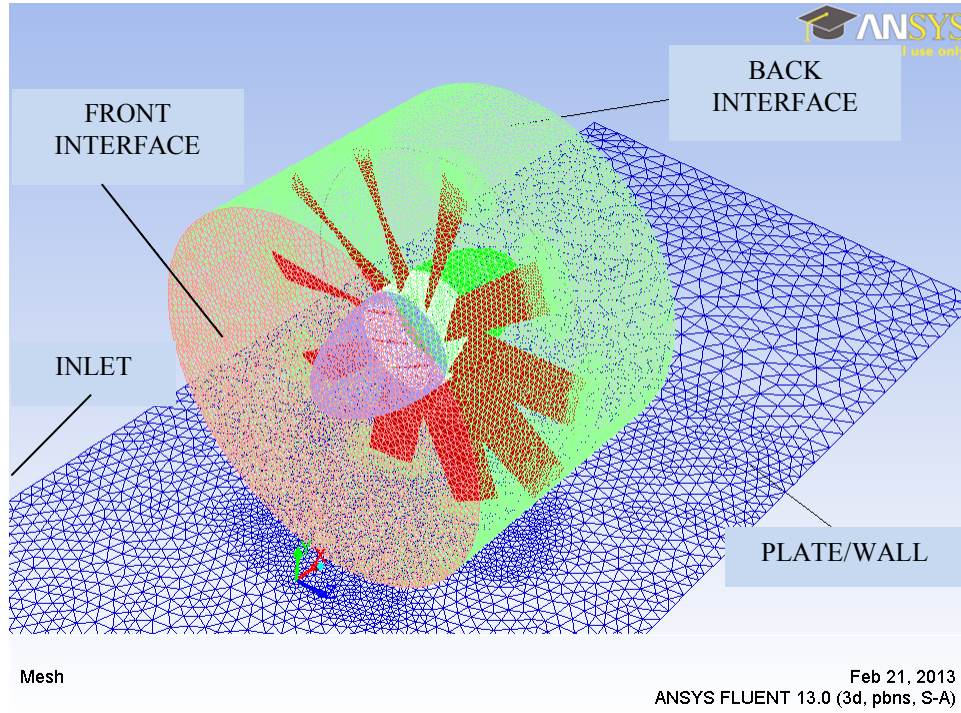
ADDITIONAL MESH GRAPHICS



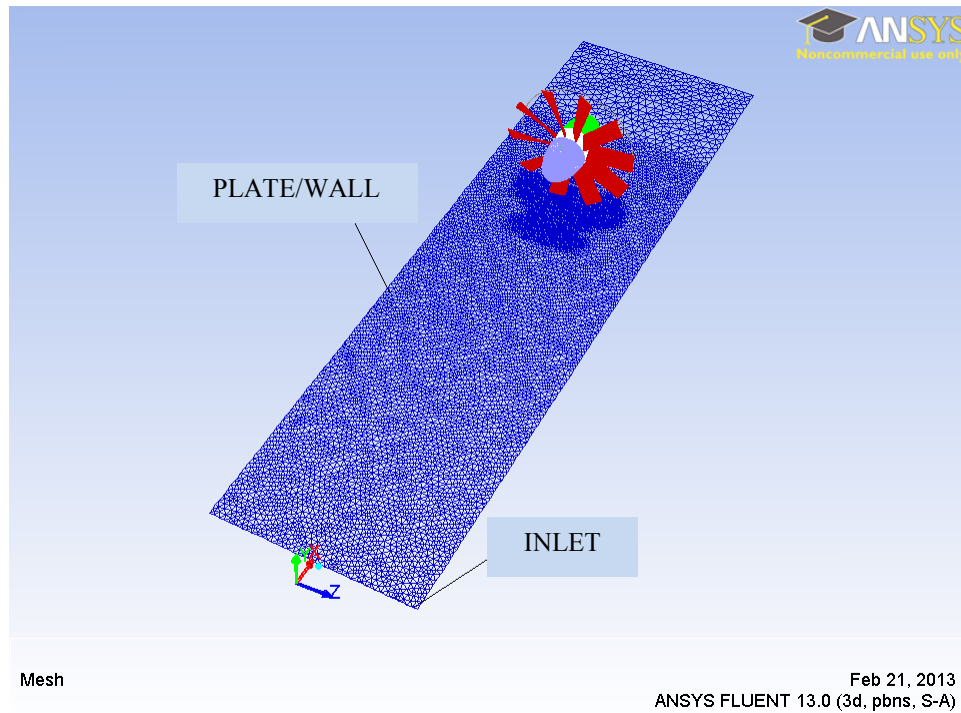
Configuration 1: Entire Domain – Showing Refinement



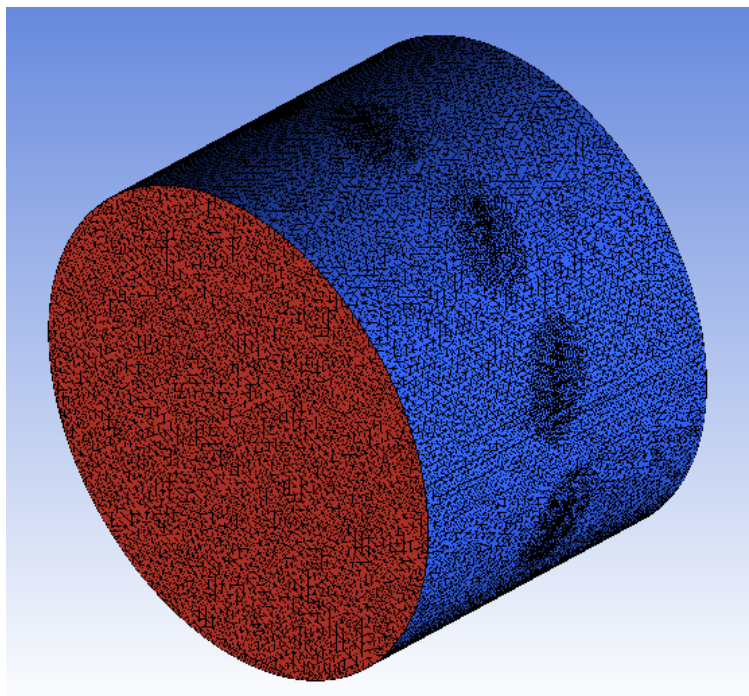
Configuration 3: Entire Domain – Showing Refinement



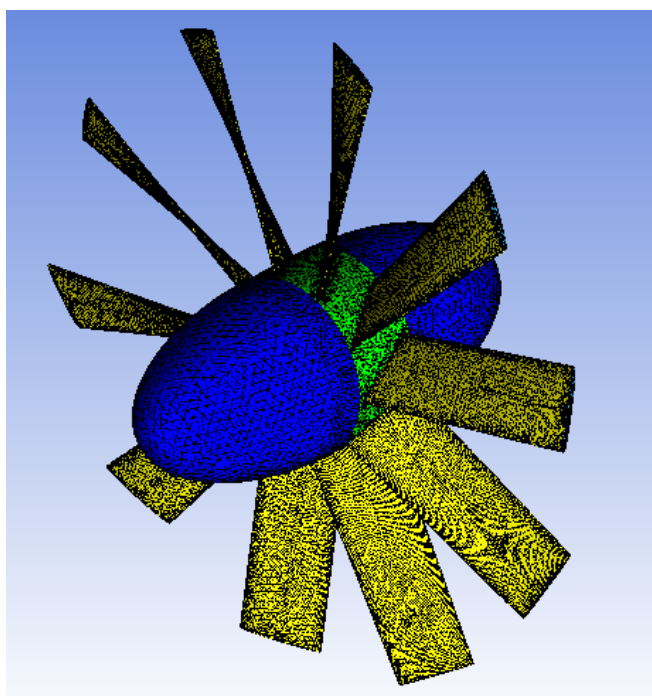
Configuration 3: Near-Wall and Rotational Domain – Showing Surface Refinement



Configuration 3: Near-Wall – Showing Surface Refinement



Rotational Domain Surface – Showing Surface Refinement



Configuration 3: Propeller Surface – Showing Surface Refinement

APPENDIX C

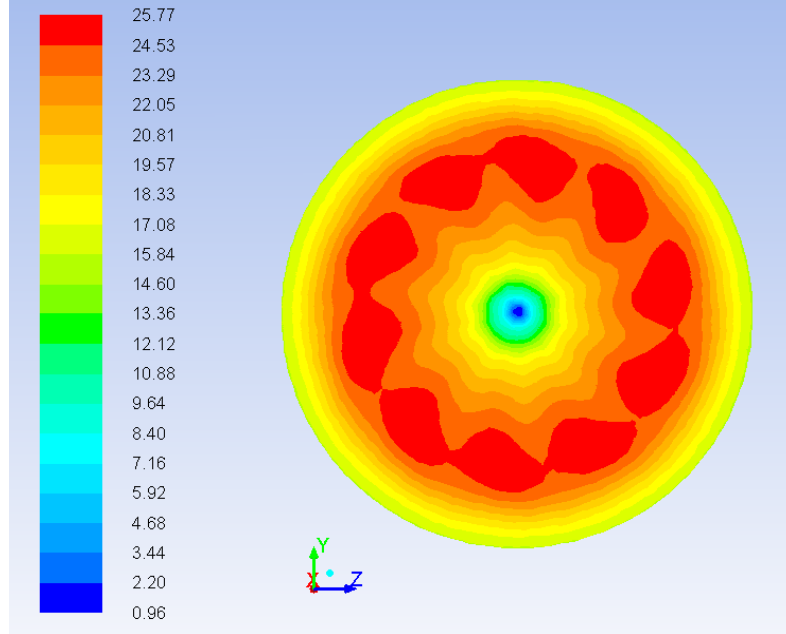
USER DEFINED FUNCTION: CELL ZONE CONDITION

(INLET VELOCITY = 15 M/S)

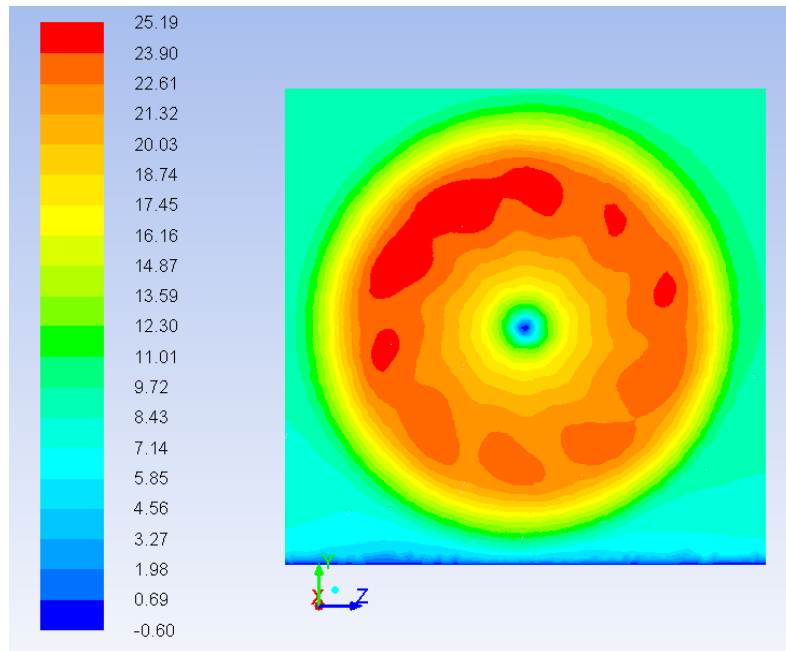
```
#include "udf.h"
DEFINE_PROFILE(inlet_x_velocity, thread, index)
{
    real x[ND_ND];
    real y;
    face_t f;
    real del;
    real bl;
    real U;
    real yorigin;
    bl = 0.102;
    U = 15;
    yorigin = -0.2489;
    del = yorigin + bl;
    begin_f_loop(f, thread)
    {
        F_CENTROID(x,f,thread);
        y = x[1];
        if (y <= del)
            F_PROFILE(f, thread, index) = U*pow(((y-yorigin)/bl),(1.0/7.0));
        else if (y > del)
            F_PROFILE(f, thread, index) = U;
    }
    end_f_loop(f, thread);
}
```

APPENDIX D

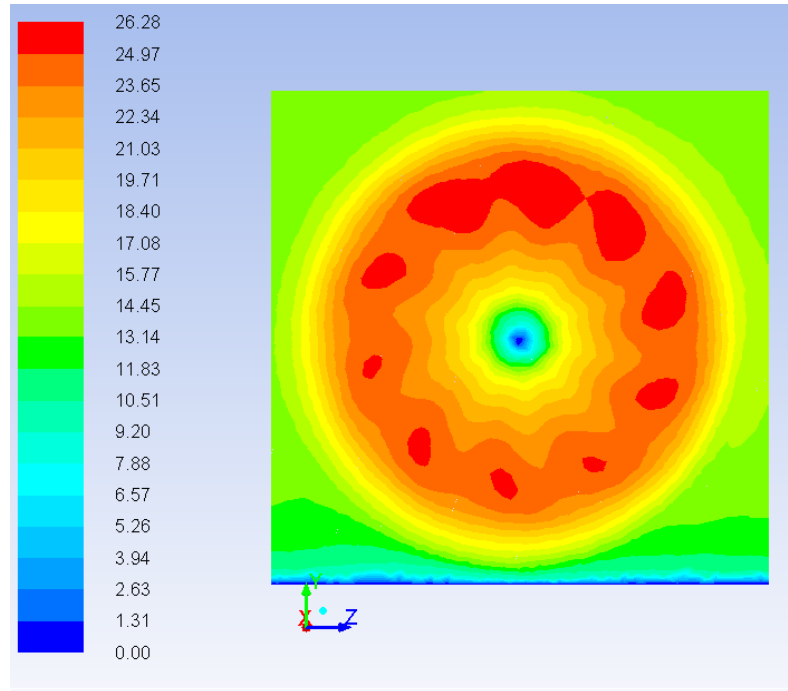
ADDITIONAL VELOCITY CONTOUR PLOTS (REAR INTERFACE)



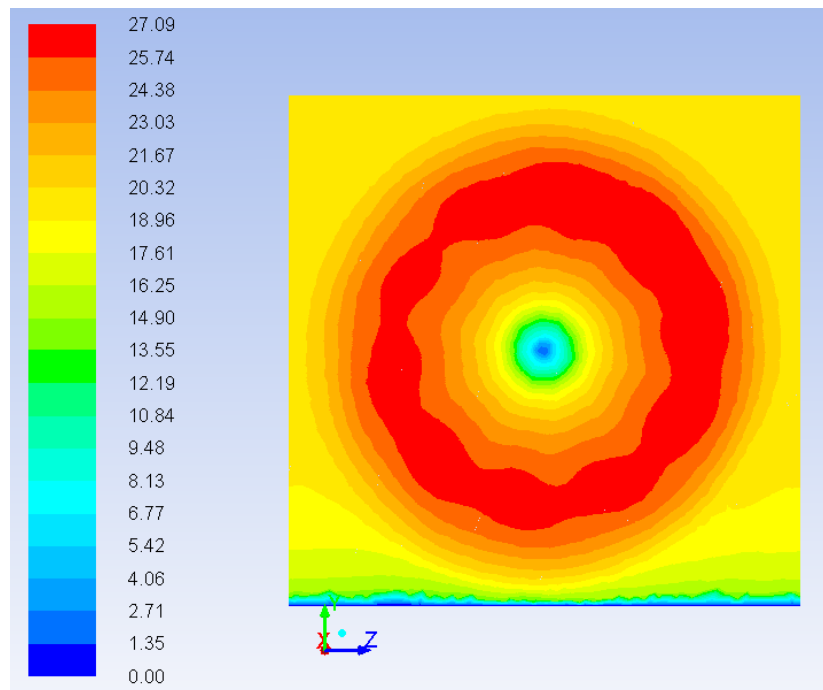
Configuration 1: Axial Velocity Contour Plot at Rear Interface, $J = 0.72$ (Local Scale)



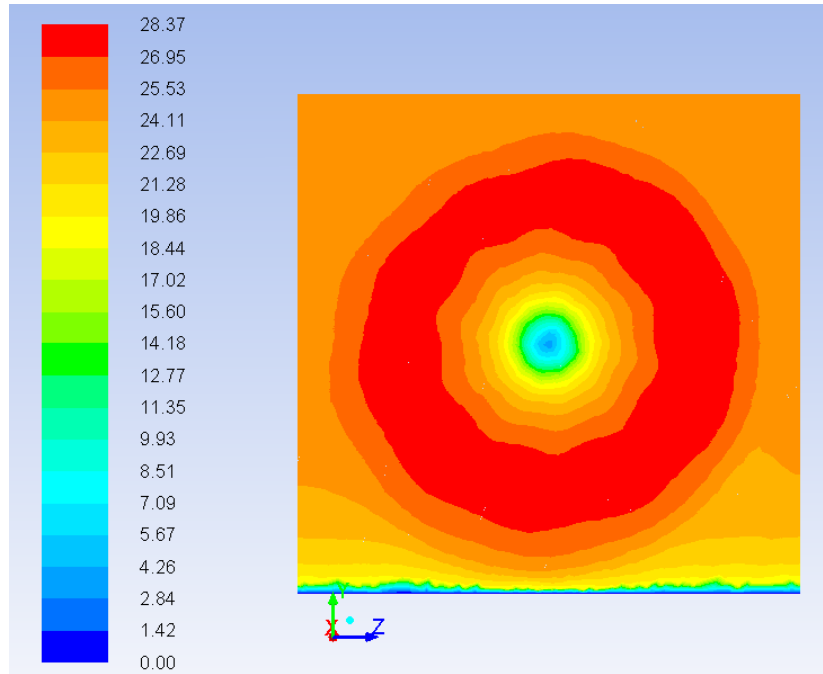
Configuration 3 – Acoustic Data Set
Axial Velocity Contour Plot at Rear Interface Plane includes Boundary Layer
 $J = 0.48$ (Local Scale)



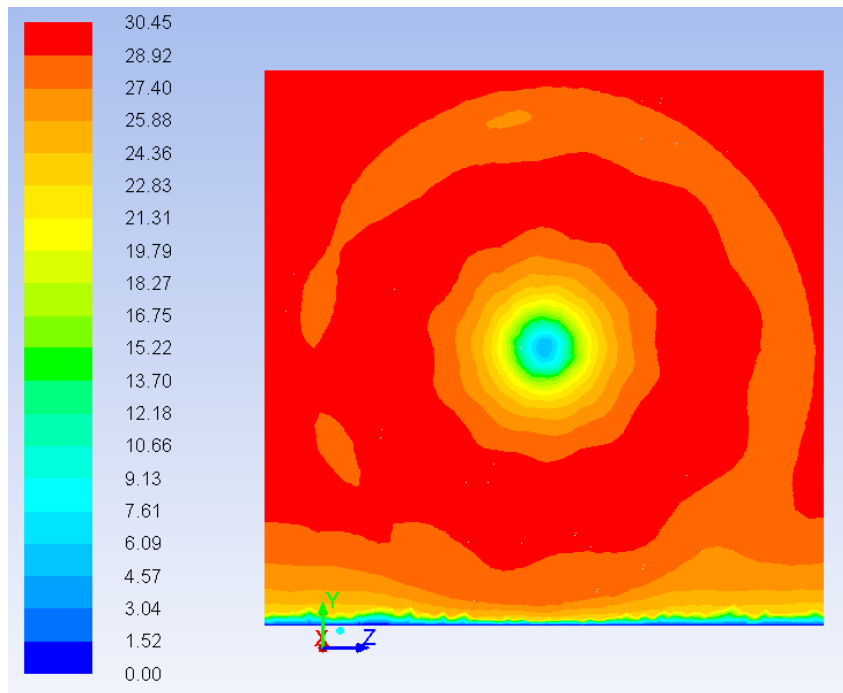
Configuration 3 – Acoustic Data Set
Axial Velocity Contour Plot at Rear Interface Plane includes Boundary Layer
 $J = 0.72$ (Local Scale)



Configuration 3 – Acoustic Data Set
Axial Velocity Contour Plot at Rear Interface Plane includes Boundary Layer
 $J = 0.96$ (Local Scale)



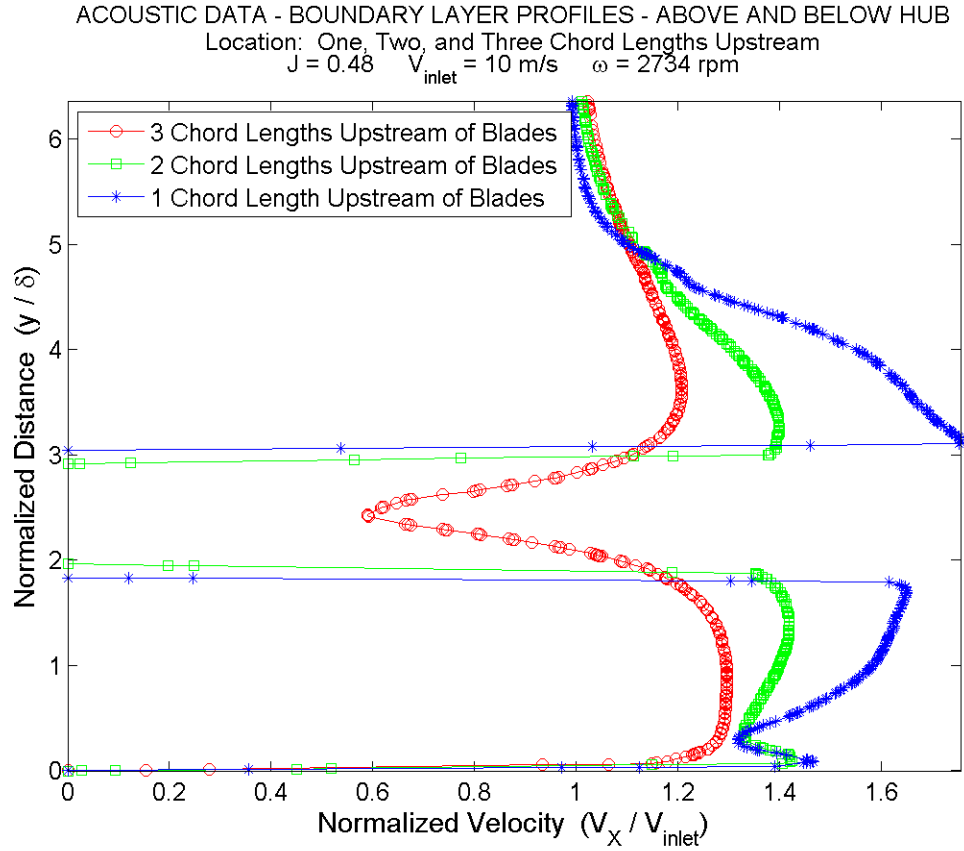
Configuration 3 – Acoustic Data Set
Axial Velocity Contour Plot at Rear Interface Plane includes Boundary Layer
 $J = 1.20$ (Local Scale)



Configuration 3 – Acoustic Data Set
Axial Velocity Contour Plot at Rear Interface Plane includes Boundary Layer
 $J = 1.44$ (Local Scale)

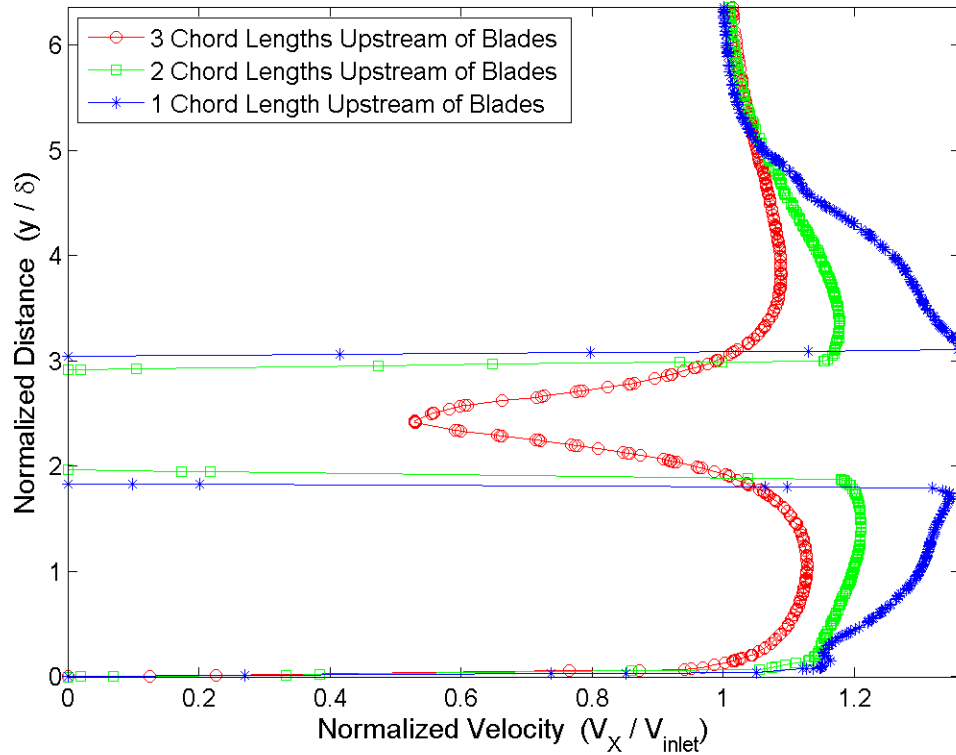
APPENDIX E

ACOUSTIC DATA: COMBINED BOUNDARY LAYER PROFILES AT NEAR STATIONS



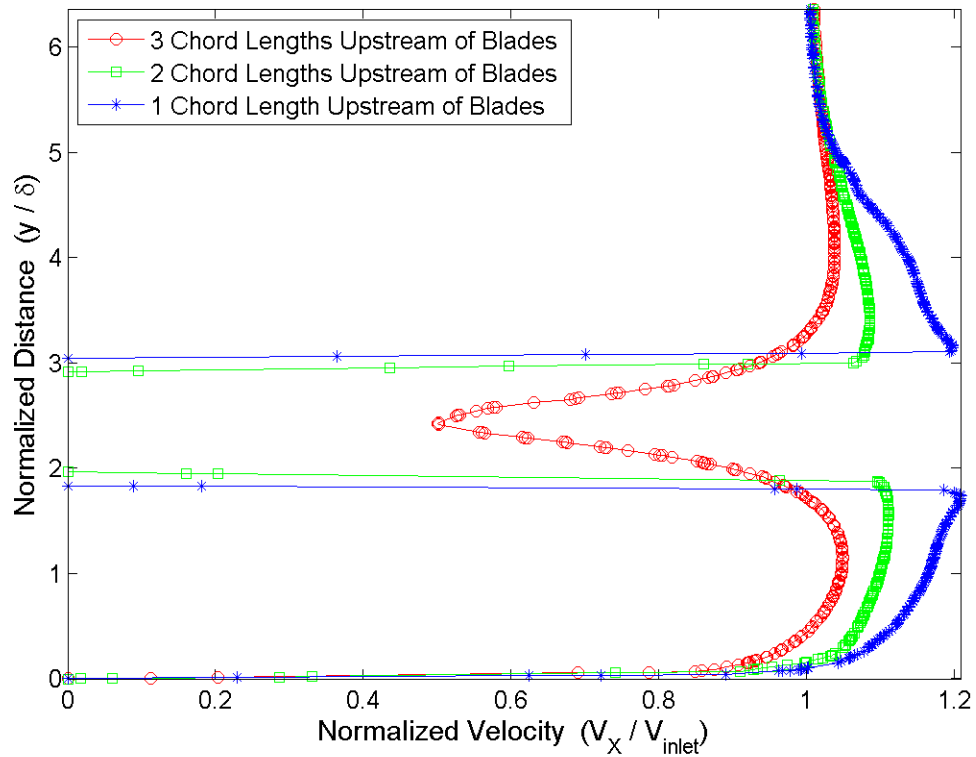
Configuration 3 Case for $J = 0.48$
 Boundary layer profiles at all near upstream stations above and below hub sections demonstrating the change in boundary layer profile with location.

ACOUSTIC DATA - BOUNDARY LAYER PROFILES - ABOVE AND BELOW HUB
 Location: One, Two, and Three Chord Lengths Upstream
 $J = 0.72$ $V_{inlet} = 15 \text{ m/s}$ $\omega = 2734 \text{ rpm}$



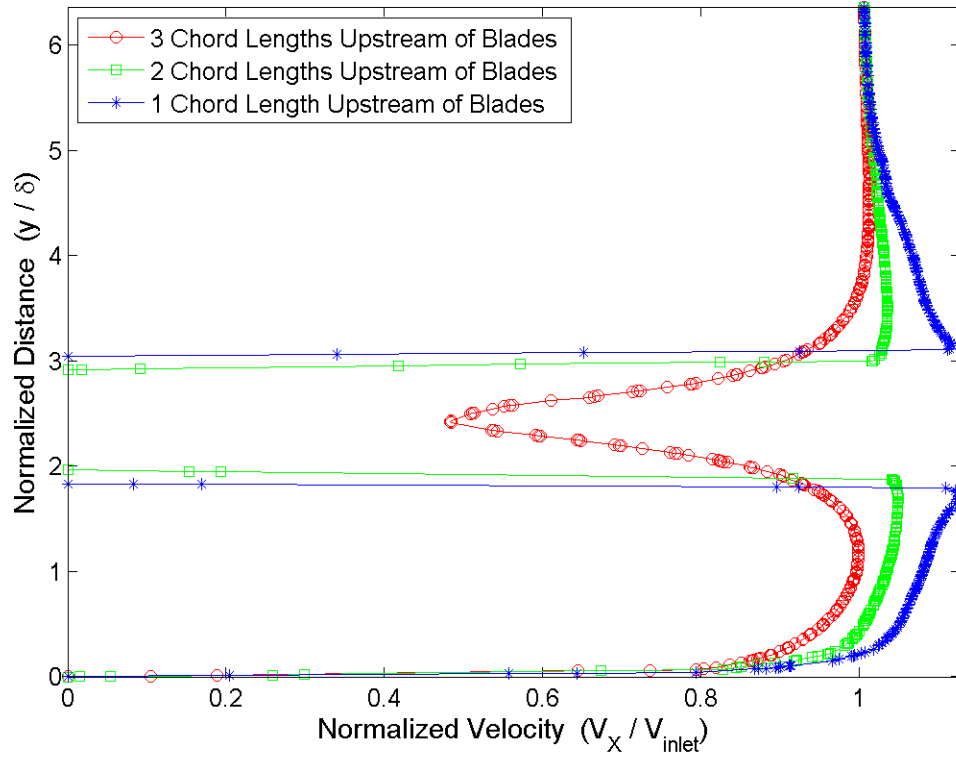
Configuration 3 Case for $J = 0.72$
 Boundary layer profiles at all near upstream stations above and below hub sections demonstrating the change in boundary layer profile with location.

ACOUSTIC DATA - BOUNDARY LAYER PROFILES - ABOVE AND BELOW HUB
 Location: One, Two, and Three Chord Lengths Upstream
 $J = 0.96$ $V_{inlet} = 20 \text{ m/s}$ $\omega = 2734 \text{ rpm}$



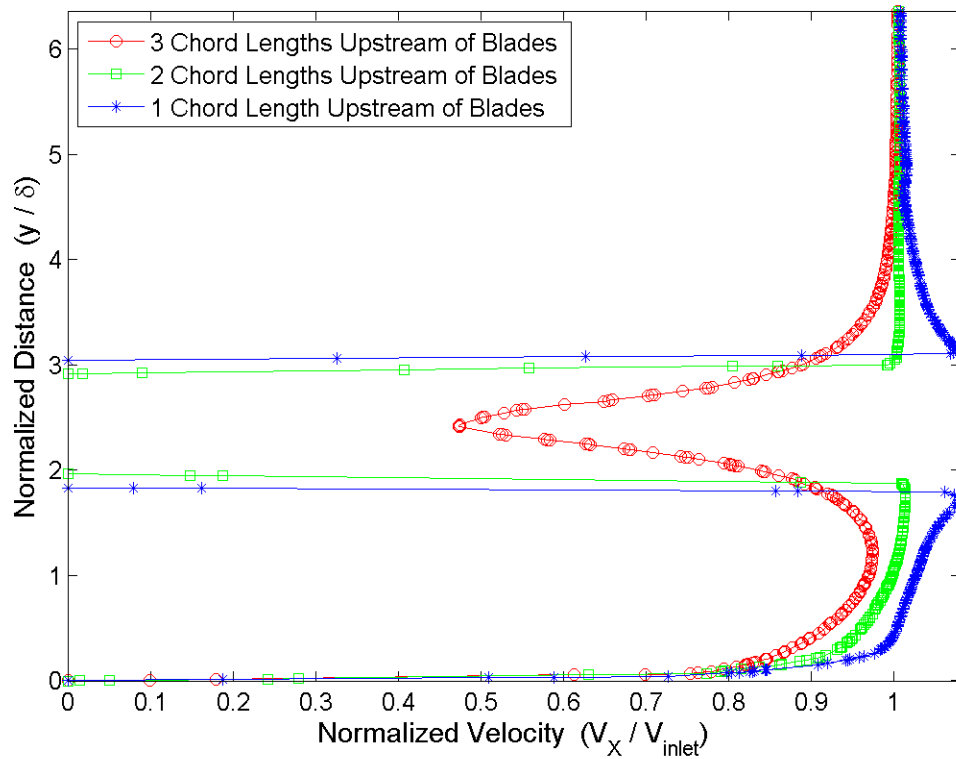
Configuration 3 Case for $J = 0.96$
 Boundary layer profiles at all near upstream stations above and below hub sections demonstrating the change in boundary layer profile with location.

ACOUSTIC DATA - BOUNDARY LAYER PROFILES - ABOVE AND BELOW HUB
 Location: One, Two, and Three Chord Lengths Upstream
 $J = 1.2$ $V_{inlet} = 25 \text{ m/s}$ $\omega = 2734 \text{ rpm}$



Configuration 3 Case for $J = 1.20$
 Boundary layer profiles at all near upstream stations above and below hub sections demonstrating the change in boundary layer profile with location.

ACOUSTIC DATA - BOUNDARY LAYER PROFILES - ABOVE AND BELOW HUB
 Location: One, Two, and Three Chord Lengths Upstream
 $J = 1.44$ $V_{inlet} = 30 \text{ m/s}$ $\omega = 2734 \text{ rpm}$



Configuration 3 Case for $J = 1.44$
 Boundary layer profiles at all near upstream stations above and below hub sections demonstrating the change in boundary layer profile with location.

REFERENCES

- [1] S. J. Majumdar and N. Peake, "Noise Generation by the Interaction between Ingested Turbulence and a Rotating Fan," *J. Fluid Mech.*, vol. 359, pp. 181-216, 1998.
- [2] J. E. Kerwin, "Marine Propellers," *Annual Reviews Fluid Mech.*, vol. 18, pp. 367-403, 1986.
- [3] J. I. Hileman, Z. S. Spakovszky, M. Drela, and M. A. Sargeant, "Airframe Design for "Silent Aircraft"," *AIAA* , vol. 8, no. 11, 2007.
- [4] A. Ko, J. A. Schetz, and W. H. Mason, "Assessment of the Potential Advantages of Distributed-Propulsion for Aircraft," Virginia Tech University, Cleveland, ISABE-2003-1094, 2003.
- [5] M. Sevik, "Sound Radiation from a Subsonic Rotor Subjected to Turbulence," Pennsylvania State University, Symposium on Fluid Mechanics, Acoustics and Design of Turbomachinery NASA SP 304, August 1970.
- [6] S. A. L. Glegg, W. Devenport, W. N. Alexander, M. Morton, and A. Borgoltz, "Rotor Inflow Noise Caused by a Boundary Layer: Inflow Measurements and Noise Predictions," Florida Atlantic University & Virginia Tech University, AIAA paper 2012.
- [7] A. M. O. Smith and H. E. Roberts, "The Jet Airplane Utilizing Boundary Layer Air for Propulsion," *Journal of the Aeronautical Sciences*, vol. 14, no. 2, pp. 97-109, 1947.
- [8] A. P. Plas, M. A. Sargeant, V. Madani, D. Crichton, E. M. Greitzer, T. P. Hynes and C. A. Hall, "Performance of a Boundary Layer Ingesting (BLI) Propulsion System," *AIAA*, vol. 8, no. 11, January 2007.
- [9] W. J. M. Rankine, "On the Mechanical Principles of the Action of Propellers," *Trans. Inst. Nav. Arch.*, vol. 6, no. 13, 1865.

- [10] S. Goldstein, "On the Vortex Theory of Screw Propellers," *Proc. R. Soc. Lond. A*, vol. 123, pp. 440-465, 1929.
- [11] L. Prandtl, "Applications of Modern Hydrodynamics to Aeronautics," *National Advisory Committee for Aeronautics*, no. 7, pp. 157-215, 1921.
- [12] H. Ludwig and J. Ginzel, "Zur Theorie der Breitblattschraube," *Aerodyn. Versuchsanst., Gottingen*, Ger, Rep. 44/A/08, 1944.
- [13] H. W. Lerbs, "Moderately loaded Propellers with a Finite Number of Blades and an Arbitrary Distribution of Circulation," *Soc. Nav. Archit. Mar. Eng. Trans.*, vol. 60, pp. 73-117, 1952.
- [14] G. G. Cox, "Corrections to the Camber of Constant Pitch Propellers," *Q. Trans. R. Inst. Nav. Archit.*, vol. 103, pp. 227-243, 1961.
- [15] M. J. Lighthill, "A New Approach to Thin Aerofoil Theory," *Aeronaut. Q.*, vol. 3, pp. 193-210, 1951.
- [16] W. M.B. Morgan, V. Silovic, and S. B. Denny, "Propeller Lifting-Surface Corrections," *The Society of Naval Architects and Marine Engineers*, vol. 76, pp. 309-347, Nov. 1968.
- [17] T. E. Brockett, "Lifting Surface Hydrodynamics for Design of Rotating Blades," in *SNAME Propellers '81 Symp*, Virginia Beach, 1981, pp. 357-378.
- [18] D. S. Greeley and J. E. Kerwin, "Numerical Methods for Propeller Design and Analysis in Steady Flow," *Soc. Nav. Archit. Mar. Eng. Trans.*, vol. 90, pp. 415-453, 1982.
- [19] C. E. Lan, "A Quasi-Vortex-Lattice Method in Thin Wing Theory," *J. Aircr.*, vol. 11, pp. 518-527, 1974.
- [20] M. K. Eckhart and W. B. Morgan, "A Propeller Design Method," *Soc. Nav. Archit. Mar. Eng. Trans.*, vol. 63, pp. 325-374, 1955.
- [21] J. D. van Manen, "Fundamentals of Ship Resistance and Propulsion. Part B: Propulsion," *Neth. Ship Model Basin*, Wageningen, Publication 132a, 1957.
- [22] J. E. Kerwin, "Machine Computation of Marine Propeller Characteristics," *Int. Shipbuild Program.*, vol. 6, pp. 343-354, 1959.

- [23] S. Tsakonas, W. R. Jacobs, and M. R. Ali, "An Exact Linear Lifting Surface Theory for a Marine Propeller in a Nonuniform Flow Field," Stevens Institute of Technology, R&D SIT-DL-72-1509, 1972.
- [24] J. Moran, "An Introduction to Theoretical and Computational Aerodynamics," New York, Wiley, 1984, p. 464.
- [25] K. H. Kim and S. Kobayashi, "Pressure Distribution on Propeller Blade Surface Using Numerical Lifting Surface Theory," in *SNAME Propellers '84 Symp.*, Virginia beach, Va., 1974.
- [26] J. L. Hess and W. O. Valarezo, "Calculation of Steady Flow about Propellers by Means of a Surface Panel Method," AIAA Paper 85-0283, 1985.
- [27] M. H. Wang, "Hub Effects in Propeller Design and Analysis," MIT, Cambridge, PhD Thesis 1985.
- [28] M. Abdel-Maksoud, M. Greve, M. Scharf, T. Rung, and K. Wockner, "Unsteady Viscous/Inviscid Coupling Approaches for Propeller Flow Simulations," Hamburg University of Technology, Hamburg, Report June 2011.
- [29] L. I. Da-Qing, "Validation of RANS Predictions of Open Water Performance of a Highly Skewed Propeller with Experiments," *Journal of Hydrodynamics, Ser.*, vol. 18, no. 3, pp. 520-528, July 2006.
- [30] A. Zachariadis and C. A. Hall, "Application of a Navier-Stokes Solver to the Study of Open Rotor Aerodynamics," *Journal of Turbomachinery*, vol. 133, July 2011.
- [31] S. Gaggero, D. Villa, and S. Brizzolara, "RANS and PANEL Method fo Unsteady Flow Propeller Analysis," *Journal of Hydrodynamics, Ser. B*, vol. 22, no. 5, pp. 564-569, October 2010.
- [32] G. Kuiper, "New Developments and Propeller Design," *Journal of Hydrodynamics, Ser. B*, vol. 22, no. 5, pp. 7-16, October 2010.
- [33] J. H. Horlock, "Actuator Disk Theory," in *Discontinuities in Thermo-Fluid Dynamics*. UK: McGraw-Hill Inc., 1978, ch. 2, pp. 26-29.
- [34] J. Carlton, "Theoretical Methods," in *Marine Propellers and Propulsion.*: Butterworth-Heinemann, 2007, pp. 138-204.

- [35] W. Froude, "On the Elementary Relation between Pitch, Slip, and Propulsion Efficiency," *Trans. RINA*, vol. 19, 1878.
- [36] R. E. Froude, "On the Part Played in the Operation of Propulsion Differences in Fluid Pressure," *Trans. RINA*, vol. 30, 1889.
- [37] J. T. Conway, "Analytical Solutions for the Actuator Disk with Variable Radial Distribution of Load," *J. Fluid Mech.*, vol. 297, pp. 327-355, 1995.
- [38] G. R. Hough and D. E. Ordway, "Developments in Theoretical and Applied Mechanics," vol. 2, pp. 317-336, 1965.
- [39] J. A. Fay, "Introduction to Fluid Mechanics," Cambridge, MIT Press, 1994, pp. 495-548.
- [40] L. Prandtl, "Königliche Gesellschaft der Wissenschaften zu Göttingen," *Tragflügeltheorie*, 1918.
- [41] F. W. Lanchester, *Aerodynamics*. London: A. Constable & co., 1907.
- [42] J. D. Anderson, *Fundamentals of Aerodynamics*. Boston: McGraw-Hill, 2001.
- [43] I. H. A. Abbott and A. E. von Doenhoff, *Theory of Wind Sections*.: Courier Dover Publications, 1959.
- [44] A. Betz, "Schraubenpropeller mit Geringstem Energieverlust," *K. Ges. Wiss. Göttingen Nachr. Math.-Phys. Klasse 1919*, pp. 193-217, 1919.
- [45] M. Strscheletsky, "Hydrodynamische Grundlagen zur Berechnung der Schiffscharanben," G. Braun, Karlsruhe, 1950.
- [46] R. Guilloton, "Calcul des Vitesses Induites en Vue du Trace des Helices," *Schiffstechnik*, vol. 4, 1957.
- [47] J. A. Sparenberg, "Application of Lifting Surface Theory to Ship Screws," *Proc. K. Ned. Akad. Wet. Ser B.*, vol. 62, 1959.
- [48] P. C. Pien, "The Calculation of Marine Propellers Based on Lifting Surface Theory," *J. Ship Res.*, vol. 5, no. 2, 1961.
- [49] J. E. Kerwin and C. Lee, "Prediction of Steady and Unsteady Marine Propeller Performance by Numerical Lifting Surface Theory," SNAME, Annual Meeting Paper No. 8, 1978.

- [50] J. L. Hess and A. M. O. Smith, "Calculation of Potential Flow about Arbitrary Bodies," *Prog. Aeronaut. Sci.*, vol. 8, 1967.
- [51] T. Hoshino, "Hydrodynamic Analysis of Propellers in Steady Flow Using a Surface Panel Method," in *Trans. Soc. Nav. Arch Jap.*, 1989.
- [52] A. N. Kolmogorov, "Equations of Turbulent Motion of an Incompressible Fluid," *Izvestia Academy of Sciences, USSR; Physics*, vol. 6, no. 1-2, pp. 56-58, 1942.
- [53] R. Muscari and A. Di Mascio, "Simulation of the Flow around Complex Hull Geometries by an Overlapping Grid Approach," in *Proc 5th Osaka Colloquium*, Japan, 2005.
- [54] C. T. Hsiao and G.L. Chahine, "Numerical Simulation Of Bubble Dynamics in a Vortex Flow Using Navier–Stokes Computations and Moving Chimera Grid Scheme," Pasadena, CAV2001, 2001.
- [55] J. Kim, E. Paterson, and F. Stern, "Verification and Validation and Sub-Visual Cavitation and Acoustic Modeling for Ducted Marine Propulsor," in *Proc. 8th Symp. on Numerical Ship Hydrodyn.*, Seoul, 2003.
- [56] P. R. Spalart and S. R. Allmaras, "A One-Equation Turbulence Model for Aerodynamic Flows ," in *AIAA, Aerospace Sciences Meeting and Exhibit, 30th*, Reno, 1992.
- [57] W. P. Jones and B. E. Launder, "The Prediction of Laminarization with a Two-Equation Model of Turbulence," *International Journal of Heat and Mass Transfer*, vol. 15, pp. 301-314, 1972.
- [58] K. Y. Chien , "Predictions of Channel and Boundary Layer Flows with Low-Reynolds-Number Turbulence Model," *AIAA Journal*, vol. 20, no. 1, pp. 33-38, 1982.
- [59] F. R. Menter, "Two Equation Eddy-Viscosity Turbulence Models for Engineering Applications," *AIAA Journal*, vol. 32, no. 8, pp. 1598-1605, 1994.
- [60] F. R. Menter, "Zonal Two Equation k-w Turbulence Models for Aerodynamic Flows," 24th Fluid Dynamics Conference, AIAA Paper 93-2906, 1993.
- [61] D. C. Wilcox, "Turbulence Energy Equation Models," in *Turbulence Modeling for CFD*. La Canada, California: DCW Industries Inc., 1993, ch. 4, pp. 73-92.

- [62] D. C. Wilcox, "Reassessment of the Scale-Determining Equation for Advanced Turbulence Models," *AIAA*, vol. 26, no. 11, pp. 1299-1310, 1988.
- [63] D. C. Wilcox, "Formulation of the k-omega Turbulence Model Revisited," *AIAA Journal*, vol. 46, no. 11, pp. 2823-2838, 2008.
- [64] S.H. Rhee and S. Joshi, "CFD Validation for a Marine Propeller Using an Unstructured Mesh based RANS Method," in *Proc. FEDSM '03*, Honolulu, 2003.
- [65] J. Smagorinsky, "General Circulation Experiments with the Primitive Equations," *Monthly Weather Review*, vol. 91, no. 3, pp. 99-164, March 1963.
- [66] S. B. Pope, *Turbulent Flows*. New York: Cambridge University Press, 2000.
- [67] F. Salvatore, H. Streckwall, and T. van Terwisga, "Propeller Cavitation Modelling by CFD- Results from the VIRTUE 2008 Rome Workshop," in *First International Symp. on Mar. Prop.*, Trondheim, 2009.
- [68] ANSYS, Inc., "ANSYS FLUENT Theory Guide," ANSYS, Inc., Canonsburg, 2012.
- [69] Ismail B. Celik. (1999, December) Introductory Turbulence Modeling. Lecture Notes. [Online].
http://www.fem.unicamp.br/~im450/palestras%26artigos/ASME_Tubulence/cds13workbook.pdf
- [70] Cuong Nguyen. (2005, November) MIT. [Online].
http://www.mit.edu/~cuongng/Site/Publication_files/TurbulenceModeling_04NOV05.pdf
- [71] Theodore von Kármán, "Mechanical Similitude and Turbulence," National Advisory Committee for Aeronautics, Washington, NACA no. 611, 1931.
- [72] C. M. Rhie and W. L. Chow, "Numerical Study of the Turbulent Flow Past an Airfoil with Trailing Edge," *AIAA Journal*, vol. 21, no. 11, pp. 1525-1532, November 1983.
- [73] ANSYS, Inc., "ANSYS FLUENT User's Manual," ANSYS, Inc., Canonsburg, 2012.
- [74] M. A. Morton, "Rotor Inflow Noise Caused by a Boundary Layer: Inflow Measurements and Noise Predictions," Virginia Tech, Blacksburg, Thesis 2012.
- [75] ANSYS, Inc., "ANSYS ICEM CFD Help Manual," 2012.

- [76] (2013, February) Research Facilities: Stability Wind Tunnel Aerodynamic Qualities. [Online].
<http://www.aoe.vt.edu/research/facilities/stabilitytunnel/aerodynamics-stabilitytunnel.html>
- [77] ANSYS UDF Tutorial. [Online]. http://www.personal.soton.ac.uk/zxie/SESS6021/udf_tut1.pdf
- [78] J. N. Newman, "Marine Hydrodynamics.," The MIT Press, Cambridge, MA., Electronic Source VM156.N48, 1977.
- [79] Virginia Tech, "Research Facilities," [Online].
<http://www.aoe.vt.edu/research/facilities/stabilitytunnel/description-stabilitytunnel.html>